Bidirectional transport by molecular motors

Online published at the
Publikationsserver der Universität Potsdam:
http://opus.kobv.de/ubp/volltexte/2008/1871/
urn:nbn:de:kobv:517-opus-18715
[http://nbn-resolving.de/urn:nbn:de:kobv:517-opus-18715]

Bidirectional transport by molecular motors

Dissertation

zur Erlangung des akademischen Grades
Doktor der Naturwissenschaften (Dr. rer. nat.)
in der Wissenschaftsdisziplin Theoretische Physik

eingereicht an der
Mathematisch-Naturwissenschaftlichen Fakultät
der Universität Potsdam

angefertigt am
Max-Planck-Institut
für Kolloid- und Grenzflächenforschung Potsdam

von

Melanie J.I. Müller

Potsdam, im Januar 2008

Für meine Mutter.

Abstract

The complex internal structure of biological cells depends to a large extent on active transport of vesicles, organelles and other types of cargo. The long-range intracellular traffic is powered by molecular motors which transport these cargos along microtubule filaments. The microtubules possess an intrinsic direction, having a 'plus' and a 'minus' end. Some molecular motors such as cytoplasmic dynein walk to the minus end, while others such as conventional kinesin walk to the plus end. Cells typically have an isopolar microtubule network. This is most pronounced in long cellular processes like neuronal axons or fungal hyphae. In these long and thin tubular protrusions, the microtubules are arranged parallel to the tube axis with the minus ends pointing to the cell body and the plus ends pointing to the tip.

In such a tubular compartment, transport by only one motor type leads to 'motor traffic jams'. Kinesins and kinesin-driven cargos accumulate at the tip, while dyneins and dynein-driven cargos accumulate near the cell body. We identify the relevant length scales and characterize the jamming behaviour in these tube geometries by using both Monte Carlo simulations and analytical calculations. In axons and hyphae, such traffic jams have been observed upon overexpression of a specific motor.

A possible solution to this jamming problem is to use cargos which can travel into both plus and minus direction. Indeed, in the cell many cargos travel bidirectionally, changing direction every few seconds. They are transported by a team of plus and a team of minus motors. The presumably simplest mechanism for such bidirectional transport is provided by a tug-of-war between the two motor teams which is governed by mechanical motor interactions only. We develop a stochastic tug-of-war model and study it with numerical and analytical calculations. We find a surprisingly complex cooperative motility behaviour.

Depending on the number and properties of the motors, the cargo is in one of seven possible motility regimes. These regimes are characterized by qualitatively different trajectories and velocity distributions. For biologically relevant parameter ranges, the cargo switches between fast plus and fast minus motion, as observed in cells. This fast motion, which is often thought to be incompatible with a 'hampering' tug-of-war, is caused in our model by a dynamic instability arising from the nonlinear reaction of single motors to force.

In our model, the motility behaviour of the cargo is very sensitive to the motor properties. Small changes in the motor properties can lead to drastic changes in cargo transport, e.g. from fast plus motion to bidirectional motion or no motion. This sensitivity can be used by the cell to regulate its cargo traffic in a simple and efficient manner.

We compare the results of our model to the available experimental data, which we reproduce qualitatively and quantitatively. Furthermore, we calculate dynamic quantities such as switch times, velocity distributions, or the reaction to external perturbations. These predictions can be tested in future experiments.

Contents

Chapter 1

Introduction

The complex internal structure of biological cells depends to a large extent on active transport: Vesicles shuttle between different cellular compartments, others travel from the cell center to the periphery or vice versa, but also filaments, RNA, chromosomes, and even viruses are permanently on the move within cells [2, 137]. An extreme example is the long-range transport of vesicles and organelles along the axons of nerve cells [38], which can be up to a metre in length. Most of this traffic is based on the molecular motors kinesin, dynein and myosin, which move along cytoskeletal filaments [54, 137]. These motors catalyze the hydrolysis of adenosine-triphosphate (ATP), and transform the free energy released from this reaction into active movements and mechanical work. In the following, we will focus on the long-range traffic inside cells which is accomplished by molecular motors walking along microtubule filaments. These motors are processive: they can make many chemo-mechanical steps while staying bound to the filament. In the remaining of this chapter, we will introduce these molecular motors and their motion on cellular length scales in more detail, and give an overview over the following chapters.

1.1 Motion on small length scales

The cell is the structural and functional unit of all living organisms. Its interior has an elaborate architecture, comparable to a metropolitan city. It contains functionally distinct units, the organelles, and a traffic network, the cytoskeleton with molecular motors moving on it.

Motors as nano-trucks. The active cellular traffic is mainly accomplished by molecular motors. These molecular motors are 'nano-trucks' which travel along a 'road-network' consisting of cytoskeletal filaments and transport various cargos like vesicles or organelles. Thereby they consume as fuel the cellular 'energy-currency' ATP, see Tab. 1.1. Although this analogy is catchy, the length and time scales of both systems are very different: while trucks are m-sized vehicles moving at a speed of km/h, molecular motors are nm-sized proteins that move at μm/s. This has important consequences for the physics of their motion. In contrast to the large trucks, inertia is negligible for the tiny motor molecules. Their motion is dominated by viscous forces and Brownian motion. Molecular motors are permanently hit by other molecules, which makes their motion like 'walking in a strong storm'.

	size	track	fuel	cargo	velocity
molecular motor	$\sim$ nm	cytoskeletal filament	ATP	vesicles, organelles etc.	$\sim \mu$m/s
street truck	$\sim$ m	asphalt road	petrol	various goods	$\sim$ km/h

Tab. 1.1: Analogy of molecular motors and trucks used by humans: While the m-sized street trucks transport various goods along asphalt roadsat a speed of km/h and consume petrol, the nm-sized molecular motors transport cargos such as vesicles and organelles along cytoskeletal filaments at a velocity of about μm/s and consume ATP.

Brownian motion. The relative importance of deterministic motion at speed v to Brownian motion with diffusion constant D can be estimated by considering the Péclet number V:

$$V = \frac{Lv}{D} = \frac{L^2/D}{L/v} \sim \frac{\text{time for diffusion over distance } L}{\text{time for active transport over } L} \tag{1.1}$$

The diffusion constant D is closely related to friction, because both diffusion and friction are based on the interaction with the many molecules of the surrounding solution. In mathematical terms, this is expressed by the Einstein relation

$$D = \mathrm{k_B}T/\gamma_\mathrm{S}, \tag{1.2}$$

where γ_S is the Stokes friction coefficient and $\mathrm{k_B}\,T$ is the thermal energy, the product of the Boltzmann constant $\mathrm{k_B}$ and the absolute temperature T. The Stokes friction coefficient is related to the particle hydrodynamic radius r via $\gamma_\mathrm{S} = 6\pi\eta r$. Thus, for a molecule of size r at room temperature in water, which has a viscosity $\eta \approx 10^{-3}\,\mathrm{pN\,s/\mu m^2}$, the diffusion constant is

$$D = \frac{\mathrm{k_B}T}{6\pi\eta r} \approx 0.25\,\frac{\mu\mathrm{m}^2}{s}\frac{1}{r/\mu\mathrm{m}}. \tag{1.3}$$

It scales inversely with the particle size r. Therefore, the time $t \sim x^2/D$ to travel a distance x by diffusion increases linearly with the particle size r and quadratically with the distance x. In consequence, small particles like ions or small proteins diffuse fast, while large particles like large proteins, vesicles or organelles diffuse slowly. For example, the diffusion of a $10\,\mu$m-sized with radius 0.1 nm over a distance of $10\,\mu$m, which is a typical cell size, takes only 25 ms. However, a 500 nm-sized organelle needs 2 min to cover the same distance. In extreme cases of distances like 1 m, the size of some neuron cells, the diffusion time is 10^{12} s, i.e. 30 millennia!

In the cell, diffusion is slowed down compared to aqueous solution due to crowdedness and filament meshworks [94]. The cytoplasm is a complicated medium with viscoelastic properties. For our purpose this can be accounted for by using an apparent viscosity which depends on the particle size: large particles feel a higher viscosity and thus have a smaller diffusion constant than small ones. For small particles with radii smaller than 50 nm, diffusion is decreased by about a factor of 10 compared to water, while for particles with radii of $0.1 - 1\,\mu$m one has

$$D(\text{cytoplasm}) \approx \left(10^{-2}\text{-}10^{-3}\right)\, D(\text{water}). \tag{1.4}$$

For even larger particles, diffusion may be completely suppressed due to 'caging' of these particles in the cytoplasmic filament network and by protein crowding [94].

In consequence, diffusion is insufficient for cellular transport. The cell needs active transport by molecular motors. The Péclet number as given by Eq. (1.1) of a motor transporting a cargo of $0.1 - 1\,\mu$m through water at a speed of $1\,\mu$m/s is of order unity. Therefore Brownian and deterministic motion are both important. Deterministic active motion by molecular motors is essential for cellular transport, but the motion is inherently stochastic.

1.2 Molecular motors

We now consider molecular motors and their motion on the cytoskeletal filaments in more detail.

The cytoskeleton. The cytoskeleton is a network of microtubules, actin filaments, and intermediate filaments, which are spread throughout the cell. Only microtubules and actin filaments are used for transport by molecular motors. The microtubules (MTs) form a structured network spanning the whole cell, and serve as 'highways' for long-range cellular traffic. The actin filaments, on the contrary, form a dense meshwork concentrated near the cell cortex, and serve as 'side roads' for short-range traffic. Both types of filaments act as 'one-way-streets' because they possess an intrinsic direction, with one end called the 'plus end' and the other end called the 'minus end'. A specific molecular motor always walks towards one end of the filament.

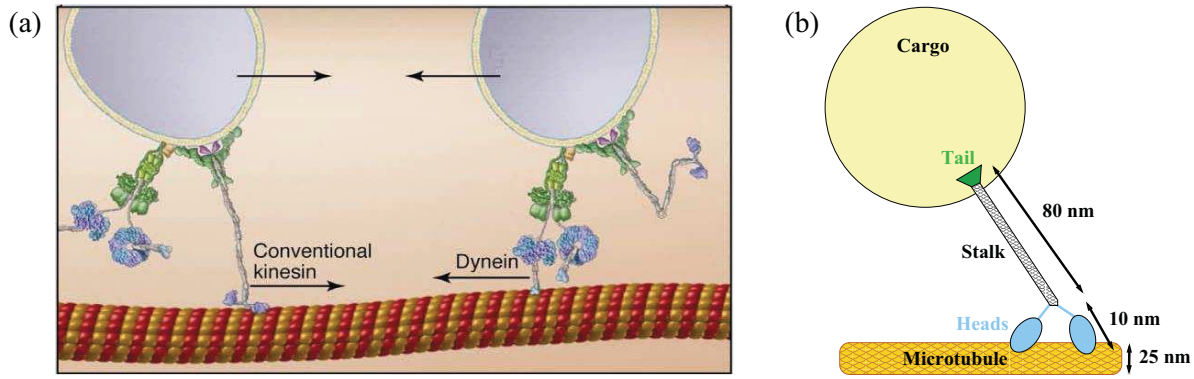

Fig. 1.1: Cargo transport by molecular motors: (a) Kinesin and dynein transport cargo to the MT plus and minus end, respectively. Both motors are complicated protein complexes. The main motor functionality is accomplished by two homodimerized heavy chains which form a stalk (gray) with one end involved in MT binding (blue) and the other in cargo binding (purple). MT binding occurs at the heads (blue) which serve as feet when the motor steps forward. ATP hydrolysis occurs in the motor domains, which are identical with the MT-binding heads for kinesin, but which are arranged in a ring-like structure at some distance from the MT for dynein. Cargo binding involves several light or intermediate chains (green). From [160]. (b) Molecular dimensions of kinesin: A kinesin has a length of about 80 nm. The MT-binding heads are globular of about 10 nm in size, even smaller than the MT diameter of 25 nm.

Motor structure. Molecular motors are rather complicated protein complexes, as illustrated for the motors kinesin 1 and cytoplasmic dynein in Fig. 1.1(a). These motors are the most prominent members of a whole 'zoo' of molecular motors, see e.g. [160]. While the dynein family consists of only two subclasses, axonemal and cytoplasmic dyneins, the kinesin family has more than ten subclasses. All dyneins walk to the MT minus end and most kinesins walk to the MT plus end. Furthermore several classes of myosins mediate transport on actin filaments.

Stepping mechanism, ATP consumption. Molecular motors rather 'walk' or 'run' than 'drive'. The motor kinesin 1 makes alternate forward steps with its two heads similar to a walking human. The MT filament consists of 13 protofilaments aligned in parallel, each of which provides a track for the motor with a binding site every 8 nm. Kinesin moves forward by a 'hand-over-hand' mechanism', alternately throwing forward one of the two heads while the other remains bound to the MT. For each step, it consumes one fuel-molecule ATP.

The motors considered here act as ATPases, i.e. as enzymes that catalyze the hydrolysis of ATP into adenosine diphosphate ADP and inorganic phosphate P_i. Since the concentrations of ATP, ADP and P_i are kept far from equilibrium in the cell, this hydrolysis releases a free energy of about $20\,k_BT \approx 80\,\mathrm{pN}\cdot\mathrm{nm}$ [54]. The motor uses this energy to move forward on the MT and thereby accomplishes chemomechanical coupling: it converts chemical energy stored in the ATP molecule into mechanical motion. This coupling assures that the order of breaking and making bonds is not the microscopically reversible. This assures that the system is out of equilibrium, which would forbid net average directed motion by the second law of thermodynamics.

1.3 *In vitro* experiments

During the past 20 years, molecular motors have attracted more and more interest. The structure of many motors has been resolved by X-ray crystallography, and the transport properties of many motors have been studied *in vivo* and *in vitro*. Two basic experimental setups are used to measure transport properties of the motor *in vitro*: the gliding and the bead assay, see Fig. 1.2.

In the **gliding assay**, motors are adsorbed with their cargo domain to a glass substrate, where they are immobilized but not inactivated. When MTs in the solution come close to the substrate, they are captured by the motors and then transported along the surface in a 'gliding' motion.

In the **bead assay**, the geometry is 'inverted': MTs are attached to the substrate, and the

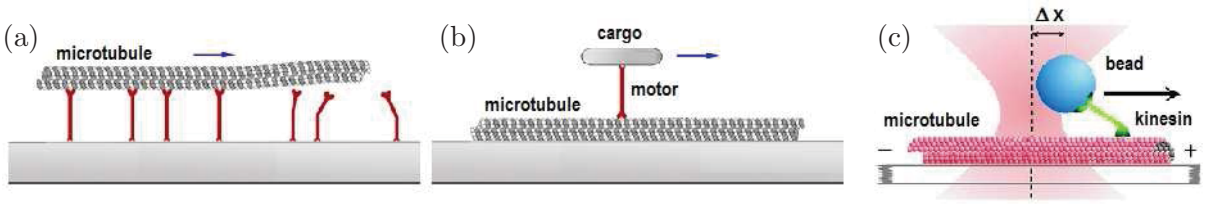

Fig. 1.2: *In vitro* motility assays: (a) In the gliding assay, the motors are attached to a surface and propel MTs. (b) In the bead assay, a motor transports a bead along a MT. (c) In an optical trap, the bead is trapped by a focused laser beam which exerts a force on the bead proportional to the distance Δx from the center of the trap. Adapted from [11, 169].

motors, bound to a bead, diffuse in the solution until they find a MT and walk on it. The motion of the bead can then be monitored in a light microscope.

Although the geometry of the two assays is different, they provide the same basic information. However, in order to acquire information about the motion of a single motor, the bead assay is more useful, because in a typical gliding assay more than one motor drives the motion of a single MT, while it is only a single motor that propels the bead in a typical bead assay. Furthermore, in a bead assay an optical trap can be employed to exert a controlled force, see Sec. 2.2.

An **optical trap** uses light to manipulate microscopic dielectric objects, see Fig. 1.2(c). The radiation pressure from a focused laser beam is able to trap small particles ranging in size from 10 nm to over 10 μm and to exert forces on them in the pN-range. When a bead with a single motor is trapped, one can study the motion of this single motor under force.

1.4 Bidirectional motor traffic

As described above, motors move in a directed way along the cytoskeletal filaments which act as 'one-way roads' for the motors: a specific motor always walks in only one direction along the filament. For example, most kinesins walk to the MT plus end, and dyneins walk to the MT minus end as shown in Fig. 1.1(a).

Isopolar cytoskeleton. Cells typically have an 'isopolar' MT cytoskeleton [83], see Fig. 1.3. In a 'round' cell like a fibroblast cell, for example, MTs are arranged radially, with their minus ends close to the nucleus at the cell centre and their plus end directed outward to the cell periphery. In epithelial cells, MTs form a parallel array with their minus ends pointing to the apical and their plus ends to the basolateral surface. The isopolar MT arrangement is most pronounced in long cellular processes like neuronal axons or fungal hyphae. In these long and thin tubular protrusions, the MTs are arranged parallel to the tube axis with their minus ends pointing to the cell body and the plus ends pointing to the tip.

Jamming problem. It is obvious that the cell needs traffic in both directions; otherwise, kinesins and kinesin-driven cargos would accumulate in the cell periphery, and dyneins and dynein-driven cargos would accumulate in the cell centre. Thus, in order to accomplish this bidirectional traffic, kinesin and dynein motors must work together: kinesins bring cargo to the cell periphery, while dyneins bring cargo back to the cell centre. How this bidirectional traffic is organized and regulated is still an open question. The most simple idea is that cargos moving to the periphery are attached to plus motors only, while cargos moving towards the cell center have only minus motors attached. However, in this case the question remains how the motors 'come back', i.e. how the kinesins that have reached the cell periphery come back to the cell centre and, analogously, how the dyneins come back from the centre to the periphery. Even if they dissociate from the cargo that they have just delivered, diffusion would be too slow to solve this problem, as discussed in Sec. 1.1.

Motor back-transport. An obvious solution to this problem is to have the motors carried by other motors. In axons, this seems to be the case for dynein, which is carried to the axon tip on vesicles propelled by kinesin 1. However, kinesin 1 apparently does not come back from the axon

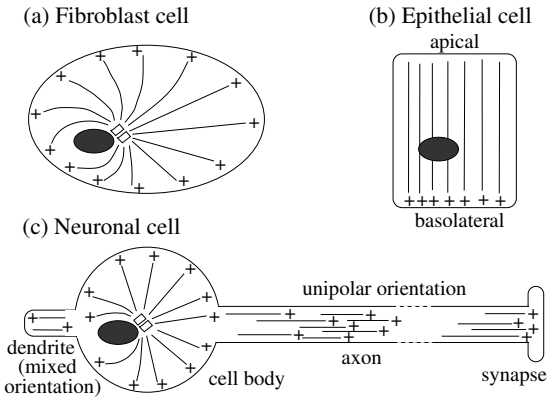

Fig. 1.3: Organization of MTs (black lines with indicated plus ends) in three different cell types for which the nuclei are represented as black ellipses and MT organizing centres as white rectangles: (a) in fibroblast cells, MT minus ends nucleate at the centrosome and the plus ends point radially outwards; (b) in epithelial cells, MTs form a parallel array with minus ends pointing to the apical and plus ends to the basolateral surface; and (c) in long axons of neuron cells, MTs form an isopolar array with the plus ends towards the synapse at the axon tip.

tip but is degraded there. In axon ligation experiments, dynein accumulated on both sides of the ligation, while kinesin accumulated only on the side close to the cell body [22, 52, 53, 76, 87, 179]. In hyphae of the fungus *Ustilago maydis*, three players are needed: endosomes are transported bidirectionally by kinesin 3 and dynein [173], and the dyneins are transported to the tip by kinesin 1 [85]. In a kinesin 1 null mutant, no dyneins are found at the MT plus ends, which abolishes endosome transport. In consequence, also no kinesin 1 motors are found at the MT minus ends because they are normally carried there on dynein-propelled endosomes [140].

Bidirectional motion. In order to bring dyneins to the MT plus end, they could simply be carried passively on plus end moving cargos. However, many cellular cargos move bidirectionally, i.e. they move in one direction for some time and then reverse direction [38, 40, 174] as shown in Fig. 1.4(a). This implies that both plus and minus motors must be simultaneously present and active on a single cargo, as has indeed been found for various cellular cargos [89, 124, 133]. Cargos that typically move in this bidirectional way include mitochondria [106] and various types of organelles like endosomes [110], protein transporting vesicles [61], pigment granules [42] or lipid-droplets [176]. Also, some viruses that hijack the cell's motor system for their own transport show bidirectional motion [149].

Melanosomes. An impressive examples of bidirectional motion is the motion of pigment granules called melanosomes in melanophores [112]. Melanophores are specialized pigment cells responsible for skin color. The frog *Xenopus* can adapt its colour to the environment by redistributing the melanosomes: If they are dispersed throughout the cell as in Fig. 1.4(b), the frog appears more black than if they are aggregated in the centre as in Fig. 1.4(c). The melanophore cytoskeleton is similar to the fibroblast cytoskeleton of Fig. 1.3(a). In order to change colour reversibly, the melanosomes must therefore travel bidirectionally and use plus and minus motors. Both during aggregation and dispersion, the melanosomes move bidirectionally with similar speeds in both directions, changing direction every few seconds. They achieve net minus end transport during aggregation because the average distance traveled in minus direction (the minus run length) is longer than the average distance traveled in plus direction (the plus run length). During dispersion, there is almost no net transport because of an increased minus run length [42]. The change from dispersion to aggregation is triggered by hormonal stimuli, which are passed to the motors via signalling cascades involving cAMP and phosphorylation [112].

Benefits of bidirectional transport. On first sight, bidirectional transport seems to be inefficient: in traveling back and forth cargos waste time and energy before reaching their targets. However, bidirectional transport has several advantages:

- When plus *and* minus motors are available, cargo motion can be easily and quickly regulated by influencing the motor activities in order to control e.g. speed or net direction.
- Cargos with both types of motors may serve as transporters of plus motors to the MT minus ends and of minus motors to the MT plus ends.
- Bidirectional cargos can explore the cell in search for their destination. This is especially

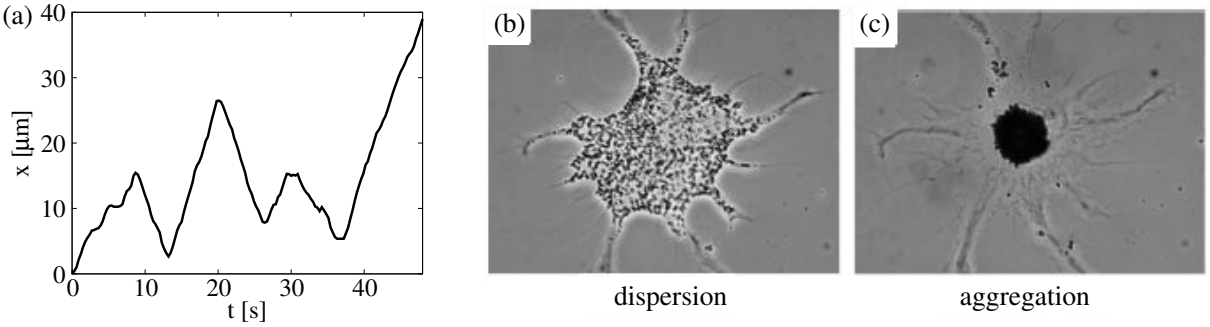

Fig. 1.4: Bidirectional transport in cells: (a) Trajectory of a bidirectionally moving endosome in a fungal hypha [30]. (b), (c) A *Xenopus* melanophore in the state of (b) dispersion and (c) aggregation. The black dots are melanosomes which are transported by kinesin 2 and dynein [112]. The cell membrane shape is similar in (a) and (b), but difficult to see in (b). The cell diameter is ca. 50 μm. Adapted from [112].

useful if the target, e.g. a vesicle, is mobile itself.

- Bidirectional transport facilitates error correction: a wrong direction can be easily changed, or a wrong choice of MT can be corrected by travelling back to an MT crossing.
- Bidirectional transport could be used to avoid obstacles on the filament. While kinesins typically walk straight on one protofilament of a MT, dyneins sometimes change the protofilament [98]. Therefore plus end directed cargos could use a minus end detour in order to bypass an obstacle which blocks a protofilament.
- For special cargos, unidirectional transport is undesirable because the cargos should be constantly relocated. Examples for such cargos are mitochondria, which should produce ATP at different locations in the cell, and melanosomes, which must remain dispersed in the cytoplasm to give colour.

1.5 Overview

This thesis is organized as follows. In Chap. 2, we introduce our description of a single molecular motor on time and length scales of a few seconds and microns. It is based on *in vitro* single molecule experiments. In the following chapters, we incorporate these single motor properties into models for traffic on larger time and length scales of many seconds and microns: first we consider the motion of many independent motors in Chap. 3, then we consider the motion of motors which are coupled mechanically by transporting a common cargo in Chap. 4 and 5.

More precisely, in Chap. 3, we describe the motion of many motors or motor-cargo-complexes in a half-open tube geometry, which mimics neuronal axons or fungal hyphae. The motors act independently and only feel each other via steric hindrance. This mutual exclusion and the confined tube geometry lead to motor traffic jams, which we investigate with simulations and analytic approximations. Furthermore, we compare it to trafficking in related systems such as closed tubes or asymmetric simple exclusion processes with Langmuir kinetics.

In Chap. 4 we consider the motion of a cargo transported by two teams of motors: a team of plus and a team of minus motors. The motors perform a 'tug-of-war' on their common cargo, governed by mechanical interactions only. This leads to surprisingly complex motility patterns and cooperative behaviour, which we investigate with simulations and analytic approximations. In particular, the motor tug-of-war leads to fast bidirectional motion, which avoids the traffic jams studied in the preceding chapter. Furthermore, it reproduces many features of experimentally studied bidirectional transport, which have previously been attributed to the action of a coordination complex, incompatible with a tug-of-war scenario. We compare our model results with experiments both qualitatively and quantitatively in Chap. 5.

Finally, we conclude with a summary and outlook in Chap. 6.

Chapter 2

Basic modelling of a single motor

In this chapter we establish our basic description of a single molecular motor. After discussing the relevant length and time scales of motor motion, we introduce a coarse grained model of a single motor, which is appropriate for our time and length scales of interest corresponding to many seconds and micrometres. This model describes a motor as an active particle which binds to a filament, moves along it and unbinds from it in a stochastic fashion. It is based on the motor transport properties measured *in vitro* in single motor experiments. In the following chapters 3 – 5 of this thesis, these single motor properties will be incorporated into models for the traffic of many motors.

2.1 Separation of scales

Molecular motors exhibit movements on several time and length scales which range from nanometers to millimeters to centimeters (up to a metre in axons) and from microseconds to days, respectively. This wide span of scales can be divided into three regimes [91]:

(I) The single step of a motor typically has a size of the order of 10 nm, and is generated through the amplification of nm-sized conformational changes in the catalytic domain of the motor. The chemical cycle takes typically of the order of 10^{-2} s, but the actual displacement is much faster.

(II) On scales of one or a few μm, the motors perform active directed walks along cytoskeletal filaments and move in a directed fashion with a velocity of circa 1 μm/s.

(III) On larger length and time scales which exceed a few microns or a few seconds, respectively, the motors perform many cycles of attachments to, walks along, detachments from and reattachments to the filament. The unbinding from the filament is a consequence of the fact that molecular motors function in a noisy environment, so that the motor–filament binding energy can be overcome by thermal fluctuations.

This work will focus on molecular motor traffic on length and times scales of micrometers and seconds or more, i.e. on the regimes (II) and (III). As these length scales are large compared to the size of the motor protein and the motor step size, the precise details of the motor step are not important. The motor can therefore be modeled as a particle of size of about 100 nm which can perform the following four basic actions:

- diffuse freely when in solution
- bind to a filament when close to it
- walk along the filament when bound to it
- unbind from the filament when bound to it

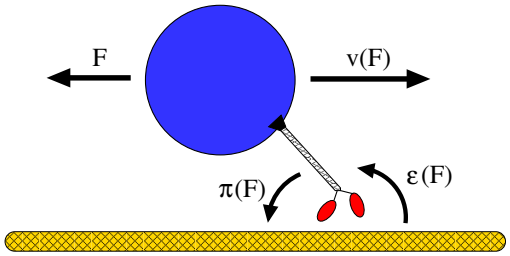

Fig. 2.1: Model for a single motor on a bead which is subject to the load force F. When the bead is close to the filament the motor binds to it with rate $\pi(F)$. When bound, it walks along the filament with velocity $v(F)$ and unbinds from it with rate $\epsilon(F)$.

These actions are associated with rates resp. probabilities because of the importance of thermal fluctuations in the noisy environment of the motor: free diffusion happens with diffusion constant D_{ub}, binding with binding rate π, walking with velocity v and unbinding with unbinding rate ϵ. Depending on the detailed situation considered, the above mentioned rates get various subscripts or arguments, as will be discussed when needed (for an overview see Tab. 6 in the symbol list on p. 134).

This course-grained view on length scales (II) and (III) describes the generic behaviour of a molecular motor and therefore applies to all motors irrespective of their detailed function. On the other hand, the rates characterizing the motor actions can be adapted to obtain results for specific molecular motors.

In this chapter we will consider the motion of a single molecular motor on length scale (II) in more detail. Using the results of single motor *in vitro* experiments as described in Sec. 1.3, we will develop a course grained model for a single motor transporting a cargo along along the filament, possibly subject to an external force.

2.2 A single motor on a bead

In this section, we consider the motion of a bead that is transported by a single motor along a filament, possibly subject to an external force F, as depicted in Fig. 2.1. The motion of such a motor can be studied in a controlled way in an optical trap experiment as described in the Sec. 1.3. We will use the result of such experiments to construct a course grained model of a single motor. Following the convention of the literature, the force F exerted by the optical tweezer is taken to be positive if it is a 'load' for the motor, i.e. if it opposes the motor motion. We will therefore call this force the 'load force'. When pulling the bead along the filament, the motor has to work against the load force. Most of the available data has been obtained for the best-studied motor kinesin 1, for which all parameters needed in our model have been measured, but we will also take into account data from cytoplasmic dynein and other kinesins, when available. In our course grained model, a motor is characterized by the filament unbinding rate ϵ, the filament binding rate π, and the velocity v. When a load force F is applied, the rates may depend on this force.

2.2.1 The unbinding rate

When the motor is bound to the filament, it walks along it into its preferred direction. However, due to stochastic thermal fluctuations which can overcome the motor–filament binding energy, the motor unbinds after some time. Assuming that the probability for unbinding is constant in time, the time that the motor stays bound to the filament is distributed exponentially and characterized by a single rate. When no force acts on the motor, we denote this rate by ϵ_0. For most motors, this rate is of the order of magnitude of $1\,\mathrm{s}^{-1}$.

When a force F acts on the bead, the unbinding rate increases because the filament-motor bond is put under strain. Kramers or Bell theory predicts that the increase of the rate for this bond breaking process is approximately exponential: [8, 78, 166]:

$$\epsilon(F) = \epsilon_0 \exp(|F|/F_d) \tag{2.1}$$

The force scale is set by the detachment force F_d. Such an exponential increase has been measured in a kinesin 1 bead assay [139], and is consistent with kinesin 1 data from [20] for forces up to the stall force. The detachment force F_d may be expressed as $F_d = \mathrm{k_B}T/x_c$, where x_c is the extension of the energy barrier between the bound and unbound state. This length scale is of the order of 1 nm, so that F_d is of the order of a few pN.

In Eq. (2.1) we assume that the unbinding rate depends only on the absolute value $|F|$ of the force and not on its direction. This is presumably wrong in general as forces perpendicular and parallel to the filament can have extremely different impact on the motor [37]. But in this work we will only consider forces acting on the bead roughly parallel to the filament, either applied by an optical tweezer, by other motors, or by friction. Mostly these forces will be opposing load forces for the motors. In this case the exponential increase with the (absolute) value of the force as been shown for kinesin 1 as described above. Only when considering external forces in Sec. 4.5.6, negative, i.e. assisting, forces appear. With Eq. (2.1) we assume that these assisting forces parallel to the filament increase the unbinding rate in the same way as the load forces parallel to the filament.

2.2.2 The binding rate

Binding of the bead-motor complex to the filament occurs in two steps:

(i) The bead (with the motor on it) diffuses randomly in the solution until it comes close to a filament. Here 'close' means a distance which is small enough for the motor to reach the filament, i.e. a distance of the order of 100 nm.

(ii) The motor binds to the filament.

The first diffusive step depends on the diffusion constant of the bead in the surrounding solution and the geometry of the setup. This is not an intrinsic property of the motor, and we therefore not consider this diffusive step (i) in this chapter. The binding step (ii) is the binding process of two proteins, the motor and the filament protein, and therefore very complicated on an atomic scale. However, on the course grained time and length scale considered here, we can describe this binding process as a single event. Because of the stochastic nature of the motion on this length scale, binding is not deterministic but occurs with a certain probability. We assume that this probability is constant in time. Therefore, the binding probability is exponentially distributed and characterized by a single rate, which we will denote by π. It is the average rate of binding of the motor when the motor is close to the filament, an issue that we will discuss later.

It is difficult to estimate the force dependence of the motor binding rate $\pi(F)$, since there are no experimental data about this dependence. If a force F acts on the bead when the motor is not bound to the filament, this affects the motion of the bead-motor complex, but not this motor: it is in its relaxed state. Therefore, when the bead is close to the filament, the motor binds with the zero-force rate π_0, independently of the force on the bead:

$$\pi(F) = \pi_0 \tag{2.2}$$

There could be a (presumably weak) force-dependence of the binding process once the motor is in contact with the filament, which is neglected here. The binding rate of molecular motors is of the order of magnitude of $1\,\mathrm{s}^{-1}$.

2.2.3 The velocity

When bound to the filament, the motor steps along it towards its plus or its minus end, depending on the intrinsic direction of the motor. For kinesin 1, this happens with a forward rate of around $100\,\mathrm{s}^{-1}$, i.e. the motor makes roughly 100 steps per second. This is much faster than the binding and unbinding process considered before. Therefore, we will often consider the forward motion as a smooth process with velocity v. When no force is applied to the motor, it moves

forward with its forward velocity v_F. The motion under force has been studied in an optical trap experiment extensively for kinesin 1, but also for other motors like cytoplasmic dynein and kinesin 3. Fig. 2.2(a) shows the force-velocity-curve obtained for kinesin 1 from [17].

When the motor is subject to an opposing load force F, it slows down. When the load force is increased, the velocity decreases further until the force reaches the stall force F_s at which the motor has zero velocity. The decrease is approximately linear, as has been observed for kinesin 1 [17, 55, 75, 104, 119, 155, 169], for kinesin 3 [157] and cytoplasmic dynein [156], although even for one motor type the shape of the decrease may look different depending on the experimental conditions, as is the case e.g. for kinesin 1 [169].

In our model we use a linear decrease:

$$v(F) = v_F\,(1 - F/F_s) \qquad \text{for } 0 \le F \le F_s \tag{2.3}$$

The stall forces F_s of single motors are of the order of a few pN.

If the motor is subjected to even higher, i.e. superstall, load forces, it is forced to walk backwards. However, motors do so only very slowly, as has been shown for kinesin 1 [17, 75, 119] and cytoplasmic dynein [74, 97, 170]; compare also Fig. 2.2. The precise form of the force-velocity-curve in this superstall regime is not clear, as the kinesin 1 force-velocity curve shown in Fig. 2.2(a) is the only experimental data in this regime so far. For simplicity, we expand the superstall force part of the force-velocity-curve around the stall force to obtain a linear force-velocity relationship

$$v(F) \approx -\beta_B\,(F - F_s) = v_B\,(1 - F/F_s) \qquad \text{for } F \ge F_s \tag{2.4}$$

where β_B is the slope of the force-velocity-curve at the stall force F_s. It has been re-parametrized as $\beta_B = v_B/F_s$ with the backward velocity v_B in order to make it similar in form to the substall force-velocity-curve Eq. (2.3) and to obtain a more intuitive parameter. We will take the backward velocity v_B resp. the slope β_B to be very small in order to account for the slow backward motion of the motor, i.e. $v_B \ll v_F$.

For large load forces $F \gg F_s$, the linear form Eq. (2.4) predicts fast backward motion. However, this regime is experimentally not relevant because the stall force of motors is larger or of the same order of magnitude as the detachment force. Therefore, a motor under a high force $F \gg F_s \gtrsim F_d$ unbinds very fast due to the exponential increase of the unbinding rate with force, see Eq. (2.1).

In this work we will consider mostly opposing load forces. However, in Sec. 4.5.6 we will also consider assisting forces, i.e. forces pulling in the same direction as the motor wants to walk. In optical trap experiments with kinesin 1, such an assisting force has been observed to increase the motor velocity [20], to leave it constant [9] or to give broadly scattered velocity values as in Fig. 2.2(a) [17]. We assume a linear form of the force-velocity-velocity-curve for assisting (i.e. negative) forces:

$$v(F) \approx v_F - \beta_A F = v_A \left(\frac{v_F}{v_A} - \frac{F}{F_s}\right) \qquad \text{for } F \le 0 \tag{2.5}$$

Here, β_A is the slope of the force-velocity-curve at zero force. It has been re-parametrized with the assisting velocity v_A as $\beta_A = \frac{v_A}{F_s}$. In total, the force-velocity relation of our model is:

$$v(F) \;=\; \begin{cases} v_A \left(\frac{v_F}{v_A} - \frac{F}{F_s}\right) & \text{for } F \le 0 \qquad \text{(assisting force)} \\ v_F \left(1 - \frac{F}{F_s}\right) & \text{for } 0 \le F \le F_s \quad \text{(substall load force)} \\ v_B \left(1 - \frac{F}{F_s}\right) & \text{for } F \ge F_s \qquad \text{(superstall load force)} \end{cases} \tag{2.6}$$

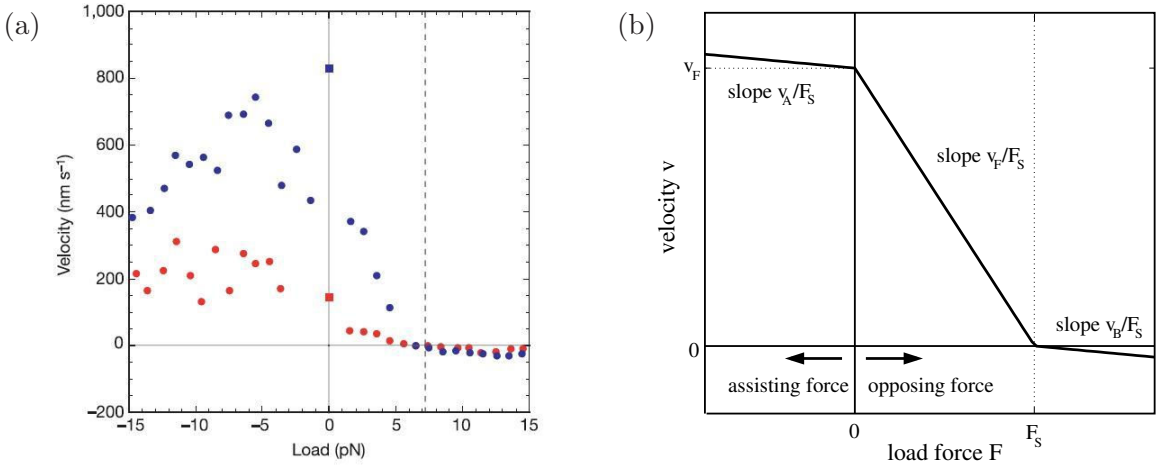

Fig. 2.2: Single-motor velocity: (a) The force-dependence of the motor velocity has been measured for kinesin 1 in an optical trap which applies a load force on the bead [17]. Red dots are for an ATP-concentration of 10 μM, blue dots for 1 mM. (b) The force-velocity relation $v(F)$ is modeled as a function consisting of three linear segments as given by Eq. (2.6)

as shown in Fig. 2.2(b). For convenience, we will often use the single motor velocity parameter

$$v_0 = \begin{cases} v_A & \text{for } F \leq 0 \quad \text{(assisting force)} \\ v_F & \text{for } 0 \leq F \leq F_s \quad \text{(substall load force)} \\ v_B & \text{for } F \geq F_s \quad \text{(superstall load force)} \end{cases} \tag{2.7}$$

or, analogously, the single motor slope parameter β, which is equal to $\beta_A = v_A/F_s$, $\beta_F = v_F/F_s$ and v_B/F_s for assisting, substall load and superstall load force, respectively. This piecewise linear form of the force-velocity relation has several advantages: it captures the essential features of the experimental force-velocity relation, it is simple with not too many parameters, it has a unique inverse (which will be of importance later) and allows for an analytic solution of the model equations considered in Chap. 4. However, in order to test whether our results depend on the detailed shape of the force-velocity-curve, we will also use an alternative form in Sec. A.4.2. We find that it does not affect our results substantially as long as the force-velocity-curve decreases monotonically and exhibits a small backward velocity.

2.3 Experimental single motor rates

We have characterized a single motor by six transport parameters, namely its stall and detachment forces F_s and F_d, the unbinding and binding rates ϵ_0 and π_0, and the forward and backward velocities v_F and v_B.[1] In this section, we will give an estimation of these parameters for the most important and best studied motors, kinesin 1 and cytoplasmic dynein, as summarized in Tab. 2.1. Most of these parameters have been obtained in optical tweezer bead assays as described in Sec. 1.3.

Kinesin 1 is a well studied motor with rather reproducible parameters. All transport parameters needed for our model have been measured for this motor. The situation for cytoplasmic dynein is different. Not all parameters have been investigated. Furthermore, the properties of dynein seem to depend strongly on experimental conditions and associative factors [98]. The estimates of the dynein parameters are therefore less reliable and sometimes not available. In the latter case we will use the value of the parameter measured for kinesin 1.

[1] Since we only use assisting forces in Sec. 4.5.6, and since there are no clear measurements of the force-velocity curve in the regime of assisting forces, we will discuss the corresponding parameter of the assisting velocity v_A only in Sec. 4.5.6.

Forward velocity v_F. The forward motor velocity v_F of a motor can be measured in a bead assay when monitoring the motor moving along a filament. The kinesin 1 velocity is about $1\,\mu$m/s [17, 66, 119, 139, 155, 161, 169]. The velocity of cytoplasmic dynein ranges from $0.1 - 1\,\mu$m/s [66, 100, 118, 156, 171] in single motor bead assays, but seems to be much higher in vivo [81]. We take the dynein velocity to be $v_F = 1\,\mu$m/s.

Stall force F_s. The stall force of a motor can be measured in an optical tweezer bead assay by determining the distance to the trap centre at which the motor stops moving, and then converting this distance into a force. The stall force for kinesin 1 is $5 - 8\,$pN [17, 75, 119, 139, 155, 169]; we will use the value $F_s = 6\,$pN. The value of the stall force for dynein is not clear. Different labs have reported conflicting results: a rather low value of 1.1 pN [97, 100], and a much higher value of $7 - 8\,$pN [156], comparable to the the kinesin 1 stall force. This may be due to experimental problems [156], or to the versatility of dynein, which is very sensitive to the experimental conditions [98]. We will use both values and compare the results for 'weak' dyneins with $F_s = 1.1\,$pN and 'strong' dyneins with $F_s = 7\,$pN.

Unbinding rate ϵ_0. The unbinding rate is related to the average walking time Δt_b of a motor, i.e. to the time a single motor stays bound to the filament before unbinding, by $\epsilon_0 = 1/\Delta t_\mathrm{b}$. However, most experiments measure the average run length Δx_b, the distance a single motor covers between binding to and unbinding from the filament. From this, the unbinding rate can be calculated as $\epsilon_0 = v_F/\Delta x_\mathrm{b}$. The kinesin run length is about $1\,\mu$m [66, 100, 119, 139]. Together with a velocity of $1\,\mu$m/s one obtains an unbinding rate of about $1\,\mathrm{s}^{-1}$. A more detailed calculation of the above ratio from the cited references leads to values in the range of $0.2-1.5\,\mathrm{s}^{-1}$. Dynein run lengths are more diverse and often longer than kinesin run lengths, ranging from $0.7 - 3.5\,\mu$m [21, 66, 100] leading to unbinding rates in the range of $0.2 - 1\,\mathrm{s}^{-1}$. We use the dynein unbinding rate $\epsilon_0 = 0.5\,\mathrm{s}^{-1}$.

Detachment force F_d. The detachment force can be determined by measuring the load-dependence of the average run length Δx_b, the average distance covered by a motor before unbinding. When the motor moves with constant velocity v, the average run length and the unbinding rate ϵ are simply related as $\Delta x_\mathrm{b} = v/\epsilon$. The measured average run length decreases roughly exponentially with the force with a force scale $F_d \sim 3$pN [139], which translates into an exponential increase of the unbinding rate with the same force scale. Thus the detachment force is half as large as the kinesin stall force.

No such measurements are available for dynein. We will therefore take the kinesin value $F_d = 3\,$pN also for dynein.

Binding rate π_0. The binding rate π_0 is the binding rate of a single motor attached to a bead that is close to the filament (e.g. because it is tethered to it by other motors). It is difficult to obtain directly in experiments. Experiments by Leduc et al. with kinesin 1 linking

parameter	kinesin 1	Refs.	dynein	Refs.
stall force F_s	6 pN	[139, 155]	1.1 pN ('weak')	[100, 135, 176]
			7 pN ('strong')	[156]
detachment force F_d	3 pN	[139]	?	
detachment rate ϵ_0	$1\,\mathrm{s}^{-1}$	[139, 161]	$0.5\,\mathrm{s}^{-1}$	[66, 100]
attachment rate π_0	$5\,\mathrm{s}^{-1}$	[84]	$2.5\,\mathrm{s}^{-1}$	[66, 129]
forward velocity v_F	$1\,\mu$m/s	[17, 161]	$1\,\mu$m/s	[66, 118]
backward velocity v_B	6 nm/s	[17]	?	

Tab. 2.1: Estimation for the single motor parameters of kinesin 1 and cytoplasmic dynein, taken from the *in vitro* experiments of the cited references. For the dynein stall force, different labs have reported conflicting results. For the dynein parameters with a '?' entry, no measurements are available. In this work we therefore use the kinesin 1 values for these parameters unless otherwise stated.

a membrane tube to a MT, as well as experiments by Beeg et al. with several kinesin 1 motors pulling a bead, could be fitted by using an close-to-the-filament attachment rate of $5\,\mathrm{s}^{-1}$ [7, 84].

A different way to obtain the binding rate is to use the experimental filament desorption constant K_{exp}, which is the ratio of the product of the concentrations of free motors and free filament sites to the concentration of bound motors. It describes the affinity of the motor to the filament and is therefore intimately related to the ratio $K = \epsilon_0/\pi_0$ of the theoretical unbinding and binding rate. However, this relation is not straightforward, mainly because it describes binding from a distance of about 100 nm. A calculation presented in App. A.1 leads to

$$K = \epsilon_0/\pi_0 \approx 0.3\, K_{\mathrm{exp}}/\mu\mathrm{M}, \tag{2.8}$$

see Eq. (A.19). This equation allows to use the experimental desorption constant K_{exp} and the unbinding rate ϵ_0 to calculate the desired close-to-the-filament attachment rate π_0.

The filament desorption constants of kinesin 1 lies in the range of $0.1-1\,\mu$M [35, 49, 93, 144]. Using the reasonable value $K_{\mathrm{exp}} = 0.7\mu$M reproduces the attachment rate $\pi_0 = 5\,\mathrm{s}^{-1}$ quoted above. We will therefore also use this value. This leads to a theoretical desorption constant of $K = \epsilon_0/\pi_0 = 0.2$. It is smaller than 1, as expected for a processive motor like kinesin 1.

The experimental desorption constant for dynein is in the range of $0.1-2\,\mu$M [66, 105, 145], similar to kinesin 1. We will therefore use the same theoretical desorption constant $K = 0.2$ as for kinesin 1, which, with the unbinding rate of $\epsilon_0 = 0.5\,\mathrm{s}^{-1}$, leads to the attachment rate $\pi_0 = 2.5\,\mathrm{s}^{-1}$.

Backward velocity v_B. The backward velocity v_B is a re-parametrization of the slope $\beta_B = v_B/F_s$ of the superstall force-velocity-relation, i.e. the force-velocity-relation for $F > F_s$. In this regime, only the kinesin 1 force-velocity-curve has been measured [17], see Fig. 2.2(a). Fitting a straight line to the superstall part of Fig. 2.2(a) leads to a slope of $\beta_B \approx 0.001(\mu\mathrm{m/s})/\mathrm{pN}$ and to a backward velocity of $v_B = \beta_B F_s \approx 0.006\,\mu\mathrm{m/s}$ (using $F_s = 6\,\mathrm{pN}$).[2]

There are no measurements of the superstall force-velocity-curve for dynein, although it has been shown that dynein walks backwards under high load forces [97, 100, 129, 156, 170]. We therefore have no experimental values for the velocity v_B and use the kinesin 1 value.

2.4 Summary

In this chapter, we have discussed the basic time and length scales of the motion of molecular motors, which range from the scale of a single step to a directed walk along the filament to many walks interrupted by unbinding and rebinding. We have then introduced a course grained model of a single motor for the intermediate regime of the walk along the filament. In this model, a motor binds to the filament with rate π, walks along it with velocity v, and unbinds from it with rate ϵ. We then used the results of *in vitro* single motor experiments to describe the force-dependence of these rates, which lead to a characterization of a single motor by six transport parameters: its stall and detachment forces F_s and F_d, its unbinding and binding rates ϵ_0 and π_0, and its forward and backward velocity v_F and v_B. This model describes the movements of a single motor in a rather generic way without making assumptions on the underlying motor mechanisms. At the same time it allows to describe specific motors by adapting the parameters to the measured transport properties. We have given such parameter estimates for the most important motors, kinesin 1 and cytoplasmic dynein, at the end of this chapter.

In the following chapters 3 – 5 of this work, we will incorporate this basic and simple model in models for the motion of many motors: In the next chapter, we will investigate the motion of many independent motors in a tubular geometry, and in the following chapter we will investigate the motion of motors which are coupled mechanically due to interaction with a common cargo.

[2] This is in rough agreement with the order of magnitude of the slope of the force-velocity-curve at the stall force $\beta_B \sim 0.05(\mu\mathrm{m/s})/\mathrm{pN}$ of the theoretical models by Qian [127] and Liepelt [88]. However, in these models the superstall force-velocity-curve is not linear but approaches a small negative constant [127] or zero [88] for very large forces, which leads to a magnitude of the slope larger than in our model.

Chapter 3

Motor traffic in a half-open tube

Because of the unidirectional nature of both the cytoskeletal filaments and the motors walking on them, bidirectional traffic in cells requires that plus and minus motors work together, compare Sec. 1.4. In this chapter we investigate what happens when this is not the case, i.e. when plus and minus motors act independently. It is obvious that plus motors will accumulate near MT plus ends and minus motors near MT minus ends. This effect is particularly prominent in long cellular protrusions like neuronal axons or fungal hyphae as shown in Fig. 3.1. In these cells, motor jams have indeed been observed experimentally for high motor densities [77, 117]. Motor traffic in these cells covers large time and length scales of tens to thousands of seconds and microns.

On these scales, the motors perform peculiar 'motor walks' which consist of many cycles of binding to the filament, walking along it, unbinding from it, diffusing in the surrounding solution, rebinding etc. [92]. In this chapter, we investigate this large length-scale traffic in half-open tubular compartments which mimic the geometries of axons or hyphae. The motors act independently according to single motor properties described in the last chapter. They interact only via direct steric hindrance. This mutual exclusion leads to traffic jams which we investigate quantitatively. A phase transition is obtained when the motor velocity changes sign. We identify the relevant length scales and characterize the jamming behavior using both analytical approximations and Monte Carlo simulations of lattice models [90, 107]. We apply the same methods to the closed tube in App. A.2.2. As our model is closely related to the asymmetric simple exclusion process (ASEP), we compare the jamming behaviour of our system to jamming in half-open ASEPs and in half-open ASEPs coupled to a large motor reservoir.

3.1 Large-scale traffic in tubular compartments

Axonal and hyphal traffic. The large size and extreme polarity of neuronal cells place tremendous demands on the intracellular traffic. These cells from long and thin cylindrical protrusions called axons, which can be several millimetres in length with a diameter of only a few microns as shown in Fig. 1.3(a). They exhibit almost no protein synthesis[1], so that their functionality must be maintained to a large extent by active traffic. For this purpose, MT filaments are aligned along the axis of the axonal cylinder. They form an isopolar array with their plus end pointing towards the axonal tip and their minus ends pointing towards the cell body, see Fig. 1.3(c). On this long one-way track, various types of cargo like vesicles, organelles, protein and mRNA complexes are permanently on the move, travelling both anterogradely to the tip and retrogradely to the cell body [2, 38]. Anterograde transport to the tip is mediated by various kinesins, while dynein powers retrograde traffic [38]. It is in axonal traffic that the motor protein kinesin 1 was discovered [12, 163].

[1] The view that there is strictly no protein synthesis in the axon has been challenged in the last decade, but the found amount of protein synthesis is too small to maintain the axon's functionality [33].

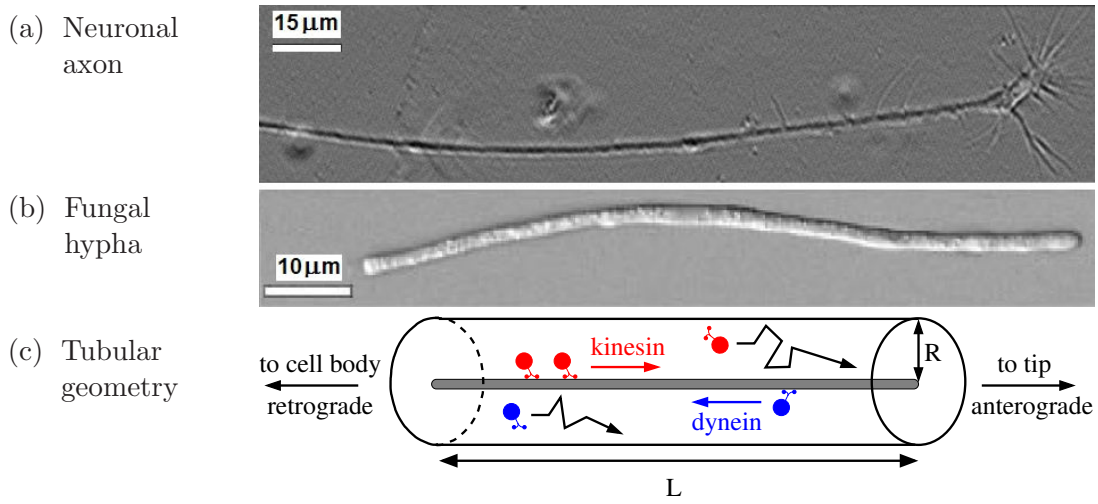

Fig. 3.1: Molecular motor traffic in tubular compartments like (a) a neuronal axon, from [1], or (b) a fungal hypha, from [140], is mimicked by (c) traffic in a cylinder of length L and radius R with a single filament aligned along the axis. Kinesin motors power anterograde transport: they walk to the MT plus end, which point to the tip. Dynein motors power retrograde transport: they walk to the MT minus end, which point to the cell body. Unbound motors diffuse freely in the cylinder.

Some fungi grow long filamentous strands called hyphae, which exhibit a similar geometry to axons: they are long thin cylinders of tens of micrometers in length and a diameter of only a few micrometres as shown in Fig. 1.3(b). They also possess an isopolar MT array aligned along the cylinder axis, with the MT ends pointing from the middle towards the hypha tip [85, 140]. There is special need for active transport in these hyphae because the hyphae grow at rates of μm/ min or mm/day [151].

Tube geometries. The geometry of axonal or hyphal traffic is theoretically appealing due to its cylindrical symmetry. It can be mimicked by a cylinder of length L and radius R with a single filament along its axis, see Fig. 3.1(c). Since the traffic of molecular motors represents a driven system, the boundary conditions are crucial for the resulting behaviour. In previous work, several types of boundary conditions have been studied: periodic boundary conditions [69], closed boundaries [73, 92], and open boundaries, which are coupled to motor reservoirs [69]. The latter systems exhibit boundary-induced phase transitions. Here we consider a half-open tube which imitates the geometry of an axon, see Fig. 3.2(a). At the right end, the tube is closed, i.e. no motors can leave or enter the system. This mimics the synaptic terminal of the axon. At the left end, the system is coupled to a motor reservoir which represents the cell body where the motors are synthesized and which therefore acts as a motor reservoir which provides fixed motor densities.[2]

Length scales. In the last chapter, we have considered the motion of a single molecular motor attached to a bead when the bead is close to the filament. In this case the motor can bind to the filament, move along it, or unbind from it. This corresponds to motion on the length scale of directed motor walks, labeled (II) in Sec. 2.1. This length scale is so large that the details of the motor step are *already* unimportant, but so small that events after unbinding of the motors from the filament are *still* unimportant. The motion of the motors far away from the filament, which becomes important on length scale (III), has been neglected so far. On this larger length scale, the motors performs peculiar motor walks which consist of alternating sequences of biased random walks in one dimension (on the filament) and unbiased random walks in three dimensions (in the surrounding solution). In the following, we will refer to the motion of 'motors', but in general the moving particle can be a single motor or a cargo-motor complex transported by a single or by many motors.

[2] The reverse situation (tube closed at the left end open at the right end) can be obtained from the previous case by particle-hole symmetry as described below Eq. (3.10).

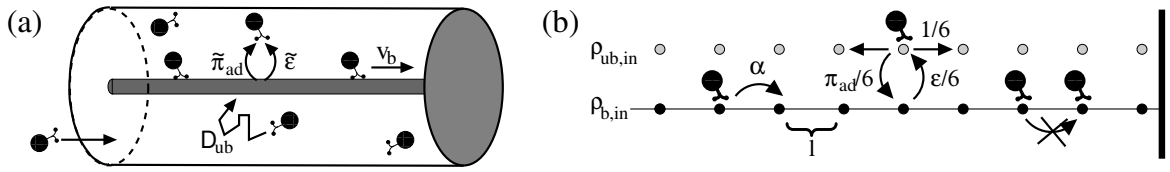

Fig. 3.2: Motion of motor particles along a filament within (a) a half-open tube and (b) the corresponding lattice model. At the left end, the system is connected to a motor reservoir with fixed bound and unbound densities $\rho_{\mathrm{b,in}}$ and $\rho_{\mathrm{ub,in}}$, while the right end is closed. Motor particles bound to the filament perform active movements with velocity v_{b}, while unbound motors perform symmetric diffusion with diffusion constant D_{ub}. Unbinding from and binding to the filament occurs with rates $\tilde{\epsilon}$ and $\tilde{\pi}_{\mathrm{ad}}$, respectively. In the lattice model, these movements are described by the forward step probability α on the filament and the symmetric hopping probability 1/6 to each neighbour site for unbound motors. In addition, unbound motors which reach the filament bind to it with probability π_{ad}, and bound motors unbind from the filament through steps to adjacent non-filament sites which occur with probability $\epsilon/6$ per non-filament neighbour site. The motors interact via hard core exclusion.

The model. Motors can bind to the filament, walk along it, and unbind from it. Unbound motors diffuse freely within the cylinder, which is a new feature of the larger length scale considered here compared to the last chapter. Each motor can thus be in two states: bound to the filament, where it moves actively to the right with velocity v_{b}, and unbound, where it performs symmetric diffusion with diffusion constant D_{ub}, see Fig. 3.2(a). The filament is taken to lie along the x-axis, so that the system at time t is characterized by the bound motor density $\rho_{\mathrm{b}}(x,t)$ and the unbound motor density $\rho_{\mathrm{ub}}(x,t)$. We neglect the variation of the unbound motor density ρ_{ub} with the transverse coordinates y and z. The motors can unbind from or bind to the filament. Since the motors are strongly attracted by the filament, the binding rate $\tilde{\pi}_{\mathrm{ad}}$ is taken to be large compared to the unbinding rate $\tilde{\epsilon}$. When motors come close to each other, they may interact. In our simple model we include only hard core exclusion which prevents motors from occupying the same site. In a mean field treatment, this can be taken into account by using exclusion factors of the form $(1-\rho_{\mathrm{b}})$ or $(1-\rho_{\mathrm{ub}})$.

The bound and unbound motor densities change in time due to various currents:

$$\frac{\partial}{\partial t}\rho_{\mathrm{b}} = -v_{\mathrm{b}}\frac{\partial}{\partial x}\rho_{\mathrm{b}}(1-\rho_{\mathrm{b}}) + D_{\mathrm{b}}\frac{\partial^2}{\partial x^2}\rho_{\mathrm{b}} + \tilde{\epsilon}\,\rho_{\mathrm{b}}(1-\rho_{\mathrm{ub}}) + \tilde{\pi}_{\mathrm{ad}}\,\rho_{\mathrm{ub}}(1-\rho_{\mathrm{b}}) \tag{3.1}$$

$$\phi\frac{\partial}{\partial t}\rho_{\mathrm{ub}} = \phi\,D_{\mathrm{ub}}\frac{\partial^2}{\partial x^2}\rho_{\mathrm{ub}} - \tilde{\epsilon}\,\rho_{\mathrm{b}}(1-\rho_{\mathrm{ub}}) + \tilde{\pi}_{\mathrm{ad}}\,\rho_{\mathrm{ub}}(1-\rho_{\mathrm{b}}) \tag{3.2}$$

where all densities are evaluated at the point (x,t). In Eq. (3.1) for the bound motor density, the first term describes the motor current on the filament with the bound motor velocity v_{b}, the second term describes bound diffusion with the bound diffusion coefficient D_{b}, and the third and fourth term describe unbinding from and binding to the filament with the effective unbinding and binding rates $\tilde{\epsilon}$ and $\tilde{\pi}_{\mathrm{ad}}$, respectively. In Eq. (3.2) for the unbound motor density, the first term describes symmetric diffusion with the unbound diffusion coefficient D_{ub}, and the second and third term describe unbinding from and binding to the filament. These unbinding and binding terms couple the unbound and bound motor densities. Note that the unbound diffusion is enhanced by the tube cross section ϕ, which is due to an integration over the cylindrical coordinates y and z and which increases the area available for free diffusion [68, 69].[3] The bound diffusion coefficient D_{b} is usually very small for motors, e.g. for kinesin $D_{\mathrm{b}} \sim 10^{-4}\,\mu\mathrm{m/s}^2$ [169], so that we will neglect bound diffusion in the following.

Lattice model. In addition to studying Eqs. (3.1) and (3.2) by analytical approximations, we perform Monte Carlo simulations of lattice models as in [69, 92]. In the simulations, the motors are represented by random walkers on a cubic lattice with lattice constant ℓ, see Fig. 3.2(b). A line of lattice sites represents the filament. The filament periodicity gives a

[3] In the discrete computer simulation, the cross section ϕ is equal to the number of unbound channels. For large tube radii, it becomes $\phi \approx \pi R^2$

natural choice for the lattice constant as the filament repeat distance, i.e. $l = 8\,\mathrm{nm}$ for MTs. Motors at the filament sites perform a biased random walk, while motors at non-filament sites perform symmetric random walks. The jump probabilities per unit time τ are α for a forward step at filament sites, and 1/6 for steps to each neighbour site at non-filament sites. As backward stepping of motors on the filament under no force are rare, see Sec. 2.2.3, backward stepping on the filament is neglected for simplicity. Unbinding from the filament occurs with probability $\epsilon/6$ to each adjacent non-filament site, and unbound motors which reach the filament bind to it with probability π_{ad}. Exclusion is implemented by rejecting all hopping attempts to sites which are already occupied by another motor. The hopping rates of the lattice models are matched to the transport properties of the motors via the discretization time τ which is chosen in such a way that diffusion in the lattice model occurs with probability 1/6, i.e. $\tau = \ell^2/(6D_{\mathrm{ub}})$. The differential equations Eqs. (3.1) and (3.2) are mean-field equations for the continuized version of this lattice model, and the parameters are related via $v_{\mathrm{b}} = \alpha\ell/\tau$, $\tilde{\pi}_{\mathrm{ad}} = 4\pi_{\mathrm{ad}}/6\tau$, $\tilde{\epsilon} = 4\epsilon/6\tau$, $D_{\mathrm{b}} = \alpha l^2/2\tau$, and $D_{\mathrm{ub}} = l^2/6\tau$ [68, 69, 92]. Since we are interested in the behaviour on the large time and length scale of the regime (III) defined in Sec. 2.1, the continuous and the lattice model should give similar results. While the lattice model is easily amenable to computer simulations, the continuum version is suitable for analytical calculations described in this chapter.

Parameter adaption. The continuous and the lattice model describe the large-scale traffic of molecular motors in a generic way without making assumptions about the detailed motor mechanism. They can also be applied to various types of 'motor particles' which consist of cargo particles with one or several motors attached, as will be studied in the next chapter. The large-scale traffic model can be adapted to the various situations and to special motors or cargos by appropriately choosing the model parameters, see App. A.2.1. However, in this chapter we will focus on general statistical properties of traffic in a half-open tube geometry rather than on specific applications. We will investigate relevant length scales, phase transitions and motor traffic jams. In App. A.2.2, we investigate the jamming behaviour with the same methods also for the closed tube.

3.2 Steady states and relevant length scales

Since axonal traffic takes place on large time scales of minutes up to days, we are interested in the large time behaviour, i.e. in the stationary state of the system. The boundary conditions are implemented as follows: At the right closed end, all motor currents must be zero. At the open left end which is coupled to a motor reservoir, the bound and unbound motor density are fixed to $\rho_{\mathrm{b,in}}$ and $\rho_{\mathrm{ub,in}}$.

In order to obtain the stationary state, we set the time derivative in Eqs. (3.1) and (3.2) to zero. For the change of the bound density, Eq. (3.1), this leads to

$$\frac{\partial}{\partial x}\left[v_{\mathrm{b}}\rho_{\mathrm{b}}(1-\rho_{\mathrm{b}})\right] = \tilde{\pi}_{\mathrm{ad}}\rho_{\mathrm{ub}}(1-\rho_{\mathrm{b}}) - \tilde{\epsilon}\rho_{\mathrm{b}}(1-\rho_{\mathrm{ub}}). \tag{3.3}$$

This equation states that in the stationary state the change of the bound current, $v_{\mathrm{b}}\rho_{\mathrm{b}}(1-\rho_{\mathrm{b}})$, is balanced by the binding and unbinding currents, $\tilde{\pi}_{\mathrm{ad}}\rho_{\mathrm{ub}}(1-\rho_{\mathrm{b}})$ and $\tilde{\epsilon}\rho_{\mathrm{b}}(1-\rho_{\mathrm{ub}})$, respectively. Here, the small diffusive part of the bound current has been neglected. For the change of the unbound density, Eq. (3.2), setting the time derivative to zero and using Eq. (3.3) leads to

$$\phi D_{\mathrm{ub}}\frac{\partial^2}{\partial x^2}\rho_{\mathrm{ub}} \;=\; \tilde{\pi}_{\mathrm{ad}}\rho_{\mathrm{ub}}(1-\rho_{\mathrm{b}}) - \tilde{\epsilon}\rho_{\mathrm{b}}(1-\rho_{\mathrm{ub}}) \;=\; \frac{\partial}{\partial x}\left[v_{\mathrm{b}}\rho_{\mathrm{b}}(1-\rho_{\mathrm{b}})\right]. \tag{3.4}$$

Integrating over the tube length and using the fact that, because of the closed boundary condition at the right end, the net current in the tube must be zero, we obtain

$$v_{\mathrm{b}}\rho_{\mathrm{b}}(1-\rho_{\mathrm{b}}) - \phi D_{\mathrm{ub}}\frac{\partial}{\partial x}\rho_{\mathrm{ub}} = 0. \tag{3.5}$$

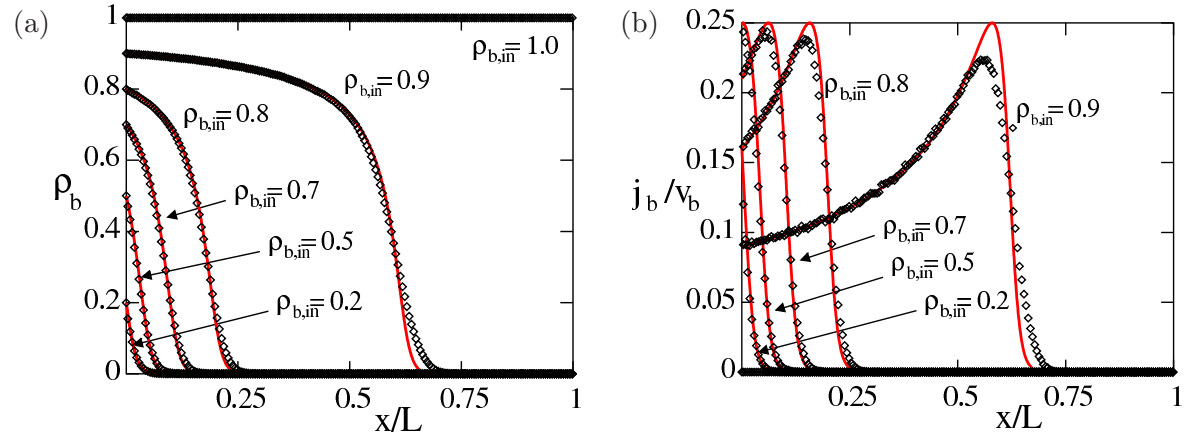

Fig. 3.3: (a) Bound density profiles ρ_b and (b) current densities j_b for different boundary densities $\rho_{b,in}$ as obtained from Monte Carlo simulation ($\diamond$) and from the adsorption equilibrium approximation (solid red lines). The simulation parameters are $\alpha = 0.001$, $\epsilon = 1/100$, $\pi_{ad} = 1$, $\phi = 4$, $L = 600$.

This equation states that the directed bound current of motors, $v_b\rho_b(1-\rho_b)$, and the unbound diffusive motor current, $-\phi D_{ub}\frac{\partial}{\partial x}\rho_{ub}$ must balance in the stationary state.

The change of the bound current described by Eq. (3.3) drives the system out of adsorption equilibrium for which the binding term $\tilde{\pi}_{ad}\rho_{ub}(1-\rho_b)$ and the unbinding term $\tilde{\epsilon}\rho_b(1-\rho_{ub})$ would be equal, i.e.

$$\tilde{\pi}_{ad}\rho_{ub}(1-\rho_b) = \tilde{\epsilon}\rho_b(1-\rho_{ub}). \tag{3.6}$$

For simplicity, we assume that the boundary densities at the left boundary, $\rho_{b,in}$ and $\rho_{ub,in}$, fulfill this adsorption equilibrium condition (3.6). This avoids extra currents which would otherwise be caused by the out-of-equilibrium boundary conditions.

When the motors on the filament move to the right, i.e. for $v_b > 0$, they jam up at the closed right end until the tube far from the left boundary is completely filled with motors. In the bulk of a long tube, one thus has bound and unbound motor densities $\rho_b = 1$ and $\rho_{ub} = 1$. Indeed, these density values are a fixed point of Eqs. (3.5) and (3.3). Within a boundary region at the left end, the densities cross over to the boundary values $\rho_{b,in}$ and $\rho_{ub,in}$.

Likewise, if the motors on the filament move to the left, i.e. for $v_b < 0$, they are driven out of the tube at the left end, so that the bulk is left empty with $\rho_b = 0$ and $\rho_{ub} = 0$, which is another fixed point of Eqs. (3.5) and (3.3). However, a boundary region at the left end survives, fed by ingoing diffusion. Typical motor density profiles for this case are shown in Fig. 3.3(a). They display a 'jam' region at the left end, separated from the 'empty' bulk region by a localized domain wall or shock. The system is thus characterized by two length scales: the bulk length scale ξ on which the densities approach their the bulk values and which is independent of the boundary densities, and the jam length L_* which describes the width of the jammed boundary region and which, of course, strongly depends on the boundary densities.

On tuning the motor velocity v_b, the system displays two phases, a high and a low density phase, which are dominated by the closed right end. Taking the bulk density as order parameter, one has a phase transition at $v_b = 0$. As will be shown both in analytical approximation and in Monte Carlo simulation, both characteristic length scales ξ and L_* diverge with the power law $1/v_b$ as the motor velocity v_b approaches zero.

In an experiment, this limit can be realized by reducing the concentration [ATP] of the motor fuel ATP, since for small [ATP], $v_b \sim$[ATP]. Changing the sign of v_b is more difficult, one possibility is to use motor particles driven by motors of two species with opposite directionality as considered in the next chapter. In this case movement could be inverted by activating one motor species and deactivating the other. If these motor particles switch stochastically between the two directions, one could change the sign of their average velocity by influencing the switching rates through regulatory molecules. For example, tau proteins which strongly suppress movements

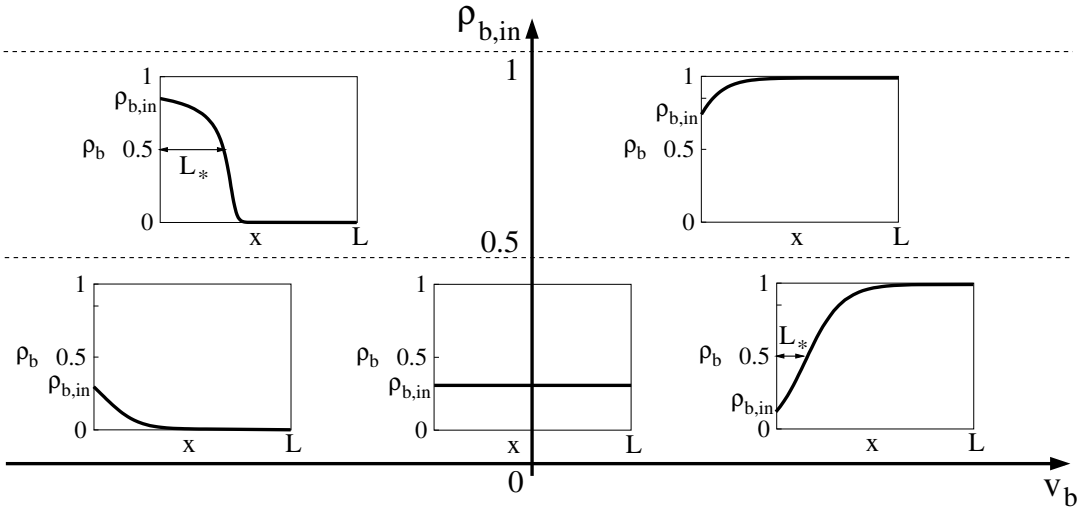

Fig. 3.4: Phase diagram for the half-open tube: For motors moving to the left, i.e. $v_\mathrm{b} < 0$, the system is essentially empty with bulk density $\rho_\mathrm{b} = 0$, while for motors moving to the right, i.e. $v_\mathrm{b} > 0$, it is essentially full with bulk density $\rho_\mathrm{b} = 1$. At the phase transition $v_\mathrm{b} = 0$, the system is dominated by the left boundary density and has the bulk density $\rho_\mathrm{b} = \rho_{\mathrm{b,in}}$. For $v_\mathrm{b} < 0$, the motors form a traffic jam with length L_* at the left end, provided that the boundary density $\rho_{\mathrm{b,in}}$ is larger than 1/2. Likewise, for $v_\mathrm{b} > 0$ and $\rho_{\mathrm{b,in}} < 1/2$, a 'jam of holes', i.e. a region with low density, separates the (completely filled) bulk of the system from the left boundary.

towards the synapse in axons can induce the retreat of vesicles into the cell body [102].

For $v_\mathrm{b} = 0$, i.e. when there is no active motion of the motors, the system is in thermodynamic equilibrium, and the adsorption equilibrium as described by Eq. (3.6) is valid for all x along the filament. Thus the bulk densities are $\rho_\mathrm{b} = \rho_{\mathrm{b,in}}$ and $\rho_\mathrm{ub} = \rho_{\mathrm{ub,in}}$. This case is the only one where the bulk values are dominated by the open left filament end. A phase diagram is shown in Fig. 3.4, the control parameters are the motor velocity v_b and the left boundary density $\rho_{\mathrm{b,in}}$.

3.3 The bulk region

To examine the bulk behaviour, we linearize Eqs. (3.5) and (3.3) around the appropriate fixed point. In the case of motors moving to the left ($v_\mathrm{b} < 0$) with bulk values $\rho_\mathrm{b} = \rho_\mathrm{ub} = 0$, the linearization leads to an exponential density profile

$$\rho_\mathrm{b}(x) \approx \mathcal{N} \exp(-x/\xi) \quad \text{and} \quad \rho_\mathrm{ub}(x) \approx \left(\frac{\tilde{\epsilon}}{\tilde{\pi}_\mathrm{ad}} - \frac{v_\mathrm{b}}{\tilde{\pi}_\mathrm{ad}\xi} \right) \rho_\mathrm{b} \tag{3.7}$$

with the bulk length scale

$$\xi = 2\Delta x_\mathrm{b} \left[1 - \sqrt{1 + 4 \left(\frac{\Delta x_\mathrm{b}}{\Delta x_\mathrm{ub}} \right)^2} \right]^{-1} \approx -\frac{(\Delta x_\mathrm{ub})^2}{\Delta x_\mathrm{b}} = -\frac{\tilde{\epsilon}}{\tilde{\pi}_\mathrm{ad}} \frac{\phi D_\mathrm{ub}}{v_\mathrm{b}}, \tag{3.8}$$

where

$$\Delta x_\mathrm{b} = v_\mathrm{b}/\tilde{\epsilon} \qquad \text{and} \qquad \Delta x_\mathrm{ub} = \sqrt{\phi D_\mathrm{ub} \tilde{\pi}_\mathrm{ad}} \tag{3.9}$$

are the average walking distance on the filament before unbinding and the average diffusion distance before binding of a motor, respectively. The approximation in Eq. (3.8) is valid for small motor velocities v_b. The exponential behaviour near the bulk value is in agreement with the result from MC simulations, see Fig. 3.5(a).

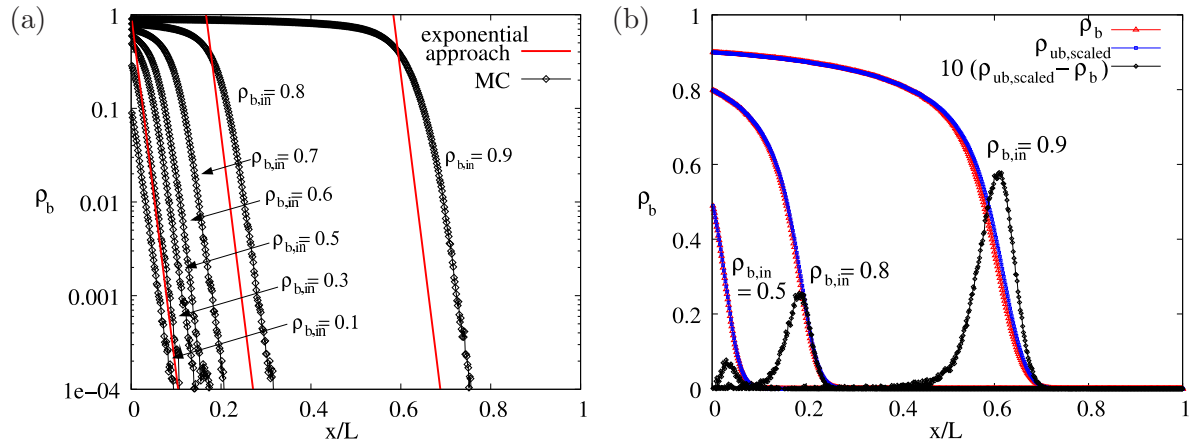

Fig. 3.5: (a) The logarithmic plot shows that the bound density profiles $\rho_b(x)$ (◇) of Fig. 3.3 approach the bulk value exponentially with the length scale ξ (red solid lines) from Eq. (3.8). (b) The bound density profiles $\rho_b(x)$ (red △) are very close to the bound density $\rho_{ub,scaled}$ (blue □) from Eq. (3.11), which is calculated using the adsorption equilibrium approximation Eq. (3.6). The ten-fold difference $\rho_{ub,scaled} - \rho_b$ (black ◇) has a significant amplitude only in the shock region.

In the case of motors moving to the right, the same reasoning leads to an exponential approach of the bulk values $\rho_b = 1$ and $\rho_{ub} = 1$ with the length scale

$$\xi = -2\Delta x_{b,h}\left[1 - \sqrt{1 + 4\left(\frac{\Delta x_{b,h}}{\Delta x_{ub,h}}\right)^2}\right]^{-1} \approx \frac{(\Delta x_{ub,h})^2}{\Delta x_{b,h}} = \frac{\tilde{\pi}_{ad}}{\tilde{\epsilon}}\frac{\phi D_{ub}}{v_b} \tag{3.10}$$

where the last expressions are again valid for small motor velocity v_b, and where $\Delta x_{b,h} = v_b/\tilde{\pi}_{ad}$ and $\Delta x_{ub,h} = \sqrt{\phi D_{ub}/\tilde{\epsilon}}$ are the average walking distance on the filament before unbinding and the average diffusion distance before binding of a hole, respectively. This result can be obtained directly from Eq. (3.8) by exploiting particle-hole symmetry, i.e. by substituting the left by the right boundary condition, ρ_b by $1 - \rho_b$, ρ_{ub} by $1 - \rho_{ub}$, v_b by $-v_b$ and x by $L - x$, and by exchanging $\tilde{\pi}_{ad}$ and $\tilde{\epsilon}$. According to Eqs. (3.8) and (3.10) the bulk length scale ξ diverges in the limit of small v_b with the power law $1/v_b$. Thus, the same power law is obtained both if $v_b = 0$ is approached from above and from below, but with different amplitudes. The divergence of the bulk length scale ξ means that the boundary dominates the whole system for small velocities $|v_b|$, and the bound density becomes equal to the boundary density everywhere, $\rho_b(x) = \rho_{b,in}$.

3.4 The jam region

In the following, we will focus on motors moving to the left, i.e. on the case $v_b < 0$. The case of motors moving to the right can easily be deduced as above by invoking particle-hole symmetry. Left-moving motors jam up in front of the left boundary, leading to a boundary dominated length scale in the system, the jam length L_*. In the jam region, the motors move slowly and thus 'have time' to equilibrate with the unbound motors before moving on. This separation of time scales leads to approximate adsorption equilibrium

$$\tilde{\pi}_{ad}\rho_{ub}(1 - \rho_b) \approx \tilde{\epsilon}\rho_b(1 - \rho_{ub}) \tag{3.11}$$

at every filament site x. If this adsorption equilibrium holds, the bound density is determined by the unbound density as

$$\rho_b(x) \approx \frac{\rho_{ub}}{K + (1 - K)\rho_{ub}} =: \rho_{ub,scaled}. \tag{3.12}$$

This is indeed a good approximation, see Fig. 3.5(b). The maximal deviation from adsorption equilibrium is in the shock region because this is the region where the motor current (parallel

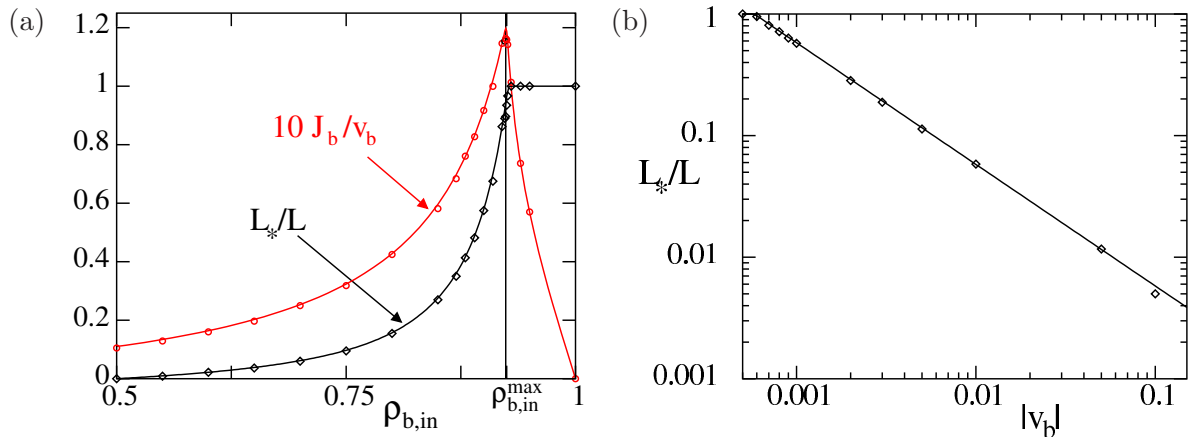

Fig. 3.6: Jam length L_* as a function (a) of the boundary density $\rho_{\mathrm{b,in}}$ (with fixed velocity $\alpha = -0.001$) and (b) of the motor velocity v_{b} (with fixed $\rho_{\mathrm{b,in}} = 0.9$). Both Monte Carlo ($\diamond$) and analytic results (solid lines) from the jam region approximation Eq. (3.17) are shown. The other parameters are as in Fig. 3.3. In (a), we also display the averaged bound current J_{b} as obtained from simulations ($\bigcirc$) and from adsorption equilibrium approximation Eq. (3.21) with its maximum at $\rho^{\max}_{\mathrm{b,in}}$.

to the tube axis) is maximal and disturbs the adsorption equilibrium, see Fig. 3.3(b). The adsorption equilibrium approximation Eq. (3.11) is also a useful approximation in related systems like the closed tube, see App. A.2.2.

3.4.1 Density profile and jam length

With the adsorption equilibrium approximation as given by Eq. (3.11), one can eliminate ρ_{ub} from the current balance Eq. (3.5) which leads to

$$\frac{\partial}{\partial x}\rho_{\mathrm{b}} = \frac{V}{L}\frac{(1-K)^2}{K}\rho_{\mathrm{b}}(1-\rho_{\mathrm{b}})\left(\frac{1}{1-K}-\rho_{\mathrm{b}}\right)^2 \tag{3.13}$$

where the dimensionless constants

$$K = \tilde{\epsilon}/\tilde{\pi}_{\mathrm{ad}} \qquad \text{and} \qquad V = Lv_{\mathrm{b}}/\left(\phi D_{\mathrm{ub}}\right) \tag{3.14}$$

have been introduced. The desorption constant K is the ratio of unbinding to binding rate, while the dynamic constant V is the ratio of the time $t_{\mathrm{ub}} = L^2/(\phi D_{\mathrm{ub}})$ needed to diffuse over the filament length L to the time $t_{\mathrm{b}} = L/v_{\mathrm{b}}$ needed to walk this distance. It is closely related to the Péclet number, which measures the relative importance of deterministic to Brownian motion, see Sec. 1.1. If the Péclet number V is small, diffusive motion is dominant; if it is large, the particle moves almost deterministically. For molecular motors, the Péclet number is of the order of 1, and therefore both Brownian and deterministic motion are important.

Separation of variables, decomposition into partial fraction and subsequent integration of Eq. (3.13) leads to an implicit equation for the bound density ρ_{b}:

$$\frac{x}{L} = \frac{1}{V}\left[g(\rho_{\mathrm{b}}(x),K) - g(\rho_{\mathrm{b,in}},K)\right]. \tag{3.15}$$

The function

$$g(\rho,K) := \frac{-1}{\frac{1}{1-K}-\rho} + K\ln(\rho) - \frac{1}{K}\ln(1-\rho) + \frac{1-K^2}{K}\ln\left|\frac{1}{1-K}-\rho\right| \tag{3.16}$$

is a continuous, monotonically increasing, and thus invertible function for $0 \le \rho \le 1$. It respects particle-hole symmetry, which is equivalent to $g(1-\rho, 1/K) = -g(\rho, K)$. In the jam region, the profiles obtained from Eq. (3.15) agree nicely with the Monte Carlo profiles, while they differ in

the shock and the bulk region, where adsorption equilibrium is no longer a good approximation, see Fig. 3.3(a). In Fig. 3.3(b), we also show the corresponding profiles of the bound current $j_\mathrm{b} = v_\mathrm{b}\rho_\mathrm{b}(1-\rho_\mathrm{b})$ which exhibits a maximum close to the domain wall between the jammed and the bulk region.

We therefore use the position of the current maximum as a definition for the jam length L_*. In the jam region the current is low due to a too high motor density while on the other side of the shock there are too few motors, also leading to a small current. As the maximal current is obtained for $\rho_\mathrm{b} = 1/2$, the jam length L_* is given by

$$\frac{L_*}{L} = \frac{1}{V}\left[g(\frac{1}{2}, K) - g(\rho_{\mathrm{b,in}}, K)\right]. \tag{3.17}$$

Note that the jam length L_* is positive only if $\rho_{\mathrm{b,in}} \geq 1/2$. For smaller boundary densities one had $L_* < 0$, which implies that the domain wall is located outside the tube, which then does not exhibit a motor traffic jam. The jam lengths determined from Eq. (3.17) are shown in Fig. 3.6 and agree well with the corresponding simulation results. As expected, the jam length increases with the boundary density $\rho_{\mathrm{b,in}}$. This is consistent with experiments where motor traffic jams have been observed in axons and hyphae for high motor densities achieved by overexpressing the motors [77, 117]. The jam length diverges logarithmically, $L_* \approx L/(VK)\ln(1-\rho_{\mathrm{b,in}})$, as $\rho_{\mathrm{b,in}}$ approaches 1 (of course this divergence is truncated by the finite system size). If the velocity v_b approaches zero, the jam length diverges as $1/v_\mathrm{b}$ and the jammed region spreads over the whole system in agreement with the fact that for $v_\mathrm{b} = 0$ the left boundary dominates the whole system, as has been discussed in Sec. 3.2 above. The exponent -1 of the divergence for small v_b, which has been obtained using mean field and adsorption equilibrium approximations, is confirmed by the Monte Carlo simulation results, see Fig. 3.6(b). The jam length Eq. (3.17) is inversely proportional to the Péclet number V. This leads to the slightly counterintuitive result that jamming occurs primarily in the diffusion dominated regime of small Péclet number.

The case K=1. In the special case $K = 1$, where binding to the filament and unbinding from the filament occur with the same rate, the implicit Eq. (3.15) for the density profile can be inverted and leads to the bound and unbound density profiles

$$\rho_\mathrm{b}(x) = \left[1 + \frac{1-\rho_{\mathrm{b,in}}}{\rho_{\mathrm{b,in}}}\,\exp\left(-V\frac{x}{L}\right)\right]^{-1} = \rho_\mathrm{ub}(x). \tag{3.18}$$

This result agrees well with the result from simulation, see Fig. 3.7(a). The jam length L_* in this case is given by

$$\frac{L_*}{L} = \frac{1}{V}\ln\left(\frac{1-\rho_{\mathrm{b,in}}}{\rho_{\mathrm{b,in}}}\right). \tag{3.19}$$

3.4.2 The average bound current

In order to characterize the overall transport in the system we consider the average bound current which is defined by

$$J_\mathrm{b} = \frac{1}{L}\int_0^L j_\mathrm{b}(\rho_\mathrm{b}(x))\,dx. \tag{3.20}$$

Since the bound density is essentially zero in the bulk, the bound current $j_\mathrm{b}(\rho_\mathrm{b}) = v_\mathrm{b}\rho_\mathrm{b}(1-\rho_\mathrm{b})$ has large absolute values only in the boundary region near the left end. It is thus appropriate to use the jam region approximation of Eq. (3.13) to calculate the average bound current J_b:

$$\frac{J_\mathrm{b}}{v_\mathrm{b}} = \frac{1}{V}\frac{K}{(1-K)^2}\left[\frac{1}{\frac{1}{1-K} - \rho_\mathrm{b}(L)} - \frac{1}{\frac{1}{1-K} - \rho_{\mathrm{b,in}}}\right] \tag{3.21}$$

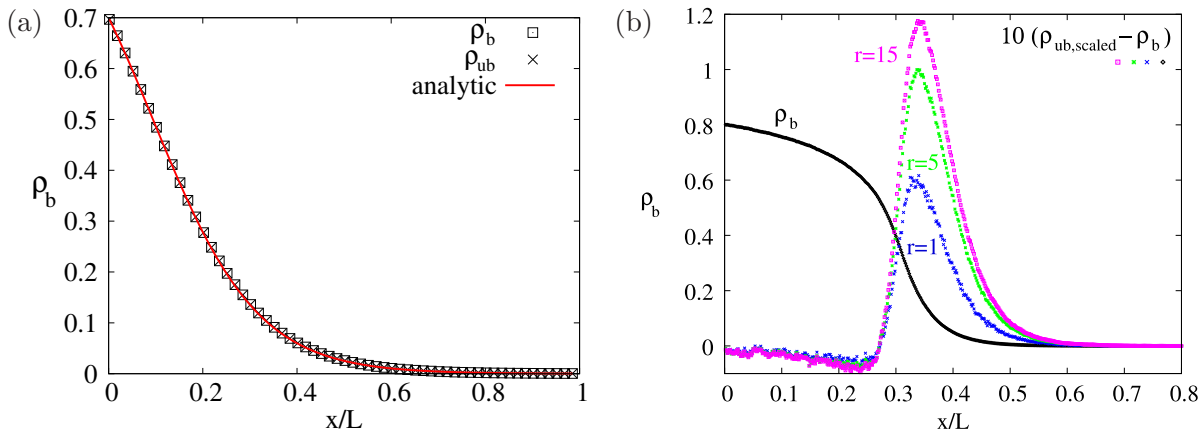

Fig. 3.7: (a) For the case of $K = 1$, the simulated bound (□) and unbound (×) density profiles are identical and agree well with the adsorption equilibrium approximation (solid red line). Simulation parameters are $\alpha = -0.01$, $\epsilon = \pi_{\mathrm{ad}} = 1$, $\phi = 4$, $L = 600$, $\rho_{\mathrm{b,in}} = 0.7$. (b) The adsorption equilibrium approximation is violated significantly only in the region of the shock of the bound density profile $\rho_{\mathrm{b}}(x)$. This violation is quantified by the difference of $\rho_{\mathrm{ub,scaled}} - \rho_{\mathrm{b}}$ (coloured data points), compare Fig. 3.5, and grows with r. Simulation parameters are $\alpha = -0.1$, $\epsilon = 0.01$, $\pi_{\mathrm{ad}} = 1$, $L = 600$, $\rho_{\mathrm{b,in}} = 0.8$.

For large system size L the right boundary density vanishes, and the average bound current is given by

$$\frac{J_{\mathrm{b}}}{v_{\mathrm{b}}} \approx \frac{1}{V}\frac{K}{(1-K)}\left[1 - \frac{1}{1-(1-K)\rho_{\mathrm{b,in}}}\right]. \tag{3.22}$$

Interestingly, as $V \sim v_{\mathrm{b}}$, the current J_{b} in the thermodynamic limit does not depend on the motor velocity v_{b}. This is because the jam length L_* decreases as $1/v_{\mathrm{b}}$, thus cancelling the expected $J_{\mathrm{b}} \sim v_{\mathrm{b}}$ behaviour.

The average bound current from Eq. (3.21) agrees well with the current from the Monte Carlo simulation, see Fig. 3.6(a). As a function of the left boundary density $\rho_{\mathrm{b,in}}$, it displays a maximum absolute value at a density $\rho_{\mathrm{b,in}}^{\max}$. This density thus optimizes the motor transport in the system. It can be calculated via

$$\begin{aligned} 0 &= \frac{\partial J_{\mathrm{b}}}{\partial \rho_{\mathrm{b,in}}} = \frac{1}{V}\left[j_{\mathrm{b}}\left(\rho_{\mathrm{b}}(L)\right) g'(\rho_{\mathrm{b}}(L))\frac{\partial \rho_{\mathrm{b}}(L)}{\partial \rho_{\mathrm{b,in}}} - j_{\mathrm{b}}\left(\rho_{\mathrm{b,in}}\right) g'(\rho_{\mathrm{b,in}})\right] \\ &= \frac{1}{V}\left[j_{\mathrm{b}}\left(\rho_{\mathrm{b}}(L)\right) - j_{\mathrm{b}}\left(\rho_{\mathrm{b,in}}\right)\right] g'(\rho_{\mathrm{b,in}}). \end{aligned} \tag{3.23}$$

The last expression follows from

$$0 = g'(\rho_{\mathrm{b}}(L))\frac{\partial \rho_{\mathrm{b}}(L)}{\partial \rho_{\mathrm{b,in}}} - g'(\rho_{\mathrm{b,in}}), \tag{3.24}$$

which is obtained by differentiating Eq. (3.15), taken at $x = L$, with respect to $\rho_{\mathrm{b,in}}$. As $g'(\rho_{\mathrm{b,in}}) > 0$ for $0 \le \rho_{\mathrm{b,in}} \le 1$, a current extremum can occur only for

$$j_{\mathrm{b}}\left(\rho_{\mathrm{b,in}}\right) = j_{\mathrm{b}}\left(\rho_{\mathrm{b}}(L)\right). \tag{3.25}$$

Since equality of the densities at the left and right end occurs only for a completely full or completely empty tube, the condition for extremal current is

$$\rho_{\mathrm{b,in}} = 1 - \rho_{\mathrm{b}}(L). \tag{3.26}$$

Using this condition in Eq. (3.15) with $x = L$, one obtains the density that extremizes the average current from

$$V = g(\rho_{\mathrm{b,in}}^{\max}) - g(1 - \rho_{\mathrm{b,in}}^{\max}) \tag{3.27}$$

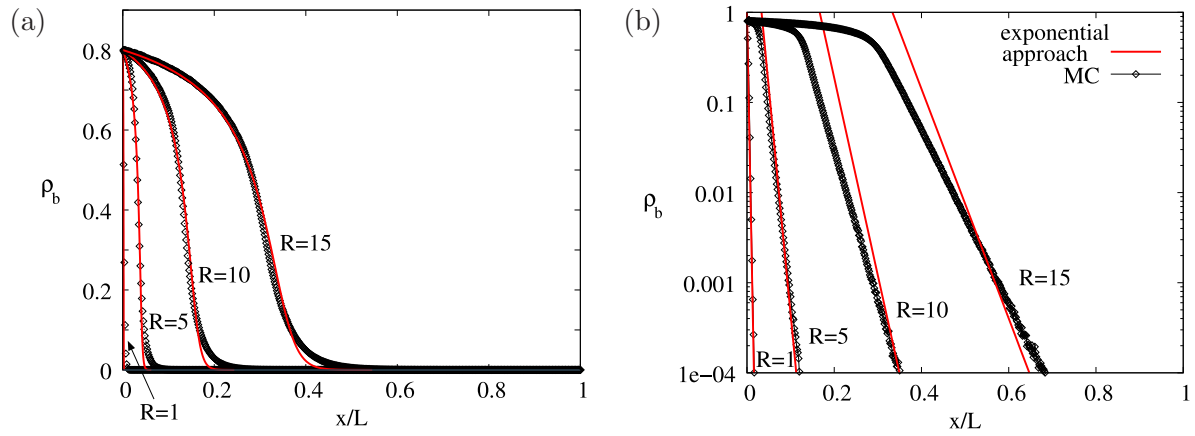

Fig. 3.8: For tubes with radii $R = 1$, $R = 5$, $R = 10$ and $R = 15$, the simulated bound density profiles ($\diamond$) agree well with the adsorption equilibrium approximation [solid red line in (a)] and approach the bulk value with an exponential length scale close to the length scale ξ of Eq. (3.8) [solid red lines in (b)]. However, both the adsorption equilibrium approximation and the theoretical exponential length scale fit less well the larger the radius. Simulation parameters are as in Fig. 3.7.

The theoretical calculation agrees well with the simulation results, see Fig. 3.6(a). The current extremum occurs when the tube is approximately full, i.e. when the jam length L_* is only slightly smaller than the tube length L. This is consistent with the assumption that the average current is mainly supported by the jam region, on which the use of the adsorption equilibrium approximation for the calculation of the average current is based.

In the limit of large L, one must jam up an infinite tube, for which one needs a boundary density $\rho_{\mathrm{b,in}} = 1$. For this case, Eq. (3.27) can be inverted approximately which leads to

$$\rho_{\mathrm{b,in}}^{\max} \approx 1 - K^{\frac{1-K^2}{1+K^2}} \mathrm{e}^{\frac{-(1-K)^2}{1+K^2}} \exp\left[-\frac{K}{1+K^2}\frac{|v_{\mathrm{b}}|}{D_{\mathrm{ub}}\phi}L\right], \tag{3.28}$$

i.e. the maximum density 1 is approached exponentially for large L.

3.5 Influence of the tube radius

So far we have only considered very thin tubes of radius $R = 1$. The bound density profiles $\rho_{\mathrm{b}}(x)$ for larger tube radii are shown in Fig. 3.8(a); they look qualitatively similar to the profiles for the case $R = 1$. However, now the unbound motor density depends on the radial coordinate r. This means that the two-state approximation that a motor at a longitudinal coordinate x is either bound or unbound, is no longer exact. Nevertheless, the density profiles are still well approximated by the adsorption equilibrium approximation, see Fig. 3.8(a), although the agreement is less well the larger the tube radius R. This is to be expected because adsorption equilibrium relies on equilibration of the radial binding and unbinding currents which is more difficult for larger tubes: motors with large radial coordinate r are far away from the filament and do not participate in binding and unbinding currents directly. Fig. 3.7(b) shows the violation of adsorption equilibrium for a fixed tube radius R as measured by the difference of $\rho_{\mathrm{ub,scaled}} - \rho_{\mathrm{b}}$ of Fig. 3.5. It is significant only in the shock region and grows with the radial coordinate r.

While the adsorption equilibrium approximation still holds for tubes with larger radii R, the characteristic bulk length scale ξ differs significantly from Eq. (3.8) as shown in Fig. 3.8(b). The reason is that the two-state approximation no longer works for thick tubes.

3.6 Jamming in related systems

The lattice model used for our computer simulations, as described briefly in Sec. 3.1 is a variant of driven lattice gas models or exclusion processes as reviewed in [138, 141]. The driven

lattice gas model was introduced as a generic model of nonequilibrium statistical mechanics [64, 65]. It consist of hard-core particles that move stochastically on a d-dimensional simple cubic lattice, where one direction is preferred due to an electric field. The simplest variant is the one-dimensional case which consist of a line of lattice points on which the particles perform a biased random walk. This is the asymmetric simple exclusion process (ASEP). Driven lattice gas models have been studied in various contexts, like ionic conductors [64] (the original motivation for driven lattice gases), motion of ribosomes along RNA [96] (the original motivation for the ASEP), traffic flow (reviewed in [19]) and nonequilibrium phase transitions (reviewed in [103]). The difference of our model and these models is that the motors in our model are 'driven', i.e. performing a biased random walk, only on the filament line, while they perform a symmetric random walk away from the filament. This lattice model has been extensively studied [68, 69, 70, 92, 115, 114, 121, 125]. In the last chapter we have considered this model in tubular compartments with half-open or closed boundary conditions and have shown that the adsorption equilibrium approximation is often a very good approximation for the bulk behaviour of the system. This means that the bound and unbound channels are strongly coupled and the system is effectively one-dimensional. In this chapter, we will therefore compare it to the ASEP which is really one-dimensional. First we consider the standard ASEP with half-open boundary conditions, which allows for an analytic solution in mean field approximation. Then we will consider the ASEP coupled to a large motor reservoir, i.e. with Langmuir kinetics, (ASEP+LK), as introduced by [121], also in mean field approximation with half-open boundary conditions.

3.6.1 Jamming in the half-open ASEP

We have seen that the stationary state of the half-open tube can be analytically well described by a mean field theory with the approximation of adsorption equilibrium Eq. (3.6). The fact that adsorption equilibrium hold well suggests that the bound and the unbound 'channels' for motor motion are effectively coupled. This leads to the question whether a one-channel system (where directed motion and undirected diffusion are superimposed) shows similar behaviour or whether the two channels lead to qualitatively different behaviour. In the following a one-dimensional system is considered where hard-core particles move diffusively with diffusion constant D in a homogeneous external field which induces a macroscopic directed particle velocity v. This corresponds to an ASEP with hopping rates α to the right and β to the left with

$$v = \alpha - \beta \qquad \text{and} \qquad D = (\alpha + \beta)/2 \tag{3.29}$$

The system is characterized by the density $\rho(x,t)$ at point x and time t. We consider half-open boundary conditions, i.e. a fixed density ρ_{in} at the left end $x = 0$ (open) and a reflecting boundary at the right end $x = L$ (closed).

Stationary state. Because of the closed right end, there is no net current in the stationary state of the system, and the diffusive current $-D\rho'(x)$ and the directed current $v\rho(x)[1-\rho(x)]$ must balance:

$$v\rho(x)[1-\rho(x)] - D\rho'(x) = 0. \tag{3.30}$$

The factor $[1-\rho]$ implements hard-core exclusion.

If the particles move to the left, i.e. $v < 0$, the bulk density is $\rho = 0$, if they move to the right, i.e. $v > 0$, the bulk density is $\rho = 1$. This is the same phase behaviour as for the two channel system considered in the last sections. The bulk value is in both cases approached exponentially with the length scale

$$\xi = D/|v|. \tag{3.31}$$

It diverges as $1/v$ as $v \to 0$. It is identical to the bulk length scale of the two channel system for $K = 1$ and for small velocities v.

The implicit solution of Eq. (3.30) which fulfills the left boundary condition $\rho(0) = \rho_{\text{in}}$ is

$$\frac{x}{L} = \frac{1}{V}\left[\ln\frac{\rho(x)}{1-\rho(x)} - \ln\frac{1-\rho_{\text{in}}}{\rho_{\text{in}}}\right] \tag{3.32}$$

with $V = vL/D$ in analogy to Eq. (3.14). This can be explicitly solved for the density profile

$$\rho(x) = \frac{1}{2}\left\{1 + \tanh\left[\frac{v}{2D}(x - L_*)\right]\right\}. \tag{3.33}$$

This is identical to the $K = 1$ profile of the adsorption equilibrium half-open tube with two channels, as then both models lead to the same Eq. (3.30) for the (bound) density. The jam length L_*, defined via $\rho(L_*) = 1/2$, is

$$\frac{L_*}{L} = \frac{1}{V}\ln\left[\frac{1-\rho_{\text{in}}}{\rho_{\text{in}}}\right] \tag{3.34}$$

The jam length shows the same divergence behaviour as in the two channel system, namely it diverges as $1/v$ for $v \to 0$, and logarithmically for $\rho_{\text{in}} \to 0$ or $\rho_{\text{in}} \to 1$.

The normalized average current

$$\frac{J}{v} = \frac{1}{L}\int_0^L \rho(x)(1-\rho(x))\,dx = \frac{1}{V}\left[\left[1 + \frac{1-\rho_{\text{in}}}{\rho_{\text{in}}}\exp\left(-V\frac{x}{L}\right)\right]^{-1} - \rho_{\text{in}}\right] \tag{3.35}$$

is maximal for the left boundary density

$$\rho_{\text{in}}^{\max} = (1 - \tanh[V/4])/2. \tag{3.36}$$

As in the two-channel system, the extremum boundary density approaches $\rho_{\text{in}}^{\max} = 1$ exponentially for large system lengths L.

Jamming dynamics. The dynamics of the one-channel system is governed by the equation

$$\frac{\partial}{\partial t}\rho(x,t) = D\,\frac{\partial^2}{\partial x^2}\rho(x,t) - v\,\frac{\partial}{\partial x}\rho(x,t)\,[1-\rho(x,t)]\,, \tag{3.37}$$

which can be explicitly solved by a mapping to the noiseless Burgers equation and a Cole-Hopf transformation, see App. A.2.3. One can then calculate the build-up of the jam from an initially empty tube to the stationary state. At small times, the jam 'diffuses' into the system with a jam length which is proportional to the square root of time, see Eq. (A.48):

$$L_*(t) \approx \frac{2\rho_{\text{in}} - 1}{\rho_{\text{in}}}\sqrt{\pi D}\sqrt{t} \tag{3.38}$$

For large times, the jam length relaxes exponentially to its stationary value with the relaxation time from Eq. (A.50):

$$t_{\text{rel}} = \left[\frac{v^2}{D}\,\rho_{\text{in}}(1-\rho_{\text{in}})\right]^{-1} \tag{3.39}$$

This relaxation time is larger than for the case without hard core exclusion, which is $4D/v^2$. It is equal to the case without hard core exclusion for $\rho_{\text{in}} = 1/2$, i.e. for maximal in-current.

Summary. We have studied the ASEP with half-open boundary condition in mean-field approximation and found this one-channel system to show similar jamming behaviour to the two-channel half-open tube considered in the last Sec. 3.1–3.2. In particular, the same type of phase transition with diverging bulk and jam lengths in the limit of small motor velocity occurs, and the jam length diverges logarithmically with the boundary density. The reason for this similarity is that a jammed two-channel system can be well described by the adsorption equilibrium approximation Eq. (3.6), which effectively couples the bound and unbound channel.

3.6.2 Filaments in contact with a large motor reservoir

For molecular motor traffic in a half-open tube, the unbound density is not constant, see Fig. 3.5(b). In *in vitro* experiments, however, unbound diffusion can be very fast and therefore smoothes out gradients in the unbound density rather fast. Also, the reservoir of unbound motors is often very large. This leads to an effectively constant unbound motor density. One then obtains active motion along the filament with velocity v_b, supplemented by binding and unbinding with rates $\tilde{\pi}_\mathrm{ad}$ and $\tilde{\epsilon}$ into a motor reservoir of constant density ρ_ub. This is the limiting case of constant unbound motor density of the large scale motor traffic model considered in Sec. 3.1–3.2. It was introduced as an ASEP with Langmuir kinetics (ASEP+LK) by [121] and has been extensively studied in the last few years [29, 57, 67, 121, 122, 125, 136].

In mean field approximation, the system is described by the motor density $\rho(x)$ on the filament. Upon setting

$$\omega_\mathrm{A} = \tilde{\pi}_\mathrm{ad}\,\rho_\mathrm{ub} \qquad \text{and} \qquad \omega_\mathrm{D} = \tilde{\epsilon}\,(1-\rho_\mathrm{ub}), \tag{3.40}$$

the current balance at each filament site in the stationary state implies

$$v_\mathrm{b}\partial_x\rho_\mathrm{b}(1-\rho_\mathrm{b}) = \omega_\mathrm{D}\rho_\mathrm{b} - \omega_\mathrm{A}(1-\rho_\mathrm{b}) \tag{3.41}$$

where the left hand side describes the change in the bound current while the right hand side describes unbinding and binding. For vanishing binding and unbinding, this is the mean field equation for the ASEP, while for vanishing velocity v_b this describes Langmuir kinetics with the equilibrium solution

$$\rho_\mathrm{LK} = \frac{1}{1+K_\mathrm{LK}}. \tag{3.42}$$

Here, K_LK is the desorption constant $K_\mathrm{LK} = \omega_\mathrm{D}/\omega_\mathrm{A}$. This Langmuir solution is also the bulk solution of Eq. (3.41). Linearization of Eq. (3.41) around this bulk solution shows that the bulk value is approached exponentially with length scale

$$\xi = \Delta x_\mathrm{b}\,\frac{K_\mathrm{LK}(1-K_\mathrm{LK})}{(1+K_\mathrm{LK}^2)}. \tag{3.43}$$

It is proportional to the average walking distance $\Delta x_\mathrm{b} = v_\mathrm{b}/\omega_\mathrm{D}$ on the filament before unbinding. In the limit of vanishing motor velocity $v_\mathrm{b} \to 0$, the the average walking distances and the bulk length scale ξ decrease to zero linearly. This is different from the case of non-constant unbound motor density, where the bulk length scale Eq. (3.8) diverges in the limit of zero motor velocity. The reason is that in the case of a reservoir with constant motor density Langmuir kinetics always dominates the bulk behaviour; the boundary therefore cannot dominate the system.

This can also be seen when considering the jam region. The current balance Eq. (3.41) can be integrated to give an implicit equation for the density ρ:

$$\frac{x}{L} = \frac{\Delta x_\mathrm{b}}{L}\left[g\left(\rho_\mathrm{b}(x), K_\mathrm{LK}\right) - g\left(\rho_\mathrm{b,in}, K_\mathrm{LK}\right)\right] \tag{3.44}$$

with the function

$$g(\rho, K_\mathrm{LK}) = 2\rho\frac{K_\mathrm{LK}}{1+K_\mathrm{LK}} - \frac{K_\mathrm{LK}(1-K_\mathrm{LK})}{(1+K_\mathrm{LK})^2}\ln\left|\rho-\rho_\mathrm{LK}\right|. \tag{3.45}$$

The bulk density of the system is determined by the Langmuir value $\rho_\mathrm{LK} = K_\mathrm{LK}/(1+K_\mathrm{LK})$, while the boundary density at the left end is fixed to $\rho_\mathrm{b,in}$. A jam develops only if $\rho_\mathrm{b,in} > \rho_\mathrm{LK}$. If in addition $\rho_\mathrm{b,in} > 1/2$, we can define the jam length L_* as the point where the density passes $1/2$. Then

$$\frac{L_*}{L} = \frac{\Delta x_\mathrm{b}}{L}\left[g\left(\frac{1}{2}, K_\mathrm{LK}\right) - g\left(\rho_\mathrm{b,in}, K_\mathrm{LK}\right)\right]. \tag{3.46}$$

If $\rho_{\mathrm{b,in}}$ is not larger than 1/2, we can alternatively define the jam length as the point where the density passes the half-value $(\rho_{\mathrm{LK}} + \rho_{\mathrm{b,in}})/2$ between the bulk density and the boundary density:

$$\frac{L_*}{L} = \frac{\Delta x_{\mathrm{b}}}{L}\left[g\left(\frac{\rho_{\mathrm{LK}} + \rho_{\mathrm{b,in}}}{2}, K_{\mathrm{LK}}\right) - g\left(\rho_{\mathrm{b,in}}, K_{\mathrm{LK}}\right)\right] \tag{3.47}$$

Comparing this to the expression for the jam length in the half-open tube with varying unbound density, the prefactor is now the ratio of the walking distance to the system length, or alternatively the ratio of the time L/v_{b} to walk the system length L and the time $1/\omega_{\mathrm{D}}$ before detaching from the filament. The jam length does not diverge in the limit of small motor velocity but instead tends to zero. In this limit, the bulk Langmuir dynamics dominates the system.

The jam length Eq. (3.46) or Eq. (3.47) is proportional to the walking distance Δx_{b}. As the function $g(\rho, K_{\mathrm{LK}})$ increases monotonously with ρ, the maximal jam length for a given K_{LK} is obtained with $\rho_{\mathrm{b,in}} = 1$. Considering then the maximum with respect to K_{LK}, we obtain

$$|L_*| \leq |\Delta x_{\mathrm{b}}|/2, \tag{3.48}$$

i.e. the jam length is always shorter than the walking distance. Thus a large jam builds up only if the walking distance is a significant fraction of the system length L. For biological systems the walking distance is of the order of 1 μm, while the system length ranges from tens of micrometers in fungal hyphae up to a metre in neurons. With a constant motor reservoir, jams thus always are restricted to a small layer near the boundary.

Summary. We have investigated the ASEP+LK, i.e. traffic on a filament in contact with a large motor reservoir, with half-open boundary conditions. Jamming in this system is very different from jamming in the half-open tube considered in Sec. 3.1–3.2: Motor traffic jams are restricted to boundary layers because the bulk is dominated by the Langmuir kinetics of binding and unbinding induced by the large reservoir of unbound motors. The authors of [29, 121, 122] circumvent this by scaling the binding and unbinding rates appropriately with the system size. They thereby consider only situations in which the jam length is of the order of the system size. In biological applications, however, the binding and unbinding rates are independent of the system size, and the jam length on a filament in a reservoir with constant motor density is small. In particular, it is smaller than the motor walking distance. Thus in *in vitro* systems in large compartments with fast diffusion where the unbound motor density can be approximated as constant, motor traffic jams should be small. This is in contrast to *in vivo* systems in confined compartments, for which the model with variable unbound densities is more reasonable. In this situation the confined geometry and finite diffusion times can lead to jam lengths much larger than the walking distance.

3.7 Summary

We have studied the large-scale molecular motor traffic in half-open tubular compartments which mimic the geometries of axons or hyphae. The motors act independently and only interact via hard-core exclusion which leads to traffic jams. We have characterized the relevant length scales of the system, and we have obtained analytical results for the jam region by using an adsorption equilibrium approximation which effectively couples the unbound and the bound channels by assuming that the currents of binding to and unbinding from the filament balance. We have used the same method to study motor traffic jams in a closed tube in App. A.2.2. Finally, we have compared the jamming behaviour in the half-open tube to the jamming in related one-dimensional systems, namely the ASEP and the ASEP with Langmuir kinetics (ASEP+LK).

Astonishingly, the half-open ASEP and the half-open tube show similar jamming behaviour: they exhibit the same type of phase transition with diverging bulk and jam lengths in the limit of small motor velocity, and the jam length diverges logarithmically with the boundary density. In particular, the jam length can become very large and dominate the whole system. This is

in contrast to the ASEP+LK, where traffic jams are restricted to boundary layers because the bulk is dominated by Langmuir kinetics.

Our results for the jam region in the half-open tube include analytical results for the motor traffic jam length and for the motor parameters which optimize the traffic in these compartments, see Fig. 3.6. However, although the current can be optimized, the stationary state of these half-open tubes is always characterized by a density which approaches either one or zero far from the open end (with a phase transition separating these two cases). The reason is that motors either walk to the open or to the closed end, and that the confined tube geometry and slow diffusion induce traffic jams. Long tubes are therefore either essentially filled or essentially empty. In axons or hyphae, which are mimicked by this tube geometry, additional processes are therefore necessary to maintain efficient stationary transport. In the next chapters, we will investigate one possibility for such a process: cargos that move bidirectionally because they are transported by motors which walk into opposite directions.

Chapter 4

Bidirectional cargo transport by two teams of motors: a tug-of-war model

In the last chapter, we have seen that particles that move in only one direction are not sufficient for intracellular transport: plus-end moving particles jam up at the MT plus ends, while minus-end particles jam up at the MT minus ends. Indeed, in the cell many cargos do not move unidirectionally but bidirectionally, changing direction every few seconds. They are transported by two teams of motors: a team of plus and a team of minus motors, as discussed in Sec. 1.4.

In this chapter, we introduce and investigate a model for cargo transport by two teams of motors as the most straightforward scenario: the motors act independently according to the single motor behaviour described in Chap. 2. They only feel each other because of the mechanical interaction with their common cargo. Such a scenario is often called a 'tug-of-war' of the motors [40]. Contrary to what might be expected from a naive picture for a tug-of-war, this first realistic tug-of-war model exhibits complex cooperative behaviour [72, 108].

After having described the biological background of the bidirectional cargo transport problem in Sec. 4.1, we introduce our tug-of-war model in Sec. 4.2. We investigate its basic transport patterns, which we call 'motility states', in Sec. 4.3. The complex dependence of these motility states on the motor properties leads to complex 'motility diagrams'. In Sec. 4.4, we explain this behaviour using four different approximations, namely approximations for 'weak' and 'strong' motors, a mean field approximation and a 'sharp maximum approximation'. In Sec. 4.5, we investigate experimentally relevant dynamic properties of the tug-of-war such as switch times, unbinding times and velocities. Finally, we discuss the effects of frictional and external forces.

4.1 Introduction: Bidirectional cargo transport in cells

Active bidirectional intracellular transport, which is faster and more persistent than Brownian motion, has been known for a long time, even before the underlying transport mechanism by molecular motors has been discovered [32, 128]. However, this bidirectional 'saltatory motion' was merely viewed as a curiosity until the late 1990's, when the improvement of experimental techniques showed that bidirectional transport is in fact widespread, including cargos such as mitochondria, endosomes, axonal vesicles, mRNA complexes, melanosomes and lipid-droplets [47, 174]. Even viruses that hijack the motor system of their host cell for their own transport move bidirectionally [149, 154].

4.1.1 Type and number of motors on a cargo

Since the bidirectional motion takes place on isopolar MT arrays, see Sec. 1.4 and Fig. 1.3, it is clear that both plus and minus motors must be involved in the bidirectional transport of a single cargo. However, how these motors work together is a matter of current debate, as reviewed in [40, 47, 174]. The 'old view' of cargo transport was that a single cargo is transported only in

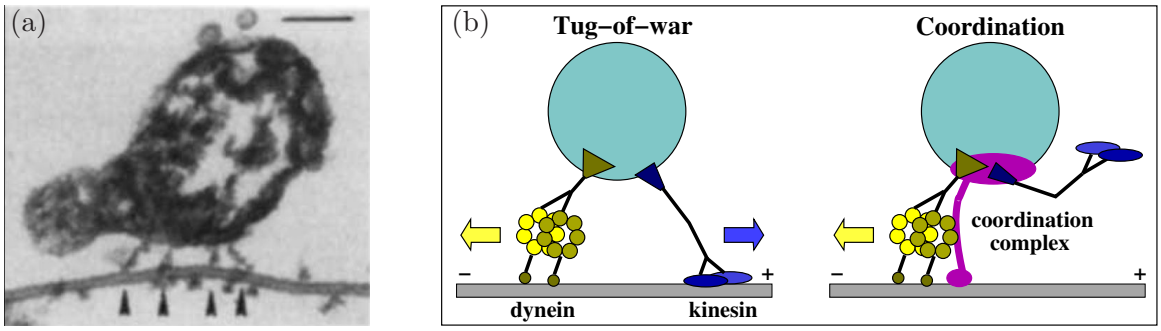

Fig. 4.1: (a) A mitochondrion transported by four motors indicated by arrows. The scale bar is 0.1 μm. From [4]. (b) A cargo transported by one plus end moving kinesin and one minus end moving dynein. In a tug-of-war model, the motors pull against each other until one wins. In a coordination model, a coordination complex prevents both motors from being active at the same time, so that the cargo is pulled by only one motor type.

one direction, and only by one species of motors. One idea was therefore that cargo direction changes due to unbinding of one motor species and binding of the other to the cargo. However, switching of direction occurs on a second time scale, see e.g. [154, 106], which is much faster than the binding and unbinding of motors to and from the cargo.

Indeed, plus and minus motors are found *simultaneously* on a single cargo. First evidence for this was collected already in the early 1990s with ligation experiments on neuronal cells. When axonal flow was stopped by a cut, a crush, a cold block, or a ligature, cargos traveling to the plus end accumulated at the proximal and cargos traveling to the minus end at the distal side of the ligation. Cargos with kinesin [22, 52] and cargos with dynein [53] were found to accumulate on *both* sides of the ligation. This means that plus-end cargos do not only carry plus-end but also minus end motors. Analogously minus-end cargos must also carry plus-end motors. In the late 1990s, bidirectional motion of purified pigment granules and endocytic vesicles *in vitro* showed that these cargos do not only carry plus- and minus-end motors concurrently, but also that both types are active [110, 133]. Recently, colocalization studies showed directly that plus- and minus-end motors are on the same cargo simultaneously *in vivo* [89, 124].

The number of motors that transport a single cargo is hard to estimate and depends on the cargo and cell type. It presumably ranges from 1 to 10 motors, as has been determined by various methods. On electron micrographs, where motors appear as crossbridges linking the cargo to the filament as in Fig. 4.1(a), counting of crossbridges results in 1-7 dyneins [48], 1-4 unknown motors [4], and 2-5 dyneins and kinesins [10] on a single cargo. From *in vivo* stall force measurements, the number of motors on a *Drosophila* lipid-droplet was estimated to range from 1 to 5 for each motor type, i.e. 1-10 motors in total [176]. The interpretation of *in vivo* velocity distributions of *Xenopus* melanosomes resulted in an estimate of 4 motors of each type, i.e. in total 8 motors [86]. The last two estimates indicate that the number of plus and minus motors on bidirectional cargos is often quite similar. For *Xenopus* melanosomes and neuroblastoma cell mitochondria, this is even independent of the direction in which they were moving [23, 42].

4.1.2 Tug-of-war versus coordination

It is now widely accepted that bidirectional cargos are bound to several plus- and minus-end motors simultaneously. But how is cargo transport by two teams of opposing motors achieved? Two types of models are discussed in the literature, see Fig. 4.1(b) [38, 40, 174]:

- **Tug-of-war model**: Plus and minus motors both try to move the cargo into their preferred direction. Thus the motors perform a 'tug-of-war' on the cargo as shown in Fig. 4.2, and the cargo moves into the direction of the 'stronger' motors. This model has also been called the 'balance of power' model [13, 16] or the 'override model' [109].

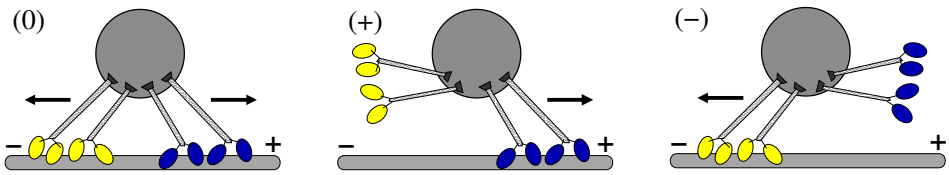

Fig. 4.2: Cargo transport by two plus motors (blue heads) and two minus motors (yellow heads). For configuration (0), the motors block each other so that the cargo does not move. For configuration (+) and (−), the cargo exhibits fast plus and minus motion, respectively.

- **Coordination model**: An additional coordination complex prevents opposing motors from being active at the same time, thereby excluding state (0) in Fig. 4.2. The nature of this coordination complex is, however, unknown so far.

In both cases, regulatory mechanisms, which may directly target the motors or the putative coordination complex, must be present in order to allow the cell to alter its motor transport in response to internal or external stimuli. Most authors favour the more intuitive coordination hypothesis for *in vivo* traffic because of the following experimental observations:

- **Fast cargo motion**: Bidirectional cargos move into each direction usually with large velocities of the order of a few μm/s. This indicates that the motors which determine the actual direction are not 'hindered' by the opposing motors, as could be naively expected in a tug-of-war scenario.

- **Interdependence of directions**: Bidirectional cargo transport was found to be affected in a complex way both by intracellular regulation and by mutational changes in the motor structure. In a naive tug-of-war model, such interference should lead to impairment of motion in one direction and enhancement of motion in the other: If, for example, the minus motors are downregulated or corrupted by a mutation, they are more likely to lose against the plus motors. Therefore, minus motion should be impaired and plus motion enhanced. Although such kind of behaviour has indeed been observed in some systems, as for adenovirus particles [154] or in an *in vitro* motility assay [162], it can also happen that both directions are impaired, as for axonal vesicles [61], or that one direction is changed while the other direction is left unchanged, as for *Drosophila* lipid-droplets [44] or for herpesvirus capsids [149]. There are even systems in which two or all different responses have been found, as for *Xenopus* melanophores [42] or *Drosophila* lipid-droplets [176].

- **Stall force balance**: In *Drosophila* embryos, the stall forces of bidirectionally moving lipid-droplets are approximately the same in both directions, independent of the net direction of the droplet transport [176]. This seems to be in contradiction with a tug-of-war in which equally strong motors should lead to equal transport in both directions.

- **Regulatory proteins**: Many proteins influence motor transport [130, 165]. Prominent examples are (i) kinases, i.e. enzymes that phosphorylate the motors or associated proteins, (ii) G-proteins, i.e. guanine nucleotide binding proteins, GTPases that use the GTP hydrolysis as a 'switch' to regulate cellular processes, or (iii) dynactin, a dynein accessory protein that regulates the processivity of dynein and also interacts with kinesin [24].

These experimental observations seem to be incompatible with a tug-of-war scenario at first sight. However, this conclusion is premature, since a realistic tug-of-war leads to a complex transport behaviour that is not easily understood intuitively and, thus, may be erroneously interpreted as coordinated transport. We will present such a tug-of-war model in this chapter, which is consistent with all experimental observations listed above.

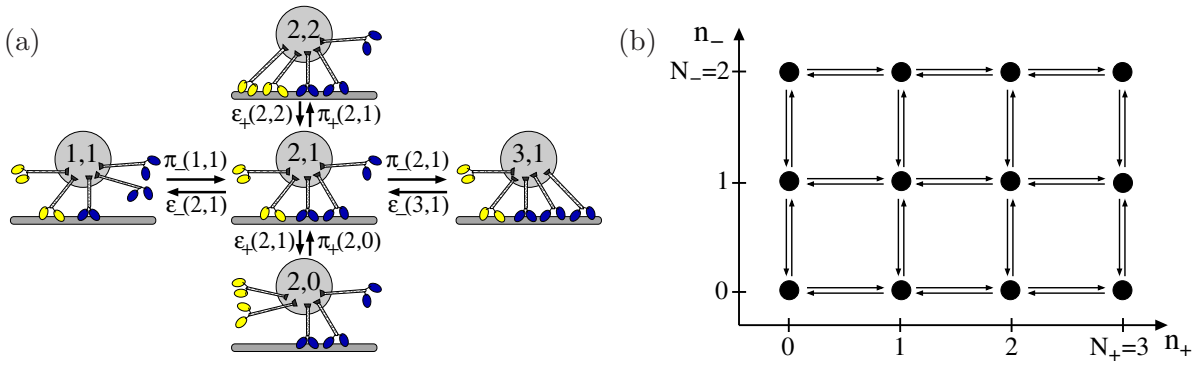

Fig. 4.3: A cargo with $N_+ = 2$ plus motors (blue heads) and $N_- = 3$ minus motors (yellow heads) is pulled by a fluctuating number of motors bound to the filament. (a) The configuration in the middle corresponds to $(n_+, n_-) = (2, 1)$ and changes when one motor binds or unbinds. (b) This stochastic binding and unbinding leads to a random walk on the state space of (n_+, n_-) configurations with $n_+ = 1, \ldots, N_+$ and $n_- = 1, \ldots, N_-$. The total number of configurations is $(N_+ + 1)(N_- + 1) = 12$.

4.2 Tug-of-war model for bidirectional cargo transport

In this section, we describe our model for the bidirectional transport of a cargo particle by one team of plus and one team of minus motors.

Cargo transport by *one* team of motors has found much theoretical interest, and interesting collective effects such as spontaneous directed motion, dynamic instabilities and spontaneous oscillations have been found [5, 14, 26, 59, 60, 71, 168]. In contrast, transport by two teams of motors has been considered only in effective ways by considering a cargo particle which, when bound to the filament, travels in plus and minus direction with different rates [101, 120, 148]. The stochastic fluctuations of the (un-)binding of the motors, the transport properties of the motors, and the effects of the motors on each other have not been considered.

4.2.1 The Master equation

We consider a cargo that is attached to constant numbers of N_+ plus and N_- minus motors. These numbers are taken to be constant because the binding of the motors to the cargo is very strong. On the time scale of experiments (usually minutes), the attachment is irreversible.[1] Typical motor numbers in cells range from 1 to 10, see Sec. 4.1.1. For $N_+ = 0$ or $N_- = 0$, the cargo is transported by only one motor species, and we recover the model studied in [71].

Each of these motors has the single motor properties described in Chap. 2. In particular, each motor stochastically binds to and unbinds from the filament. At each time t, the state of the cargo is characterized by the numbers n_+ and n_- of plus and minus motors that are bound to the filament and thus actively pull on the cargo at that time. We call these motors the 'bound' or the 'active' motors. The cargo state changes when a plus or a minus motor binds to or unbinds from the filament, see Fig. 4.3(a). This leads to a random walk on the state space (n_+, n_-) with $0 \le n_+ \le N_+$ and $0 \le n_- \le N_-$, as shown in Fig. 4.3(b). This walk is described by a Master equation for the probability distribution $p(n_+, n_-, t)$ to have n_+ active plus and n_- active minus motors at time t:

$$\begin{aligned}\frac{\partial}{\partial t}p(n_+,n_-,t) \;=\; & \epsilon_+(n_+ + 1, n_-)\, p(n_+ + 1, n_-, t) + \epsilon_-(n_+, n_- + 1)\, p(n_+, n_- + 1, t) \\ & + \pi_+(n_+ - 1, n_-)\, p(n_+ - 1, n_-, t) + \pi_-(n_+, n_- - 1)\, p(n_+, n_- - 1, t) \\ & - \left[\pi_+(n_+,n_-) + \pi_-(n_+,n_-) + \epsilon_+(n_+,n_-) + \epsilon_-(n_+,n_-)\right] p(n_+,n_-,t)\end{aligned} \tag{4.1}$$

[1] The numbers N_+ of plus and N_- of minus motors only count the motors on the cargo that are in a position from which they can bind to the filament. These numbers fluctuate when the cargo rotates; we neglect this here.

The rates $\pi_{+(-)}(n_+, n_-)$ and $\epsilon_{+(-)}(n_+, n_-)$ describe binding and unbinding of a single plus (minus) motor when the cargo is in the state (n_+, n_-). They are determined from the single motor rates of Chap. 2 using the assumptions that the motors act independently and only feel each other because of two effects:

(i) opposing motors act as mutual load, and

(ii) same-directional motors share this load.

If each plus motor feels the load F_+ (and generates the force $-F_+$) and each minus motor feels the load $-F_-$ (and generates the force F_-), this means that the force balance on a cargo pulled by n_+ plus and n_- minus motors is

$$n_+ F_+ = -n_- F_- \equiv F_{\rm C}(n_+, n_-) \tag{4.2}$$

Here, the sign of the force is chosen positive if it is a load on the plus motors, i.e. if it points into the minus direction. If only one motor type is bound, i.e. if $n_+ = 0$ or $n_- = 0$, then $F_+ = F_- = F_{\rm C} = 0$. The force balance Eq. (4.2) represents Newton's third law: each motor feels the same force as it exerts.

A single bound plus motor thus feels the force $F_+ = F_{\rm C}/n_+$. Using the single motor unbinding and binding rates, Eq. (2.1) and Eq. (2.2), and the independence assumption, this implies that the effective rate for the unbinding of one plus motor is

$$\epsilon_+(n_+, n_-) = n_+ \, \epsilon_{0+} \, \exp\left[F_{\rm C}(n_+, n_-)/(n_+ F_{d+})\right], \tag{4.3}$$

and the effective rate for the binding of one plus motor is[2]

$$\pi_+(n_+, n_-) = (N_+ - n_+) \, \pi_{0+}. \tag{4.4}$$

Here and in the following, the index '+' labels plus motor properties. Analogous expressions apply to the minus motors with the parameters indexed by '−'. A detailed derivation of the product form of the rates can be found in App. A.3.4. The binding/unbinding dynamics as given by Eqs. (2.1) and (2.2), but without the active movement in the bound state, also arises for the forced rupture of adhesion molecule clusters [8, 28, 143].

4.2.2 Cargo force and velocity

The cargo force is determined by the condition that both plus motors, which experience the force $F_{\rm C}/n_+$, and minus motors, which experience the force $-F_{\rm C}/n_-$, move with the same velocity v_C as given by

$$v_C(n_+, n_-) = v_+(F_{\rm C}/n_+) = -v_-(F_{\rm C}/n_-). \tag{4.5}$$

Here, the sign of the velocity is taken to be positive in the plus direction and negative in the minus direction. The force and velocity balances as given by Eqs. (4.2) and (4.5) determine the cargo force and velocity, as illustrated in Fig. 4.4, with the result:

$$F_{\rm C}(n_+, n_-) = \lambda(n_+, n_-) \, n_+ F_{s+} + [1 - \lambda(n_+, n_-)] \, n_- F_{s-}, \tag{4.6}$$

$$v_C(n_+, n_-) = \frac{n_+ F_{s+} - n_- F_{s-}}{n_+ F_{s+}/v_{0+} + n_- F_{s-}/v_{0-}} \tag{4.7}$$

with $\lambda(n_+, n_-) = 1/\left[1 + (n_+ F_{s+} v_{0-})/(n_- F_{s-} v_{0+})\right]$. Note that the single motor velocity parameters $v_{0\pm}$ are equal to the plus resp. minus motor forward velocity $v_{F\pm}$ or backward velocity $v_{B\pm}$, depending on whether the respective motor moves forward or backward, see Eq. (2.7). The direction of the cargo is determined by the intuitive 'majority rule' contained in Eq. (4.7):

$$v_C > 0 \qquad \text{for } n_+ F_{s+} > n_- F_{s-}, \qquad \text{i.e. plus motors 'win'}$$

[2] Motor binding from the state $(n_+, n_-) = (0, 0)$ could in principle be different, as in this state the cargo is not tethered to the filament and could therefore be too far away for the motors to bind with the rate π_{0+} of a single motor on a bead of Sec. 2.2.2. We will deal with this issue in Sec. 4.2.4.

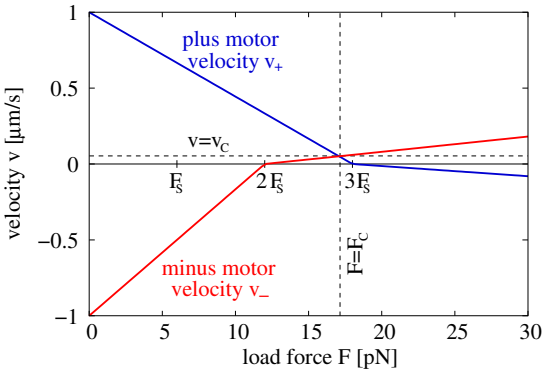

Fig. 4.4: Graphical solution for the cargo force F_C and velocity v_C as intersection point of the plus and minus motor force-velocity-curves v_+ (blue) and v_- (red), according to Eq. (4.5). The parameters are $n_+ = 3$ plus and $n_- = 2$ minus motors, the kinesin-like stall force $F_s = 6\,\mathrm{pN}$, and the rather large backward velocity $v_B = 0.3\,\mu\mathrm{m/s}$ for both plus and minus motors. For the small kinesin-like backward velocity $v_B = 0.006\,\mu\mathrm{m/s}$, the result would be $F_C \approx 3\,F_s$, close to the maximal stall force, and $v_C \approx 0$.

$$\begin{aligned} v_C < 0 \quad &\text{for} \quad n_+F_{s+} < n_-F_{s-}, \quad \text{i.e. minus motors 'win'} \\ v_C = 0 \quad &\text{for} \quad n_+F_{s+} = n_-F_{s-}, \quad \text{i.e. 'tie'} \end{aligned} \tag{4.8}$$

The force F_C and velocity v_C given by Eqs. (4.6) and (4.7) are continuous functions of the single motor parameters and of the numbers n_+ and n_- of bound motors[3]. Since $0 \le \lambda \le 1$, the cargo force as in Eq. (4.6) is a convex combination of the maximal plus and minus motor stall forces n_+F_{s+} and n_-F_{s-}. Therefore, if the plus motors win, these motors walk under substall and the minus motors under superstall load force, i.e.

$$n_-F_{s-} < F_C(n_+, n_-) < n_+F_{s+}, \tag{4.9}$$

which is consistent with the single motor force-velocity relation Eq. (2.6).

The velocity balance Eq. (4.5) assumes that all motors walk with the same velocity. This can be justified by considering what happens when this steady state is disturbed, e.g. by the binding of a minus motor on a cargo that is steadily moving into the plus direction. The 'new' motor has bound in a relaxed state and feels a low load force. It therefore steps forward, gets stretched and burdens itself with part of the load force imposed by the plus motors, taking away part of the load force of the other minus motors. It does so until all minus motors feel roughly the same load force. This justifies our mean field treatment that each plus resp. minus motor feels on average the *same* force F_+ resp. $-F_-$. The new force balance depends on whether the plus or minus motors are 'stronger'. If the plus motors together can produce a larger force than the minus motors, i.e. if $n_+F_{s+} > n_-F_{s-}$ (with the 'new' number n_- of bound minus motors), then the new minus motors runs forward until it feels a superstall load force and then starts to run backwards. The total force on the cargo increases, and all motors slow down until a new force balance is achieved. If the minus motors can produce a larger force than the plus motors, i.e. if $n_-F_{s-} > n_+F_{s+}$, the minus motors 'take over': the new minus motor runs forward and takes away more and more load force from the other minus motors until they all feel a substall load force $-F_- < F_{s-}$. The plus motors, on the contrary, start to move backward as soon as they feel a superstall load force $F_+ > F_{s+}$. The forward and backward stepping of motors thus provides a relaxation mechanism which rapidly establishes the force and velocity balances as provided by Eqs. (4.2) and (4.5).

The cargo force given in Eq. (4.6) determines the plus motor rates Eqs. (4.3) and (4.4) and the corresponding minus motor rates for the Master equation 4.1. However, one has to take the non-natural reflecting boundary conditions

$$\pi_+(-1, n_-) = 0, \quad \pi_-(n_+, -1) = 0, \quad \epsilon_+(N_+ + 1, n_-) = 0, \quad \epsilon_-(n_+, N_- + 1) = 0, \tag{4.10}$$

into account, which ensure that the numbers of active motors stay within the intervals $0 \le n_+ \le N_+$ and $0 \le n_- \le N_-$.

[3] Although the single motor velocities v_{0+} and v_{0-} change abruptly at $n_+F_{s+} = n_-F_{s-}$, there is no discontinuity because in this case the cargo force $F_C = n_+F_{s+} = n_-F_{s-}$ and the cargo velocity $v_C = 0$ become independent of v_{0+} and v_{0-}.

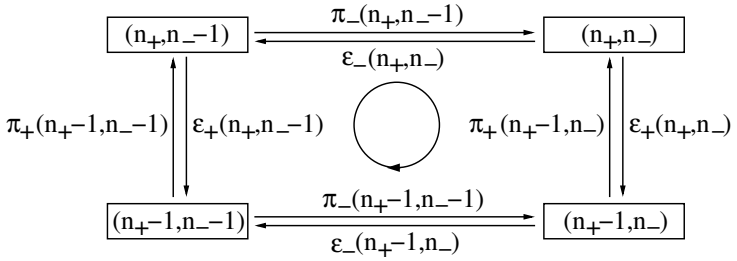

Fig. 4.5: The cycle $(n_+, n_-) \to (n_+ - 1, n_-) \to (n_+ - 1, n_- - 1) \to (n_+, n_- - 1) \to (n_+, n_-)$ is one of the $N_+ \cdot N_-$ fundamental cycles of the network for the cargo random walk.

4.2.3 Nonequilibrium and entropy production

The Master equation Eq. (4.1) describes a random walk on the state space shown in Fig. 4.3(b). This state space is a network with many cycles. A set of fundamental cycles are the $N_+ \cdot N_-$ 'small squares' as shown in Fig. 4.5. An interesting quantity is the ratio of forward and backward rates in these cycles defined via

$$\Pi(n_+, n_-) \equiv \frac{\epsilon_-(n_+ - 1, n_-) \cdot \pi_+(n_+ - 1, n_- - 1) \cdot \pi_-(n_+, n_- - 1) \cdot \epsilon_+(n_+, n_-)}{\pi_+(n_+ - 1, n_-) \cdot \pi_-(n_+ - 1, n_- - 1) \cdot \epsilon_+(n_+, n_- - 1) \cdot \epsilon_-(n_+, n_-)} \tag{4.11}$$

If $\Pi(n_+, n_-) = 1$ for all cycles, detailed balance holds and the stationary solution of the Master equation is an equilibrium solution. In our case, each cycle is driven by the thermodynamic force or entropy production for one completion of this cycle, $X(n_+, n_-) = \ln \Pi(n_+, n_-)$, as given by

$$X(n_+, n_-) = \frac{F_{\mathrm{C}}(n_+, n_-) - F_{\mathrm{C}}(n_+, n_- - 1)}{n_+ F_{d+}} - \frac{F_{\mathrm{C}}(n_+, n_-) - F_{\mathrm{C}}(n_+ - 1, n_-)}{n_- F_{d-}}, \tag{4.12}$$

which is in general different from zero because of the forces generated by the motors. Therefore, the ratio Π is different from 1 and our system is out of equilibrium.

4.2.4 Stationary state and cargo unbinding

Experiments *in vivo* usually monitor cargos which move along a filament and have been doing so for some (unknown) time. Cargo binding to and unbinding from the filament is ignored. This has two implications for our calculations:

Stationarity. First, we are interested in long-time properties of cargo motion, i.e. in the time-independent stationary state probability $p(n_+, n_-)$ to have n_+ active plus and n_- active minus motors, which is obtained by setting the time-derivative in the Master equation Eq. (4.1) to zero:

$$\begin{aligned} 0 \;=\; & \epsilon_+(n_+ + 1, n_-)\, p(n_+ + 1, n_-) + \epsilon_-(n_+, n_- + 1)\, p(n_+, n_- + 1) \\ & + \pi_+(n_+ - 1, n_-)\, p(n_+ - 1, n_-) + \pi_-(n_+, n_- - 1)\, p(n_+, n_- - 1) \\ & - \left[\pi_+(n_+, n_-) + \pi_-(n_+, n_-) + \epsilon_+(n_+, n_-) + \epsilon_-(n_+, n_-)\right] p(n_+, n_-) \end{aligned} \tag{4.13}$$

Condition on bound cargos. Second, we are interested in probabilities that are conditioned on the cargo being bound to the filament. We can separate cargo unbinding into two steps: (i) the last motor unbinds from the filament so that the cargo is in the state $(0, 0)$ but still close to the filament, and (ii) the cargo diffuses away from the filament and then freely diffuses in the surrounding solution. We call this diffusing state U. The rates for cargo unbinding into and rebinding from the state U depend on the geometry of the system and the viscosity of the surrounding solution. In App. A.3.2 we show that the probability $p(n_+, n_-)$ which solves the stationary Master equation Eq. (4.13) is in fact the stationary probability conditioned on the cargo being bound to the filament, i.e. not to be in state U, and that this probability is independent of the rates linking the state $(0, 0)$ to state U. We can therefore ignore cargo unbinding and diffusion. Furthermore, a cargo in the state $(0, 0)$ is close to the filament. Binding of plus and minus motors from this state is therefore described by the intrinsic motor rates $\pi_{0\pm}$,

which justifies our choice of the binding rates Eq. (4.4) also for the state $(n_+, n_-) = (0, 0)$.

Processivity enhancement. The neglect of cargo unbinding in experiments is justified by the fact that *in vivo* cargos rarely unbind from their track[4]. The reason is presumably that the cargo is tethered to the filament by many motors, see Sec. 4.1.1, which dramatically increases the cargo processivity. This has been shown theoretically for cargos transported by several motors of the same kind [71]. We will show that it is also true for a cargo transported by two teams of opposing motors in Sec. 4.5.3.

4.2.5 External and frictional forces

Our model can be easily extended to include external or frictional forces. An external force F_{ext} can be applied by an optical trap as described in Sec. 1.3. A frictional force $\gamma_{\text{S}} v_C$ with the Stokes friction coefficient γ_{S} is important for a large cargo or large viscosity of the surrounding solution, as might be the case in cells, see Sec. 1.1.

With external and frictional forces, the force balance equation Eq. (4.2) becomes

$$n_+ F_+ = -n_- F_- + F_{\text{ext}} + \gamma_{\text{S}} v_C \tag{4.14}$$

where the sign of the forces is positive if they point into the minus direction. This force balance Eq. (4.14) and the velocity balance

$$v_C = v_+(F_+) = -v_-(-F_-) \tag{4.15}$$

determine the plus and minus motor load forces F_+ and $-F_-$, and the cargo velocity v_C:

$$\begin{aligned}
n_+ F_+ &= n_+ F_{s+} \frac{n_- F_{s-} \left(\frac{\nu_{FA+}}{v_{0-}} + \frac{\nu_{FA-}}{v_{0+}} \right) + F_{\text{ext}}/v_{0+} + \gamma_{\text{S}} \nu_{FA+}}{n_+ F_{s+}/v_{0+} + n_- F_{s-}/v_{0-} + \gamma_{\text{S}}} \\
-n_- F_- &= n_- F_{s-} \frac{n_+ F_{s+} \left(\frac{\nu_{FA+}}{v_{0-}} + \frac{\nu_{FA-}}{v_{0+}} \right) - F_{\text{ext}}/v_{0-} + \gamma_{\text{S}} \nu_{FA-}}{n_+ F_{s+}/v_{0+} + n_- F_{s-}/v_{0-} + \gamma_{\text{S}}} \\
v_C &= \frac{n_+ F_{s+} \nu_{FA+} - n_- F_{s-} \nu_{FA-} - F_{\text{ext}}}{n_+ F_{s+}/v_{0+} + n_- F_{s-}/v_{0-} + \gamma_{\text{S}}}
\end{aligned} \tag{4.16}$$

where, as in Eq. (2.7), the single motor velocity parameter v_{0+} is equal to v_{A+}, v_{F+}, v_{B+} for assisting, substall load and superstall load force, respectively. As the external force can lead to an assisting force on the motors, all three linear segments of the force-velocity-curve Eq. (2.6) come into play, leading to four cases:

$$\begin{aligned}
&-n_- F_{s-} \tfrac{v_{B-}+v_{F+}}{v_{B-}} - \gamma_{\text{S}} v_{F+} \geq F_{\text{ext}} && \text{plus motors win, assisting force} \\
&-n_- F_{s-} \tfrac{v_{B-}+v_{F+}}{v_{B-}} - \gamma_{\text{S}} v_{F+} \leq F_{\text{ext}} \leq n_+ F_{s+} - n_- F_{s-} && \text{plus motors win, load force} \\
&+n_+ F_{s+} \tfrac{v_{B+}+v_{F-}}{v_{B+}} + \gamma_{\text{S}} v_{F-} \geq F_{\text{ext}} \geq n_+ F_{s+} - n_- F_{s-} && \text{minus motors win, load force} \\
&+n_+ F_{s+} \tfrac{v_{B+}+v_{F-}}{v_{B+}} + \gamma_{\text{S}} v_{F-} \leq F_{\text{ext}} && \text{minus motors win, assisting force}
\end{aligned}$$

In addition, we have defined:

$$\nu_{FA+} = \begin{cases} v_{F+}/v_{A+} & \text{for winning plus motors under assisting load} \\ 1 & \text{else} \end{cases} \tag{4.17}$$

and analogously for the minus motors. Note that the criterion for the cargo direction is still the intuitive weighted majority rule (now including the external force F_{ext}):

$$\begin{aligned}
&\text{plus motors win} \quad \text{if} \quad n_+ F_{s+} - n_- F_{s-} \geq F_{\text{ext}} \\
&\text{minus motors win} \quad \text{if} \quad n_+ F_{s+} - n_- F_{s-} \leq F_{\text{ext}}
\end{aligned} \tag{4.18}$$

[4] Cargo unbinding is not ignored in single motor *in vitro* experiments where unbinding is likely and is, for example, characterized by the run length, see Chap. 2.

4.2.6 Calculational methods

We model cargo transport by two (small) teams of opposing molecular motors as a random walk on the state space (n_+, n_-) of fluctuating numbers of active plus and minus motors as shown in Fig. 4.3, described by the Master equation Eq. (4.1).

For given numbers N_+ and N_- of plus and minus motors on the cargo with a given set of single motor parameters, we numerically calculate the steady state solution as the nullspace of the transition matrix of the Master equation Eq. (4.1) [166]. We use a self-written routine in *Mathematica* [177], or a self-written C++ program with included routines from the NAG-library [111].

In order to obtain dynamical quantities such as first passage times, we generate individual cargo trajectories with a self-written C++ program using the Gillespie algorithm for the binding/unbinding dynamics and let the cargo move with velocity v_C in the intervals between (un-)binding events [36]. At the start of the simulation, the cargo is bound to the filament by a random number of n_+ plus and n_- minus motors. In order to suppress transient behaviour due to initialization bias, measurement of our quantities of interest are started only after a sufficient warm-up period. We then average over many trajectories.

Besides these numerical methods we will perform various analytical calculations.

4.3 Motility states and their characteristics

In this section we investigate the basic motility patterns of a cargo transported by two teams of opposing motors which are engaged in a tug-of-war. We classify the motility states of the cargo and investigate them for the symmetric and asymmetric tug-of-war.

4.3.1 Classification of cargo states: fast plus, fast minus, and no motion

For a cargo pulled by n_+ active plus and n_- active minus motors, there are three qualitatively different cases which correspond to the configurations (+), (−) and (0) depicted in Fig. 4.2:

- **Fast plus motion** (+) with $n_+ > 0,\ n_- = 0$: Only plus motors are bound to the filament so that they do not feel any force, $F_+ = F_C = 0$. Therefore, the cargo moves into the plus direction with their maximal forward velocity $v_C = v_{F+}$, see Eqs. (4.6) and (4.7).
- **Fast minus motion** (−) with $n_+ = 0,\ n_- > 0$: Only minus motors are bound to the filament, and, analogous to the previous case, the cargo moves into the minus direction with maximal velocity $v_C = -v_{F-}$, see Eq. (4.7).
- **Slow motion** (0): Both types of motors are bound to the filament, $n_+ \neq 0$ and $n_- \neq 0$. In this case the cargo direction is determined by the 'stronger motors', see Eq. (4.8). The losing motors walk backwards. As the motor back velocities are typically small, see Chap. 2, the cargo velocity is low. This can be seen, e.g. for for winning plus motors, by looking at Fig. 4.4, or mathematically by expanding Eqs. (4.6) and (4.7) in v_{B-}/v_{F+}:

$$\begin{aligned} F_C(n_+,n_-) &= n_+F_{s+}\left[1-\left(\tfrac{n_+F_{s+}}{n_-F_{s-}}-1\right)\tfrac{v_{B-}}{v_{F+}}+\mathcal{O}\left(\tfrac{v_{B-}}{v_{F+}}\right)^2\right] &&\approx n_+F_{s+} \\ v_C(n_+,n_-) &= v_{B-}\left(\tfrac{n_+F_{s+}}{n_-F_{s-}}-1\right)\left[1-\tfrac{n_+F_{s+}}{n_-F_{s-}}\tfrac{v_{B-}}{v_{F+}}+\mathcal{O}\left(\tfrac{v_{B-}}{v_{F+}}\right)^2\right] &&\sim -v_{B-} \quad \approx 0 \end{aligned}$$

  where the last approximations are exact for zero backward velocity. In this case, the cargo force is equal to the maximal stall force, $F_C(n_+,n_-) = \max\{n_+F_{s+}, n_-F_{s-}\}$, and the cargo velocity is exactly zero, $v_C = 0$.

In the case of $n_+ = n_- = 0$, the cargo is unbound and does not move.

Since the cargo motion is stochastic, all these states occur with probabilities $p(n_+,n_-)$ described by the Master equation Eq. (4.13). However, since the cargo spends most of its time

in states with high probability, observable cargo motion is dominated by such high-probability states. We will therefore in the following look at the maxima of the motor number probability distribution $p(n_+, n_-)$ and classify 'motility states' of the cargo according to these maxima.

4.3.2 Definition of some experimentally relevant quantities

Our theoretical modeling is based on the probability $p(n_+, n_-)$ that the cargo is pulled by n_+ active plus and n_- active minus motors. However, this probability is hard to access experimentally since it is difficult to monitor the number of active motors on a cargo. We will therefore also look at some experimentally more easily accessible quantities, which we define in this section.

Velocity distribution. One such quantity is the velocity distribution, which in our model can be calculated as

$$p(v) = \sum_{n_+,n_-} \delta\left[v - v_C(n_+, n_-)\right]\, p(n_+, n_-) \tag{4.19}$$

It has sharp peaks at $v_C(n_+, n_-)$. Also interesting are the average velocity of plus motion

$$\langle v \rangle_+ = \sum_{v>0} v\, p(v) \;\; = \sum_{v_C(n_+,n_-)>0} v_C(n_+, n_-)\, p(n_+, n_-) \tag{4.20}$$

and analogously the average velocity of minus motion.

Run and switch times. Bidirectional cargo motion is often characterized by the switch times and lengths, i.e. the times and distances a cargo moves in one direction before it switches direction. However, one has to be careful in the treatment of slow motion periods of the cargo, which we call 'pauses'. We define the plus *switch time* as the time from the beginning of plus end directed motion until minus end motion begins (including pauses), and the plus *run time* as the time from the beginning of plus end directed motion until minus motion or a pause begins. The pause time is the time from the beginning until the end of a pause. The plus *switch, run and pause lengths* are the distances covered in the respective times. The minus switch, run and pause times and lengths are defined analogously.

The run and switch times are first passage times of the Markov process described by the Master equation Eq. (4.1), compare App. A.3.3. The average plus run time T_+ is equal to the average sojourn time in the plus motion states (+), which is according to Eq. (A.67):

$$T_+ \;=\; \tau_{(+)} \;=\; p\left((+)\right) \Big/ \sum_{(n_+,n_-)\in(+),(n'_+,n'_-)\notin(+)} p(n_+, n_-)\, \omega_{(n_+,n_-)(n'_+,n'_-)} \tag{4.21}$$

where $p((+))$ is the stationary state probability of the state set (+) and $\omega_{(n_+,n_-)(n'_+,n'_-)}$ is the rate from state (n_+, n_-) to state (n'_+, n'_-) (which is non-zero only if these two states are connected by binding or unbinding of a single motor). The average plus run length X_+ is the sum of the average distances covered in each of the states (n_+, n_-) of the set (+), which are each the product of the velocity $v(n_+, n_-)$ and the time $T_+\, p(n_+, n_-)/p((+))$ spent in this state:

$$X_+ = \sum_{(n_+,n_-)\in(+)} v(n_+, n_-)\, T_+\, p(n_+, n_-)/p((+)). \tag{4.22}$$

The average minus run times and lengths and pause times and distances are defined analogously. The plus (and analogously the minus) switch time is difficult to calculate because it is neither a sojourn time nor a return time, but a first passage time from the subset (+) to the subset (−).

The distributions of the run, switch and pause times can be obtained from the cargo Master equation Eq. (4.1) as first passage times into absorbing states [166]: replace the end states of the considered motion by absorbing states (e.g. for the plus run time the pause and minus states,

and for the plus switch time the minus states are turned into absorbing states), and solve the new Master equation. As the Master equation is a linear differential equation, the solutions are sums of exponentials. The run, switch and pause time distributions are then the time derivative of the probability of the absorbing state, and therefore a sum of exponentials.

4.3.3 Motility states of the symmetric tug-of-war

It is instructive to consider the case where plus and minus motors have identical single-motor parameters except for their preferred direction, and where the numbers of plus and minus motors on the cargo are the same. We call this the 'symmetric tug-of-war'. Apart from being theoretically attractive for its simplicity and its intuitive appeal, this symmetric situation can be realized *in vitro* if cargos are transported by a single motor species along antiparallel MT bundles, or for a cargo transported by a single motor species with no preferred direction such as a (non-processive) kinesin 14 mutant [27]. It is also not unrealistic for transport *in vivo* where plus end and minus end transport are often astonishingly similar. This is the case for *Xenopus* melanosomes during dispersion [42], lipid-droplets in the developmental phase I of *Drosophila* embryos [176], and for endosomes in human skin cells [120]. Furthermore, the effects of the tug-of-war are most pronounced in the symmetric case because the opposing motors are 'equally strong'. The symmetric situation means that the indices for plus and minus motors for the single-motor parameters can be dropped: $\pi_0 = \pi_{0+} = \pi_{0-}$, $\epsilon_0 = \epsilon_{0+} = \epsilon_{0-}$, $F_s = F_{s+} = F_{s-}$, $F_d = F_{d+} = F_{d-}$, and $v_0 = v_{0+} = v_{0-}$.

In this symmetric case, inspection of the Master equation Eq. (4.13) for the motor number probability $p(n_+, n_-)$ and its rates Eqs. (4.3) and (4.4) with Eq. (4.6) show that the stationary state probability only depends on the four dimensionless parameters:

$$\begin{aligned} \text{motor number:} \quad & N &=& \; N_+ = N_- \\ \text{desorption constant:} \quad & K &=& \; \epsilon_0/\pi_0 \\ \text{force ratio:} \quad & f &=& \; F_s/F_d \\ \text{velocity ratio:} \quad & \nu &=& \; \beta_B/\beta_F = v_B/v_F \end{aligned} \tag{4.23}$$

4.3.3.1 Definition of motility states

Upon varying the single motor parameters, the model exhibits qualitatively different solutions, which we we will call 'motility states' in the following. These motility states exhibit distinct cargo trajectories and velocity distributions as shown in Fig. 4.6, and can formally be distinguished by the number of maxima of the motor number probability distribution $p(n_+, n_-)$. This number of maxima is found to be either 1, 2, or 3. Three types of maxima with the configurations of Fig. 4.2 occur: a maximum with only plus and no minus motors bound (+), one with only minus and no plus motors bound (−), and one with equal numbers of plus and minus motors bound (0). These maxima are found in the combinations (0), (−+), and (−0+), leading to three qualitatively different motility states:

- **'No motion'** (0).
  For 'weak' motors with a small force ratio $f = F_s/F_d$ the probability distribution $p(n_+, n_-)$ has a single maximum at a state with an equal number of bound plus and minus motors[5] $(n_+, n_-) = (n, n)$, see Fig. 4.6(a1). The corresponding cargo trajectories exhibit little movement; the cargo only fluctuates around its initial position, and the distribution of the cargo velocity is dominated by a strong peak at zero velocity [6], see Fig. 4.6(a2,a3). These

[5] In a small parameter region also neardiagonal maxima at $(n, n+1)$ and $(n+1, n)$ appear, see Fig. 4.7(a). They are counted as a single diagonal maximum with $n_+ = n_-$ which in a continuous state space would be at $(n+1/2, n+1/2)$. [6] The small peak near velocities of $\pm 1\,\mu$m/s correspond to contributions from low-probability fast motion states with only one motor type bound, see Fig. 4.6(a1).

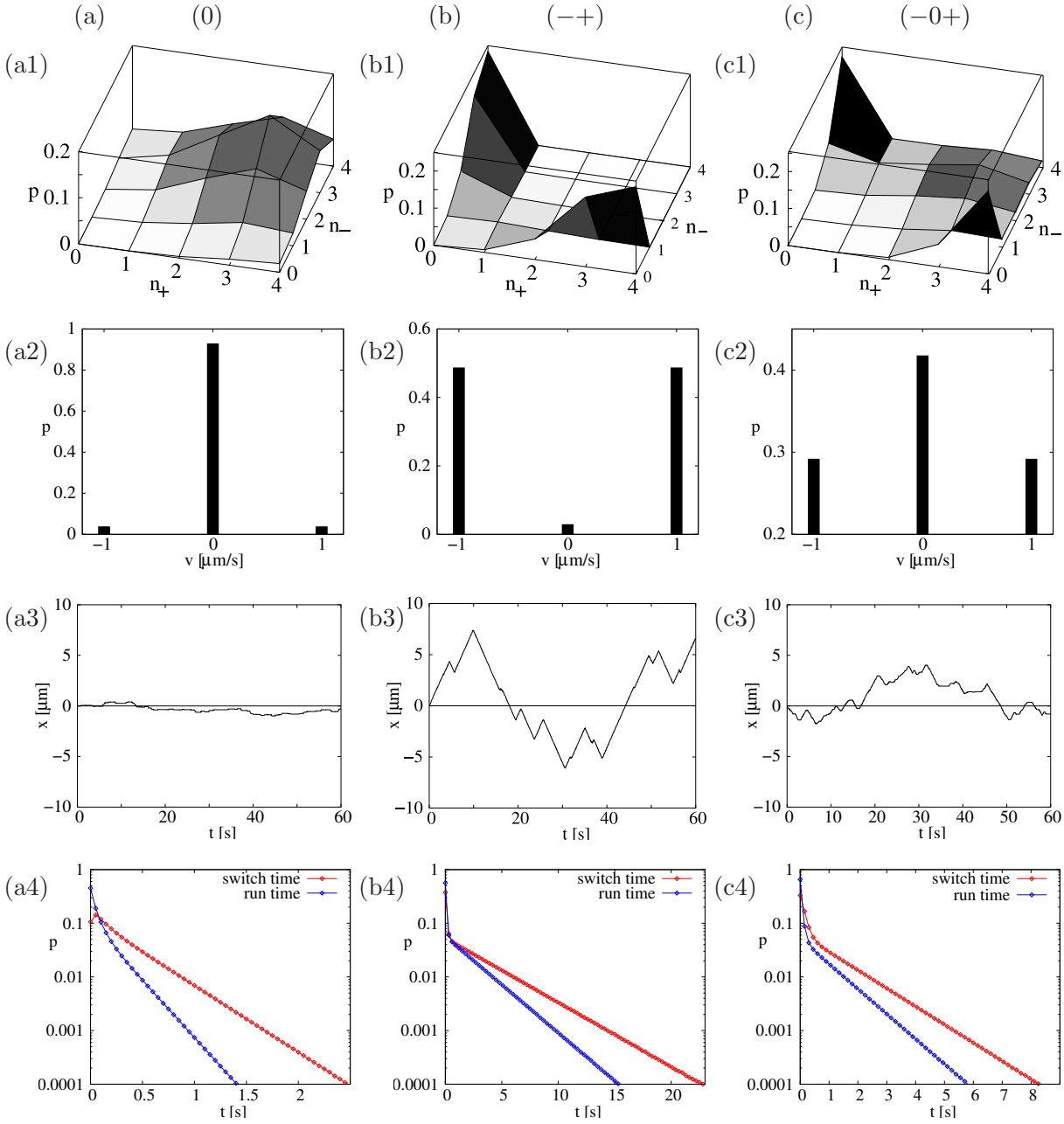

Fig. 4.6: Characteristic properties of the motility states for the symmetric tug-of-war of 4 plus against 4 minus motors. The three columns (a), (b) and (c) correspond to the three motility states (0), (−+) and (−0+). The four rows show (a1)-(c1) the probability distributions $p(n_+, n_-)$ for n_+ active plus and n_- active minus motors, (a2)-(c2) the cargo velocity distributions $p(v)$, (a3)-(c3) the cargo trajectories $x(t)$, and (a4-c4) the (red) switch and (blue) run time distributions $p(t)$. (a) In the no motion state (0), the probability to be in a state with an equal number of bound plus and minus motors is maximal as in (a1), corresponding to a high probability for zero velocity as in (a2), only little cargo motion as in (a3), and short run and switch times as in (a4). (b) In contrast, in the (−+) motility state, the probability to have only one motor type bound is large as in (b1), leading to a high probability for the maximal plus resp. minus cargo velocities $v_C = \pm 1\,\mu$m/s as in (b2), and switching between fast plus and minus motion as in (b3), with run and switch times of several seconds as in (b4). (c) In the (−0+) motility state, there are three maxima with only plus, only minus and an equal number of bound plus and minus motors as in (c1), which leads to three peaks in the velocity distribution as in (c2) and switching between fast plus motion, fast minus motion, and pauses as in (c3), with intermediate values of run and switch times as in (c4). Parameters for both motors are kinesin-like as in Tab. 2.1 except (a) $F_s = 2\,$pN, (b) $F_s = 8\,$pN, (c) $F_s = 4.75\,$pN, $\epsilon_0 = 0.4\,\mathrm{s}^{-1}$.

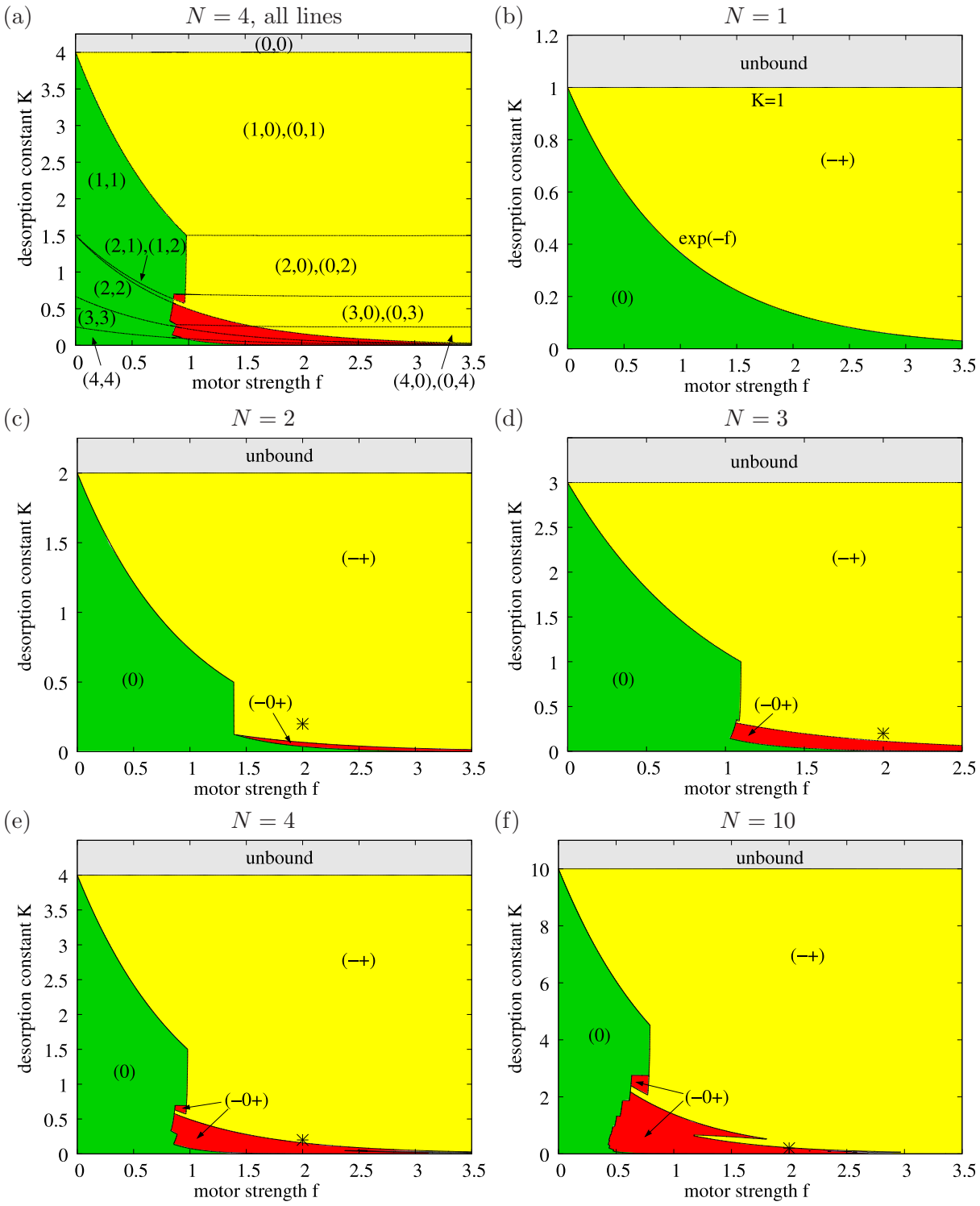

Fig. 4.7: Motility diagrams for the symmetric tug-of-war of $N = N_+ = N_-$ plus and minus motors. Depending on the motor strength $f = F_s/F_d$ and the filament desorption constant $K = \epsilon_0/\pi_0$, the motor number probability $p(n_+, n_-)$ displays maxima which are either at a plus motion state $(n_+, 0)$, a minus motion state $(0, n_-)$ or a zero velocity state (n, n) as shown in (a). This leads to three different motility regimes: no motion (0) (green), switching between fast plus and minus motion $(-+)$ (red), and switching between fast plus and minus motion and pauses $(-0+)$ (yellow). Each motility state is characterized by qualitatively motility behaviours as shown Fig. 4.6. For large desorption constants $K \geq N$ the cargo is unbound (grey). (b)-(f) show the motility diagrams for different motor numbers $N = 1$, 2, 3, 4, and 5. The motor parameters are kinesin-like except for the stall force F_s and the unbinding rate ϵ_0 which are varied. The asterisk at $(f, K) = (2, 0.2)$ corresponds to the complete set of kinesin parameters. The analytic expressions for the transition lines in the $N = 1$ motility diagram in (b) are calculated from the stationary state of the Master equation (4.1), which can be solved analytically in this case.

observations indicate that the motility state (0) represents the blockade situation shown in in Fig. 4.2(0) which one naively expects for a tug-of-war scenario.

- **'Fast plus and minus motion'** $(-+)$.
  For 'strong' motors with large f, cargo movement is completely different. The cargo switches between fast plus-directed and minus-directed motion as shown in Fig. 4.6(b3), and the motor number probability $p(n_+, n_-)$ displays two maxima, one with only plus motors bound to the filament ($n_+ > 0$, $n_- = 0$) and one with only minus motors bound ($n_+ = 0$, $n_- > 0$), see Fig. 4.6(b1). This behavior, which is usually associated with coordinated transport rather than with a tug-of-war scenario, can be understood as follows: When more plus than minus motors are bound to the filament ($n_+ > n_-$), every plus motor experiences the load force F_C/n_+, while every minus motor experiences the larger load force F_C/n_-, where F_C denotes the total force on the cargo. Since the unbinding rate increases strongly with increasing force (Eq. (2.1)), minus motors are more likely to unbind from the filament than plus motors, so that the predominance of the plus motors is further enhanced. After the unbinding of a minus motor the remaining minus motors experience an even larger load force and are even more likely to unbind. As a consequence, the cargo experiences a cascade of minus motor unbinding events which only stops when no minus motor remains bound.

  A prerequisite for this unbinding cascade is that the motors can exert a sufficiently large force to pull off opposing motors from the MT, i.e. the stall force F_s has to be comparable or larger than the detachment force F_d. For small force ratios $f = F_s/F_d$, the pulling force has only a small effect on motor unbinding, so that no instability occurs and the cargo exhibits the blocked motility state (0). For large motor force ratio, the transient predominance of one motor type is thus amplified by a dynamic instability, and in consequence the cargo spends most of the time in configurations like $(+)$ and $(-)$ in Fig. 4.2 with only one motor type bound. During a plus or a minus run, the effective velocity is however slightly reduced compared to the single motor velocity by the sporadic binding and subsequent fast unbinding of an opposing motor. The velocity distribution in Fig. 4.6(b2) has two peaks close to the single motor velocities[7] $\pm 1\,\mu$m/s. The direction of motion of the cargo is reversed when, due to a fluctuation, the defeated motors become predominant.

- **'Fast plus and minus motion with interspersed pauses'** $(-0+)$.
  Finally, in some intermediate parameter ranges, the probability distribution $p(n_+, n_-)$ displays three maxima as shown in Fig. 4.6(c1), a symmetric one corresponding to no motion as for motility state (0) and two nonsymmetric ones corresponding to steady plus and minus motion as for state $(-+)$. The velocity distribution in Fig. 4.6(c2) has three corresponding peaks, and cargo trajectories therefore exhibit bidirectional motion interspersed with pauses, see Fig. 4.6(c3).

4.3.3.2 Run, switch and pause times

The three different motility states (0), $(-+)$ and $(-0+)$ differ in the distributions of run, switch and pause times, defined in Sec. 4.3.2, see Fig. 4.6(a4-c4) and Fig. 4.8(a). The run times are shorter than the switch times because the latter may involve pauses. Experimental run or switch times are usually of the order of seconds, while run or switch lengths are of the order of microns.

In the no-motion motility state (0), the run and switch times are very small, see Fig. 4.6(a4), because the cargo only fluctuates around a state (n, n) with zero velocity. In the $(-+)$ motility state of switching between fast plus and minus motion, run and switch time are larger, with a time scale of several seconds, see Fig. 4.6(b4). In the $(-0+)$ motility state, the switch times are still on a second time scale but shorter than in the $(-+)$ case, see Fig. 4.6(c4). Pause times are rather short and non-negligible only in the motility states (0) and $(-0+)$, which feature a

[7] The small peak near zero velocity corresponds to the low-probability no-motion states for which both n_+ and n_- are non-zero.

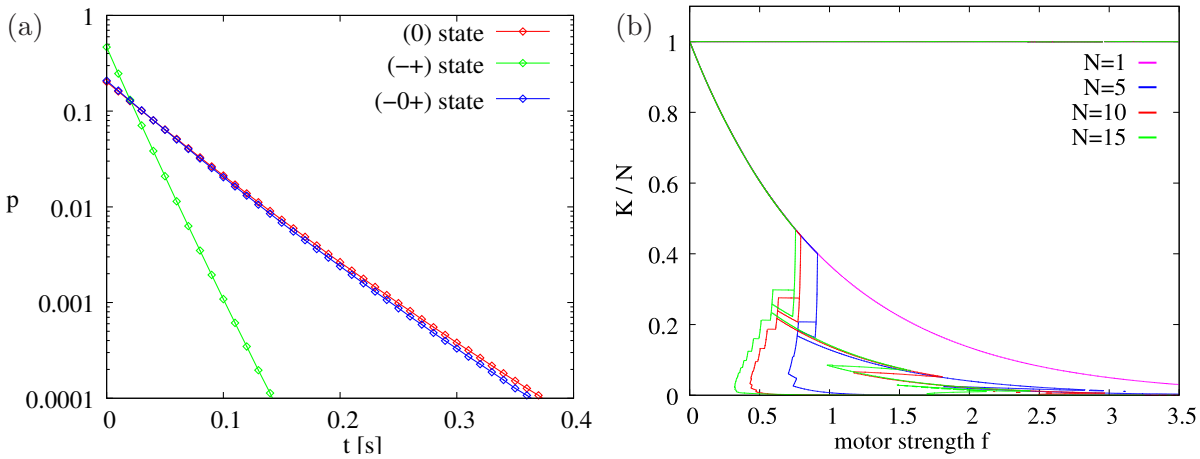

Fig. 4.8: Symmetric tug-of-war: (a) Logarithmic plot of the pause time distributions $p(t)$ for the symmetric tug-of-war of 4 against 4 motors for the three motility states. Pause times are extremely short in the $(-+)$ motility state (green data) and longer in the (0) (red) and $(-0+)$ (blue) motility states. Parameters are as in Fig. 4.6. (b) Motility diagram for the symmetric tug-of-war of $N = N_+ = N_-$ symmetric plus and minus motors for $N = 1$, 5, 10 and 15. Scaling of the desorption constant K with the motor number N almost overlays the different diagrams of Fig. 4.7.

probability maximum at a no-motion state, see Fig. 4.8(a).

Run, switch and pause time distributions are sums of exponentials, as discussed at the end of Sec. 4.3.2. However, run and switch times are well fitted with a double exponential function[8], see Fig. 4.6(a4-c4), while pause times are usually well fitted by a single exponential function, see Fig. 4.8(a). These functional forms of run, switch and pause time distributions have also been observed in experiments [42, 44, 45], see also Sec. 5.1 and 5.2.

Although a cargo in the $(-+)$ motility state displays net motion on the time scale of seconds of the switch times, it does not achieve net motion on large time scales because of symmetry: motion in plus and minus direction are equally probable. This is similar to Brownian motion, but here the diffusion is scale-dependent: On short time scales, the mean square displacement grows quadratically with time, which corresponds to directed motion. On large time scales, the mean square displacement grows linearly in time as for ordinary diffusion. Such a transition from ballistic motion at short and diffusive motion at large time scales has indeed been found for the symmetric bidirectional motion of endosomes [120]. The large scale diffusion constant is of the order of D_{eff} ∼(switch length)^2/(switch time) ∼ $(2.5\,\mu\text{m})^2/(2.5\,\mu\text{m}) \approx 2.5\,\mu\text{m}^2/\text{s}$ for the $(-+)$-state shown in Fig. 4.8(a). This is larger than the diffusion constant $D = 0.5\,\mu\text{m}^2/\text{s}$ of a $0.5\,\mu$m-cargo in water and much larger than the diffusion constant $D = 0.005\,\mu\text{m}^2/\text{s}$ of the same cargo in the viscous cytoplasm, compare Sec. 1.1. The fast diffusion is a benefit of bidirectional motion for cargos in search of their direction as discussed in Sec. 1.4.

4.3.3.3 Motility diagrams

In cells, cargo motion must be regulated in order to adjust the cellular traffic to internal or external stimuli. This requires change of the motor parameters. To show the effect of parameter changes explicitly, we calculate the 'motility diagrams' shown in Fig. 4.7.[9]

[8] An exception is the switch time distribution in the (0) regime, which displays a maximum at a small but nonzero time. This is due to pauses: a switch from e.g. plus to minus motion cannot occur directly, i.e. with a single transition from a plus to a minus motion state, but is always delayed because a pausing state (n, n) has to be passed. [9] The detailed calculation procedure is as follows: The single-motor parameters are taken to be equal to the kinesin 1 values as given in Tab. 2.1 except for the plus and minus motor unbinding rates $\epsilon_0 = \epsilon_{0+} = \epsilon_{0-}$ and the stall forces $F_s = F_{s+} = F_{s-}$. All other parameters, i.e. F_d, π, v_F and β_B, are kept constant. The parameter space (ϵ_0, F_s) is then explored systematically, and for each point the maxima of the motor number probability $p(n_+, n_-)$ is calculated as described in Sec. 4.2.6. When the maxima between two scanned points change, we zoom in between these points in order to determine the transition point more accurately. The lines shown in Fig. 4.7 consist of these points.

Fig. 4.7(a) shows the 'motility diagram' for the symmetric tug-of-war of $N = N_+ = N_- = 4$ plus and minus motors. Depending on the force ratio f and the desorption constant K, the cargo is in one of the three motility states (0), $(-+)$ or $(-0+)$ discussed in the last section. The lines in the motility diagram separate regions in which the maxima of the motor number probability distribution $p(n_+, n_-)$ are located at different motor number states (n_+, n_-). The colors separate regions with different motility states. In motility state (0) (green) the motor number distribution has a single maximum at a no-motion state with an equal number of plus and minus motors bound at (n, n) with $1 \leq n \leq 4$. The two neardiagonal maxima at (1,2) and (2,1) are also counted as a single diagonal maximum, which in a continuous state space would be at (n, n) with $1 < n < 2$. If the maximum is at (n, n)=(0,0) the cargo is considered as 'unbound' (gray). In the $(-+)$ regime (yellow), the probability distribution exhibits two maxima with only plus or only minus motors bound at $(n, 0)$ and $(0, n)$ with $1 \leq n \leq 4$. The cargo is in the $(-0+)$ regime (red) if the probability distribution exhibits three maxima.

For large desorption constants K, the motors have a low affinity to the MT; therefore the number of bound motors in Fig. 4.7(a) is low for low K. For very high desorption constants K, the maximum is at $n = 0$, and the cargo is 'unbound'. For small force ratios f, the probability distribution $p(n_+, n_-)$, the cargo is in the no-motion motility state (0). For large force ratios f, the motors can generate forces large enough to rip off opposing motors since the stall force is large compared to the detachment force. This leads to the unbinding cascade described in the last section, and the motor number probability has two maxima, one at a state with only active plus and one at a state with with only active minus motors. In the latter situation, the cargo is in the $(-+)$ motility state. For intermediate values of f, both types of maxima coexist, and the cargo is in the $(-0+)$ motility state (red). The effect of the motor parameters can be summarized in the following way:

- high processivity (small K) $\rightarrow$ no-motion maximum (0), high n_+ and n_-
- large forces (high f) $\rightarrow$ fast motion maxima $(+)$, $(-)$

Fig. 4.7(b-f) show the motility diagrams, only displaying the motility states and not the positions of the maxima (n_+, n_-), for varying motor numbers N. If the cargo is carried by only 1 plus and 1 minus motor, the motor number probability $p(n_+, n_-)$ has its maxima either at $(1, 1)$ (motility state (0)), at $(0, 0)$ (unbound) or at $(1, 0)$, $(0, 1)$ (motility state $(-+)$), see Fig. 4.7(b). The region with the motility state $(-0+)$ only appears when the number N of motors on the cargo is larger or equal to 2, and becomes larger for larger motor numbers, see Fig. 4.7(c)-(f).

The locations of the transition lines are determined by the balance of binding and unbinding of single motors under the load force generated by the opposing motors. As all unbinding rates are proportional to ϵ_0, and all binding rates are proportional to π_0, this means that the transition lines should scale with $K = \epsilon_0/\pi_0$, as is indeed the case, see Fig. 4.8(b). As a specific example, cargo unbinding occurs when the rate of unbinding of the last bound motor, ϵ_0, becomes larger than the rate for binding of all motors, $N\pi_0$, i.e. when $K = \epsilon_0/\pi_0 > N$. For the other transition lines, this reasoning is not exact but leads to a good approximation as we will see in Sec. 4.4.3.

In the symmetric case, the cargo motility can also be classified by using the maxima of the probability distribution of the difference of active plus and minus motors, see App. A.4.1.

4.3.4 Motility states of the asymmetric tug-of-war: kinesin versus dynein

So far we have considered the symmetric tug-of-war of plus and minus motors with identical properties except their forward direction. Bidirectional cargo motion *in vivo* is typically dependent on two different motor species for plus and minus motion. In this section we therefore discuss the asymmetric tug-of-war. As the most important *in vivo* case is transport by kinesin 1 and cytoplasmic dynein, we do this for plus and minus motors with the kinesin 1 and dynein parameters as in Tab. 2.1. For the unknown dynein parameters, we use the kinesin 1 values.

Fig. 4.9: The figure on p. 48 shows the motility states for the asymmetric tug-of-war of 5 plus against 5 minus motors: Each row shows a velocity distribution $p(v)$ (left), a cargo trajectory $x(t)$ (middle) and the plus and minus switch time distributions $p(t)$ (right) for one of the seven motility states (+), (−), (0), (−+), (0+), (−0), and (−0+). In the plus motion state (+), the probability for motion with maximal positive velocity $v_C = 1\,\mu$m/s is high; accordingly the cargo moves almost exclusively to the plus end, and the plus switching time is extremely large. The same is true for minus motion in the minus motion state (−). In the no-motion state (0), in contrast, the cargo has a high probability for low velocities $v_C \approx 0$, almost does not move and shows rapid switching. Two or all three of these three types of maxima can appear together, leading to stochastic switching between these maxima. The cargo then displays successive plus and minus motion ((−+) state), plus motion and pauses ((0+) state), minus motion and pauses ((−0) state), or plus and minus motion and pauses ((−0+) state). Note the different time axes in the switch time graphs (right column). Parameters are for kinesin 1 and 'strong' dynein as in Tab. 2.1, except $(F_{s-}/\mathrm{pN}, \epsilon_{0-}/\mathrm{s}^{-1}) = (1.5,1.25)$ for (+), (4.5,0.003) for (−), (0.03,0.003) for (0), (9,0.625) for (−+), (9,0.25) for (0+), (2.7,0.003) for (−0), and (3.75,0.375) for (−0+).

As conflicting values have been reported for the dynein stall force, we will discus both 'strong' dyneins with the stall force $F_{s-} = 7\,\mathrm{pN}$ and 'weak' dyneins with $F_{s-} = 1.1\,\mathrm{pN}$.

4.3.4.1 Motility states

In the asymmetric tug-of-war, the probability distribution $p(n_+, n_-)$ still exhibits the three types of maxima (+), (−), and (0) defined in Sec. 4.3.1, and the cargo switches stochastically between these maxima. However, since cargo motion is no longer symmetric with respect to plus and minus motion, seven motility states are now possible, corresponding to the different combinations (+), (−), (0), (−+), (0+), (−0) and (−0+) of these three types of maxima.

The motility states (0), (−+) and (−0+) exhibit similar properties as in the symmetric case, compare Figs. 4.6 and 4.9. However, while there is no net transport in the symmetric case, the plus-minus asymmetry can lead to net transport of the cargo in one direction. For example, in the (−0+) motility state, the minus motion maximum (−) of the motor number probability can be larger than the minus motion maximum (+), so that the velocity distribution shows a higher peak for minus than for plus motion, which leads to longer minus runs compared to plus runs and to net minus motion of the cargo, see last row of Fig. 4.9.

In the 'new' (+) motility state, the motor number probability distribution $p(n_+, n_-)$ exhibits a single maximum at a (+) state, which leads to a velocity distribution with a large peak near the single plus motor velocity $1\,\mu$m/s and fast plus motion of the cargo, with extremely long plus and short minus switch times, see the first row of Fig. 4.9. In the (0+) motility state, the motor number probability has one maximum at the plus motion state (+) with only plus motors active and one maximum at the no-motion state (0) with both types of motors active. The corresponding velocity distribution has two corresponding peaks, one close to zero velocity and one at large plus motor velocity, and the cargo switches between fast plus motion and pauses, see fifth row of Fig. 4.9. The other new motility states (−) and (−0) are analogous with plus and minus motion interchanged.

The run and switch times of plus motion tend to be larger than those of minus motion because the kinesin dynamics is slower than the dynein dynamics: the binding and unbinding rates of kinesin are twice as large as those for dynein, see Tab. 2.1. The run and switch time distributions are roughly double exponential in all cases, in agreement with experimental observations [44, 42].

4.3.4.2 Motility diagrams

Cellular regulation. In cellular cargo transport, the properties of kinesins and dynein must be regulated in order to adjust the cellular traffic to internal or external stimuli. Dynein presents itself as the most prominent target for regulation, as it has been shown that it is very sensitive to regulatory and accessory proteins [98]. A prominent example is the dynein cofactor dynactin,

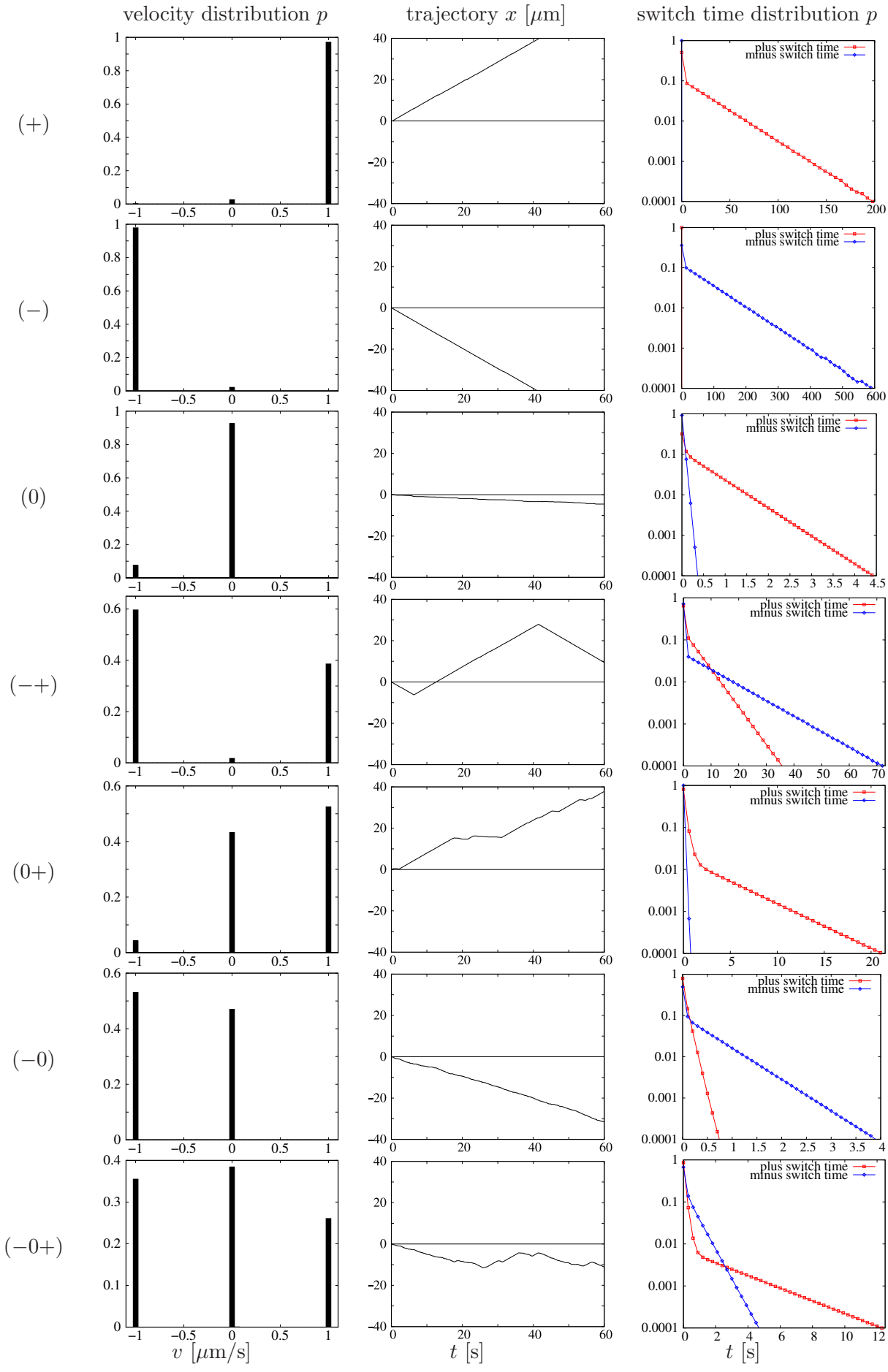
velocity distribution p
trajectory x [μm]
switch time distribution p
(+)
(−)
(0)
(−+)
(0+)
(−0)
(−0+)
plus switch time
minus switch time
v [μm/s]
t [s]
t [s]

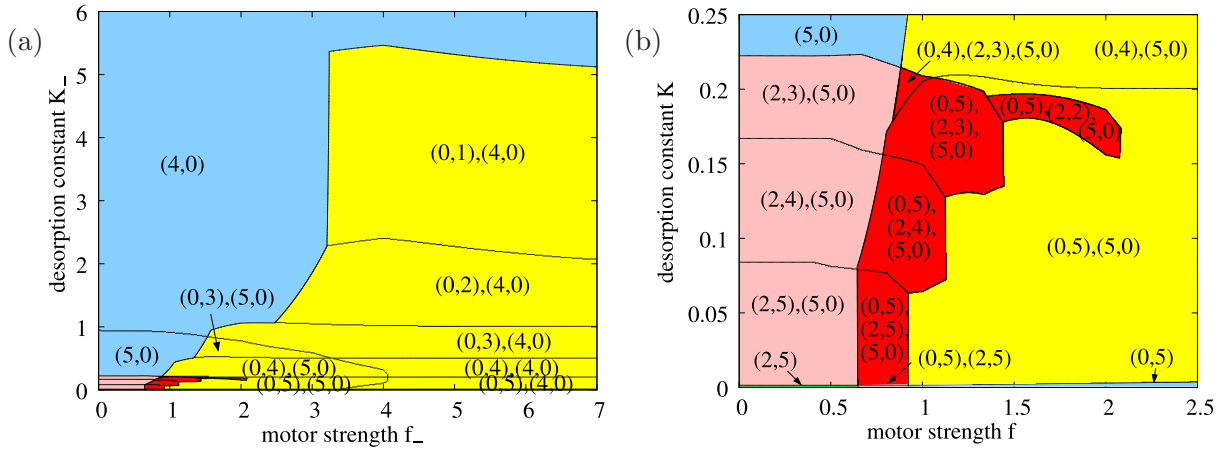

Fig. 4.10: Motility diagrams for the asymmetric tug-of-war of $N_+ = 5$ kinesin-like plus motors against $N_- = 5$ dynein-like minus motors. Depending on the minus motor strength $f_- = F_{s-}/F_{d-}$ and desorption constant $K_- = \epsilon_{0-}/\pi_{0-}$, the cargo transport is in one of seven motility states which are characterized by the maxima of the motor number probability $p(n_+, n_-)$. The lines separate regions in which these maxima are located at different motor number states (n_+, n_-), while the colours separate regions with different motility states. (b) is a magnified detail of (a). The maxima of $p(n_+, n_-)$ are either at a plus motion state $(n_+, 0)$ (+), a minus motion state $(0, n_-)$ (−) or a slow motion state (n_+, n_-) (0) with $n_+ > 0$, $n_- > 0$. They appear in seven combinations, leading to seven motility regimes: no motion (0) (green), fast plus motion (+) (blue), fast minus motion (−) (blue), coexistence between two of these states as indicated by (0+) (pink), (−0) (pink), and (−+) (yellow), and three-state coexistence (−0+). The same motility diagram without the locations of the maxima states in shown in Fig. 4.11 (a5) and (b5). Parameters are for kinesins and dyneins as in Tab. 2.1 except for the minus motor stall force F_{s-} and detachment rate ϵ_{0-}, which are varied.

which dramatically increases the run time of dynein, i.e. decreases its unbinding rate ϵ_{0-} [66]. The sensitivity of dynein may also be the reason for the conflicting stall force results of [100, 156] shown in Tab. 2.1.

Regulating dynein. We therefore vary both the unknown stall force F_{s-} and the regulated unbinding rate ϵ_{0-}. We fix the other parameters of the minus motors and all plus motor parameters according to the dynein and kinesin values in Tab. 2.1. Fig. 4.10 shows motility diagrams for the asymmetric tug-of-war of $N_+ = 5$ kinesins against $N_- = 5$ dynein-like motors.[10] It exhibits seven motility states, which are indicated by colours. The 'new' motility states (+), (−), (0+) and (−0) are asymmetric with respect to plus and minus motors and, thus, were not present for the symmetric tug-of-war. As kinesin is a rather strong and processive motor, and as its rates are not varied in the motility diagrams of Fig. 4.10, motility states without a plus motion maximum are rare and restricted to very processive minus motors with small K_-. The irregular shape of the bifurcation lines between the motility states is a discretization effect and corresponds to transitions between different locations (n_+, n_-) of the maxima of the motor number probability distribution $p(n_+, n_-)$, as indicated by the lines in Fig. 4.10. The exact location of the lines is hard to guess, but can be understood and calculated to a good approximation in the sharp maximum approximation, which we will introduce in Sec. 4.4.3.

These lines show that minus motors with high affinity to the MT, i.e. with low desorption constant K_-, favour a high number of active minus motors and therefore minus motion of the cargo (−), or at least blocking of motion (0). A high force ratio f_- means strong minus motors, which favours minus motion (−). Furthermore, it enhances the unbinding cascade that leads to cooperativity and to fast motion, i.e. to the motility states (−+) and (−0+). Altogether, this leads to a 'plus-minus symmetry' around a $K_- \sim f_-$ axis as indicated by the colouring, with the

[10] The asymmetric motility diagrams in Fig. 4.10 are generated in a similar way as Fig. 4.7. The single-motor parameters correspond to the kinesin and dynein values of Tab. 2.1, except for the minus motor unbinding rate ϵ_{0-} and stall force F_{d-}. The parameter space (ϵ_{0-}, F_{s-}) is then explored systematically in the same way as for the symmetric case.

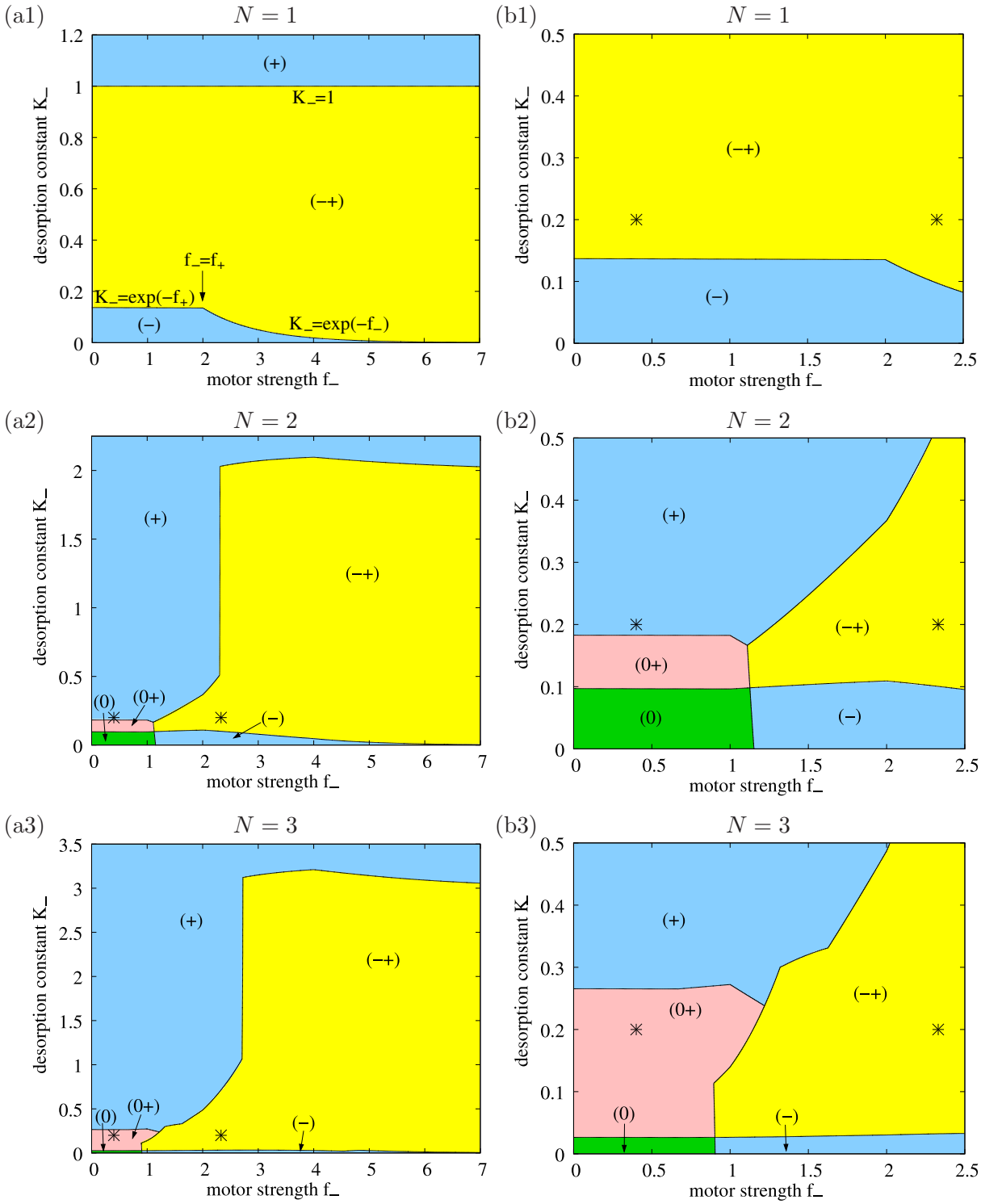

Fig. 4.11: Motility diagrams for the tug-of-war of $N = N_+ = N_-$ kinesin-like plus against dynein-like minus motors: Parameters are as in Tab. 2.1 except for the minus motor stall force F_{s-} and detachment rate ϵ_{0-}, which are varied. The right column diagrams labeled (bN) are magnified details of their left column counterparts labeled (aN), for N=1, 2, 3, 4, 5 and 10. The two asterisks at $f_- = 1.1\,\mathrm{pN}/3\,\mathrm{pN}$ and $f_- = 7\,\mathrm{pN}/3\,\mathrm{pN}$ correspond to weak and strong dyneins, respectively. The analytic expressions for the transition lines in the $N = 1$ motility diagram in (a1) are calculated from the stationary state of the Master equation (4.1), which can be solved analytically in this case.

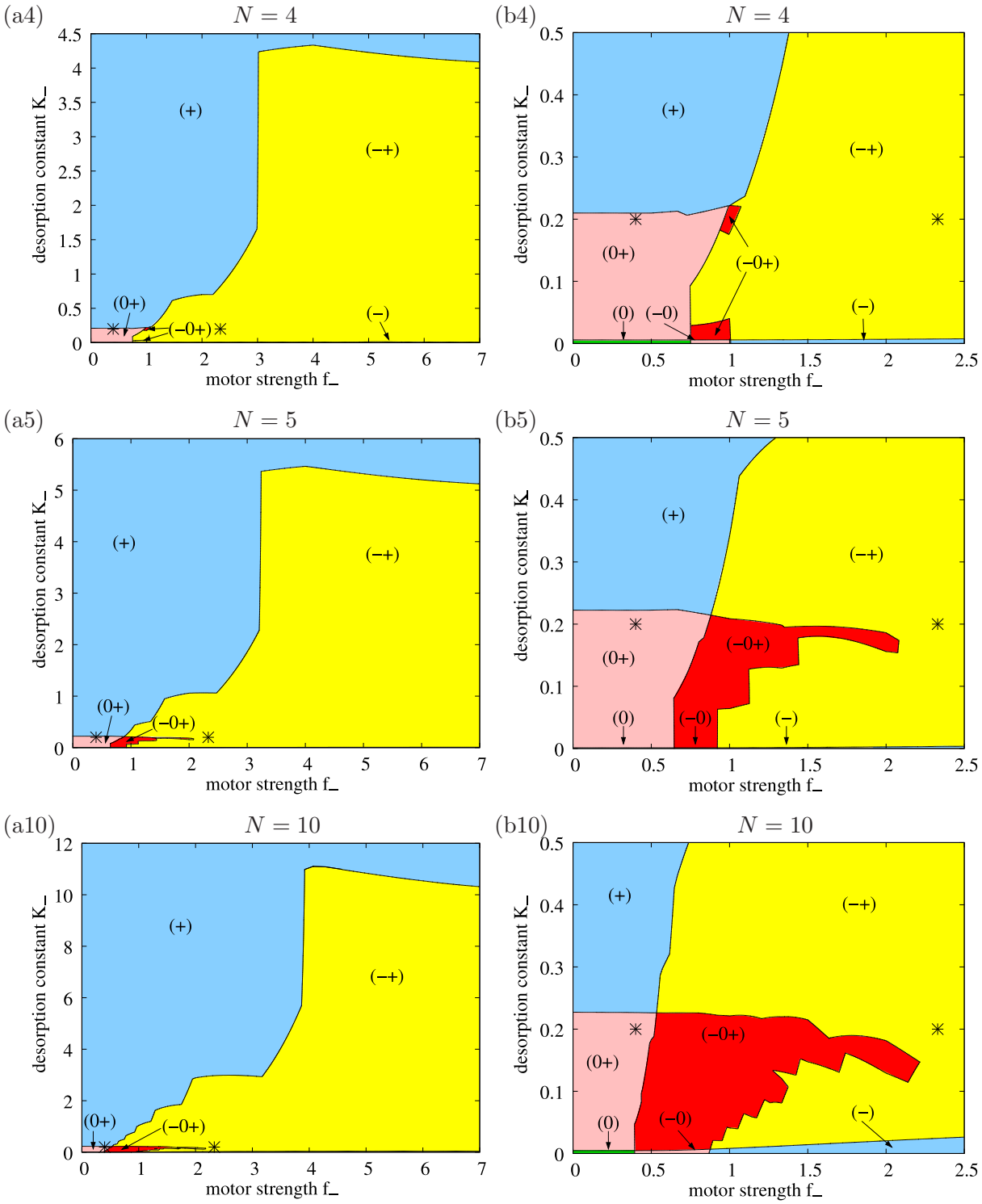

Fig. 4.11: The colours indicate the seven possible cargo motility states of no-motion (0) (green), fast plus motion (+) resp. minus motion (−) (blue), switching between fast plus and fast minus motion (−+) (yellow), switching between pauses and fast plus motion (−+) resp. minus motion (−0) (pink), and switching between fast plus motion, fast minus motion and pauses (−0+) (red).

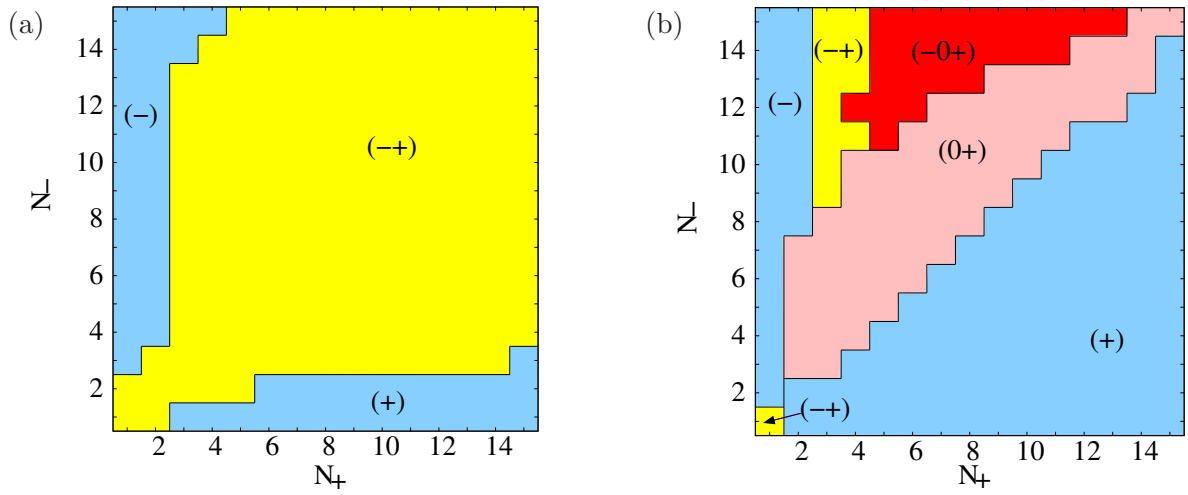

Fig. 4.12: Motility states for the tug-of-war of N_+ kinesins against N_- (a) strong dyneins or (b) weak dyneins with the parameters of Tab. 2.1.

motility states (0), (−0+) and (−+) which contain both plus and minus states in a symmetric way on this axis and the 'asymmetric' motility states (+) resp. (−), and (0+) resp. (−0) lying to its left resp. right.

Fig. 4.11 shows similar motility diagrams for different motor numbers $N = N_+ = N_-$. For $N = 1$, the tug-of-war of one against one motor, only the (−) and (−+) motility states exist. With increasing motor number, more and more motility states appear, and the transition lines shift. The (−0+) motility state only appears for $N \geq 4$, and its region becomes larger with increasing N.

Biological parameter ranges. In cells, the number of motors ranges from $N = 1$ to 5 motors of each motor type, see Sec. 4.1.1. The asterisks in the motility diagrams of Fig. 4.11 indicate the most likely parameter sets of dynein with the parameters given in Tab. 2.1. For 'strong' dyneins with $F_{s-} = 7\,\mathrm{pN}$, plus and minus motors have a high and almost equal force ratio. Therefore the cargo switches between fast plus and minus motion (−+). On the contrary, for 'weak' dyneins with a stall force of $F_{s-} = 1.1\,\mathrm{pN}$, the dynein motors lose against the stronger kinesins and can at most block plus motion. In consequence the cargo exhibits fast plus motion (+), or fast plus motion interspersed with pauses (0+). In this case, more dyneins than kinesins are needed to achieve bidirectional motion.

Regulating the motor numbers. This can be seen in the motility diagram of Fig. 4.12(b), which shows the motility states of a tug-of-war of N_+ kinesin 1 and N_- weak dynein motors. The plus motion state (+) dominates. One needs $N_- \gtrsim N_+$ weak dyneins even to block motion and reach the (0+) motility state. And it is not until very large numbers of dynein $N_- \gg N_+$ that fast minus motion appears with the (−+) and (−0+) motility states.

This picture changes when the kinesins compete against similarly strong dyneins, see Fig. 4.12(a). For the tug-of-war of N_+ kinesins against N_- strong dyneins, the cargo is mostly in the (−+) motility state, except when one motor number is much larger than the other. In this case the outnumbering motor species determines the direction. In the biologically relevant range of 1 to 5 motors of each species, an increase or decrease of the motor number by only one motor can change the cargo motion dramatically from fast plus motion (+) to fast bidirectional motion (−+) to fast minus motion (−).

The cell can thus regulate motor traffic in various ways. Besides changing the motor properties of e.g. dynein, it can also change the number of motors on the cargo. Regulation is most effective when both motors are similarly strong, as then a small change in the motor properties or the motor numbers can lead to a drastic change of cargo motion due to a change of the motility state, see Figs. 4.10 and 4.12. We will investigate the effect of parameter and motor number changes on the dynamic observables such as run times and velocities in Sec. 4.5.

4.3.5 Summary and discussion

We have discussed the motility patterns of our tug-of-war model for bidirectional cargo transport by two teams of opposing motors. The motors act independently according to the single motor properties described in Chap. 2 and feel each other only via the mechanical interaction with their common cargo. The used single motor properties incorporate the experimentally determined load-dependent transport properties of the motors in a simple and straightforward way. Our results do not depend crucially on details of this modeling such as the functional form chosen for the single motor force-velocity relation, see App. A.4.2.

In our tug-of-war model, the cargo is transported by a fluctuating number of motors. Three types of cargo states exist: slow motion (0), fast plus motion (+), and fast minus motion (−), which represent corresponding maxima in the probability distribution of active plus and minus motors. For the symmetric tug-of-war of identical plus and minus motors except for their preferred direction, three combinations of these maxima lead to three cargo motility states: no-motion (0), switching between fast plus and minus motion (−+), and switching between fast plus and minus motion interspersed with pauses (−0+). These motility states exhibit qualitatively distinct velocity distributions and trajectories, see Fig. 4.6. We have obtained a complete classification of the possible motility states for the symmetric tug-of-war, see Fig. 4.7.

Even for this symmetric tug-of-war of equally strong plus and minus motors, the tug-of-war does not necessarily lead to the expected blockade situation with almost no cargo motion as in Fig. 4.2(0), but can also lead to switching between fast plus and fast minus motion as in Fig. 4.2(+) and (−). This surprising behaviour is caused by a dynamic instability arising from the strongly nonlinear force-dependence of the single-motor unbinding rate. This instability leads to an unbinding cascade and thereby to a high probability of having only one motor type active at a given time. The emergence of cooperative behaviour arising from the nonlinear force-dependence of the motor unbinding rate has also been proposed as an explanation for collective effects in muscles [25, 26] and in mitotic spindle oscillations [39, 123]. In the latter case, the bending rigidity of the clamped MTs provides an elastic element which leads to oscillations instead of bidirectional transport [60].

Switching between fast plus and minus motors has also been found for a motility assay with only one type of non-processive motors, which walk to the plus and minus end with equal probability [27]. This is formally equivalent to two equal teams of non-processive unidirectional motors. This situation has been investigated theoretically in the framework of two-state ratchet models, and also leads to bidirectional motion with bimodal velocity distributions [5]. However, due to the non-processivity of the motors, a minimal motor number of five motors is required to produce bidirectional motion in this model, and a regime with plus and minus motion and pauses is not observed. This is consistent with our results for unprocessive motors, i.e. for high desorption constants K, compare the motility diagrams in Fig. 4.7.

For the asymmetric tug-of-war, which comprises the most important *in vivo* tug-of-war of kinesin 1 and cytoplasmic dynein, seven motility states are possible, corresponding to the different combinations (+), (−), (0), (−+), (0+), (−0) and (−0+) of the three types of maxima, see Fig. 4.9. The corresponding motility diagrams of Figs. 4.10–4.12 show a complex dependence of these motility states on the single motor parameters. For biologically relevant situations, such as the tug-of-war of a few kinesins against a few dyneins, the cargo is mostly in the motility state (−+) of fast bidirectional motion. The parameters are however close to transition lines to other motility states, so that a small variation of the parameters can lead to a drastic change in motility behaviour. This can be used for cellular regulation, which is mimicked by this parameter change.

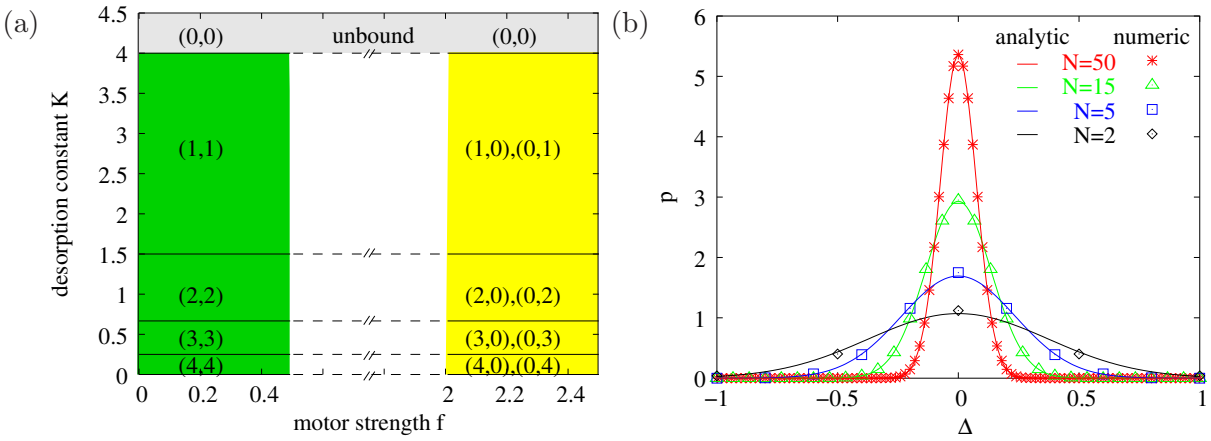

Fig. 4.13: (a) Motility diagram of the symmetric tug-of-war of $N_+ = N_- = 4$ plus and minus motors for small and for large motor forces f: the maxima at (n, n) (for small f) resp. $(n, 0)$ and $(0, n)$ (for large f) change location at the values of K given by Eq. (4.27) resp. Eq. (4.41). These lines reproduce the maxima transition lines for the full motility diagram Fig. A.6(a) for small resp. large motor forces f. (b) For the symmetric tug-of-war of N against N motors with zero strength $f = 0$, the probability $p(\Delta)$ for the difference $\Delta = n_+ - n_-$ of active plus and minus motors (data points) peaks at $\Delta = 0$, corresponding to the (0) motility state, see (a). Upon increasing the motor number N, this peak sharpens and the Gaussian approximation Eq. (4.28) (solid lines) becomes accurate.

4.4 Analytic approximations for the tug-of-war

In this section we use various analytical approximations in order to characterize the motility patterns of the tug-of-war. In Sec. 4.4.1 we consider the limiting cases of small and large motor force ratios $f = F_s/F_d$. In Sec. 4.4.2 we investigate the mean field approximation, and in Sec. 4.4.3 a 'sharp maximum approximation' which assumes that the maxima of the motor number probability distribution $p(n_+, n_-)$ are very sharp.

4.4.1 Approximation for small and large motor forces

In this subsection we analytically solve the tug-of-war model in the limiting cases of small and large motor force ratios $f = F_s/F_d$.

4.4.1.1 The equilibrium case of small motor force

As discussed in Sec. 4.2.3 the system is not in equilibrium due to the action of the motors. However, when the motors are not able to produce force, i.e. $F_{s+} = F_{s-} = 0$, e.g. because they are lacking ATP, but are able to bind and unbind to resp. from the filament, the system becomes an equilibrium system: Now the cargo forces Eq. (4.6) and therefore the thermodynamic force Eq. (4.12) of each cycle vanish, $F_C = X = 0$. This means that the rates fulfill detailed balance and allows for an analytic solution.

Solution of the Master equation. In the case of zero stall forces, the plus motor (un)binding rates Eqs. (4.3) and (4.4) of the Master equation for $F_C = 0$ become

$$\pi_+(n_+, n_-) = \pi_+(N_+ - n_+) := \pi_+(n_+) \qquad \text{and} \qquad \epsilon_+(n_+, n_-) = n_+\epsilon_+ =: \epsilon_+(n_+)$$

(and analogously for the minus motors) and thus depend on one of the motor numbers n_+ or n_- only. Therefore, the two motor species become independent, i.e. they do not feel the presence of the other motor species. The probability distribution decouples, $p(n_+, n_-, t) = p_+(n_+, t)\, p_-(n_-, t)$, where each probability distribution fulfills the Master equation:

$$\frac{\partial}{\partial t} p_\pm(n_\pm) = \epsilon_\pm(n_\pm + 1)\, p_\pm(n_\pm + 1) + \pi_\pm(n_\pm - 1)\, p_+(n_\pm - 1) - [\epsilon_\pm(n_\pm) + \pi_\pm(n_\pm)]\; p_\pm(n_\pm)$$

This is a one-dimensional birth-and-death processes and can be solved for the stationary state (which is now an equilibrium state) by establishing a recursion relation [166]. As the rates fulfill detailed balance, one can also construct an energy landscape and calculate the probabilities as Boltzmann probabilities.[11] The result is a binomial distribution, leading to a double binomial distribution for $p(n_+, n_-)$:

$$p(n_+, n_-) = \binom{N_+}{n_+} p_+^{n_+} (1-p_+)^{N_+-n_+} \binom{N_-}{n_-} p_-^{n_+} (1-p_-)^{N_--n_-} \tag{4.24}$$

where

$$p_+ = \frac{1}{1+K_+} = \frac{\pi_+}{\epsilon_+ + \pi_+} \quad \text{and} \quad p_- = \frac{1}{1+K_-} = \frac{\pi_-}{\epsilon_- + \pi_-} \tag{4.25}$$

are the probabilities for a single plus and minus motor, respectively, to be bound to the filament. As the binomial distribution has exactly one maximum, so has the motor number probability $p(n_+, n_-)$, and the maximum is at (n_+, n_-) if

$$n_+ \in \left[\frac{N_+ + 1}{1+K_+} - 1, \frac{N_+ + 1}{1+K_+}\right] \text{ and } n_- \in \left[\frac{N_- + 1}{1+K_-} - 1, \frac{N_- + 1}{1+K_-}\right] \tag{4.26}$$

Symmetric tug-of-war. For the symmetric tug-of-war of $N = N_+ = N_-$ plus and minus motors with identical properties except their preferred direction, the maximum of the motor number probability $p(n_+, n_-)$ is always at a zero motion state with $n = n_+ = n_-$, which changes location according to

$$K_+ = (N_+ - n)/(n+1). \tag{4.27}$$

for $0 \le n \le N$. The cargo is always in the no-motion motility state (0) (or unbound), see Fig. 4.13(a). No cooperative behaviour, especially no bidirectional motion, occurs. Thus, the interesting features of the model are caused by the nonequilibrium properties of the model.

The probability $p(\Delta)$ for the difference $\Delta = n_+ - n_-$ of active plus and minus motors as defined in Eq. (A.76) can be calculated from the motor number probability $p(n_+, n_-)$ in Eq. (4.24) and is related to the hypergeometric functions. It is shown in Fig. 4.13(b). For large motor numbers N, where the binomial distribution of $p(n_+, n_-)$ can be approximated by a Gaussian distribution, the probability $p(\Delta)$ also becomes a Gaussian distribution with mean 0 and variance $2Np(1-p)$:

$$p(\Delta) \approx \frac{1}{\sqrt{4\pi N p(1-p)}} \exp\left[-\frac{1}{2}\frac{(\Delta/N)^2}{2p(1-p)/N}\right] \tag{4.28}$$

Thus, upon increasing the motor numbers N, the peak of the distribution of Δ/N becomes sharper (the variance is proportional to $1/N$) and approaches a Delta-Peak for infinite motor numbers, see Fig. 4.13(b). This limit corresponds to the mean field theory discussed in Sec. 4.4.2, where the probability distribution maxima become 'deterministic' fixed points $x_\pm = \langle n_+ \rangle / N_\pm$.

The pausing states (0) are the diagonal states. Switching from plus motion states (+) to minus motion states (−) always passes (0) states, and coming to (0) from (+) leads to a switch in half of the cases, because the probability to go to (−) from (0) is 1/2. Therefore the switching time $T_{+-} = T_{-+}$ is twice the return time to the pausing states and thus, according to Eq. (A.69):

$$T_{+-} = 2T_{(0)} = \frac{2}{\sum_{n=0}^{N} p(n,n)\left[2\pi(n,n) + 2\epsilon(n,n)\right]} = \frac{1}{\sum_{n=0}^{N} p(n,n)\left[\pi_0(N-n) + \epsilon_0 n\right]} \tag{4.29}$$

[11] The energy landscape can be constructed by starting with zero energy for the state with $n_+ = n_- = 0$ and then calculating the other energies $E(n_+, n_-)$ in the following way: $\exp[-E(n_+, n_-)]$ is equal to the product of all forward rates divided by the product of all backward rates of a path leading from $(0,0)$ to (n_+, n_-). The detailed balance condition guarantees that this procedure leads to a well defined energy landscape; especially it guarantees the independence of this definition of the path. The result is $\exp[-E(n_+, n_-)] = \binom{N_+}{n_+} K_+^{-n_+} \binom{N_-}{n_-} K_-^{-n_-}$.

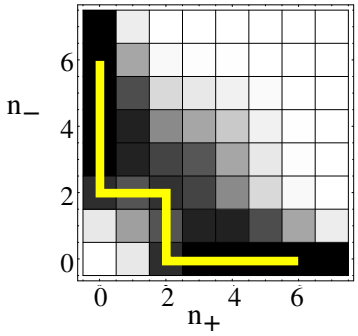

Fig. 4.14: Density plot of the probability distribution $p(n_+, n_-)$ for the symmetric tug-of-war of $N_+ = N_- = 7$ kinesin-like motors with parameters from Tab. 2.1. Darker colour corresponds to higher probability. Two maxima at $(n_+, n_-) = (6, 0)$ and $= (0, 6)$ are connected by a one-dimensional path, indicated by the yellow line. It passes through $s = s_+ = s_- = 2$, which is close to the value $s = 1.8$ of Eq. (4.32).

This is equal to twice the run time $T_+ = T_-$ plus the pause time

$$T_{+-} = 2\,T_+ + T_{\rm P}. \tag{4.30}$$

The sum is related to the hypergeometric functions and does not have a simple form. In the Gaussian approximation for large motor numbers N, it becomes

$$T_{+-} = T_{-+} \approx \sqrt{\pi K}/\left(\epsilon_0\sqrt{N}\right), \tag{4.31}$$

which decreases with increasing motor number N. This is because for large N the maximum of the probability distribution becomes sharper and the random walk therefore stays always close to this maximum, which leads to a decrease of the switch time. Eq. (4.31) overestimates the switch time for finite N, but gives the right scaling behaviour with the motor number N, as we will see in Sec. 4.5.1.

4.4.1.2 Large motor force: approximation as a one-dimensional walk

Mapping to a 1D walk. When the motors have a large force f, the cargo is in the $(-+)$ motility state and exhibits switching between two fast motion maxima of the probability distribution $p(n_+, n_-)$, see Sec. 4.3. In the state space network (n_+, n_-) shown in Fig. 4.3(b) and in Fig. 4.14, this corresponds to a random walk between two maxima $(n_+, 0)$ and $(0, n_-)$ on the boundary of the newtwork. There is a preferred path for this switching[12], corresponding to a low free energy path in the 'free energy landscape' $-\ln p(n_+, n_-)$. If one only considers motion along this path and neglects deviations, the system reduces from a two-dimensional network (with cycles) to a one-dimensional line (without cycles) as illustrated in Fig. 4.14.

When the random walk is on the plus motion boundary $(n_+, 0)$, it stays there as long as the rate leading away from the boundary, $\pi_-(n_+, 0) = (N_- - n_+)\pi_-$, is smaller than the rate going back to the boundary, $\epsilon_-(n_+, 1) = \epsilon_- \exp\left[F_{\rm C}(n_+, 1)/(n_+ F_{d-})\right]$, and it leaves the boundary when it reaches the point $(s_+, 0)$ where these two rates become comparable:

$$N_-\pi_- \sim \epsilon_- \exp\left[F_{\rm C}(s_+, 1)/(n_+ F_{d-})\right]. \tag{4.32}$$

An analogous expression holds for the point s_- where the walk leaves the boundary $(0, n_-)$. This leads to the approximation of the walk as the one-dimensional walk on $N_+ + N_- + 1$ points as shown in Fig. 4.14 and, in a relabeled version, in Fig. 4.15. The rates r_n and g_n for the corresponding Master equation

$$\partial_t p_n = r_{n+1}p_{n+1} + g_{n-1}p_{n-1} - (r_n + g_n)p_n \tag{4.33}$$

can be directly inferred from the original random walk as:

$$g_n = \begin{cases} \epsilon_-(s_+, s_- - n) = (s_- - n)\epsilon_{0-}\, e^{\frac{F(s_+, s_- - n)}{F_{d-}(s_- - n)}} & \text{for } n \in [0, s_- - 1] \\ \pi_+(n + s_+ - s_-, 0) = (N_+ - n - s_+ + s_-)\pi_{0+} & \text{for } n \in [s_-, N_+ - s_+ + s_-] \end{cases} \tag{4.34}$$

[12] If the cargo is in the $(-0+)$ motility state, there is a no motion maximum with $n_+ > 0$ and $n_- > 0$ present, and the preferred path passes through this maximum.

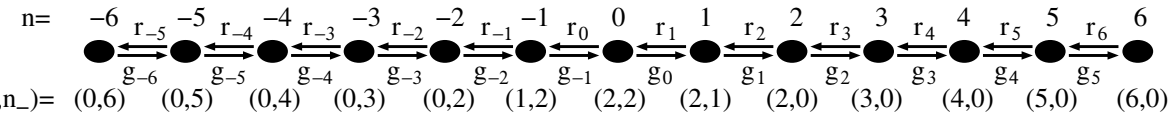

Fig. 4.15: Random walk on the one-dimensional path of Fig. 4.14 with the original labeling (n_+, n_-) (lowest line), the new labeling n (highest line), and the new rates r_n and g_n.

$$r_n = \begin{cases} \pi_-(s_+, s_- - n) = (N_- - s_- + n)\pi_{0-} & \text{for } n-1 \in [0, s_- - 1] \\ \epsilon_+(n + s_+ - s_-, 0) = (n + s_+ - s_-)\epsilon_{0+} & \text{for } n-1 \in [s_-, N_+ - s_+ + s_-] \end{cases} \tag{4.35}$$

Analogous equations hold for negative n resp. $n-1$.

Stationary state. The stationary state fulfills $\partial_t p_n = 0$, i.e. the current $J_n = r_n p_n - g_{n-1} p_{n-1}$ is a constant independent of n. Because of the reflecting boundaries, it must be equal to zero, i.e. the probabilities fulfill detailed balance $r_n p_n = g_{n-1} p_{n-1}$. This leads to a recursion relation with the solution [166]

$$p_n = \frac{g_{n-1} g_{n-2} \cdots g_1 g_0}{r_n r_{n-1} \cdots r_2 r_1} p_0 = p_0 \prod_{i=0}^{n-1} \frac{g_i}{r_{i+1}} \qquad \text{for } n \geq 0 \tag{4.36}$$

where p_0 is determined by the normalization condition

$$p_0 = \left[1 + \sum_{n=-(N_- + s_+ - s_-)}^{-1} \prod_{i=n+1}^{0} \frac{r_i}{g_{i+1}} + \sum_{n=1}^{N_+ - s_+ + s_-} \prod_{i=0}^{n-1} \frac{g_i}{r_{i+1}} \right]^{-1} . \tag{4.37}$$

Inserting the tug-of-war rates leads to

$$\frac{p_n}{p_0} = \begin{cases} K_-^n e^{S_-(n)} \binom{s_-}{n} / \binom{N_- - s_- + n}{n} & \text{for } n \in [0, s_- - 1] \\ \frac{N_-}{K_-} K_-^{s_-} K_+^{s_- - n} e^{S_-(s_- - 1)} \binom{N_+}{n + s_+ - s_-} / \binom{N_+}{s_+} / \binom{N_-}{s_-} & \text{for } n \in [s_-, N_+ - s_+ + s_-] \end{cases} \tag{4.38}$$

with the factors

$$S_+(n) = -\left(f_+ \frac{v_-}{v_+} + f_+ \right) s_- \left[\psi(|n| - s_- \frac{v_-}{v_+} - s_+) - \psi(-s_- \frac{v_-}{v_+} - s_+) \right] \tag{4.39}$$

Here, $\psi(z) = \Gamma'(z)/\Gamma(z)$ is the digamma function (the logarithmic derivative of the Gamma function). Analogous expressions hold for negative n.

Approximation for large forces. If the motors are very strong with large force ratios $f = F_s/F_d$, the unbinding cascade described in Sec. 4.3.3 leads to high probabilities that only one motor species is bound. This means that the random walk stays on the boundary of the two-dimensional network of Fig. 4.14, and switching occurs for $s_+ = s_- = 0$, in agreement with Eq. (4.32) for large motor forces f. In this case the motor number probability Eq. (4.38) becomes a binomial distribution on the (+) states with $n = 1, \ldots, N_+$:

$$\frac{p_n}{p_0} = \binom{N_+}{n} p_+^n \left(1 - p_+\right)^{N_+ - n} \left(1 - p_+\right)^{-N_+} = \binom{N_+}{n} \left(\frac{1}{K_+} \right)^n , \tag{4.40}$$

where $p_+ = 1/(1 + K_+)$ is the probability of a plus motor to be bound to the filament. Analogously, the probability distribution on the (−) states $n = -1, \ldots, -N_-$ is proportional to a binomial distribution with parameters N_- and $p_- = 1/(1 + K_-)$. The normalization is given by the probability for the state $n = 0$, $p_0 = \left[(1 + 1/K_+)^{N_+} + (1 + 1/K_-)^{N_-} - 1 \right]^{-1}$. For the one-dimensional walk, the state number n is equal to the difference $\Delta = n_+ - n_-$ of active plus and minus motors. The motor number probability $p_n = p(\Delta)$ exhibits two peaks which correspond

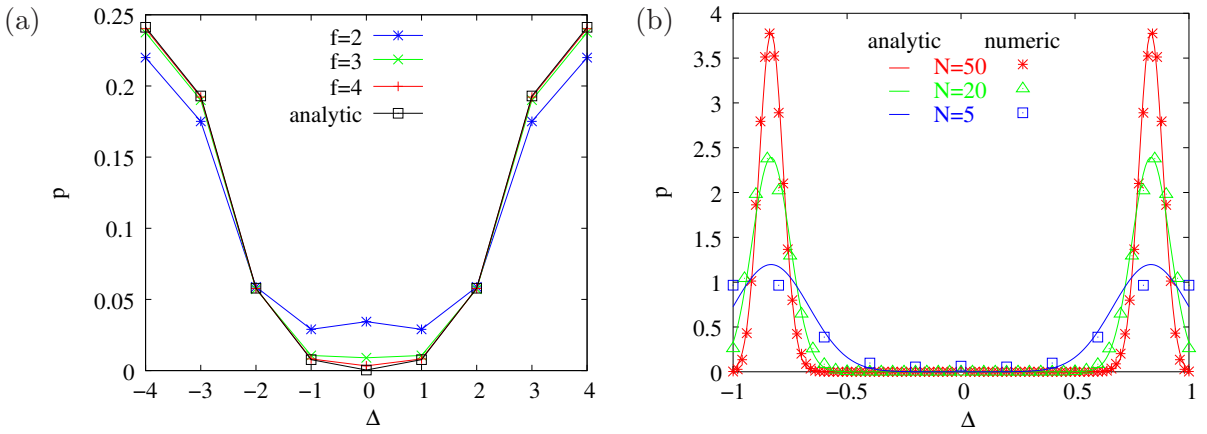

Fig. 4.16: Probability distributions $p(\Delta)$ of the difference $\Delta = n_+ - n_-$ of active plus and minus motors for the symmetric tug-of-war: (a) For the tug-of-war of 4 against 4 kinesin motors with $f = 2$ (blue asterisks) and motors with kinesin parameters except a larger f (green and red crosses), the distribution has two peaks at large absolute values of Δ. The analytic approximation Eq. (4.40) (black squares) works well in this $(-+)$ regime and becomes accurate for large f. (b) For N against N kinesin motors, the maxima of the distribution $p(\Delta)$ sharpen with increasing motor number N (data points). The Gaussian approximation Eq. (4.42) (solid lines) becomes accurate for large N.

to the maxima of the binomial distributions for the $(+)$ and $(-)$ states, respectively. The one-dimensional approximation works well for motors with high force ratios f and in particular for kinesin motors with $f = 2$, see Fig. 4.16(a).

The two maxima at $(n_+, 0)$ and $(0, n_-)$ change location at

$$K_+ = (N_+ - i)/(i + 1) \qquad \text{and} \qquad K_- = (N_- - i)/(i + 1) \tag{4.41}$$

for $i = 1, \ldots, N_+$ and $i = 1, \ldots, N_-$, respectively. This is the same result as for the location of the symmetric maxima (n, n) for the opposite limiting case of $f = 0$ in Sec. 4.4.1.1. For the symmetric case of identical plus and minus motors, the motility diagram is shown in Fig. 4.13(a). It agrees with the stochastic motility diagram in Fig. 4.7(a) for small resp. large f.

For large motor numbers, each of the binomial distributions can be approximated by a Gaussian distribution, so that the total distribution is a double Gaussian distribution

$$p_n = \frac{1}{\sqrt{8\pi N_+ p_+ (1-p_+)}} e^{-\frac{(n-N_+p_+)^2}{2N_+p_+(1-p_+)}} + \frac{1}{\sqrt{8\pi N_- p_- (1-p_-)}} e^{-\frac{(n+N_-p_-)^2}{2N_-p_-(1-p_-)}} \tag{4.42}$$

For the distribution of $n_\pm/N_\pm$, the variance of each Gaussian peak scales inversely with the motor number, and the peaks become sharper with increasing motor numbers, see Fig. 4.16(b). These peaks correspond to fixed points in the mean field approximation Sec. 4.4.2. Accordingly, the probabilities outside the maxima and therefore the probability if a transition between the maxima become smaller with larger motor numbers N, until transitions become impossible for infinite N resp. in mean field theory.

Run and switch times. Using the analytic large force results and App. A.3.3, we can calculate the plus run time

$$T_+ = \frac{p((+))}{p_1 \epsilon_+(1,0)} = \frac{1}{N_+ \pi_+} \left[(1 + 1/K_+)^{N_+} - 1 \right]. \tag{4.43}$$

and the pausing time

$$T_\mathrm{P} = \frac{1}{r_0 + g_0} = \frac{1}{\pi_+(0,0) + \pi_-(0,0)} = \frac{1}{N_+\pi_+ + N_-\pi_-}. \tag{4.44}$$

The switch time T_{+-} cannot be calculated as easily because a plus run may involve pauses, i.e. a visit to the state $n = 0$ followed by a return to the plus states $(+)$. Switching occurs only

when the walk passes form (+) to (0) and then to (−). If the walk is in the pausing state (0), it continues to the (+)-states with rate $\pi_+(0,0) = N_+\pi_+$ and to (−) with rate $\pi_-(0,0) = N_-\pi_-$. Thus the probability to go to (−) is $w_- = N_-\pi_-/\left(N_+\pi_+ + N_-\pi_-\right)$, and the probability to go to (+) is $w_+ = 1 - w_-$. If the walk starts its plus run in (+) and then moves to (0), it makes a switch with probability w_-. For this it needs on average the sum of of the sojourn times in (+) and (0), $T_+ + T_\mathrm{P}$. With probability w_+, it does not switch but goes back to (+) and restarts the procedure. The switch time thus is

$$T_{+-} = \sum_{n=1}^{\infty} w_- w_+^{n-1}\, n\,(T_+ + T_\mathrm{P}) \tag{4.45}$$

where the term $w_- w_+^{n-1}\, n\,(T_+ + T_\mathrm{P})$ means that the walk has returned to the pausing states n times before a switch occurred. $(n-1)$ times it then went back to (+) (probability w_+^{n-1}, and only in the nth try it proceeded to (−) (probability w_-). For each return it needed the time $T_+ + T_\mathrm{P}$ on the average. Performing the summation leads to

$$T_{+-} = \frac{T_+ + T_\mathrm{P}}{w_-} = \frac{N_+\pi_+ + N_-\pi_-}{N_+\pi_+ N_-\pi_-}\left[(1 + 1/K_+)^{N_+} - 1\right] + \frac{1}{N_-\pi_-} \sim \exp\left[N_+ \ln\frac{1+K_+}{K_+}\right] \tag{4.46}$$

where the exponential scaling holds for large motor numbers N_+. Analogous formulas hold for the minus switch times T_- and T_{-+}. Eq. (4.46) overestimates the switch times because it neglects directional switches via states that are not on the one-dimensional channel of the approximation, but it gives the correct scaling with N, as we will see in Sec. 4.5.1.

In order to calculate the mean switch lengths, one can simply replace the rates, which are inverse times, by the corresponding inverse distances. The velocities in the states $(n_+, 0)$ and $(0, n_-)$ are v_{F+} and v_{F-}, respectively. As these velocities are independent of the motor numbers n_+ and n_-, and as the rates are proportional to either the single motor binding or unbinding rates, see Eqs. (4.3) and (4.4), this means that one can simply replace

$$\epsilon_{0+} \to \epsilon_{0+}/v_{F+} \quad \text{and } \pi_{0+} \to \pi_{0+}/v_{F-}, \tag{4.47}$$

and likewise for the minus motor rates.

4.4.1.3 Summary

We have analytically calculated the stationary state probabilities, the motility diagrams and the switch times for the tug-of-war model in the limit of small and large motor force ratios $f = F_s/F_d$. As expected, the results are good approximations for low and large motor forces f, respectively, but fail for intermediate f. The motility diagram in these approximations, for example, looks rather simple and does not capture the interesting behaviour for intermediate and biologically relevant f, compare Fig. 4.13(a) and Fig. A.6. However, for 'strong' biological motors like kinesin, the approximation for large motor forces often works well.

4.4.2 Mean field approximation

In this section we consider the bidirectional cargo transport in mean field approximation.

4.4.2.1 Mean field equations

In the mean field approximation, we do not care about the probability for n_+ active plus and n_- active minus motors, but only about the mean value of active plus and minus motors. For this purpose, we define the rescaled and averaged motor numbers

$$x_+ = \langle n_+ \rangle / N_+ \qquad \text{and} \qquad x_- = \langle n_- \rangle / N_-, \tag{4.48}$$

which range between 0 and 1, and which become continuous variables for large numbers N_+ and N_- of plus and minus motors on the cargo. Multiplying the Master equation Eq. (4.1) by n_+ resp. n_-, averaging and using the mean field approximation[13] leads to the mean field equations:

$$\frac{\partial}{\partial t}\, x_+ = \pi_{0+}\,(1-x_+) - x_+\epsilon_{0+}\,\mathrm{e}^{F_\mathrm{C}(x_+,x_-)/(N_+x_+F_{d+})} =:\; g_+(x_+,x_-) \tag{4.49}$$

$$\frac{\partial}{\partial t}\, x_- = \pi_{0-}\,(1-x_-) - x_-\epsilon_{0-}\,\mathrm{e}^{F_\mathrm{C}(x_+,x_-)/(N_-x_-F_{d-})} =:\; g_-(x_+,x_-) \tag{4.50}$$

with the cargo force $F_\mathrm{C}(x_+,x_-)$ from Eq. (4.6). The mean field equations have a very intuitive interpretation: the first term $\pi_{0+}(1-x_+)$ in Eq. (4.49) describes binding of unbound plus motors with rate π_{0+}, while the second term describes unbinding of bound plus motors with rate $\epsilon_{0+}\exp\left[F_\mathrm{C}(x_+,x_-)/(N_+x_+F_{d+})\right]$. An analogous interpretation holds for the change of the minus motor density x_- in Eq. (4.50).

We are interested in the stationary state of the system. In the mean field approximation, this corresponds to the fixed points (FP) (x_+,x_-) defined by

$$\frac{\partial}{\partial t}\, x_+ = g_+(x_+,x_-) = 0 \qquad \text{and} \qquad \frac{\partial}{\partial t}\, x_- = g_-(x_+,x_-) = 0. \tag{4.51}$$

Depending on the values of the single motor parameters, these nonlinear algebraic equations have 1, 3 or 5 solutions. These FPs can be (locally) stable, which means that a sufficiently small fluctuation of the values (x_+,x_-) near the FP damps out in time. Once the system reaches this FP, it will stay there. The FPs can also be unstable, which means that even a small fluctuation of the values (x_+,x_-) will lead the system away from the FP. The stability of the FPs is determined by the signs of the two eigenvalues of the Jacobian matrix:

$$J(x_+,x_-) = \begin{pmatrix} \frac{\partial}{\partial x_+}\, g_+(x_+,x_-) & \frac{\partial}{\partial x_-}\, g_+(x_+,x_-) \\ \frac{\partial}{\partial x_+}\, g_-(x_+,x_-) & \frac{\partial}{\partial x_-}\, g_-(x_+,x_-) \end{pmatrix} \tag{4.52}$$

If they both have a negative real part at the FP, the FP is stable; if at least one of them has a positive real part, the FP is unstable, see e.g. [152]. Obviously only the stable FPs are of interest: They are average values of numbers of active plus resp. minus motors which are stable in time; they are closely related to the maxima of the probability distribution $p(n_+,n_-)$ in the stochastic theory. We therefore define the motility states in the mean field theory via the number and properties of the stable FPs. A stable FP with $F_{s+}x_+ \gg F_{s-}x_-$ defines a plus motion state $(+)$, one with $F_{s+}x_+ \ll F_{s-}x_-$ a minus motion state $(-)$, and one with $F_{s+}x_+ \sim F_{s-}x_-$ a zero motion state (0). As we will see below, the following combinations of stable FPs appear: $(+)$, $(-)$, (0), $(-+)$, $(0+)$, (-0) and $(-0+)$, leading to the same motility states as for the stochastic theory. The transitions between these motility states correspond to changes in the number and stability of the FPs, i.e. to bifurcations.

4.4.2.2 Symmetric tug-of-war

FPs and bifurcations. In the symmetric case of identical plus and minus motors (except their forward direction), the equations for the FPs are:

$$(1-x_\pm) - x_\pm\, K\,\mathrm{e}^{f(1+G)x_\pm/(Gx_++x_-)} = 0 \tag{4.53}$$

They depend on the dimensionless motor strength $f = F_s/F_d$, desorption constant $K = \epsilon_0/\pi_0$ and the ratio $G = \beta_{0-}/\beta_{0+}$ of minus to plus motor slope of the force-velocity relation. One has $G = \nu = \beta_B/\beta_F < 1$ for winning plus motors, i.e. for $x_+ > x_-$, and $G = 1/\nu > 1$ for winning

[13] The mean field approximation replaces the mean value $\langle f(n_+,n_-)\rangle$ of any function f of the motor numbers n_+, n_- by the function $f(\langle n_+\rangle,\langle n_-\rangle)$ of the mean values of the motor numbers. This means that any moments of order 2 and higher in a cumulant expansion are neglected.

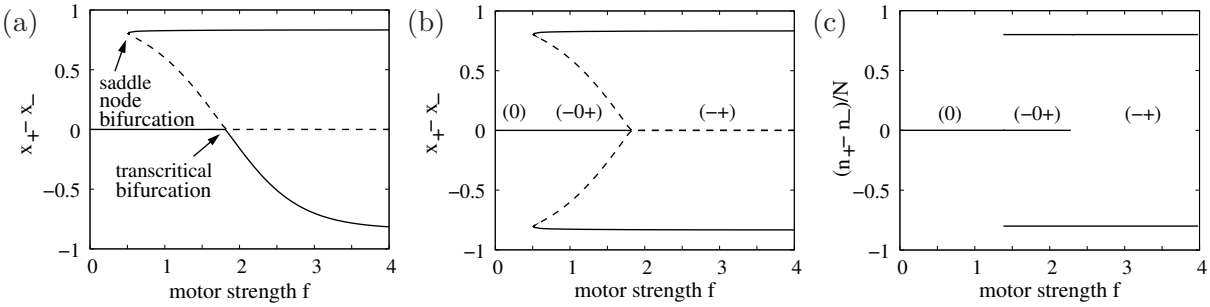

Fig. 4.17: (a) and (b): Bifurcation diagrams for the symmetric tug-of-war with $K = 0.2$ and $\beta_B = 0.05\,\mu$m/s/pN: difference of the mean field FPs $x_+ - x_-$ as a function of the motor strength f. Solid lines mark stable, dashed lines unstable FPs. (a) shows all FPs for $G = \nu$, and (b) all physical FPs. (c) The location of the scaled difference $(n_+ - n_-)/N$ of the maxima of the motor number probability $p(n_+, n_-)$ in the stochastic theory with the same parameters for $N = N_+ = N_- = 5$ looks very similar to the mean field bifurcation diagram. In (b) and (c), the motility states (0), (−0+) and (−+) are indicated.

minus motors, i.e. for $x_+ < x_-$. This abrupt change of G at $x_+ = x_-$ leads to a non-analyticity. We therefore solve the set Eq. (4.53) for $G = \nu$ in the whole (x_+, x_-)-plane and then only use the solutions with $x_+ > x_-$. The solutions with $x_+ < x_-$, corresponding to solutions of Eq. (4.53) with $G = 1/\nu$, then follow from symmetry.

Eq. (4.53) can be rearranged to define the nullcline functions

$$x_\mp = \frac{x_\pm G \ln\left[(1 - x_\pm)/(K x_\pm)\right]}{f(1+G) - \ln\left[(1 - x_\pm)/(K x_\pm)\right]} =: h_\pm(x_\pm) \tag{4.54}$$

They intersect in either one or three points, which are the FPs. A bifurcation occurs when, upon changing the motor parameters, the number of intersections changes, i.e. when the nullclines become tangent in a FP, leading to the bifurcation conditions

$$h_-(h_+(x_-)) = x_- \qquad \text{and} \qquad h'_-(h_+(x_-)) = 1/h'_+(x_-). \tag{4.55}$$

Fig. 4.17(a) shows a bifurcation diagram upon changing the motor strength f for $G = \nu$. For small f, there is only a single stable FP with $x_+ = x_-$. When f is increased, a saddle-node bifurcation occurs and two FPs with $x_+ > x_-$ appear 'out of the blue', one of them stable, one unstable. When f is increased further, the unstable FP coalesces with the $x_+ = x_-$ FP, and both exchange stability. This is a transcritical bifurcation.

As $G = \nu$, only the FPs with winning plus motors, $x_+ > x_-$, are 'physical'; the physical FPs with $x_+ < x_-$ are solutions from Eq. (4.53) with $G = 1/\nu$. They can be inferred by symmetry by interchanging x_+ and x_-. This leads to the 'physical' bifurcation diagram in Fig. 4.17(b). For small f, there is only the single stable zero motion FP; this is the (0) motility state. When f is increased, two saddle node bifurcations lead to four new FPs, of which two are stable and correspond to plus resp. minus motion. This is the (−0+) motility state. When f is increased further, the unstable and the zero motion FPs coalesce, and only the zero motion FP survives this collision as an unstable FP, leaving one plus and one minus motion stable FP. This is the (−+) motility state. Note that the bifurcation near $f = 1.8$ in Fig. 4.17(b), which looks like a subcritical pitchfork bifurcation on first sight, is the combination of parts of two transcritical bifurcations of two sets of mean field equations, the one shown in Fig. 4.17 and its symmetric counterpart. The bifurcation curves near the bifurcation point are linear and not square roots.

Fig. 4.17(c) shows the bifurcation diagram for the same set of parameters for the stochastic theory. It looks very similar to the mean field bifurcation diagram Fig. 4.17(b): the stable FPs correspond to maxima in the probability distribution $p(n_+, n_-)$. The unstable FPs correspond to minima in the probability distribution p and are not shown.

Eq. (4.55) allows for a numerical calculation of the bifurcation lines in the (f, K)-plane. The resulting motility diagram shown in Fig. 4.18(a) shows the same qualitative features as the

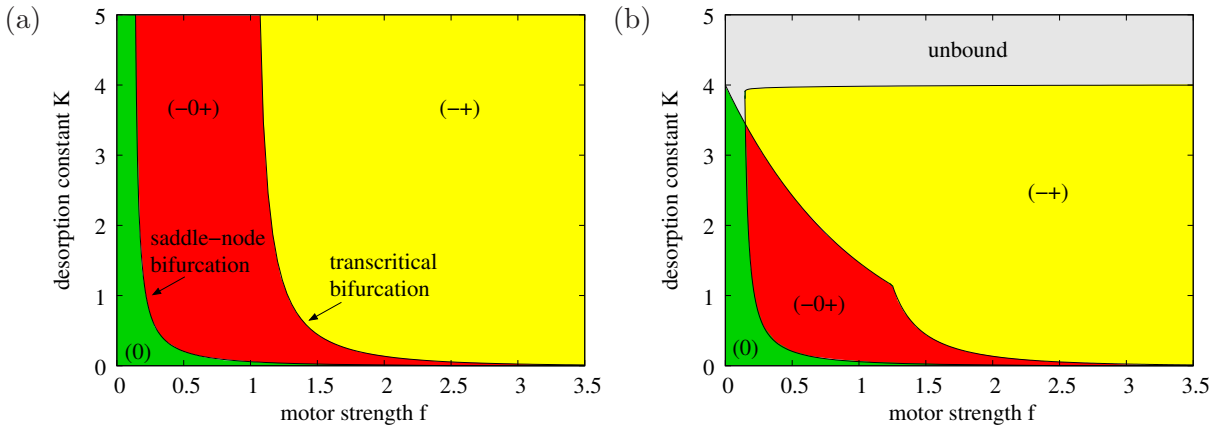

Fig. 4.18: Mean field motility diagrams for the symmetric tug-of-war with $\beta_B = 0.05\,\mu$m/s/pN: (a) The mean field motility diagram exhibits three motility regimes (0) (green), $(-+)$ (red), and $(-0+)$ (yellow) defined via the locations of the FPs. (b) When a cutoff for cargo unbinding at $x_\pm \geq 1/N$ with $N = 5$ is introduced, the mean field motility diagram is very similar to the stochastic motility diagrams of Fig. 4.7.

stochastic motility diagrams of Sec. 4.3.3, displaying the (0) no motion state for small motor strengths f, the $(-+)$ motility state for large f, and the $(-0+)$ state for intermediate f. We investigate the dependence of the motility diagram on the only left parameter, the backward velocity v_B, in App. A.4.3.

Small and large force ratio. For small motor strengths f, the mean field equations become linear and have only the zero motion solution

$$x_+ = x_- = \frac{1}{1 + K(1+f)}, \tag{4.56}$$

which is always stable, so that the cargo is in the (0) motility state. This reproduces the results Eq. (4.26) and Eq. (4.28) of the stochastic theory in the small f and large N approximation.

In the case of large f, the detachment term in the mean field equation is dominant unless either x_+ or x_- is very small. In this limit the mean field equations again become linear with the stable solution:

$$\begin{aligned} x_+ &= \tfrac{1}{1+K} - \tfrac{fK(G+1)}{G(1+K)\left(1+K\exp\left[f\frac{1+G}{G}\right]\right)} \overset{f\to\infty}{\longrightarrow} \tfrac{1}{1+K} \\ x_- &= \tfrac{1}{1+K\exp\left[f\frac{1+G}{G}\right]} \overset{f\to\infty}{\longrightarrow} 0 \end{aligned} \tag{4.57}$$

Together with the corresponding stable minus motion FP from the mean field equation of $G = 1/\nu$, this leads to the $(-+)$ motility state for large f. This reproduces the result Eq. (4.42) of the stochastic theory in the large f and large N approximation.

Main directions and linear stability analysis. The mean field equations Eq. (4.53) always have the zero motion FP

$$x_S := x_+ = x_- = \frac{1}{1 + K\,\mathrm{e}^f} \tag{4.58}$$

with the eigenvalues of the Jacobian $\lambda_1 = -(1 + K\,e^f)$ and $\lambda_2 = -(1 + K\,e^f) + fK\,e^f$. The first eigenvalue is always negative, while the second eigenvalue changes sign at

$$K = \frac{e^{-f}}{f-1} \tag{4.59}$$

This is the transcritical bifurcation line shown in Fig. 4.18(a); it does not depend on the slope ratio ν resp. G. The Jacobian matrix can be diagonalized at the zero motion FP with the

transformation matrix $T = ((-G, 1), (1, 1))$ leading to

$$J_{\text{diag}}(x_{\text{S}}, x_{\text{S}}) = T^{-1}\, J(x_{\text{S}}, x_{\text{S}}) T = \begin{pmatrix} K\, e^f (f-1) - 1 & 0 \\ 0 & -\left(1 + K\, e^f\right) \end{pmatrix} \tag{4.60}$$

The transformation matrix T identifies the two main directions (Δ, Σ) near the FP[14]:

$$\begin{pmatrix} \Delta \\ \Sigma \end{pmatrix} := (1+G)\, T^{-1} \begin{pmatrix} x_+ - x_{\text{S}} \\ x_- - x_{\text{S}} \end{pmatrix} = \begin{pmatrix} x_+ - x_- \\ (1+G) x_{\text{S}} - (x_+ + G x_-) \end{pmatrix} \tag{4.61}$$

Calculating the differential equations for the new variables Δ and Σ and expanding them near the FP, i.e. near $(\Delta, \Sigma) = (0, 0)$, gives

$$\begin{aligned} \partial_t \Delta &= \mu\, \Delta - a\, \Delta^2 + \mathcal{O}_3 \\ \partial_t \Sigma &= -\kappa\, \Sigma + \mathcal{O}_2 \end{aligned} \tag{4.62}$$

with

$$\mu = K\, e^f (f-1) - 1 = \begin{cases} < 0 & \text{for } K < \frac{e^{-f}}{f-1} \\ > 0 & \text{else} \end{cases} \tag{4.63}$$

$$a = \frac{K\, e^f f^2 (1 + K\, e^f)}{2(1+G)} (1-G) > 0 \qquad \text{for } G < 1 \tag{4.64}$$

$$\kappa = \left(1 + K\, e^f\right) > 0 \tag{4.65}$$

Here, $\mathcal{O}_n$ signifies terms of order n, e.g. $\Delta^2\Sigma$ would be a term of $\mathcal{O}_3$. Eq. (4.62) is the prototype form of a two-dimensional transcritical bifurcation. The Σ-direction is a stable manifold irrespective of the parameter values and plays no role in the bifurcation. The variable Δ is the 'order parameter' of the bifurcation, the variable along the manifold which changes stability at the bifurcation. The bifurcation occurs at $\mu = 0$ where two FPs (one with $\Delta = 0$, and one with $\Delta \neq 0$) collide and change stability (the FP with $\Delta \neq 0$ also changes sign):

$$\text{if } \mu = K\, e^f (f-1) - 1 \begin{cases} < 0, & \text{then } \Delta = 0 \quad \text{stable, } \Delta > 0 \text{ instable} \\ > 0, & \text{then } \Delta = 0 \text{ instable, } \Delta < 0 \quad \text{stable} \end{cases} \tag{4.66}$$

Cargo unbinding. In the stochastic case we defined the cargo as unbound from the filament when the maximum of the probability distribution $p(n_+, n_-)$ is at $n_+ = n_- = 0$. In mean field theory, $x_+ = \langle n_+ \rangle / N < 1/N$ means that the average value of bound plus motors is below 1, which means that the cargo is effectively unbound. We therefore define that unbinding occurs when the both x_+ and x_- are smaller than $1/N$. For the zero motion FP, this happens at $K > (N-1)\exp(-f)$; for the plus or minus motion FP, this line has to be determined numerically and is roughly at $K = N - 1$. The result is shown in Fig. 4.18(b) for $N = 5$. This mean field motility diagram looks qualitatively and even quantitatively similar to the stochastic motility diagrams, compare Fig. 4.7.

4.4.2.3 Kinesin versus dynein

The most relevant in *in vivo* tug-of-war is the one of kinesins and dyneins, which we investigated in Sec. 4.3.4. We calculated the motility diagram of $N = N_+ = N_-$ kinesins and dyneins in the

[14] Here, Δ and Σ are defined in such a way that they pass through zero at the symmetric FP. The arbitrary factor $(1 + G)$ is introduced for convenience.

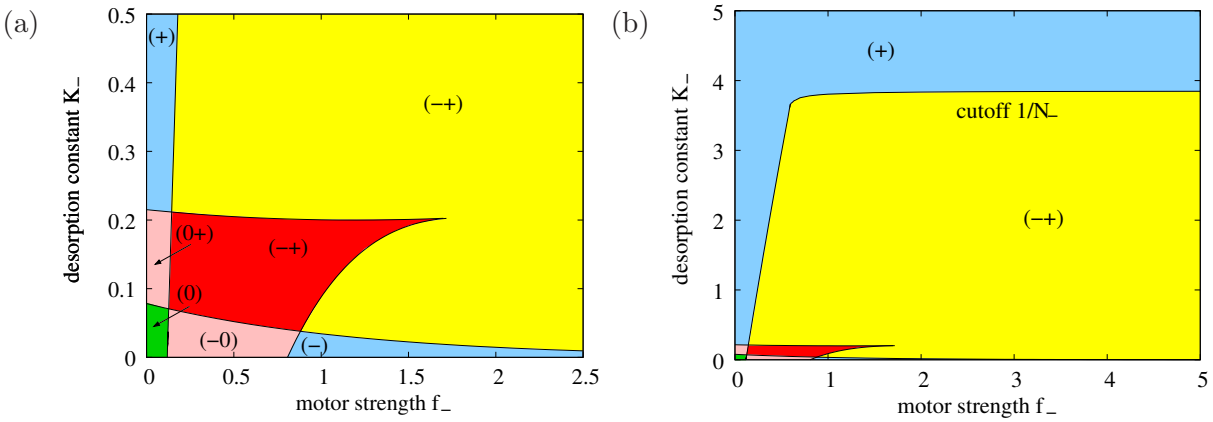

Fig. 4.19: Mean field motility diagrams for the tug-of-war of kinesin-like plus against dynein-like minus motors except for the minus motor stall force F_{s-} and unbinding rate ϵ_{0-} which are varied, and backward velocity $0.05\,\mu$m/s. The diagram in (b) also shows the cutoff line $x_- = 1/N_-$ for $N_- = 5$. The mean field motility diagram is similar to the stochastic motility diagram shown in Fig. 4.10.

(f_-, K_-)-plane. The same can be done in mean field theory. The calculations are cumbersome, however, and are outlined in Sec. A.4.3.2 in App. A.4.3. The resulting motility diagram is shown in Fig. 4.19. The mean field motility diagram looks very similar to the stochastic motility diagram in Fig. 4.10, especially for large motor number N. In particular, the same seven motility states (+), (−), (0), (−+), (0+), (−0) and (−0+) appear in similar regions of the (f_-, K_-) phase space.

4.4.2.4 Discussion

Mean field theory describes the tug-of-war model with two intuitive nonlinear differential equations for the average numbers of active plus and minus motors, see Eqs. (4.49) and (4.50). It captures the essential features of the stochastic theory, namely all motility states. For sufficiently large motor numbers, the motility diagrams even show quantitative similarity, compare Fig. 4.18 and Fig. 4.7 for the symmetric and Fig. 4.19 and Fig. 4.10 for the asymmetric tug-of-war. A similar mean field theory has been discussed for the symmetric case in order to describe mitotic spindle oscillations [39]. It exhibits the same motility states when the elastic element of the mitotic spindle is set to zero [58].

The motility states in mean field theory are defined via the stable fixed points (FPs) of the mean field equations, which are analogous to maxima of the motor number probability in the stochastic case. However, there are no kinetic transitions between such stable mean field FP. This means that for example in the (−0+) motility state the cargo shows either plus motion, minus motion or no motion, but does not switch between these motion types. Such transitions are a stochastic effect which occur only for finite motor numbers N_+, N_-. Upon increasing the motor numbers, the transitions occur more and more seldom, as can be seen by the increase in switch times with the motor number in Sec. 4.5.1, and finally vanish in mean field theory.

Mean field theory thus allows to understand what happens when cargos are transported by a large number of motors. In cells, however, the number of involved motors is usually small, ranging from 1-10 motors, see Sec. 4.1.1. This leads to stochastic switching between different maxima of the motor number probability $p(n_+, n_-)$, and therefore to switching between plus motion, minus motion and/or pauses.

4.4.3 Sharp maximum approximation

In Sec. 4.3 we have determined numerically the motility states of the cargo depending on the single motor parameters. The obtained motility diagrams have a rather complex shape, see e.g. Figs. 4.7 and 4.10. In this section we derive analytical expressions for the transition lines in the

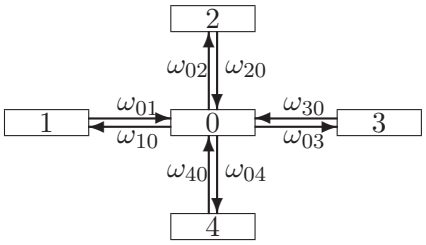

Fig. 4.20: The maximum point, labeled by 0, and its direct neighbours, labeled by 1, 2, 3 and 4, and the rates connecting them.

motility diagrams using a simple 'sharp maximum approximation'.

4.4.3.1 The sharp maximum approximation

We have characterized the motility states of the cargo by the maxima of the motor number probability $p(n_+, n_-)$ for the number n_+ of active plus and n_- of active minus motors, because the cargo spends most of its time in such maxima states. This characterization is good if the maxima are sufficiently 'sharp', meaning that the probability is very concentrated around the maximum points. Numerical results indeed indicate that this is the case, especially for maxima with only one motor type bound. Here we therefore assume that the probability is non-zero only on the maximum points and its nearest neighbours, i.e. that the maximum is sharp. For simplicity, we label this maximum point by 0 and its nearest neighbours by 1, 2, 3 and 4, as shown in Fig. 4.20. Under this premise, the Master equation 4.1 simplifies to

$$\partial_t P_0 = -\sum_{i=1}^{4} \omega_{0i} P_0 + \sum_{i=1}^{4} \omega_{i0} P_i \tag{4.67}$$

$$\partial_t P_i = -\omega_{i0} P_i + \omega_{0i} P_0 \qquad \text{for } i = 1, \dots 4 \tag{4.68}$$

where ω_{ij} denotes the rate connecting states i and j. In the stationary state, this leads to the detailed balance relations $\omega_{i0} P_i = \omega_{0i} P_0$. The condition for the point 0 to be a maximum is $P_0 > P_i$, i.e.

$$\omega_{0i} < \omega_{i0} \qquad \text{for } i = 1, \dots 4 \tag{4.69}$$

This is intuitive, stating that the rates ω_{i0} leading into the maximum state 0 should be larger than the corresponding out rates ω_{0i}.

From Eq. (4.69) we derive the conditions for having a probability maximum at a point (n_+, n_-), which corresponds to the point 0, by substituting the rates ω_{ij} with the rates from Eqs. (4.3) and (4.4) which connect (n_+, n_-) with its nearest neighbours. As biological motors the backward velocity is very small, see Chap. 2, we set the superstall slope β_B to zero, so that the cargo force is $F_C(n_+, n_-) = \max(n_+ F_{s+},\, n_- F_{s-})$, see Sec. 4.3.1. With this, Eq. (4.69) leads to the four conditions:

$$\begin{aligned}
&(1): && K_- < \tfrac{N_- - n_- + 1}{n_-} \exp\left[-\tfrac{\max(n_+ F_{s+}, n_- F_{s-})}{n_- F_{d-}}\right] && (n_- > 0)\\
&(2): && K_+ > \tfrac{N_+ - n_+}{n_+ + 1} \exp\left[-\tfrac{\max((n_+ + 1) F_{s+}, n_- F_{s-})}{(n_+ + 1) F_{d+}}\right] && (n_+ < N_+)\\
&(3): && K_- > \tfrac{N_- - n_-}{n_- + 1} \exp\left[-\tfrac{\max(n_+ F_{s+}, (n_- + 1) F_{s-})}{(n_- + 1) F_{d-}}\right] && (n_- < N_-)\\
&(4): && K_+ < \tfrac{N_+ - n_+ + 1}{n_+} \exp\left[-\tfrac{\max(n_+ F_{s+}, n_- F_{s-})}{n_+ F_{d+}}\right] && (n_+ > 0)
\end{aligned} \tag{4.70}$$

4.4.3.2 Cargo unbinding

We say that the cargo is unbound from the filament if the motor number probability $p(n_+, n_-)$ is maximal at $(0, 0)$. This happens if conditions (2) and (3) of Eq. (4.69) are fulfilled for $n_+ = n_- = 0$, i.e. for:

$$K_+ > N_+ \quad \text{and} \quad K_- > N_- \tag{4.71}$$

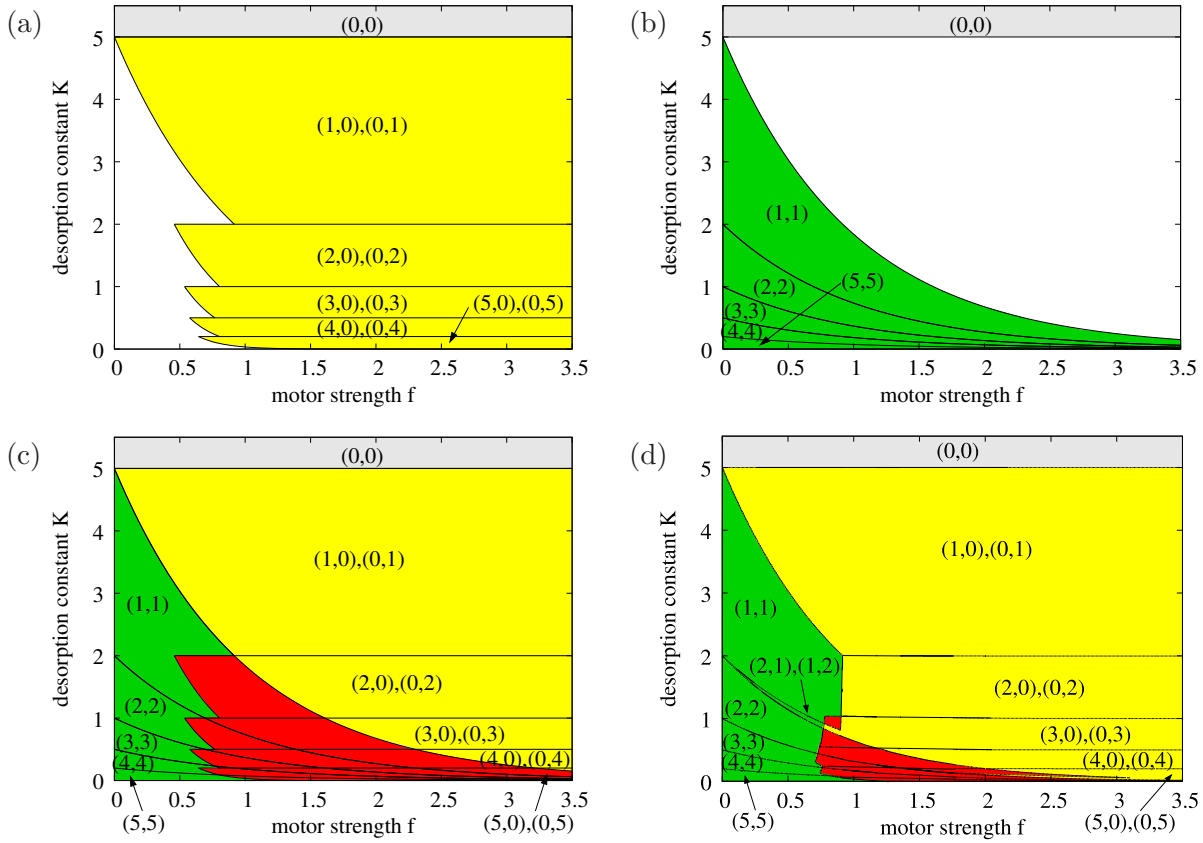

Fig. 4.21: Constructing the motility diagram for the symmetric tug-of-war of $N_+ = N_- = 5$ plus against minus motors in the sharp maximum approximation: The transition lines for (a) the plus and minus motion maxima at $(n, 0)$ and $(0, n)$ according to Eq. (4.72) and (b) for the zero motion maxima at (n, n) according to Eq. (4.73) form (c) the full motility diagram with the motility states 'no motion' (0) (green), 'fast plus and minus motion' $(-+)$ (yellow), and 'fast plus and minus motion interspersed with pauses' $(-0+)$ (red). This motility diagram is very similar to the exact numeric motility diagram shown in (d). Parameters are for kinesin except for the stall force F_s and the unbinding rate ϵ_0 which are varied. In the sharp maximum approximation, the superstall velocity slope β_B is set to zero.

As to be expected, unbinding occurs if the motors are non-processive, i.e. have a high filament desorption constant K_+ resp. K_-. A single motor is processive if it is more likely to be bound to the filament than not, i.e. if its desorption constant is smaller than 1. Eq. (4.71) states that, analogously N_+ plus motors are processive if they all are more likely to be bound to the filament than not, i.e. if $K_+ < N_+$. Thus many motors lead to an enormous processivity enhancement.

4.4.3.3 Symmetric tug-of-war

In the symmetric tug-of-war of $N = N_+ = N_-$ plus and minus motors with identical parameters, two types of maxima occur, as discussed in Sec. 4.3.3:

- **fast motion maxima**: The maxima with only one active motor species at $(n, 0)$ and $(0, n)$ (they always occur in pairs because of the symmetry) lie on the boundary of the state space (n_+, n_-). The four conditions Eq. (4.70) reduce to three with the result that there are maxima at $(n, 0)$ and $(0, n)$ if

$$\max\left(\frac{N-n}{n+1},\ N\mathrm{e}^{-nf}\right) < K < \frac{N-n+1}{n} \qquad \text{for } n = 1, \ldots, N \tag{4.72}$$

  These transition lines are shown in Fig. 4.21(a).

- **no-motion maximum with**: The maxima with an equal number $n = n_+ = n_-$ of active plus and minus motor lie on the diagonal of the state space (n_+, n_-). The symmetry allows to compare only to the neighbours 1 and 2 in Eq. (4.70), leading to two conditions for a maximum at (n, n):

$$\frac{N-n}{n+1}\,\mathrm{e}^{-f} < K < \frac{N-n+1}{n}\,\mathrm{e}^{-f} \qquad \text{for } n = 1, \ldots, N \tag{4.73}$$

  The transition lines between these maxima are shown in Fig. 4.21(b).

Motility diagram. Putting together the transition lines for both maxima types leads to the motility diagram shown in Fig. 4.21(c). The maxima $(n, 0)$ and $(0, n)$ with only one motor type bound define the $(-+)$ phase (yellow), while the maxima (n, n) with both types of motors bound define the (0) phase (green). The overlap region is the $(-0+)$ phase (red). This motility diagram agrees well with the exact motility diagram shown in Fig. 4.21(d). The rather simple analytic equations of the sharp maximum approximation can therefore be used to estimate the transition lines. The sharp maximum approximation however tends to overestimate the existence region of a maximum (and therefore the many-maximum $(-0+)$ region) because the maximum is only compared to its next neighbours as shown in Fig. 4.20. When the maximum is also compared to its diagonal neighbours, the sharp maximum approximation becomes more accurate, but also more cumbersome and therefore less useful, see App. A.4.4.

4.4.3.4 Kinesin versus dynein

In Sec. 4.3.4 we have considered the tug-of-war of N_+ kinesins against N_- dynein-like motors and calculated the motility diagrams for varying minus motor stall force F_{s-} and detachment rate ϵ_{0-}. The motility diagram for $N_+ = N_- = 5$ is reproduced in Fig. 4.22(c,d). Here we calculate the same diagrams in the sharp maximum approximation with zero backward velocity for $N_+ = N_- = 5$. Because of the loss in symmetry, the motility diagram becomes more complicated. As discussed in Sec. 4.3.4, there are three types of maxima:

- **fast minus motion maximum**: A maximum at $(0, n_-)$ is subject to conditions (1)-(3) from Eq. (4.70):

$$\frac{N_- - n_-}{n_- + 1} < K_- < \frac{N_- - n_- + 1}{n_-} \quad \text{and} \quad f_- > \frac{1}{n_-} \ln \frac{N_+}{K_+} \tag{4.74}$$

- **fast plus motion maximum**: For a maximum at $(n_+, 0)$, the conditions (2) and (4) from Eq. (4.70) lead to

$$\frac{N_+ - n_+}{n_+ + 1} < K_+ < \frac{N_+ - n_+ + 1}{n_+} \tag{4.75}$$

  The solution for kinesin parameters is $n_+ = 4$ or $n_+ = 5$, as $p(4, 0) = p(5, 0)$ in this approximation. Therefore the sharp maximum approximation cannot decide whether the plus motion maximum is at $n_+ = 4$ or $n_+ = 5$. We display $n_+ = 5$ in Fig. 4.22(a,b). This ambiguity can also be seen in the full numeric motility diagram in Fig. 4.22(d), which displays maxima at $(5, 0)$ for low f_- and K_-, and at $(4, 0)$ for high f_- and K_-. The condition (3) leads to

$$K_- > \begin{cases} N_+\,\mathrm{e}^{-n_+ f_+} & \text{if} \quad f_- < n_+ f_+ \\ N_+\,\mathrm{e}^{-f_-} & \text{if} \quad f_- > n_+ f_+ \end{cases} \qquad \text{with } n_+ = 4,\, 5 \tag{4.76}$$

  For kinesin parameters, both limits on K_- are so small that they cannot be seen in the motility diagram shown in Fig. 4.22(a); the plus motion maximum at $(n_+, 0)$ with $n_+ = 4$ or $n_+ = 5$ exists in basically the whole phase space (f_-, K_-).

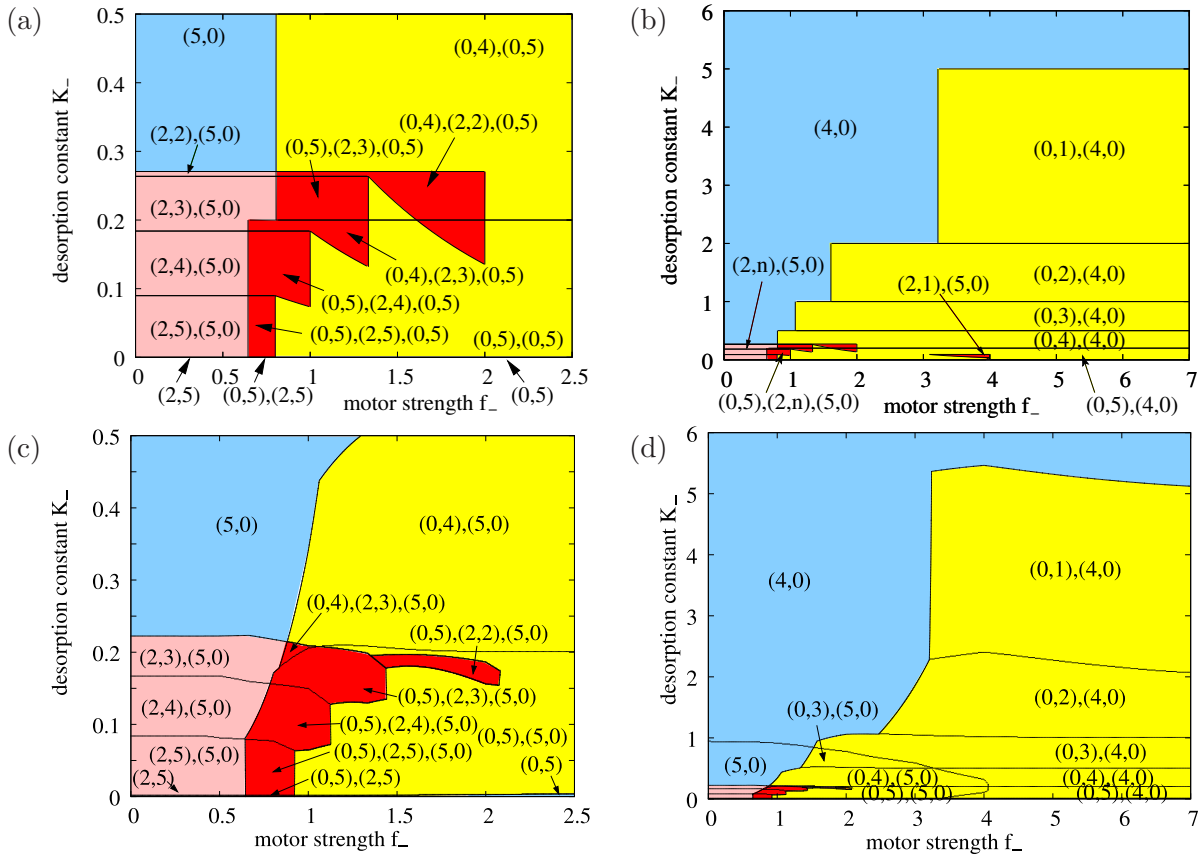

Fig. 4.22: Motility diagrams for the tug-of-war of 5 kinesin against 5 dynein-like motors: (a),(b) In the sharp maximum approximation, the transition lines for the maxima $(n_+, 0)$ and $(0, n_-)$ with only one motor type bound according to Eqs. (4.74) and (4.76) and (n_+, n_-) with both motor types bound according to Eq. (4.77) form the full motility diagram with the motility states (+) and (−) (light blue), (0) (green), (0+) and (−0) (pink), (−+) (yellow), and (−0+) (red). This motility diagram is very similar to the exact numeric motility diagram shown in (c),(d). Parameters are for kinesin and dynein as in Tab. 2.1 except for the minus motor stall force F_{s-} and unbinding rate ϵ_{0-} which are varied. In the sharp maximum approximation, the superstall velocity slope β_B is set to zero.

- **slow motion maximum**, $n_+ > 0$ and $n_- > 0$: In this case the conditions Eq. (4.70) can be rewritten as

$$K_- \quad < \quad \frac{N_- - n_- + 1}{n_-} \, \mathrm{e}^{2f_+/n_-} \qquad \text{for } f_- < \frac{n_+}{n_-} f_+ \tag{4.77}$$

$$K_- \quad > \quad \begin{cases} \frac{N_- - n_-}{n_- + 1} \, \mathrm{e}^{-2f_+/(n_-+1)} & \text{for} \quad f_- < \frac{n_+}{n_- + 1} f_+ \\ \frac{N_- - n_-}{n_- + 1} \, \mathrm{e}^{-f_-} & \text{for} \quad \frac{n_+}{n_- + 1} f_+ < f_- < \frac{n_+}{n_-} f_+ \end{cases} \tag{4.78}$$

  The point (N_+, N_-) needs special care with the result that there is never a maximum at this point.

Combining these results, we obtain the motility diagram shown in Fig. 4.22(a,b). It is very similar to the corresponding full numerical diagram shown just below in Fig. 4.22(c,d). However, the sharp maximum approximation overestimates regions with 2 or 3 maxima.

4.4.3.5 Discussion

The sharp maximum approximation is based on the simple idea that the probability is highly concentrated on single cargo states (n_+, n_-). It reproduces well the motility diagrams of the full numeric calculation both for the symmetric and the asymmetric tug-of-war as shown in

Figs. 4.21 and 4.22. The transition lines are described by four simple inequalities Eq. (4.70). These inequalities can thus be used to estimate the motility state of a given experimental system without having to resort to numerics or simulations.

Furthermore the inequalities Eq. (4.70) show that a transition between motility states occurs when the rates for binding and unbinding of a single motor in a maximum state (n_+, n_-) become comparable. This gives an indication for the range of biologically relevant motor parameters. On first sight a motor with a high affinity to the filament, i.e. with $\pi_0 \gg \epsilon_0$ seems to be favourable for motor transport. However, if a motor is to be used for bidirectional transport, its unbinding rate should be roughly of the same order of magnitude as its unbinding rate, i.e. $\epsilon_0 \sim \pi_0$. Only in this case bidirectional motion and regulation of bidirectional motion is possible. Biological motors involved in bidirectional transport like kinesin 1 and cytoplasmic dynein do indeed fulfill this requirement, compare Tab. 2.1.

4.4.4 Summary and discussion

We have investigated the motility behaviour of the tug-of-war model in various approximations.

We have obtained analytic solutions in the limits of small and large motor force ratios $f = F_s/F_d$. For small motor force ratios, the system only exhibits the non-cooperative (0) motility state with almost no motion, while for large motor force ratios the system is in the highly cooperative $(-+)$ motility state with stochastic switching between fast plus and minus motion. In the latter case, the cargo random walk on the two-dimensional state space of active plus and minus motors is approximated by a one-dimensional walk, see Fig. 4.14. A high stall to detachment force ratio f is thus necessary for fast bidirectional transport and is realized for biological motors such as kinesin 1, for which the large force approximation often works well.

In mean field approximation, the motility states are characterized by fixed points instead of maxima of the probability distribution, and the transitions between different motility states become bifurcations. Although mean field theory captures all qualitative features of the model, see Fig. 4.18, in particular all motility states, it does not exhibit stochastic switching, which is a prominent feature of bidirectional cellular transport. Furthermore, the bifurcation lines show the correct qualitative but not quantitative dependence on the motor parameters.

Finally, we have used the sharp maximum approximation to give a simple and intuitive approximation of the locations of these transition lines in the stochastic regime of small motor numbers. This approximation reproduces the complex tug-of-war motility diagrams quantitatively, see Fig. 4.22. It can therefore be used to determine the motility state of a given experimental system without having to do simulations or numerical calculations. In addition, the sharp maximum approximation shows that the transitions between the motility states are determined by the motor binding/unbinding dynamics under force.

4.5 Dynamic properties of the tug-of-war

In this section we investigate dynamic properties of the tug-of-war model. In Secs. 4.5.1–4.5.4 we consider cargo velocities, and run, switch and unbinding times, and their dependence on the motor parameters. In Sec. 4.5.5 and 4.5.6 we investigate the effects of external and frictional forces.

4.5.1 Run and switch times in the symmetric tug-of-war

Run times and lengths related to motion in one direction without pauses, and switch times and lengths arising from motion in one direction including pauses as defined in Sec. 4.3.2 are easily accessible experimentally. In this section we investigate the dependencies of these quantities on the single motor parameters. This mimics cellular regulation, and is also accessible to *in vitro* experiments. Since the run and switch lengths show the same qualitative behaviour as the

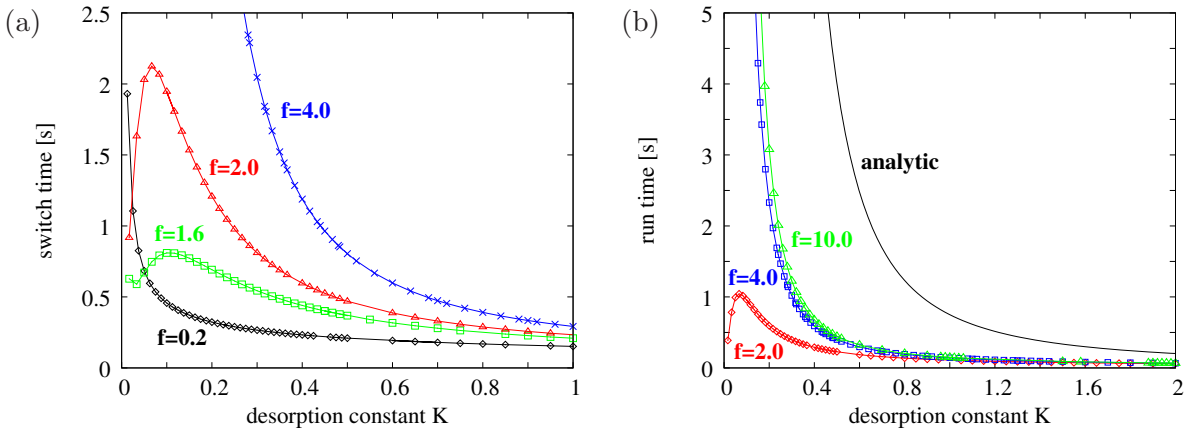

Fig. 4.23: (a) Switch times and (b) run times for the symmetric tug-of-war with $N_+ = N_- = 4$ as a function of the desorption constant $K = \epsilon_0/\pi_0$ for different force ratios $f = F_s/F_d$. All other motor parameters are kinesin-like. (a) The switch times decrease with K unless when passing the $(-0+)$ region, compare the motility diagram in Fig. A.6(e), where they display a peak. (b) The run times are approximately half as large as the switch times, compare (a) and (b), and otherwise show the same behaviour. The analytic approximation of Eq. (4.43) (black line) for large motor strengths f overestimates the run times, but reproduces the decrease with K.

corresponding times, we will only discuss the run and switch times. In this section, we consider the dependence of the run and switch times on the single motor parameters and illustrate this for the symmetric tug-of-war of 4 against 4 kinesin-like motors.

Dependence on the desorption constant. Motors with high desorption constant $K = \epsilon_0/\pi_0$ drop off from the filament easily. Therefore opposing motors are likely to take over, and run and switch times are short. Indeed, the run and switch times decrease with the desorption constant $K = \epsilon_0/\pi_0$, see Fig. 4.23. This is in qualitative agreement with the Eq. (4.43) from the large force approximation of Sec. 4.4.1.2, see Fig. 4.23(b). However, the approximation overestimates the switch times because it neglects all paths for switching which are not on the predominant one-dimensional path see Sec. 4.4.1.2. For small K, the switch times diverge as then all probability is concentrated on the state (N, N) with a maximal number of bound plus and minus motors and no motion occurs. There is however, an exception to the decrease of the run and switch times with K, when transitions between motility states are passed. As shown in Fig. 4.23, the run and switch times show a peak in the $(-0+)$ region. The run and switch times can therefore be used as an indicator for the transition between different motility states.

Dependence on the motor strength. The run and switch times increase with the motor strength $f = F_s/F_d$, see Fig. 4.24(a) because for large motor forces, losing motors can hardly gain a foothold against the winning motors: they rip off easily under the high load forces because of the exponential increase of the unbinding rate given by Eq. (2.1). This general behaviour is, again, violated when a transition line between motility states is passed, though the corresponding dip in the switch times in Fig. 4.24(a) is not very pronounced.

Pauses. For small motor force ratios f, the cargo is in the pause dominated (0) motility state. Nevertheless, pause times are rather short, see Fig. 4.24(b). They decrease even further when f is increased. Since that the pausing states of the symmetric tug-of-war form a disconnected set of states (n, n), each (un)binding of a motor on a pausing cargo leads to (at least slow) motion of the cargo and, thus, ends the pause. Because of the small pausing times, the switch times for the symmetric tug-of-war are approximately twice as large as the run times, compare Fig. 4.23(a) and (b), in agreement with Eq. (4.30).

Spontaneous symmetry breaking. The symmetric tug-of-war is symmetric with respect to plus and minus motors, i.e. exchanging plus and minus motor parameters leaves the Master equation 4.1 invariant. The appearance of two non-symmetric maxima in the $(-+)$ motility state is reminiscent of spontaneous symmetry breaking in continuous phase transitions in

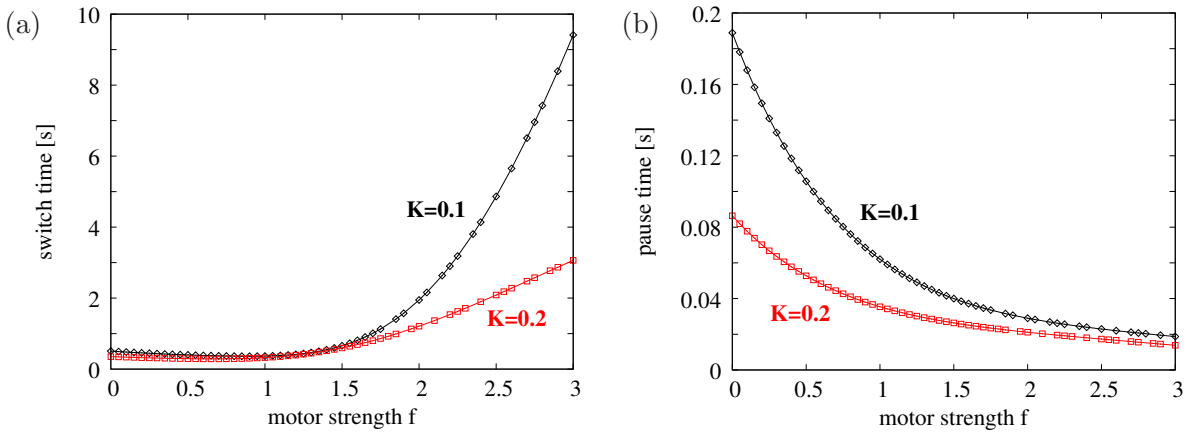

Fig. 4.24: (a) Switch times and (b) pause times for the symmetric tug-of-war with $N_+ = N_- = 4$ as a function of the motor strength $f = F_s/F_d$ for different desorption constants $K = \epsilon_0/\pi_0$. All other motor parameters are kinesin-like. (a) The switch times increase with f, expect for a small dip near $f = 1$, where the transition from the (0) to the $(-+)$ region via the $(-0+)$ region occurs. (b) The pause times are generally small and decrease with f.

statistical physics, as e.g. in the Ising model: two non-symmetric states, the $(+)$ and the $(-)$ maximum, appear and only together fulfill the symmetry of interchanging plus and minus motors. Indeed, the transitions between the motility states become bifurcations in mean field theory, see Sec. 4.4.2. Furthermore, the times for switching between the two maxima increase exponentially with the motor number N, see Fig. 4.25(a), as predicted by the large force approximation Eq. (4.43). This indicates that for large N the transition between the two fast-motion maxima corresponds to a nonequilibrium phase transition. This was also seen in the behaviour of the probability distribution, which approaches two delta-Peaks for large N, see Fig. 4.16. A similar behaviour has been found for non-processive motors in the framework of ratchet models [5].

Contrary to the run times in the $(-+)$ motility state, the run times in the no-motion motility state (0) decrease with increasing motor numbers N as $1/\sqrt{N}$, see Fig. 4.25(b) and Eq. (4.31). This decrease corresponds to the decrease of the width of the probability distribution around the single no-motion maximum, which scales as $1/\sqrt{N}$, see Eq. (4.28). The width and the run times reach zero for infinite N when the system is constrained to the no-motion maximum of the probability distribution, which then becomes a delta-distribution, see Fig. 4.13(a).

Summary. The run and switch times for biological motors numbers ($1 - 5$ motors of each species) and parameters are of the order of seconds, see inset of Fig. 4.25(a), as found in experiments. Their behaviour upon varying motor parameters could be used in *in vitro* experiments to detect transitions between motility states, see Fig. 4.23(a). The exponential increase of the switch time with the motor numbers indicates a dynamic phase transition.

4.5.2 Run and switch times in the kinesin-dynein tug-of-war

Cellular regulation may act by modifying the properties of the involved motors. In this section we discuss this aspect for the tug-of-war of kinesin 1 and cytoplasmic dynein, which is more relevant for *in vivo* transport than the symmetric tug-of-war considered in the last section. Dynein presents itself as the most prominent target for regulation, since it is very sensitive to regulatory and accessory proteins [98, 99]. We therefore consider how the minus motor parameters affect the transport properties such as switch times and velocities. Such a variation of motor properties does not only mimic cellular regulation but also the effect of mutation of the motor protein. Since we want to obtain experimentally relevant predictions, we use experimental values for the time resolution $\Delta t = 1/30\,\mathrm{s}$ and the velocity cutoff $v_{\mathrm{cut}} = 0.05\,\mu\mathrm{m/s}$, i.e. cargos with smaller velocities count as pausing, those with larger velocities as moving. This is crucial

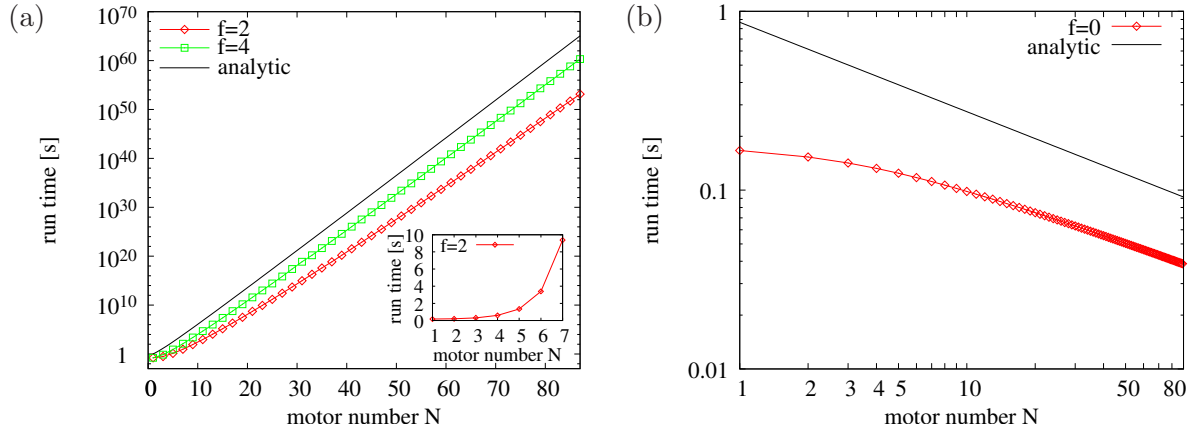

Fig. 4.25: Run times for the symmetric tug-of-war as function of the number $N = N_+ = N_-$ of motors on the cargo. The motors have kinesin-like parameters except the force ratios $f = F_s/F_d$ shown in the legends. (a) For high forces with $f = 2$ (red data) and $f = 4$ (green data), where the cargo is in the motility state $(-+)$, the run times increase exponentially with the motor number N for large N, as predicted by the large f approximation Eq. (4.46) (solid black line). For kinesin parameters and small motor numbers N, the run times are of the order of seconds (inset). (b) For zero stall force with $f = 0$, the run times (red data) decrease as $1/\sqrt{N}$ for large motor numbers N, as predicted by the large N approximation Eq. (4.31) (solid black line). The analytical approximations in (a) and (b) overestimate the run times but give the correct scaling behaviour for large N.

for the numerical values of switch times or velocities as discussed in App. A.5.1.[15]

Changing one parameter. We first investigate the effect of changing only a single minus motor parameter. This leads to enhancement of one direction, i.e. increased switch times and velocities, and impairment of the other direction, i.e. decreased switch times and velocities, see Figs. 4.26 and 4.27. In Figs. 4.26 and 4.27, the minus motors are put in a better position when (a),(d) their stall or detachment force is increased ('stronger' minus motors), (b) their unbinding rate is decreased or (e) their binding rate is increased ('more processive minus motors'), or (c) their forward velocity is increased ('faster minus motors'). All cases very intuitively lead to an increase in minus motor switch time and velocity and to a decrease in the plus switch times and velocities. When (f) the minus motor superstall slope is increased ('easily backing minus motors'), the minus motor switch time and velocity remain unaffected, but the plus switch time and velocity decrease. The reason for this at first sight counterintuitive result is that an easy backward motion of the minus motors leads to less load forces in cargo states where both motor species are bound to the filament. Therefore the losing minus motors do not unbind as fast, and the states with both motor species bound, which have reduced velocities, are more probable, see also Sec. 4.5.4.

Velocities vary only little. While the switch times are very sensitive to the change of the motor parameters and vary by factors of up to 10, see Fig. 4.26, the velocities change comparatively little, varying by less than 20 %, except for the case where the single motor velocity itself is changed. This is also observed in experiment, where cellular regulation usually affects switch times or lengths, but not the velocities, compare Sec. 5.1.

The velocities in Fig. 4.27 are always smaller than the maximal value of the single motor forward velocity, which is $v_{F+} = v_{F-} = 1\,\mu\text{m/s}$ except in (c). The reason is that short binding events of opposing motors remain undetected because of the finite time resolution and velocity cutoff and slow down the effective velocity. The velocity is, however, mostly rather close to this maximal value, which means that the tug-of-war does not reduce cargo motion substantially.

[15] Especially pauses are often buried in experimental noise. Furthermore, in *in vivo* experiments pauses may also be caused by obstacles or binding of the cargo to a cellular organelle etc. Pauses are therefore not a good quantity for comparing theory and experiment. For this reason we will not discuss pause times here. We will not discuss run times and run and switch lengths because they behave qualitatively similar to the discussed switch times.

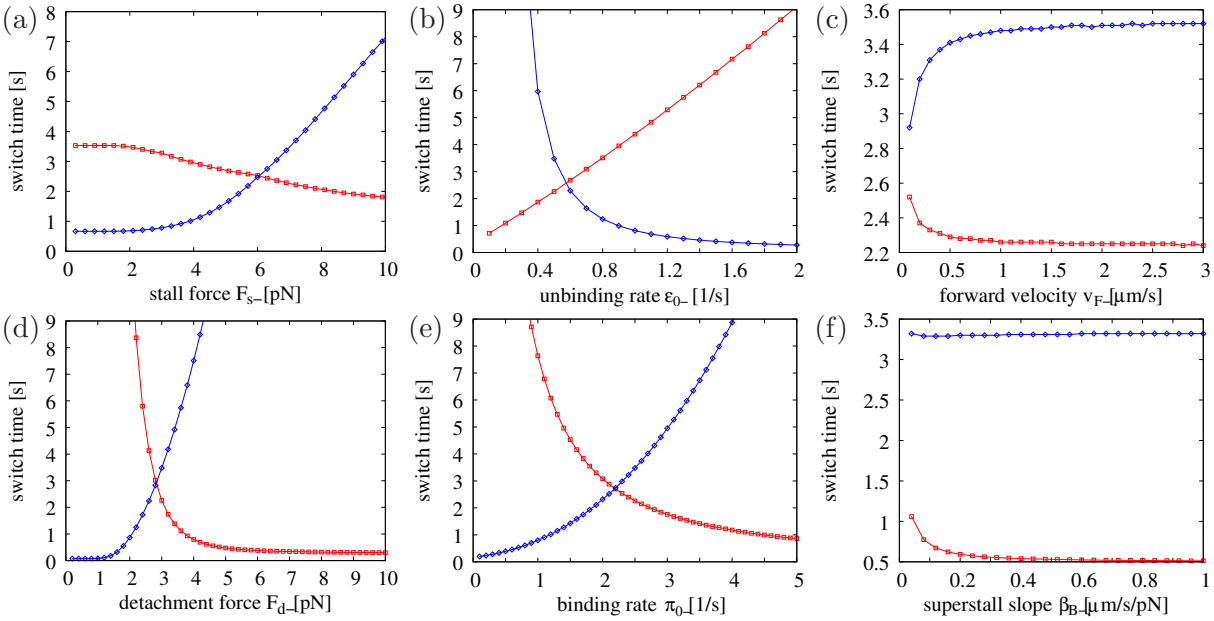

Fig. 4.26: Dependence of the plus switch time (red data) and minus switch time (blue data) on the minus motor parameters for the tug-of-war of 4 kinesins against 4 strong dyneins with parameters as in Tab. 2.1, except for the parameter that is varied.

Changing many parameters. The modification of only a single dynein parameter always leads to the intuitive effect of enhancing one and impairing the other direction. However, when more than one parameter is modified, the effect is difficult to anticipate intuitively, because the parameter changes can have competing comsequences. The net result can be (i) enhancement of one direction and impairment of the other, (ii) impairment of both directions, or (iii) enhancement of both directions. Fig. 4.28 illustrates this for the change of two dynein parameters, the unbinding rate ϵ_{0-} and the detachment force F_{d-}. Increasing only ϵ_{0-} increases the plus and decreases the minus switch time, while increasing only F_{d-} has the opposite effect.

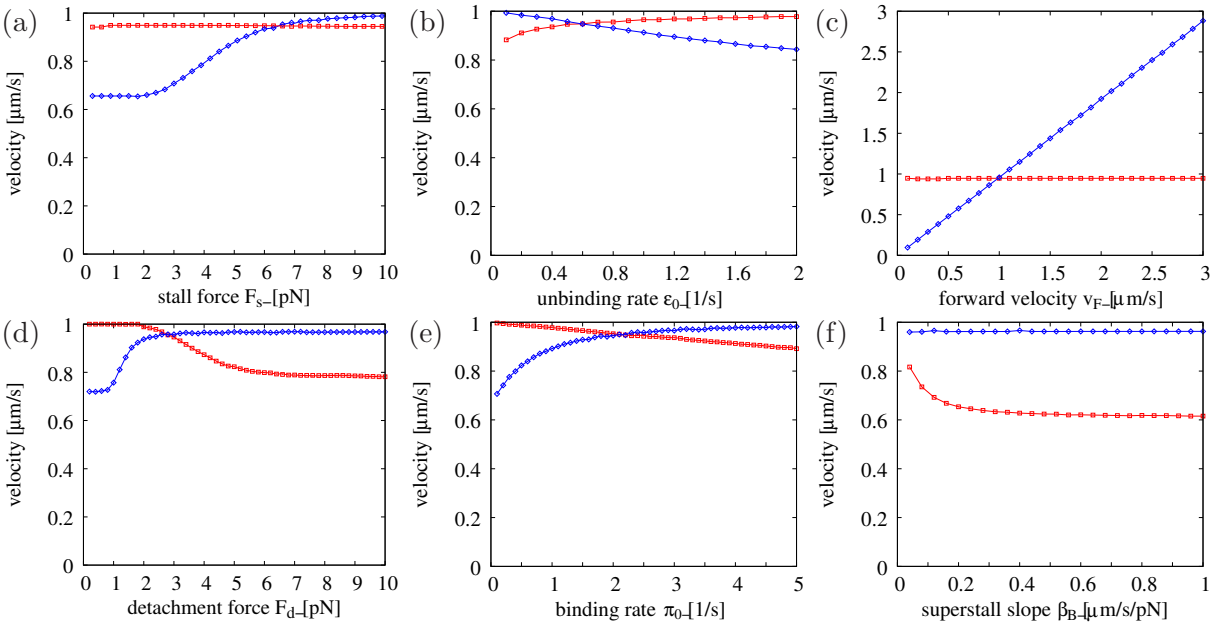

Fig. 4.27: Dependence of the plus run velocity (red data) and minus run velocity (blue data) on the minus motor parameters for the tug-of-war of 4 kinesins against 4 strong dyneins with parameters as in Tab. 2.1, except for the parameter that is varied.

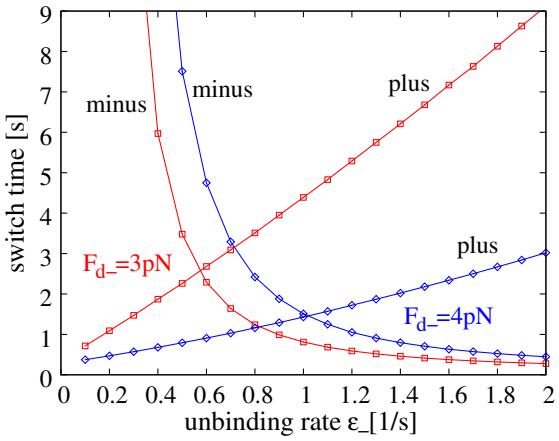

Fig. 4.28: Plus and minus switch times as a function of the minus motor unbinding rate ϵ_{0-} for different values of the detachment force F_{d-} (red: 3 pN, blue: 4 pN): When only ϵ_{0+} is increased, the plus switch time increases and the minus switch time decreases. However, when ϵ_{0-} is varied in the region $\epsilon_{0-} \sim$ 1.5-2 s^{-1}, this effect is noticeable only for the plus switch time. When ϵ_{0-} and F_{d-} are both changed, both switch times can decrease, e.g. when going from the intersection of the (red) $F_{d-} = 3$ pN lines to the intersection of the (blue) $F_{d-} = 4$ pN lines.

When both ϵ_{0-} and F_{d-} are increased, the net result can be a decrease of both the plus and minus switch time.

Effect on one direction may be weak. Although modification of motor parameters always affects both direction, the effect on one direction may be very weak. For example, changing the detachment force in the region $F_{d-} > 5$ pN in Fig. 4.26(d) affects only the minus switch times. Analogously, changing the unbinding rate in the region $\epsilon_{0-} > 1.5$ pN in Fig. 4.28 affects only the plus switch time.

Stall force variation. One might expect that varying the minus motor stall force F_{s-} produces jumps in the switch times every time the equation $F_{s-}n_- > F_{s+}n_+$ jumps to a different integer solution (n_+, n_-). This is not the case in Fig. 4.26(a) because of finite time resolution and velocity cutoff: only cargo motion with velocities slower than this velocity scores as a pause. For infinite time resolution with $\Delta t = 0$ s[16] and zero velocity cutoff, the jumps indeed appear, see Fig. 4.29(a). They are very pronounced in the plus run times because a plus run is terminated roughly when the minus motor pulling forces (proportional to the single minus motor stall force F_{s-}) become larger than the force needed to rip off the minus motors (which is related to the plus motor detachment force F_{d+}). They are not so pronounced for the minus runs because the termination of the minus runs is, analogously, roughly determined by the plus motor stall force F_{s+} and the minus motor detachment force F_{d-} and not by the minus motor stall force F_{s-}.

Changing the motor number. Another possibility to put the minus motors into a better position is to increase the number N_- of minus motors on the cargo, which, as expected, leads to an increase in the minus switch times and a decrease in the plus switch times, see Fig. 4.29(b).

Discussion. The dynamic properties of the kinesin-dynein tug-of-war reproduce various experimental observations. The switch times in the kinesin-dynein tug-of-war are of the order of seconds, and the cargo velocities of the order of the single motor velocities, see Figs. 4.26 and 4.27. We mimicked the effect of cellular regulation or of mutation of a motor protein by varying the single motor parameters. This affects switch times more strongly than velocities, which change only within less than 10 %. When only one motor parameter is varied, motion in one direction is enhanced and motion in the other direction is impaired. The effect of modifications of more than one motor parameter, as should be the typical case in cellular regulation or upon mutating a motor protein, is hard to anticipate intuitively and can lead to various scenarios: (i) motion is affected only in one direction, (ii) motion is impaired in one direction and enhanced in the other, and (iii) motion is enhanced or impaired in both directions. This variability agrees with experimental observations where all three scenarios have been observed, see Sec. 5.1.

4.5.3 Processivity enhancement: cargo unbinding times

In our tug-of-war model, we neglect unbinding of the cargo from the filament, as is usually also done in experiments, see the discussion in Sec. 4.2.4. This is justified due to the fact that

[16] Infinite time resolution is possible numerically because of the Gillespie algorithm which works with the waiting time for the next event.

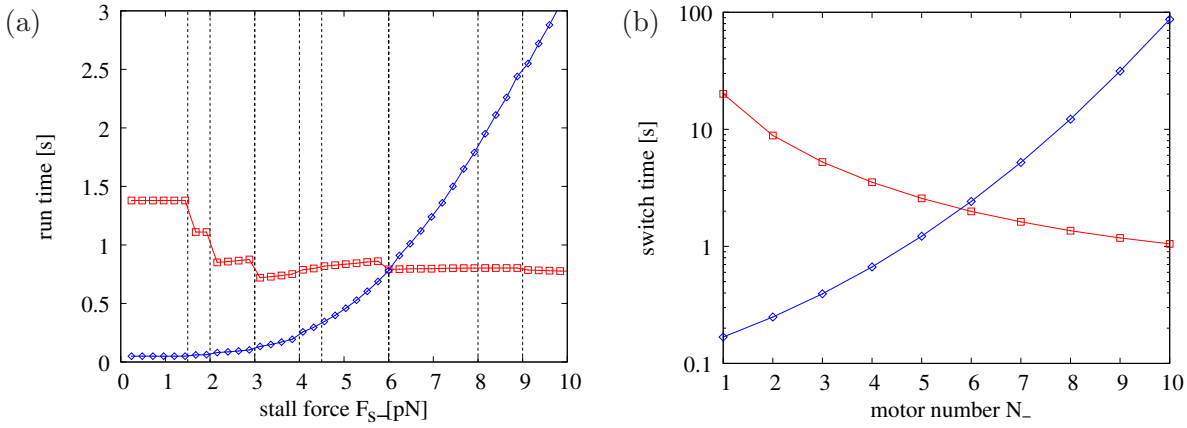

Fig. 4.29: (a) The plus (red) and minus (blue) run times for the tug-of-war of 4 kinesins and 4 dyneins (except the varied minus motor stall force F_{s-}) with time resolution $\Delta t = 0\,\mathrm{s}$ and zero velocity cutoff $v_{\mathrm{cut}} = 0\,\mu\mathrm{m/s}$ show jumps every time the change in minus motor stall force F_{s-} produces a jump in the integer solution (n_+, n_-) of the inequality $n_+ F_{s+} > n_- F_{s-}$. (b) Plus (red) and minus (blue) switch times for the tug-of-war of 4 kinesins and N_- strong dyneins.

cargo unbinding is a rare event: *In vivo* cargos are often monitored for several minutes without unbinding from their tracks. In this section we will quantify cargo unbinding in our tug-of-war model and see that it is indeed rare for biologically relevant parameters.

Two unbinding steps. The cargo unbinding occurs when the cargo (i) reaches the state $(n_+, n_-) = (0, 0)$ with no motors bound, and then (ii) diffuses away from the filament. We will consider both steps in this order.

Unbinding with one team of motors. The time to reach the state $(0, 0)$ is the first passage time from binding of the first until unbinding of the last motor; we call it the *unbinding time* Δt_{b}. When the cargo is transported by a single motor, the unbinding time is the run time of this motor. When there are several motors of the same type, e.g. N_+ plus and no minus motors on the cargo, this time increases roughly exponentially with the motor number [71]

$$\Delta t_{\mathrm{b}}^{+}(N_+) = \frac{1}{\pi_{0+} N_+} \left[(1 + 1/K_+)^{N_+} - 1 \right], \tag{4.79}$$

see Fig. 4.30(a). The reason is that when the cargo is attached to the filament by more than one motor, it stays tethered to the filament even when one motor unbinds, and subsequently this motor has the chance to rebind to the filament.

Unbinding with two teams of motors. If there are plus *and* minus motors on the cargo, the effect on the unbinding time is not obvious. There are more motors tethering the cargo to the filament, which should increase the unbinding time, but the motors perform a tug-of-war and therefore tend to pull each other off the filament, which should decrease the unbinding time. When a cargo binds to the filament spontaneously, it does so with a single motor. This motor is a plus motor with probability $w_+ = (N_+ \pi_{0+}) / (N_+ \pi_{0+} + N_- \pi_{0-})$ and a minus motor with probability $w_- = 1 - w_+$.

For large motor stall forces, the cargo walk can be approximated as a random walk on the one dimensional line $(n_+, 0)$ and $(0, n_-)$ with only one motor species bound as described in Sec. 4.4.1.2. In this approximation, the cargo unbinding time Δt_{b} is the mean return time T_0 to the state $0 \hat{=} (0, 0)$, minus the average time τ_0 spent in this state. Using the results of App. A.3.3 and Sec. 4.4.1.2, the unbinding time is:

$$\begin{aligned} \Delta t_{\mathrm{b}}(N_+, N_-) &= T_0 - \tau_0 = \frac{1}{(g_0 + r_0) p_0} - \frac{1}{(g_0 + r_0)} \\ &= \frac{1}{\pi_{0+} N_+ + \pi_{0-} N_-} \left[(1 + 1/K_+)^{N_+} + (1 + 1/K_-)^{N_-} - 2 \right] \end{aligned} \tag{4.80}$$

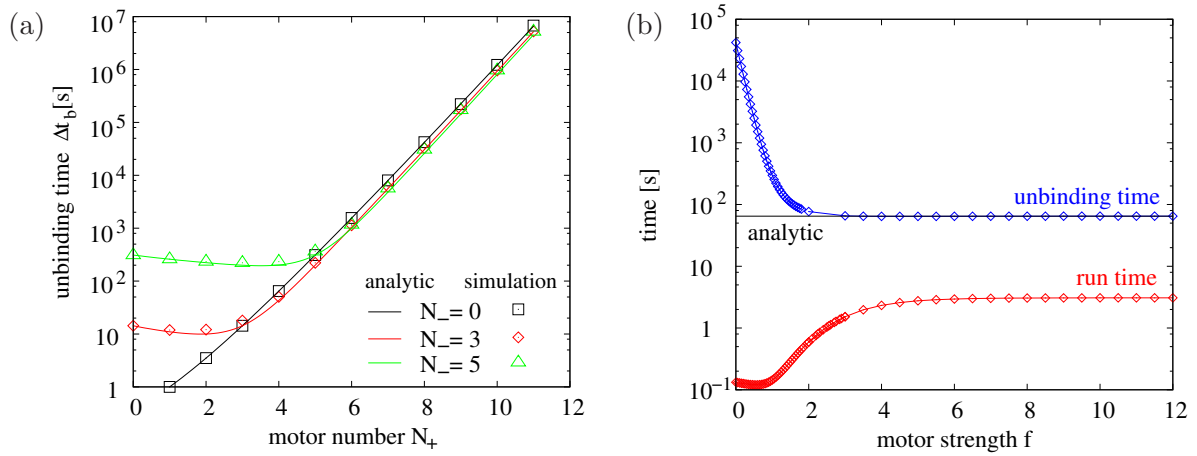

Fig. 4.30: (a) Average unbinding times Δt_b of a cargo with N_+ plus and N_- minus motors as a function of the number N_+ of plus motors on the cargo. All motors have kinesin-like parameters. For large motor numbers the unbinding times increase exponentially with the motor number N_+. The approximation Eq. (4.80) (solid lines) agrees well with the simulation results. (b) In the symmetric tug-of-war of 4 against 4 kinesins (except the varied motor strength f) the unbinding time (blue) decreases with the motor strength f, while the run time (red) increases with f, except a dip near $f \sim 1$ where a transition of motility states occurs. For large f, the analytical approximation Eq. (4.43) (solid black line) becomes accurate for the unbinding time.

which is equal to the weighted average of the unbinding times $\Delta t_\mathrm{b}^+(N_+)$ and $\Delta t_\mathrm{b}^-(N_-)$ of the restricted walks on $0 \le n_+ \le N_+$, and $0 \le n_- \le N_-$, respectively:

$$\Delta t_\mathrm{b}(N_+, N_-) = w_+ \, \Delta t_\mathrm{b}^+(N_+) + (1 - w_+) \, \Delta t_\mathrm{b}^-(N_-) \tag{4.81}$$

This is a good approximation for the unbinding times for kinesin-like motors, especially for high motor forces, see Fig. 4.30. The times from simulation are higher because of the additional available states (n_+, n_-) with plus *and* minus motors bound to the filament, in which the cargo also spends time bound to the filament but which have been neglected in the approximation. For large N_+ or N_-, the unbinding time Δt_b increases exponentially with the motor number, which can both be seen from Fig. 4.30(a) and Eq. (4.80). If one type of motor dominates, e.g. $N_+ \gg N_-$, one obtains approximately the single motor result for $N_- = 0$.

As follows from Eq. (4.81) and Fig. 4.30(a), the unbinding times for a cargo transported by N_+ plus and N_- minus motors are larger than for a cargo transported by only N_+ plus motors as long as $N_+ < N_-$. The reason is that for $N_+ < N_-$ the comparatively large number of minus motors leads to long minus runs without detaching. For $N_+ > N_-$, the minus motors are a 'nuisance' for the plus motors during the long plus runs and reduce the unbinding times.

These unbinding times are large compared to the run times of the tug-of-war, see Fig. 4.30(b). For example, a cargo carried by $N_+ = N_- = 4$ kinesin-like motors unbinds on average after 77 s, which is large compared to the run time of 0.59 s. The reason are the cargo states with both motor species bound. Via these states the cargo switches direction, but only reaching the state $(0, 0)$ leads to unbinding. The run times increase with the motor force f because for large f the opposing motors cannot easily gain a foothold due to the unbinding cascade described in Sec. 4.3.3. The unbinding times decrease with f because for large f, the states effectively available for the cargo are reduced to states with only one motor species bound.

Diffusion. Once the cargo reaches the state $(0, 0)$ with no motors bound, it only unbinds when it diffuses away from the filament before a motor rebinds to the filament. The average time for rebinding of a motor in the state is $1/(N_+\pi_{0+} + N_-\pi_{0-})$, which for a cargo with $N_+ = N_- = 4$ kinesin-like motors is equal to 0.025 s. This is to be compared to the time the cargo needs to diffuse away from the filament a distance of the order of the motor size $x = 100\,\mathrm{nm}$. For a cargo of about 1 μm size, this is only $x^2/2D \sim 0.01\,\mathrm{s}$ in water but $1 - 10\,\mathrm{s}$ in the cytoplasm, compare

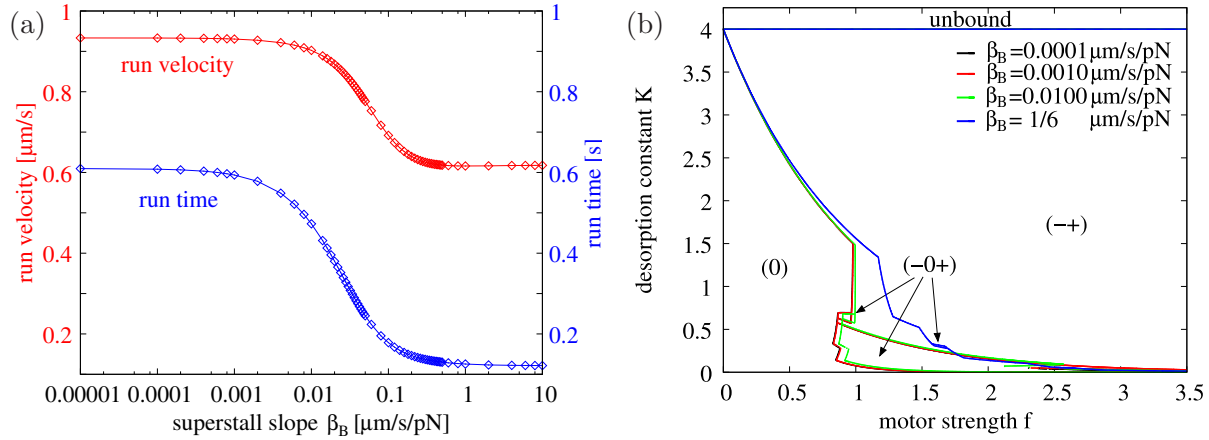

Fig. 4.31: (a) The effective velocity of a run (red data) and the average run time (blue data) of the symmetric tug-of-war of 4 against 4 motors decrease with increasing backward slope β_B, but are almost independent of the exact value of β_B for the biologically relevant range $\beta_B < 0.01\,\mu$m/s/pN. Motor parameters are kinesin-parameters (except β_B). (b) Motility diagram for the symmetric tug-of-war of 4 against 4 motors. Motor parameters are kinesin-like except the stall force F_s and unbinding rate ϵ_0, which are varied, and the superstall velocity slopes β_B which are as given in the legend. For small superstall slopes in the range of the kinesin ratio $\beta_B = 0.001\,\mu$m/s/pN, the motility diagram does not change very much with β_B (black, red and green lines; the black and red lines are almost indistinguishable). For large β_B (blue lines), the no-motion region (0) becomes larger, and the $(-0+)$ region almost disappears.

Sec. 1.1. Thus, in *in vitro* experiments, a cargo that reaches the state $(0,0)$ often diffuses away from the filament, while in the cell usually a motor rebinds to the filament before this happens.

Discussion. The unbinding times increase roughly exponentially with the number of involved motors and reach hundreds of seconds for motor numbers larger than 4, see Fig. 4.30. They are much larger than the run times, which characterize the time scale of bidirectional motion. Furthermore, a cargo in the state $(0,0)$ often rebinds with a motor to the filament before it diffuses away. In conclusion, the cargo processivity is dramatically enhanced when it is transported by many motors instead of one, even when the motors perform a tug-of-war. On the time scales of bidirectional motion, cargo unbinding can be neglected.

4.5.4 Influence of the backward velocity: to block or to follow

During the tug-of-war, the winning motors determine the cargo direction while the losing motors have to walk backwards and oppose cargo motion. The backward motion of the motors is determined by the backward velocity v_B or the slope $\beta_B = v_B/F_s$ in the superstall regime of the piecewise linear force-velocity relation, compare Fig. 2.2. If β_B is small, the motors walk backwards 'only reluctantly', i.e. they tend to walk backwards only under high load forces and only slowly; they block the motion of the forward moving motors very strongly. On the other hand, if β_B is large, the motors comply easily with the forward moving motors. Thus on first sight, it seems that a high β_B would enhance cargo motion, and that the low kinesin superstall slope $\beta_B = 0.001\,\mu$m/s/pN is unfavourable. This is however not the case, as shown in Fig. 4.31(a): For small slopes β_B, the effective velocity of a run (defined as the quotient of run length and run time) is higher than for large β_B. The same is true for the average run time.

The reason for this counter-intuitive behaviour is that motors with a high tendency to block motion (small β_B) cause a large cargo force when they actively pull on the cargo moving into the opposite direction. As the unbinding rate increases exponentially with the force, this high force triggers an unbinding cascade of the weaker (i.e. losing) motors until only the winning motor type is bound. This leads to the large cargo velocities in Fig. 4.31(a), which are as high as if only one motor species was present. Furthermore, because of the high load forces, opposing motors literally have difficulties to gain a foothold: they get ripped off fast. Therefore, once a motor

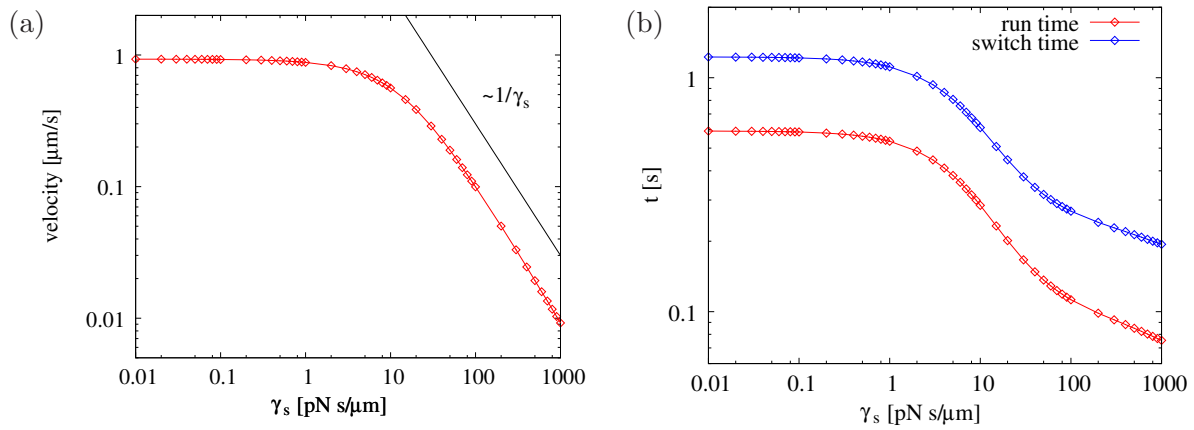

Fig. 4.32: With increasing Stokes friction γ_s, the average cargo velocities shown in (a) as well as the run and switch times shown in (b) are reduced in the symmetric tug-of-war of 4 against 4 kinesin-like motors. Note the double-logarithmic scale in both graphs. For large friction, the velocities in (a) decrease like $1/\gamma_s$, see Eq. (4.82).

species has won the tug-of-war, it determines the cargo direction for a long time, leading to the large run times in Fig. 4.31(a). In the opposite case of compliant motors with high velocity ratio β_B, the effect of the unbinding cascade is not so strong, leading to a high probability of states with both motor types bound, low velocities and fast switching. Increasing the slope β_B has similar effects to decreasing the stall force F_s: in both cases, the motors 'feel' each other less, which leads to less cooperative effects. This results in an increase of the (0) motility state region at the expense of the 'cooperative' motility states $(-+)$ and $(-0+)$, see Fig. 4.31(b).

Biological motors like kinesin with $\beta_B = 0.001\,\mu$m/s/pN have a low backward velocity, which is favourable for cargo motion. The exact value of the backward velocity in this range is not important, as seen in Fig. 4.31: As long as $\beta < 0.01\,\mu$m/s/pN, neither the velocities or switch times nor the motility states change.

4.5.5 Frictional forces: motion *in vivo*

The Stokes friction of a cargo of size $0.5\,\mu$m, such as an endosome or melanosome, $10^{-2}\,$pNs/μm in water, but $1-100\,$pNs/μm in the cell, compare Sec. 1.1. For a typical velocity of $1\,\mu$m/s, this leads to friction forces which are small compared to a typical motor stall force of $1-10\,$pN in water, but large in the cell. Here we assume that the friction coefficients measured for diffusion in the cytoplasm also apply to motor transport, which is, however, under debate [43]. In this section we investigate the influence of frictional forces on the motion of a cargo transported by two teams of opposing motors.

Effects of friction. Small friction up to $1\,$pNs/μm has little effects: it does not substantially change the cargo velocity or switch times in Fig. 4.32 nor the motility diagram in Fig. 4.33(a), nor the velocity distribution in Fig. 4.34(a,b). Therefore, in *in vitro* experiments with a typical friction coefficient of $10^{-2}\,$pNs/μm, friction effects are negligible. However, when friction becomes comparable to *in vivo* friction of $1-100\,$pNs/μm, it imposes a non-negligible load forces on the motors. Therefore, the average cargo velocity decreases, see Fig. 4.32(a). Furthermore, due to the increase of the unbinding rate with load force, motor unbinding is enhanced. Therefore, opposing motors can take over more easily, and the run and switch times decrease, see Fig. 4.32(b). Furthermore, cargo unbinding occurs for lower desorption constants K, see Fig. 4.33(a). However, *in vivo* friction has mostly quantitative and not qualitative effects: the motility diagrams for zero and $\sim 10\,$pNs/μm look very similar both for the symmetric tug-of-war shown in Fig. 4.33(a) and the asymmetric tug-of-war shown in Fig. 4.33(b).

Large friction expansion. For large friction, we expand the forces $F_\pm$ on a single plus

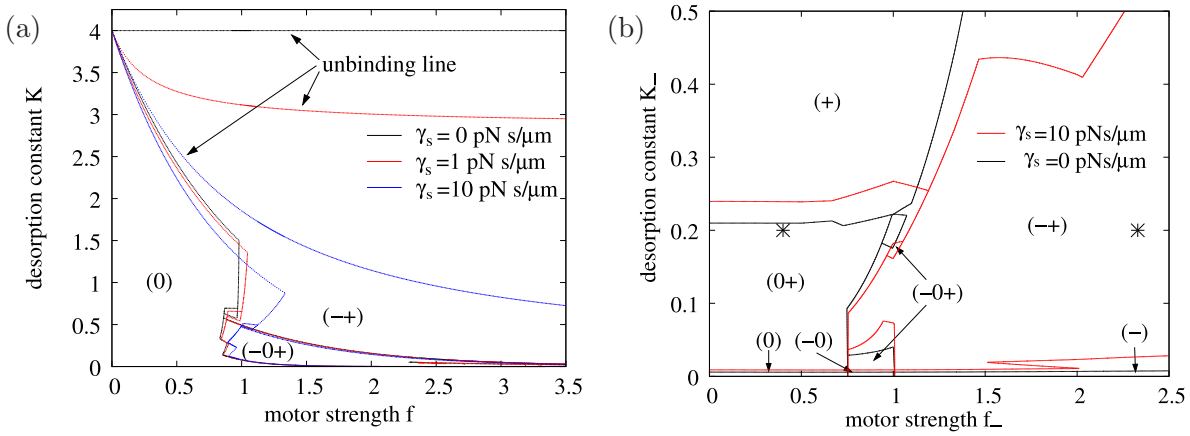

Fig. 4.33: Motility diagrams for the symmetric tug-of-war of 4 against 4 kinesin-like motors for various Stokes friction coefficients γ_S: (a) For small friction $\gamma_S \lesssim 1\,\mathrm{pNs}/\mu\mathrm{m}$, the motility diagram remains almost unchanged (black and red lines). *In vivo*-like large friction (blue lines) leads to an extension of the (0) motility state and to cargo unbinding for smaller desorption constants K. (b) Motility diagrams for the tug-of-war of $N_+ = N_- = 4$ kinesin-like plus against dynein-like minus motors for zero Stokes friction (black lines) and 'intracellular' Stokes friction of $10\,\mathrm{pNs}/\mu\mathrm{m}$ (red lines). Parameters are as in Tab. 2.1 except for the stall force F_{s-} and the detachment rate ϵ_- of the minus motors which are varied. The two asterisks at $f_- = 1.1\,\mathrm{pN}/3\,\mathrm{pN}$ and $f_- = 7\,\mathrm{pN}/3\,\mathrm{pN}$ correspond to weak and strong dyneins, respectively.

resp. minus motor and the cargo velocity from Eq. (4.16) in $1/\gamma_S$:

$$\begin{aligned} F_\pm(n_+,n_-) &= \mp F_{s\pm}\,\frac{n_\pm F_{s\pm}(1/v_{0-}+1/v_{0+})+\gamma_S}{n_+F_{s+}/v_{0+}+n_-F_{s-}/v_{0-}+\gamma_S} &&= F_{s\pm}\left[1+\mathcal{O}\left(\tfrac{1}{\gamma_S}\right)\right] \\ v_C(n_+,n_-) &= \frac{n_+F_{s+}-n_-F_{s-}}{n_+F_{s+}/v_{0+}+n_-F_{s-}/v_{0-}+\gamma_S} &&= \frac{n_+F_{s+}-n_-F_{s-}}{\gamma_S}\left[1+\mathcal{O}\left(\tfrac{1}{\gamma_S}\right)\right] \end{aligned} \tag{4.82}$$

To leading order in the large-friction expansion, the motor forces F_+ and F_- become independent of the number of motors bound to the filament and equal to the motor stall forces, $F_\pm = F_{s\pm}$. This means that the motors almost stall and the cargo moves only very slowly due to the high friction. It also means that the motors in a large-friction environment decouple; they always feel the same load force independent of the other motors. This leads to a suppression of the cooperative motility states $(-+)$ and $(-0+)$, see Fig. 4.33(a). Furthermore, it leads to an equilibrium-like behaviour as discussed in Sec. 4.4.1.1. The calculations of this section apply to the high friction limit if one replaces the off-rates of the equilibrium system with $F_{s+} = F_{s-} = 0$ by the off-rates of the high-friction system: $\epsilon_{0\pm} \to \epsilon_{0\pm}\exp\left[F_{s\pm}/F_{d\pm}\right]$. Unbinding in the symmetric tug-of-war therefore occurs at the line $K = N\exp(-f)$, which is a good approximation only for very large friction of the order of $\gamma_S = 1000\,\mathrm{pNs}/\mu\mathrm{m}$.

Velocity distribution. In the $(-+)$ and $(-0+)$ motility states, fast cargo motion occurs during periods in which only one motor species is active. In particular, when no friction is present and n_+ plus and no minus motors are active, the cargo moves with the single plus motor velocity v_{F+} independent of the value of n_+, see Eq. (4.7) and Fig. 4.34(a). When friction is present in such a cargo state, it acts as a load force on the motors. As the same-directional motors share the load force, a cargo with more active plus motors moves faster, and the cargo velocity depends on n_+. Therefore, the velocity distribution develops peaks which correspond to the states $(n_+, 0)$ resp. $(0, n_-)$ for the different values n_+ and n_- of active plus and minus motors, see Fig. 4.34. For very large frictional forces, these peaks are at n_+F_{s+}/γ_S, see Eq. (4.82), which is an integer multiple of F_{s+}/γ_S. Therefore the velocity distribution develops equidistant peaks for high friction, see Fig. 4.34(d).

This could be used to determine the stall force or the number of motors *in vivo*. This has indeed been done: Levi et al. [86] find equidistant peaks in the plus- and minus-end directed velocity distributions of bidirectionally moving *Xenopus* melanosomes. By fitting equidistant Gaussian peaks to the distribution, they determine the number of active motors

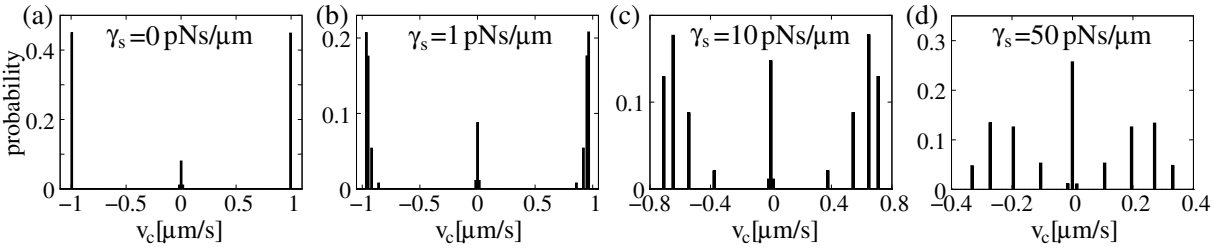

Fig. 4.34: Distributions of the cargo velocity v_C for the symmetric tug-of-war of 4 against 4 kinesin-like motors for various Stokes friction coefficients γ_S: (a) Without friction the cargo either moves with the single motor velocity $\pm 1\,\mu$m/s or pauses with ca. $0\,\mu$m/s. (b)-(d) With increasing friction, the peaks at $\pm 1\,\mu$m/s each separate into four peaks with lower velocity, which become equidistant for very large friction as in (d).

on the melanosome to be 1 to 4 dynein and 1 to 4 kinesin 2 motors. The distance between the peaks was found to be $\sim 0.25\,\mu$m/s both for dynein and kinesin. This fits to Eq. (4.82), which predicts a distance of F_s/γ_S, with the reasonable values $F_s = 5\,$pN for the stall force and $\gamma_S = 10\,$pNs/μm for the Stokes friction of the $0.5\,\mu$m-sized melanosomes.

Discussion. We have found that *in vitro* friction forces have negligible consequences, while *in vivo* friction has quantitative but not qualitative effects: e.g. the transition lines between the different motility states shift, while the type of motility states stays the same. Cargos unbind more easily, move at lower velocities and switch direction more often. The velocity distribution develops peaks which become equidistant for large friction. The number of these peaks indicates the number of involved motors and their distance the motor's stall forces. This could be used for motor number or stall force measurements *in vivo*.

4.5.6 External forces: cargo stall forces and hysteresis

In this section we investigate the cargo behaviour under an external force. Experimentally, this can be studied by using an optical trap as described in Sec. 1.3.

Assisting forces. An external force can exert an opposing or an assisting force on a motor. Unfortunately, the behaviour of a single motor under assisting force is not clear even for the best-studied motor kinesin 1: While Block et al. report a constant value equal to the zero-force velocity [9], Coppin et al. find a strong increase in velocity for assisting load forces [20], and Carter et al. find a broad scattering of velocity values [17], see Fig. 2.2(a). In Sec. 2.2.3 we have characterized the velocity under assisting load force by the assisted velocity v_A, for which we will use the the values $0.1\,\mu$m/s and $1\,\mu$m/s in this section.

Cargo stall forces. The velocity of a cargo under external force is given by Eq. (4.16). When the external force is opposing the winning motors, the velocity is zero when the external force equals the cargo stall force

$$F_{s,\mathrm{C}}(n_+, n_-) = n_+ F_{s+} - n_- F_{s-}, \tag{4.83}$$

as is intuitively expected.[17] When the cargo is in the $(-+)$ motility state of fast plus and minus motion, the cargo spends most of its time in states with only one motor type bound. In this case the stall force is $F_{s+}n_+$ during plus and $F_{s-}n_-$ during minus motion and thus an integer multiple of the single motor stall forces. Such a behaviour of the cargo stall force has indeed been found in *in vivo* measurements of the stall force of the bidirectionally moving lipid-droplets in *Drosophila* embryos [176]. In these experiments, the stall force was measured and found to be 3, 4 or 5 times 1.1 pN for both the plus and minus end directed transport in phase I, III and II of the embryonic development, respectively. The authors interpreted this as the stall forces of a cargo transported by 3, 4 or 5 plus resp. minus motors, where the number of motors varies

[17] The external force acts as load force on the plus motors; therefore $\nu_{FA+} = 1$ in Eq. (4.83), see Eq. (4.17). Eq. (4.83) assumes that the stall force measurement is 'fast enough' in order not to disturb the cargo state (n_+, n_-).

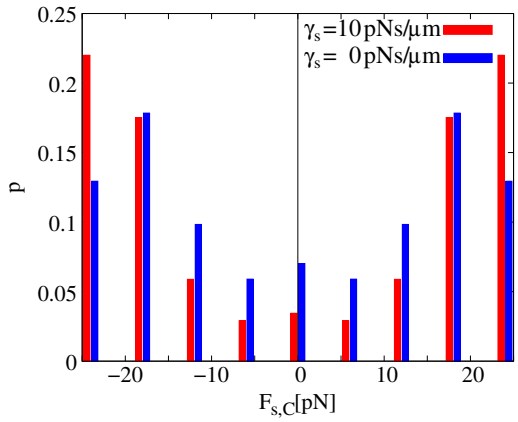

Fig. 4.35: Symmetric tug-of-war of 4 against 4 kinesin-like motors under external force. The distribution p of the cargo stall force $F_{s,\mathrm{C}}$ for zero Stokes friction $\gamma_\mathrm{S} = 0\,\mathrm{pNs}/\mu\mathrm{m}$ (red) and *in vivo* Stokes friction $\gamma_\mathrm{S} = 10\,\mathrm{pNs}/\mu\mathrm{m}$ (blue) exhibits equidistant peaks at integer multiples of the single motor stall forces $F_s = 6\,\mathrm{pN}$.

with the embryonic phase.

However, the stall force of the cargo does not have a well defined value but rather has a distribution corresponding to the number of motors bound to the cargo, see Eq. (4.83). If the stall forces of the plus and minus motors have the same value, as for the symmetric tug-of-war and as for the transport of *Drosophila* lipid droplets mentioned above, it displays equidistant peaks with a distance of the stall force F_s, see Fig. 4.35. This could be easily tested in experiments or be used in order to measure the *in vivo* stall force of the involved motors.

Hysteresis. If the external force is varied in time, the tug-of-war system shows hysteresis effects, see Fig. 4.36. If the external force has a large negative value (compared to the minus motor forces), this large assisting force for the plus motors makes the plus motors 'win' the tug-of-war. The cargo therefore moves into the plus direction with the velocity of the n_+ plus motors under assisting force F_ext (which is shared by the n_+ plus motors):

$$v_C(F_\mathrm{ext}) = v_F - v_A \frac{F_\mathrm{ext}}{n_+ F_s}, \tag{4.84}$$

see Eq. (4.16) with $\gamma_\mathrm{S} = 0$. If the force is now increased from this negative value to zero and then to positive values, it finally assists the minus motors strongly so that they will take over and make the cargo move into the minus direction. If the change rate of the external force is fast enough, this leads to hysteresis effects. The cargo will not switch direction when the external force reaches zero, $F_\mathrm{ext} = 0$, but slightly later, see Fig. 4.36(a), because the takeover from plus to minus motors takes some time. In the same way, when reducing the external force from large positive to large negative values, the directional switch from net minus to net plus motion does not occur for zero external force but for negative force. This leads to a hysteresis loop in the cargo velocity, see Fig. 4.36(a). This loop becomes smaller when the force change rate is reduced, see Fig. 4.36(b), because then the number of active motors can adjust to the external force. The loop vanishes for infinitely slow force change, i.e. for constant external force at each force value. The assisting velocity parameter v_A determines the cargo velocity in the range of large external forces but does not change the hysteresis loop, compare Fig. 4.36(a).

Discussion. We have found that the cargo stall force of a cargo in the $(-+)$ motility regime has a distribution with peaks at integer multiples of the single motor stall forces. This could be used to determine *in vivo* the number of involved motors and their stall forces. Furthermore the cargo velocity shows hysteretic behaviour when the external force is varied with appropriate speed. Hysteretic behaviour is intimately linked to dynamic instabilities and anomalous force-velocity relations in nonlinear dynamical systems [79, 167] and could be easily observed in an experiment conducted with an optical trap.

4.5.7 Summary and discussion

In this section we investigated the dynamic properties of the tug-of-war. Our results indicate that a tug-of-war is favourable for bidirectional cellular transport.

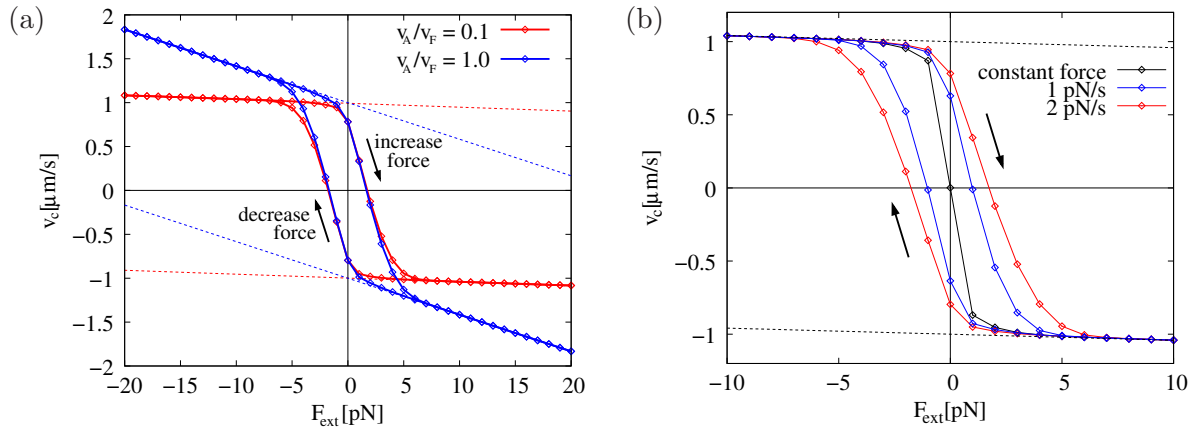

Fig. 4.36: Trajectory-averaged velocity v_C of a cargo transported by 4 plus and 4 minus motors with kinesin-like parameters as a function of external force F_{ext}: (a) When F_{ext} is increased at a rate of 2 pN/s from from −20 pN to +20 pN and then back to −20 pN, the velocity shows a hysteresis loop. For external forces with large absolute values, the velocities follow the limiting curves Eq. (4.84) (dotted lines) with $v_A = 0.1\,\mu$m/s (red) resp. $v_A = 0.1\,\mu$m/s (blue), and with $n_+ = 4$ which is the location maximum of the maximum of $p(n_+, n_-)$ for the used parameters. The value of the assisting velocity changes these large-force velocities but not the hysteresis loop. (b) The hysteresis loop becomes smaller for slower changes of the external force, compare the red data with a change rate of 2 pN/s to the blue data with 1 pN/s. The loop vanishes when the system is allowed to reach the stationary state, as shown by the black data with constant force F_{ext} for each data point.

The run and switch times are very sensitive to the single motor parameters. They decrease with the motor desorption constant K and increase with the motor force ratio f. For biological parameter ranges, they are of the order of seconds. This can be used by the cell to regulate its transport on a second time scale by finetuning the motor properties. The switch times increase roughly exponentially with the motor number, see Fig. 4.25, in agreement with the large force approximation of Sec. 4.4.1.2. The exponential increase indicates a dynamic phase transition for large motor numbers. The cargo unbinding times also increase exponentially with the number of involved motors. Thus, even though the motors are engaged in a tug-of-war, the processivity of a cargo transported by even a few motors can be sufficient to travel through the whole cell without unbinding. The tug-of-war exhibits fast cargo motion, which is, against intuition, partly due to the small backward velocity of biological motors. Thus, biological motors seem to have optimized their filament affinity $K = \epsilon_0/\pi_0$, force ratio $f = F_s/F_d$ and backward velocity in order to allow for efficient and regulable bidirectional transport.

For the biologically relevant tug-of-war of a few kinesins and a few dyneins, the switch times are of the order of seconds, and the cargo velocities are of the order of the single motor velocities, as in experiments. Changing the motor parameters affects the switch times strongly, whereas the velocities remain mostly unaffected, see Figs. 4.26 and 4.27. This is also often observed in experiments with cellular regulation or mutations of the motor proteins, which are mimicked by these parameter changes. Regulation and mutation should usually affect several motor properties. In our model, this can have various effects on cargo motion: (i) motion is affected only in one direction, (ii) motion is impaired in one direction and enhanced in the other, and (iii) motion is enhanced or impaired in both directions. This variability agrees with experimental observations where all three scenarios have been observed, see Sec. 5.1.

Finally, we investigated the influence of frictional and external forces. While *in vitro* frictional forces of motion in aqueous solution have negligible effects, large frictional forces in the cell can lead to slower velocities and faster directional switching. As shown in Fig. 4.34, the velocity distribution develops peaks, whose number indicates the number of involved motors and whose distance is related to the motor stall forces. This could be used for motor number or stall force measurements *in vivo*. External forces lead to peaks in the stall force distribution which could be

used for the same purpose. Furthermore, they lead to interesting hysteresis effects, see Fig. 4.36.

4.6 Summary

In this chapter we have introduced and investigated a model for bidirectional cargo transport based on a tug-of-war between plus and minus motors governed by mechanical interactions only. It incorporates in a straightforward and simple way the load-dependent transport parameters of motors as measured in single-molecule experiments and as described in Chap. 2. We have characterized the motility states of this tug-of-war model, and investigated their transport behaviour in numerical simulations and various analytic approximations. We have investigated both the symmetric tug-of-war of two teams of motors with identical properties except their forward directions, and the asymmetric tug-of-war, which comprises the biologically relevant transport by a team of kinesin 1 and a team of cytoplasmic dynein motors.

Motility states. In our model, the cargo is pulled by a stochastically fluctuating number of plus and minus motors, see Fig. 4.3. Cargo motion is dominated by states with high probability, which are either states with both types of motors active as in Fig. 4.2(0), corresponding to almost no motion, or states with only one type of motors active as in Fig. 4.2(+) and (−), corresponding to fast plus or fast minus motion. Depending on the number and properties of motors attached to the cargo, the cargo switches stochastically between either 1, 2 or 3 of these high-probability states. This leads to the seven motility states (+), (−), (0), (−+), (0+), (−0) and (−0+). They are characterized by distinct cargo trajectories, velocity distributions, and run time distributions. We have obtained a complete classification of these motility states for the symmetric tug-of-war, see Figs. 4.6 and 4.7, and for the asymmetric tug-of-war, see Figs. 4.9–4.11. In particular, the model exhibits the motility states (−+) and (−0+) of fast bidirectional motion without and with pauses, respectively, which are characteristic for experimental bidirectional transport. The somewhat surprising existence of fast plus and minus motion in our tug-of-war model is caused by a dynamic instability arising from the strongly nonlinear force-dependence of the single-motor unbinding rate. This instability, which takes place when the motor stall forces become larger than their detachment forces, leads to only plus or only minus motors being active most of the time.

Motility diagrams and analytic approximations. Cellular regulation or mutation of the motor proteins is mimicked in our model by varying the parameters of the single motors. The dependence of the motility states on the single motor parameters is surprisingly complex as illustrated by the complex shapes of the motility diagrams e.g. in Fig. 4.11. However, it can be rationalized in various approximations. We obtained analytic solutions in the limiting cases of weak motors, in which the cargo displays no motion (0), and strong motors, in which the cargo displays fast motion (+) or (−). In the latter case, the cargo random walk on the two-dimensional space of active plus and minus motors can be approximated by a one-dimensional walk, see Fig. 4.14. The full motility diagram also for intermediate motor strengths can be reproduced qualitatively in mean field approximation, where the probability maxima become fixed points and the transition between motility states become bifurcations, see Fig. 4.18. Finally, the sharp maximum approximation gives a good approximation for the motility diagrams, see Fig. 4.22, and thereby allows to estimate the motility state of an experimental system without resorting to numerical calculations. Furthermore, the sharp maximum approximation shows that the transition between motility states are determined by the balancing of rates for motor binding and unbinding.

Dynamics. The most prominent feature of bidirectional transport is the directional switching. The times between such directional switches are very sensitive to the single motor parameters, while cargo velocities are less affected, Figs. 4.26 and 4.27. The switch times show signatures of the transitions between motility states. When the motor number is increased, the switch times increase roughly exponentially, see Fig. 4.25, as predicted by the large force approximation as a 1D walk. The exponential increase indicates a dynamic phase transition for

large motor numbers. The unbinding times also increase exponentially with the motor numbers, so that cargos transported by two teams of motors can travel processively over long distances.

The parameters of biological motors employed in long-range cellular transport, such as kinesin 1 and cytoplasmic dynein, are well adapted to the requirements of bidirectional transport: A high stall to detachment force ratio and a small backward velocity allow for fast bidirectional motion, while the intermediate processivity is large enough for long unbinding times of many minutes and low enough for switching times of a few seconds.

Our model can be easily extended to include frictional and external forces. Friction may be important in the viscous cytoplasm. It leads to peaks in the velocity distribution, see Fig. 4.34, which can be used to estimate the number of involved motors or the motor stall forces *in vivo*. External forces, as e.g. applied by an optical trap, lead to hysteresis effects, see Fig. 4.36.

Experimental relevance. Our *tug-of-war model* exhibits many features that are observed in experiments, although many of these are usually attributed to a *coordination mechanism* as discussed in the introduction of this chapter. For biologically relevant parameter ranges, such as teams consisting of a few kinesin- and dynein-like motors, the cargo exhibits stochastic switching between **fast motion** into the plus and the minus direction on a time scale of seconds and a length scale of microns, sometimes interspersed with pauses. This behaviour emerges if the involved motors have high stall to detachment force ratios, high filament affinities and small backward velocities – features that are typical for many motors employed in cellular transport. A motor in our model is characterized by six transport parameters, the stall and detachment forces, the unbinding and binding rates, and the forward and backward velocities. *All* these parameters determine the net cargo direction, not only the motor forces, so that **stall forces can be balanced**, while nevertheless cargo transport may be biased towards either plus or minus direction.

We have mimicked cellular regulation, such as the action of **regulatory proteins**, and motor mutations in our model by changing the single motor parameters. We found that the motility behaviour of the cargo is very sensitive to such changes. Changing the motor stall force or filament affinity, for example, can lead to qualitatively different motility behaviour such as fast plus motion, no motion, or bidirectional transport. Even if the motility state is not changed, a change in transport characteristics, such as run times or velocities, can lead to a change in net cargo transport. The cell can use this sensitivity for efficient cellular regulation. In addition, we found that the response to regulatory or mutational perturbances could affect motion in plus and minus direction in various ways. We found cases for which (i) motion was affected only in one direction, (ii) motion was impaired in one direction and enhanced in the other, and (iii) motion was enhanced or impaired in both directions. This variable **interdependence of directions** agrees with experimental observations where different systems also exhibit widely varying reactions to regulation or mutation. In the next chapter, we will compare the results of our model and of experiments in qualitative and quantitative detail.

Chapter 5

Motor tug-of-war in experiments

In this chapter we discuss experiments concerning bidirectional cargo transport in the framework of the tug-of-war model of the last chapter. Unfortunately, for many experimental systems only a small amount of quantitative data is available. We will therefore first compare our model and the experimental results in a qualitative way. In particular, we will address the arguments raised against a tug-of-war scenario in Sec. 4.1.2. Then we will give a quantitative comparison for the *Drosophila* lipid-droplet transport and an *in vitro* kinesin-dynein motility assay.

5.1 Qualitative comparison to experiments

Many cellular cargos move bidirectionally, employing plus and minus motors in rapid succession during their travels along isopolar MT networks. In this chapter we review biological systems with bidirectional transport, and we explain the experimental observations within our tug-of-war model. In particular, we address the arguments raised against a tug-of-war scenario in Sec. 4.1.2.

5.1.1 Bidirectional transport in experiments

Mitochondria. In neuronal axons, mitochondria are present almost everywhere, but they accumulate at sites with high demand for ATP production [106]. Furthermore, their motion is regulated during axonal growth: they show net transport towards active growth cones, but become uniformly distributed in the axon when axonal growth ceases [18, 106, 124]. The change of net transport is achieved by modifying the plus run length [18, 106]. This modulation can be induced with nerve growth factor [18], and involves a pleckstrin homology domain [23]. Mitochondria in dendrites display submicroscopic shape changes during transport which can be interpreted as a result of motors pulling on them in opposite directions [34].

Melanosomes. In specialized pigment cells of fish and frog, melanosomes move bidirectionally along a radial MT array, pulled by kinesin 2 and dynein [133, 159]. They travel at velocities of $\sim 0.5\,\mu$m/s and change direction every $\sim 0.5\,\mu$m. Melanosome redistribution allows the organism to adapt its skin colour to the environment, see Fig. 1.4 in Sec. 1.4. During 'aggregation', minus end motion dominates, and the melanosomes accumulate in the cell centre. During 'dispersion', the melanosomes spread out in the cell due to an decrease in minus run length [42]. Aggregation and dispersion are triggered by hormonal stimulation, which is transmitted to the motors via a signal cascade involving cAMP and protein kinase A (PKA) [131, 158]. Run length distributions are roughly double exponential with the two length scales of ca. $0.1\,\mu$m and $1\,\mu$m [42]. Only the long length scale is altered from aggregation to dispersion. The velocity distribution displays four equidistant peaks which can be correlated with the number of pulling motors [86].

Inactivation of kinesin 2 leads to disruption of plus-end transport, and to increased minus run lengths [42]. Inhibition of dynein disrupts minus end transport and enhances plus-end transport [116]. Interference with the dynein accessory protein dynactin, which can interact both with dynein and kinesin 2, leads to impairment of transport in both plus and minus direction [24].

Besides travelling along MTs, melanosomes are also pulled along actin filaments by myosin 5, which is up-regulated during dispersion: While aggregating and dispersing melanosomes carry the same amount of kinesin 2 and dynein, dispersing melanosomes carry more myosin 5 than aggregating melanosomes [42]. Disruption of actomyosin transport leads to malfunction of dispersion: in frog melanophores it causes aggregation even in cells stimulated for dispersion, while it causes hyperdispersion in fish [132, 150].

Lipid-droplets. Lipid-droplets are storage organelles for neutral lipids. In early *Drosophila* embryos, they travel bidirectionally on an isopolar MT array in the embryo periphery at velocities of $0.5\,\mu$m/s, changing direction every few seconds and microns. Their transport is developmentally regulated: their motion changes from net plus end directed during the developmental 'phase II' to net minus end directed in 'phase III' by modulation of only the plus run length [44, 176]. Some proteins involved in this regulation, such as Halo, LDS2 and Klar, have been identified [41, 46, 175]. The stall forces of the droplets are of the same magnitude in plus and minus direction, independent of the net transport direction [176]. Similarly to melanosome transport, the run length distributions are double exponential functions with length scales of ca. $0.1\,\mu$m and $1\,\mu$m, and only the large length scale is varied from phase II to III. [44]. Pause time distributions are single exponential [44]. An interesting correlation between run length and velocity has been observed: long runs have higher velocities [44, 45]. Mutations in the motor dynein or in the dynein cofactor dynactin lead to impairment of both plus and minus end transport by reducing run lengths, velocities, and stall forces [45].

Endosomes. Endosomes move bidirectionally along MTs in various cell types with velocities of μm/s and directional changes every few seconds and microns [30, 110, 178], see e.g. the trajectory in Fig. 1.4(a). Inhibition of either kinesin, dynein or dynactin impairs both plus and minus end transport [164, 178]. Kinases and Rab proteins seem to play a role in regulating endosome motility [6, 178]. Endosomes have been reported to get stretched in opposite direction along MTs, sometimes even until fission, presumably by opposing motors [110].

Viruses. Many viruses hijack the cell's motor system for their own transport. Herpesvirus capsids, for example, move bidirectionally in axons at velocities of about $1\,\mu$m/s, changing direction every few microns [149, 95]. Infection occurs near the axon terminal and is followed by net minus-end transport to the nucleus (entry), where the virus establishes latent infection. Upon reactivation of the virus, it exhibits net plus-end transport from the cell body to the axon (egress). The change in net directions is obtained by increasing the average plus-end run length [149]. The velocity distribution displays two Gaussian peaks around the average plus and minus end velocity, respectively [149]. Adenovirus also moves bidirectionally at speeds $\sim \mu$m/s [154]. During entry, signal pathways acting through PKA and MAP kinases increase the velocity and frequency of minus motion and thus promote net minus motion towards the nucleus [153].

***In vitro* motility assay**. In an *in vitro* motility assay with kineins 1 and axonemal or cytoplasmic dynein an increase in kinesin density causes minus end motility to go over into bidirectional movement and finally into plus end motility [162].

5.1.2 Comparison of experiment and model results

In this section we explain the above experiments in the framework of our tug-of-war model. As for most experimental systems only a small amount of quantitative data is available, our discussion in this section remains largely qualitative.

All systems listed above exhibit fast plus and minus motion, sometimes interspersed with pauses. In our model, this corresponds to a cargo in the $(-+)$ or $(-0+)$ motility state. We will therefore assume in the following discussion that the cargo is in one of these states. Indeed, for the tug-of-war in bidirectionally relevant parameter ranges, such as for transport by one to five 'strong' motors of each species like kinesin 1 or 'strong' dynein, the cargo is often in the $(-+)$ or $(-0+)$ motility state, see Sec. 4.3 and Figs. 4.11 and 4.12. Cargos which travel unidirectionally, i.e. cargos in the $(+)$, $(-)$, $(0+)$ or (-0) motility states, are not addressed as 'bidirectional' by

experimenters, and it is typically not known whether they are transported by only one or by more than one motor type.

Fast cargo motion, time and length scales. Bidirectional transport in all systems described in the last section is characterized by fast bidirectional motion with velocities $\sim \mu$m/s, which is of the order of the velocities observed for single motors *in vitro*, see Sec. 2.2.3. This is also the case in our tug-of-war model which, contrary to what one might expect, reduces the single motor velocity only about 10 % in the motility state $(-+)$ of fast bidirectional motion, see Sec. 4.5.2. The reason is that because of a dynamic instability only one motor type is active most of the time, so that the motors seldomly hinder each other. Experimental cargos switch direction on time and length scales of seconds and microns. This corresponds to the switch times and lengths obtained in our model for biologically relevant parameters, see Sec. 4.5.2.

Regulation. Cellular traffic must be adjusted to internal or external stimuli, which may be as diverse as the need for ATP production for mitochondria in axons, developmental regulations for lipid-droplets in *Drosophila* embryos, or colour change of the organism's skin for melanosomes in *Xenopus* melanophores. Regulatory mechanisms may be similarly diverse and include the activity of hormones, regulatory proteins or kinases. This regulation could operate at two levels by: (i) controlling the properties of single motors, (ii) controlling how multiple motors work together. We propose that regulatory mechanisms target the motors directly and change their properties. In our model, regulation is therefore mimicked by a change of the single motor parameters such as the motor velocity, the stall force etc. Cellular regulation usually affects only the switch time and length of one direction and leaves all other transport characteristics (almost) unaltered, as for mitochondria [18, 106], melanosomes [42], lipid-droplets [44, 176] and viruses [149]. This also happens in the tug-of-war model when certain motor parameter changes are not too large, see Sec. 4.5.2, as is to be expected of cellular regulation. The effect of the parameter change then affects one direction much more than the other. Furthermore, velocities remain almost unaffected, as they change only within roughly 10 %.

Mutations. Mutations of the motor proteins affect transport usually in a more drastic way than cellular regulation. Often transport in the direction of the motor that has been mutated breaks down almost completely, while transport in the other direction is enhanced, as for various mutations in the melanosome system [24, 42, 116]. Some mutations impair transport in both directions, as for lipid-droplet [45] or endosomes [164, 178]. In our model, mutation is mimicked in the same way as regulation: by changing the motor parameters. The impairment of the mutated and the enhancement of the other direction is then an intuitive consequence of the tug-of-war scenario: the mutated motor has parameters which are less favourable than before, e.g. a lower stall or detachment force. Therefore, it can no longer sustain effective transport and can also not hinder the motion of the opposing motors, which leads to the impair/enhance scenario. The unintuitive effect of some mutations of impairing motion in both directions is obtained in our tug-of-war model when the mutation changes several motor parameters with competing effects on the motion. For example, if the mutation of the minus motor causes an increase of the minus motor unbinding rate and of its detachment force, the net effect is impairment of both directions, see Fig. 4.28 and the discussion of the lipid-droplet data in the next section.

Stall force balance. Cargo stall forces have been measured only in the lipid-droplet system. They were found equal in plus and minus direction, independent of the net transport direction of the droplets. This is also possible in our tug-of-war model, since other parameters than the motor forces also determine the cargo direction such as the motor's filament affinity or velocities. We will discuss this in quantitative detail in the next section.

Run length distribution. Run length distributions display a roughly double exponential shape in the lipid-droplet and the melanosome system [42, 44, 45]. Although in our model these distributions are multi-exponential, see Sec. 4.3.2, the distributions of run time or length can usually be well fitted by a double exponential function, see Sec. 4.3.3 and 4.3.4.

Velocity distribution. Experimental velocity distributions typically exhibit Gaussian peaks. In the simplest case, there are two Gaussian peaks centered at the plus and minus

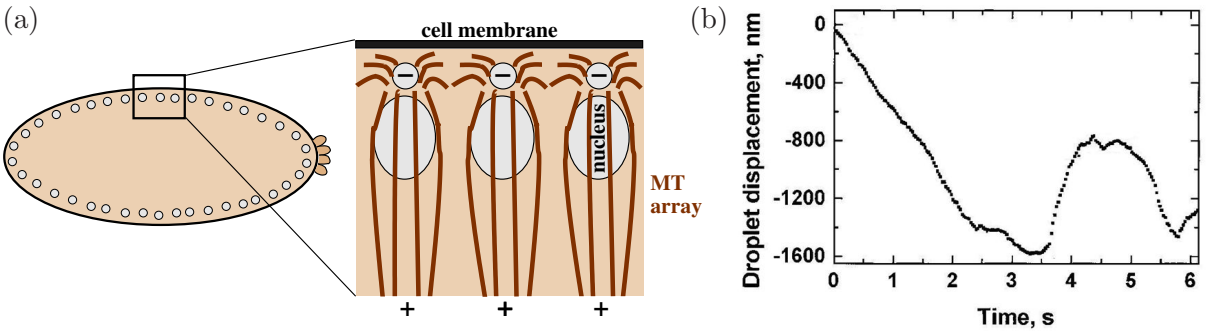

Fig. 5.1: Lipid-droplet transport in early *Drosophila* embryos: (a) The nuclei are arranged in a monolayer below the plasma membrane. The MTs radiate from the centrosomes directly above each of the nuclei and form an $\sim 40\,\mu$m isopolar array with their plus ends pointing inwards. (b) The trajectory of a lipid-droplet moving on this array exhibits motion into both directions. From [44].

velocities, as for viruses [149]. In the melanosome system, the velocity distribution displays four equidistant Gaussian peaks for each direction [86]. The first case is obtained in our tug-of-war model for low friction, and the second case for high friction, see Sec. 4.5.5, provided that the model velocity peaks are 'smeared out' by experimental noise to Gaussian peaks. That friction should be noticeable for melanosomes but not for viruses could be related to the inferior experimental resolution of the virus experiments, to the smallness of the $0.1\,\mu$m-sized viruses compared to the $0.5\,\mu$m-sized melanosomes, to differences of the cytoplasmic composition in the different cell types, or to different stall force values of the involved motor teams.

Correlation of run length and velocity. A correlation of run length and velocity was found for the *Drosophila* lipid-droplet system [44, 45]. This correlation is also present in the tug-of-war model, as we will discuss quantitatively in the next section.

Shape changes. Some cargos, such as mitochondria, peroxisomes and endosomes, display small changes in their size and shape during transport, which can be interpreted as a direct result of motors pulling on them in opposite directions [34, 110].

5.2 Bidirectional transport of *Drosophila* lipid-droplets

In this section we apply our tug-of-war model to the bidirectional movements of lipid-droplets in *Drosophila* embryos, which have been extensively studied in a series of experiments by [44, 45, 176]. We chose this particular experimental system because it is unique in providing an estimate for the number of motors on the cargo, a high number of quantitative measurements of transport characteristics including cargo force measurements, and observations in two different developmental phases and in three different dynein mutation backgrounds. A large amount of quantitative data is essential in order to allow for a quantitative comparison of our model with these data. Measurements of the cargo stall forces and in different backgrounds are necessary to address the objections against a tug-of-war model raised in Sec. 4.1.[1]

5.2.1 Transport of lipid-droplets in *Drosophila* embryos

***Drosophila* embryogenesis**. The fruit fly *Drosophila melanogaster* is a well-studied model system for genetics and embryogenesis because of its small size and short generation times. During early *Drosophila* embryogenesis, the first 13 nuclear division cycles occur synchronously and without cell division [31]. In the following interphase, which lasts between one and two hours, the cell membrane grows inwards and forms cells around each of the nuclei. The experimenters of

[1] The only other system for which a comparable amount of quantitative experimental data has been obtained is the melanosome system. However, this system is more complex because it involves transport by the actin motor myosin in addition to the MT motors kinesin and dynein. There are data without acto-myosin transport, but not as many as for the lipid-droplet system, and stall force measurements have not been reported.

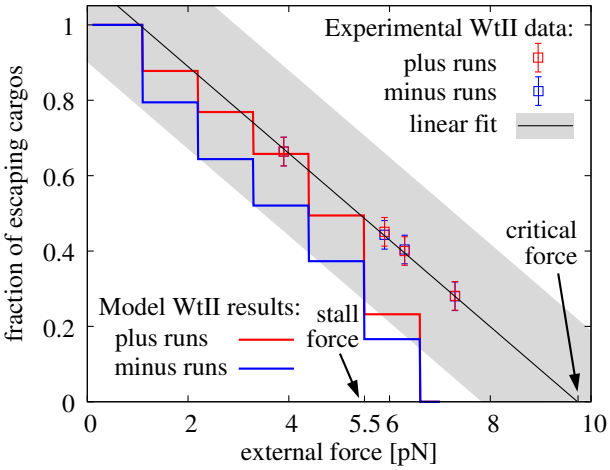

Fig. 5.2: Fraction of Wt II droplets that escape from the optical trap at an external force. The red (blue) squares are for experimental plus (minus) runs from [45]. The shaded region indicates the experimental force uncertainty of 1.89 pN which is due to the droplet size variation of 0.09 μm. The data can be fitted by a straight line (black) which intercepts the force axis at a 'critical force'. The experimenters correct this force by two times the force uncertainty to obtain the stall force of 5.5 pN. The red (blue) lines are escape forces for plus (minus) runs from simulation. There is a jump whenever the external force passes an integer multiple of the single motor stall force $F_{s+} = F_{s-} = 1.1$ pN.

[44, 45, 176] term the period from the beginning of this interphase until the end of cellularization 'phase II'. Shortly afterwards, gastrulation begins, which the experimenters term 'phase III'. During both phases, the nuclei are evenly distributed in a monolayer just under the embryo surface. MTs radiate from the centrosomes directly above each of the nuclei between nucleus and plasma membrane, extending into a depth of about 40 μm throughout the cortical region of the cytoplasm with the plus ends pointing inwards [63], see Fig. 5.1(a).

Lipid-droplet transport. Lipid-droplets travel bidirectionally on this isopolar MT array, see Fig. 5.1(b). They are transported by an unknown plus motor, presumably an unconventional kinesin, and cytoplasmic dynein [44]. They move in both directions at similar speeds of ca. 0.5 μm/s, and change direction after about 2 s, or 1 μm. Their motion is regulated during embryonic development: during phase II, they achieve net plus motion due to longer plus run lengths, while they exhibit net minus motion in phase III because of longer minus run lengths.

5.2.2 Experimenter's observations and interpretations

The experimenters of [44, 45, 176] tracked the droplets with video frequency 1/30s and nanometre resolution in wild type phase II and III (labeled Wt II and Wt III), and in three different dynein mutation backgrounds labeled $Dhc^{6-10}/+$, $Dhc^{8-1}/+$ and Dhc^{8-1}/Dhc^{6-10}during phase II.[2] They segmented the obtained trajectories into plus runs, minus runs, and pauses, and determined the run length and pause time distributions as well as various average values. Furthermore, they measured the escape forces of droplets travelling into the plus or into the minus direction with an optical trap, and extrapolated these to determine the average cargo stall forces, see Fig. 5.2. The numerical results of the measurements are summarized in Tabs. A.1 and A.3 in App. A.5.2.

The experimenter's observations and interpretations can be summarized as follows:

- **Stall force balance**. In both wild type phases, escape and stall forces in plus and minus direction are approximately equal. This is independent of the average net transport direction of the droplets, which is plus end directed in Wt II and minus end directed in Wt III. The experimenters interpret this to be in contradiction with a tug-of-war in which equally strong motors should lead to equal transport in both directions.
- **Stall forces indicate the number of involved motors**. The average stall forces in wild type are 5.5 pN in Wt II and 4.4 pN in Wt III, see Tab. A.1. These values are integer multiples of 1.1 pN, which is the value of the dynein stall force reported by [100, 135].

[2] These mutations are heterozygous dynein heavy chain mutations. The corresponding homozygous mutations are lethal. The names Dhc^{6-10} and Dhc^{8-1} label two different heavy chain mutations, and + labels the wild type (Wt) heavy chain. As one dynein contains two heavy chains, this means that in the $Dhc^{6-10}/+$ background, the functional dyneins consists of either one Dhc^{6-10} and one Wt heavy chain, or of two Wt heavy chains. Analogously, a dynein in the $Dhc^{8-1}/+$ background has either one Dhc^{8-1} and one Wt heavy chain, or two Wt heavy chains. A dynein in the Dhc^{8-1}/Dhc^{6-10} backgrounds always contains one Dhc^{6-10} and one Dhc^{8-1} chain.

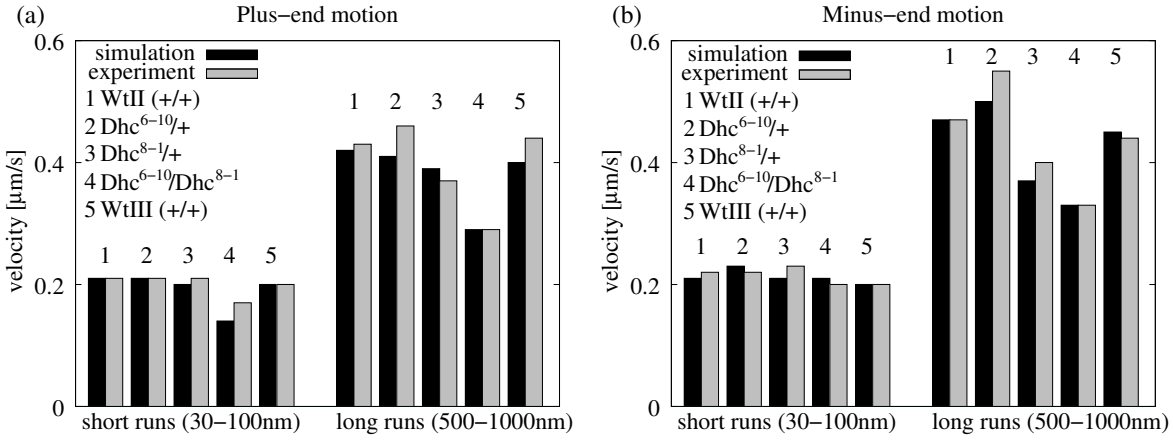

Fig. 5.3: Mean run velocity of short (30-100 nm) and long (500-1000 nm) runs for the *Drosophila* embryonic phases Wt II and Wt III, and for the dynein mutation backgrounds $Dhc^{6-10}/+$, $Dhc^{8-1}/+$ and $Dhc^{8-1}/Dhc^{6-10}$for (a) plus motion and (b) minus motion. Short runs have shorter velocities than long runs, and only the long run velocities change for the different phases or genotypes. The simulations values (black) agree well with the experimental values (gray). For the numerical values see Tab. A.1.

The experimenters deduce from this that the droplets are pulled by 5 resp. 4 plus (minus) motors during plus (minus) runs in Wt II resp. Wt III.

- **Complex response to perturbations**. During embryogenesis, the net transport direction of the droplets changes from net plus directed in phase II to net minus directed in phase III due to a change in the plus end run length, while all other quantities remain almost unaltered, see Tab. A.1. Dynein mutations, on the contrary, always lead to impaired movement in *both* directions by reducing run lengths and stall forces, see Tab. A.1. The experimenters interpret this to be in contradition with a tug-of-war, which should lead to impairment of motion in one direction and enhancement of the other.
- **Run lengths and velocities are correlated**. The experimenters divide runs into 'short runs' of 30-100 nm and 'long runs' of 500-1000 nm. They find that short runs have a velocity of ca. $0.2\,\mu$m/s, while long runs have a higher velocity of $0.4\,\mu$m/s, see Fig. 5.3.
- **Run lengths distributions are double exponential**. In all developmental phases and dynein mutation backgrounds, the run length distributions are well fitted by a double exponential function with a small length scale of ca. $0.1\,\mu$m and a long length scale of about $1\,\mu$m. Only the long length scale varies in the different backgrounds, see Tab. A.3.
- **Pause time distributions are single exponential**. Pause time distributions of pauses after plus and minus runs are found to be very similar and of single exponential form.

Motor coordination by a 'switch'. The experimenters propose that the droplet transport by two teams of motors is organized by a coordination complex, which switches on and off the motor activities so that only one type of motors is active at a time. This 'switch' also regulates the plus and minus run lengths and causes the run length variations in the different embryonic phases and mutational backgrounds. Only long runs are terminated by the 'switch', while short runs are terminated by a (not specified) tug-of-war mechanism. This leads to the different velocities of short and long runs and to the two lengths scales of the double-exponential run length distributions.

5.2.3 Fit to the lipid-droplet data with the tug-of-war model

In defiance of the experimenter's refutation of a tug-of-war scenario, we are able to fit the lipid-droplet data of Refs. [44, 45, 176] with our tug-of-war model, as we describe in this section.

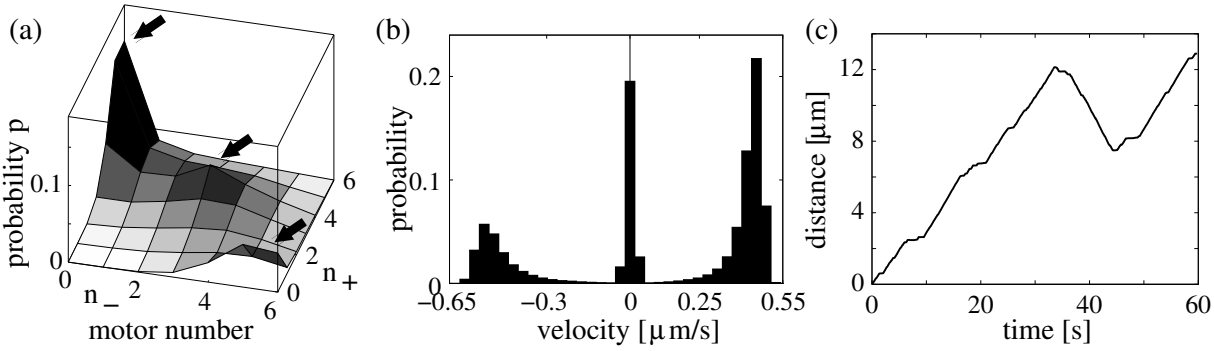

Fig. 5.4: Simulated lipid-droplet transport in Wt II: (a) The system is in the $(-0+)$ motility state characterized by three maxima of the motor number probability distribution $p(n_+, n_-)$, corresponding to fast plus, fast minus and no motion. (b) The velocity distribution has three corresponding peaks, and (c) the cargo trajectory shows stochastic switching between these three types of motion. Net motion is plus end directed because plus motion is more probable than minus motion.

Fitting procedure. We first considered the Wt II data. Cargo stall force measurements indicated that both plus and minus motors have a stall force of 1.1 pN, and that the droplets are pulled by 5 plus and 5 minus motors. Since the number of active motors fluctuates stochastically, this should be the average number of pulling motors. We therefore fixed the total number of plus and minus motors to $N_+ = N_- = 6$. We set the motor stall forces to $F_{s+} = F_{s-} = 1.1\,\mathrm{pN}$.

We then performed simulations that mimicked the experiments as closely as possible. In particular, we used the same time resolution and definitions of runs and pauses as in the experiments, which is crucial for the numerical values of run lengths or velocities, see App. A.5.1. We then varied the 10 undetermined single motor parameters $F_{d\pm}$, $\epsilon_{0\pm}$, $\pi_{0\pm}$, $v_{F\pm}$ and $v_{B\pm}$ in order to fit 10 experimentally measured transport characteristics, namely plus and minus run lengths, plus and minus stall forces, pause times after plus and minus travel, and plus and minus velocities of short and long runs, with an accuracy of ca. 10%. The detailed fitting procedure and the numerical results are described in App. A.5.2.

The resulting parameters for dynein and the unknown plus motor are listed in Tab. A.2. They are within the expected range of motor parameters. The unbinding and binding rates are of the order of $1\,\mathrm{s}^{-1}$ as measured for motors like kinesin 1 [84, 139, 161] and kinesin 3 [157]. The dynein parameters are in agreement with *in vitro* measurements of dynein properties when available, compare Tab. 2.1. The motor forward velocities are of the order of $0.5\,\mu\mathrm{m/s}$ which is close to the droplet velocity measured during long runs. This means that the tug-of-war does not substantially reduce the single-motor velocity. The backward velocity is two orders of magnitude smaller than the forward velocity but one order of magnitude larger than the kinesin 1 backward velocity. For dynein, this is in agreement with experiments [100, 170]. The wild type detachment forces obtained from the fit are approximately half of the stall force, similar as for kinesin 1, for which however both force scales are larger, see Tab. 2.1.

Motility characteristics. Fig. 5.4 shows the motor number probability and the velocity distribution and a trajectory for Wt II. The cargo switches between fast plus and minus motion and pauses but exhibits net plus motion because the probability for $(+)$ states is higher than for $(-)$ states. The cargo stall forces in plus and minus direction are equal, see Tab. A.1. This shows that the cargo direction is not only determined by the motor forces but also by other motor properties, see Tab. A.2. In this case, the higher plus motor detachment force makes it difficult to rip off the plus motors and thus favours plus motion.

A nontrivial consistency check of our model is provided by four additional features that we obtained from this model in close agreement with experimental observations even though these features were not used in the fitting procedure. First, the distribution of plus and minus run lengths can be fitted by a sum of two exponentials with length scales of the same order of magnitude (within 50%) as obtained experimentally, see Fig. 5.5(a) and Fig. A.15. Second,

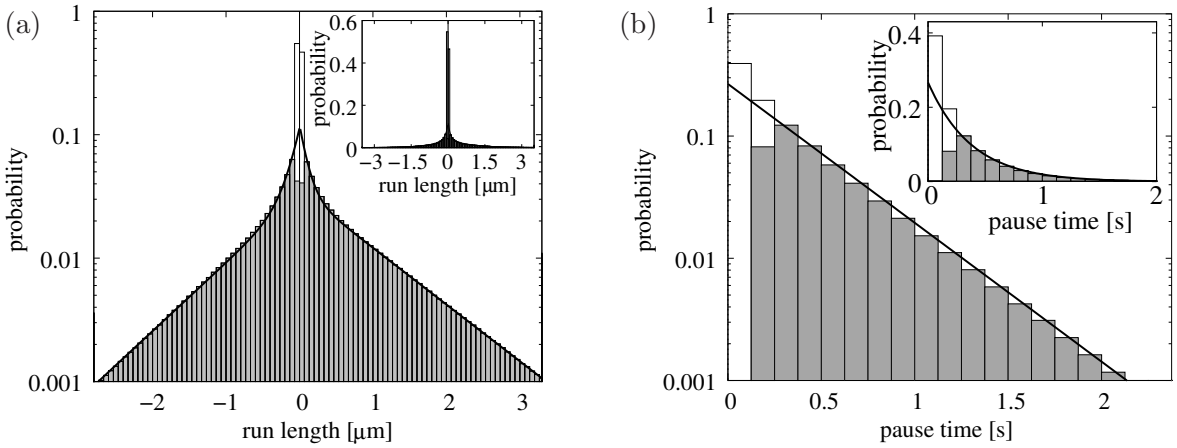

Fig. 5.5: (a) Run length distribution in Wt II from simulation. Minus (plus) run lengths are negative (positive). The full graph is a semi-logarithmic plot of the original distribution in the inset. The gray bars are obtained when using the experimental cutoffs of a minimum length of 0.16 s and 30 nm, while the white bars are obtained without the cutoffs. The lines are double exponential fits to the simulation data with decay lengths of ca. 0.1 μm and 1 μm in both directions, as in experiments. See Tab. A.3 for numerical values. (b) The pause time distribution (gray histogram) in Wt II can be fitted by a single exponential function (line) with time scale 0.38 s. We do not distinguish pauses after plus and after minus motion because they are statistically identical. The first bar has reduced counts because of the experimental definition of a pause to be longer than 0.23 s. The experimental distributions of pauses after plus and after minus motion have been fitted with single-exponentials with time scales 0.24 s and 0.29 s [44]. These time scales are smaller than the experimental average pause times of 0.55 s for pauses after plus and 0.62 s for pauses after minus motion. Similarly, in simulation, the time scale 0.38 s of the exponential fit is smaller than the average pause time of 0.61 s. This indicates that the distribution is in fact not single exponential but has another, smaller time scale. This smaller time scale is below experimental resolution, but shows up when the lower time cutoff 0.23 s is removed (white bars).

the pause time distributions of pauses after plus and after minus runs are very similar and can be fitted by a single exponential function with a time scale of the same order of magnitude as in the experiments (again within 50%), see Fig. 5.5(b). Third, the percentage of droplets that escape at a given force decreased approximately linearly with the force, see Fig. 5.2.[3] Fourth, there is a correlation between run length and run velocity: long runs have larger average velocities with a Spearman rank correlation coefficient larger than 0.7 with a significance level below 10^{-10}, see Fig. 5.6(a).[4] The correlations persist when considering velocity and run time instead of run length, see Fig. 5.6(b). This is more meaningful since run length and velocity are trivially linearly correlated due to the fact that high velocities lead to larger displacement. In the experiments, this has been quantified by dividing the runs into short and long runs. Short runs have approximately half the velocity of long runs, see Fig. 5.3. In our model, this property reflects the correlation of the average number of active winning motors with the run length, see Fig. 5.6(c), and can be understood as follows.

During a certain run, e.g. in the plus direction, minus motors bind from time to time to the MT. This slows down the motion and causes a 'pause'. However, the active plus motors generate a large force on this single minus motor, which is then ripped off fast from the MT. As a consequence, the 'pauses' are too short to be detected experimentally and are only noticeable via the decreased average cargo velocity in the plus direction. If a cargo is pulled by many plus motors, this has two effects: (i) The effective cargo velocity is increased because opposing minus motors do not create large forces on each of the many plus motors and because the minus motor

[3] The fraction of escaping droplets in simulation drops to zero at smaller forces than in experiment. The reason is presumably the maximal number of pulling motors was fixed to $N_+ = N_- = 6$ in simulation, while in experiments droplets with larger motor numbers are likely to be selected for experimental force measurements which require 'very long' runs in one direction, see App. A.5.2. Such droplets can endure higher forces. [4] The Spearman rank correlation nonparametrically measures monotonic correlation, see App. A.5.3.

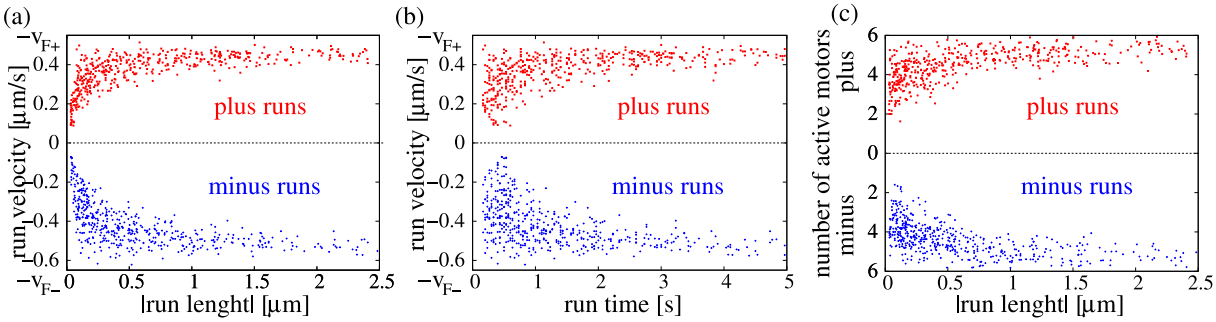

Fig. 5.6: Scatter plots of (a) the run velocity versus the run length, (b) the run velocity versus the run time, and (c) the number of winning motors versus the run length of 500 plus runs (red data) and 500 minus runs (blue data) in Wt II. (a,b) The run velocity exhibits a positive correlation with the run time and length: longer runs have higher velocities. Very long runs have almost the maximal velocity which is the single motor velocity, $v_{F+} = 0.55\,\mu$m/s in plus and $-v_{F-} = -0.65\,\mu$m/s in minus direction. (c) The reason for the correlation is that longer runs also have a higher average number of active pulling motors, compare the discussion in the text. There are no data points for small run times, lengths and velocities because runs have been defined as having a velocity of at least 50 nm/s for at least 30 nm and 0.16 s.

drops off very fast. (ii) The plus run length is larger because it is less probable that the minus motors take over. Both effects together lead to a correlation of run length and velocity.

Mutation and regulation. For the dynein mutation fits, we only varied the minus motor paramaters and kept the plus motor parameters fixed to their Wt II values, because the mutations only affected the dyneins (in an unknown way) and were investigated in phase II. The dynein mutations, both in experiment and in our fit, affect motion in both directions, reducing run length, stall forces and velocities, see Tab. A.1. In our model, these mutations simultaneously modify several dynein parameters, among which are its unbinding rate, its binding rate, and its detachment force, see Tab. A.2. If only one of these parameters were modified, the resulting motor behaviour would be easy to understand. First, if only the unbinding rate is increased, the minus motors unbind from the MT faster and produce less force on the plus motors, which leads to longer plus and shorter minus runs. Second, increasing only the minus motor binding rate has the opposite effect because dyneins are more likely to rebind to the MT. Third, if only the minus motor detachment force is enhanced, the ability of the minus motors to resist the plus motors is enhanced, which increases minus and decreases plus run lengths. Therefore, if only a single minus motor parameter is modified, motion in one direction is enhanced whereas motion in the opposite direction is impaired. In contrast, the overall effect of changes in several motor parameters is difficult to anticipate intuitively and can lead to impairment of both directions.

Furthermore, two different embryonic phases Wt II and Wt III allow to assess the effect of cellular regulation. In Wt II net transport is plus-end directed, while it is minus-end directed in Wt III due to a reduction in plus run length. Apart from the cargo stall forces, all other transport characteristics remain unchanged. We propose that the cellular regulation that causes this change targets the motor properties. We therefore fitted the Wt III data by varying the motor parameters as for the Wt II data. The successful fit shows that a tug-of-war can lead to impairment of motion in one direction while leaving the other direction unaffected, see Tab. A.1. The obtained single motor parameters for Wt II and Wt III are rather similar.

5.2.4 Discussion

The agreement of simulation and experiment shows that our tug-of-war model can describe the lipid-droplet data. Two features are particularly remarkable because they are not expected within a naive picture of a tug-of-war: First, the Wt II and Wt III data represent motion with balanced stall forces in plus and minus direction, but motion is net plus end-directed in phase II and net minus-end directed in phase III. Second, the dynein mutation data, which exhibit an impairment of both plus and minus motion, could be reproduced by varying the dynein

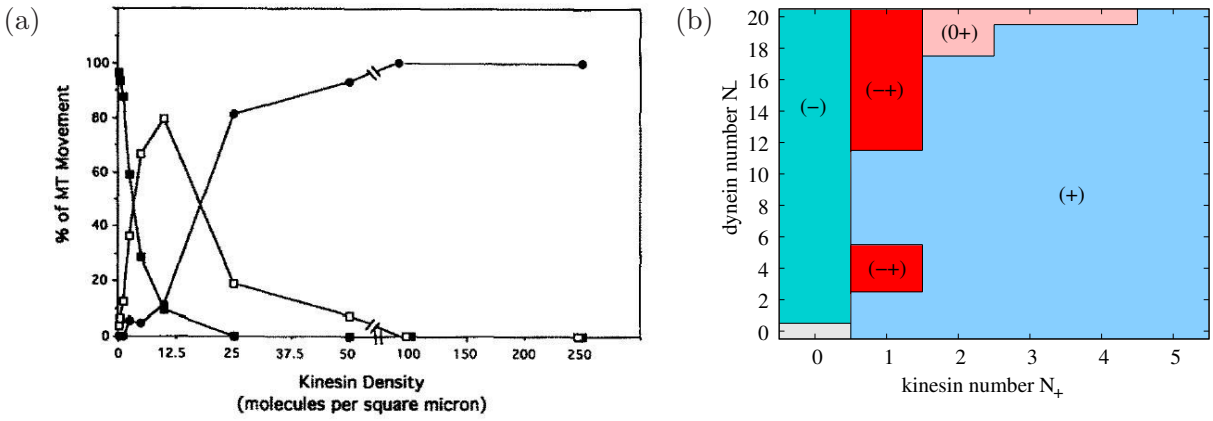

Fig. 5.7: Transition from dynein directed to bidirectional to kinesin directed motion in the motility assay of kinesin 1 and ciliary dynein: (a) Fig. 3 from [162] shows the fraction of MTs which, in the observation period of 1 minute, moved only into the kinesin direction (●), only into the dynein direction (■) or bidirectionally (□). Bidirectional motion occurs mainly at a kinesin surface density of 10 molecules/μm^2. For lower kinesin densities, motion is dynein directed, and for larger kinesin densities, motion is kinesin directed. The dynein surface density was kept constant at 900 molecules/μm^2. (b) The motility diagram of our model tug-of-war of N_+ kinesins and N_- ciliary dyneins shows the same transition from dynein directed motion ($-$) via bidirectional motion ($-+$) to kinesin directed motion ($+$) when the number of kinesins on one MT is increased from $N_+ = 0$ to $N_+ = 2$ with a fixed number of $N_- \sim 13$ dyneins. Motor parameters are for kinesin 1 and ciliary dynein as explained in the text.

parameters only. The reason for theses two observations is that in our model cargo motion depends on six different motor properties (stall and detachment force, binding and unbinding rate, and forward and backward velocity) for each motor type, which leads to complex behaviour. In particular, cargo motion is not only determined by the motor forces but also by other motor properties, which leads to a variable response to perturbations such as mutation or regulation. As shown in Tab. A.1, it is possible (i) to change only one direction and leave the other direction unaffected (Wt III, or change of only minus motor stall force or forward or backward velocity) (ii) to impair one direction and enhance the other (change of only minus motor unbinding or binding rate or detachment force), or (iii) to impair both directions (dynein mutations).

5.3 Tug-of-war in a motility assay: a disproportionate fight

A motility assay with kinesin 1 and ciliary or cytoplasmic dynein was investigated already in 1992 [162]. To our knowledge, until today this has remained the only *in vitro* experiment for transport by two opposing motor species. The MTs gliding over the kinesin- and dynein-coated surface showed fast motion in the kinesin or the dynein direction, or switching between these two directions on length scales of several microns, depending on the motor densities. This can be readily explained within our tug-of-war model, as described in this section.

In the experiments, a glass surface was covered with a high and constant density of ciliary dyneins and a varying density of kinesins. For very low kinesin densities, the MTs moved into the dynein direction, and for large kinesin densities into the kinesin direction. They moved bidirectionally for intermediate kinesin densities, see Fig. 5.7(a). The directional switching was stochastic and without pauses.

Motor parameters. In order to compare the experimental results to our model, we need the single motor parameters for the involved motors. The kinesin 1 parameters are listed in Tab. 2.1. Unfortunately, ciliary dyneins are not as well characterized. The stall force has been estimated as $F_{s-} = 1.2\,\mathrm{pN}$ [62, 135], although a higher stall force of 6 pN has also been reported [146]. Ciliary dynein is a non-processive motor with a low duty-ratio [50, 56, 142], although also this is controversial [146]. We take the 'run-length' of the motor to be only one step, $\Delta x_\mathrm{b} = 8\,\mathrm{nm}$.

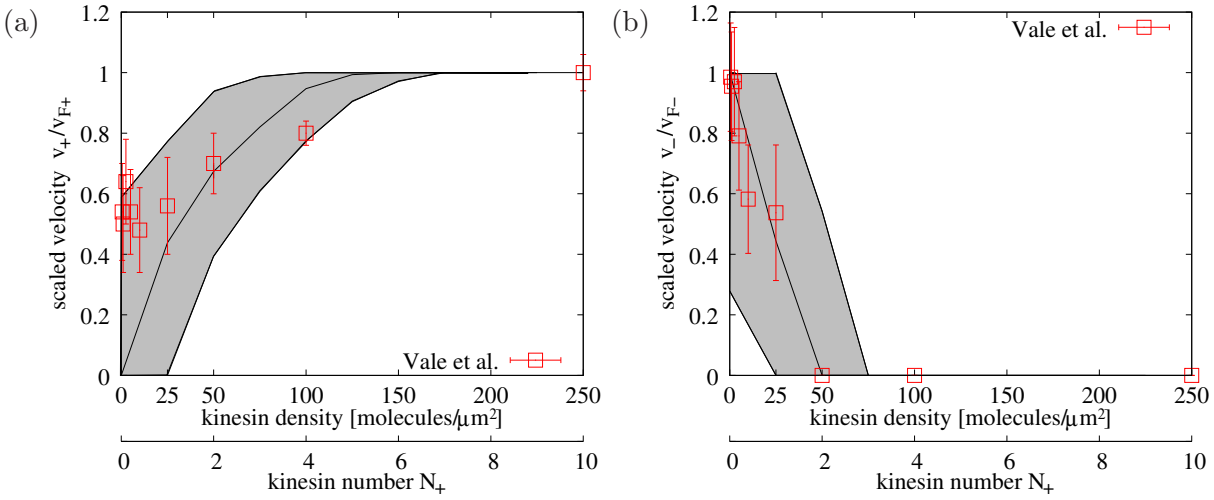

Fig. 5.8: Normalized average velocities in (a) kinesin direction and (b) dynein direction for the motility assay of kinesin 1 against ciliary dynein as a function of the experimental kinesin density resp. the number N_+ of kinesins that can bind to the MT. The grey shaded area comprises the velocities of the model tug-of-war for $N_+ \pm 1$ kinesins and $N_- = 13 \pm 4$ ciliary dyneins. The black middle line of this region is for N_+ kinesins and $N_- = 13$ dyneins. The data points (□) from Fig. 4 of [162] fit well into the region obtained from the model. Motor parameters are as explained in the text. Time measurement interval is $\Delta t = 1\,\mathrm{s}$ as read from Fig. 2 in [162]. The velocity cutoff has been taken as $0.1\,\mu\mathrm{m/s}$, and motion into one direction had to persist for at least 3 time frames to be counted as plus or minus motion.

Together with the velocity $v_{F-} = 6.7\,\mu\mathrm{m/s}$ [162], this leads to an extremely high unbinding rate $\epsilon_- = 800\,\mathrm{s}^{-1}$. The MT desorption constant is $K_{\mathrm{exp}} = 5\,\mu\mathrm{M}$ [172], so that we choose $K = 3$. The other parameters have not been measured. We simply use the kinesin parameters in Tab. 2.1[5].

Bidirectional motion. The tug-of-war of kinesin 1 and ciliary dynein is thus rather disproportionate: Ciliary dynein is a weak and unprocessive motor compared to kinesin 1. Therefore only a few kinesins are required in order to overpower many dyneins. By looking at the surface motors densities and the MT motion, the authors of [162] estimate that the number of motors on a single MT in the bidirectional motion regime is about one kinesin and 10 dyneins, and that 2 kinesins suffice to make the MTs move into the kinesin-direction. The transition from dynein-directed to bidirectional and further to kinesin-directed motion occurs in a narrow range of kinesin densities, see Fig. 5.7(a).

The motility diagram for the model tug-of-war N_+ kinesins against N_- ciliary dyneins is shown in Fig. 5.7(b). As kinesin is a strong motor, kinesin directed motion (+) dominates, and only with no kinesins, i.e. $N_+ = 0$, dynein directed motion (−) is possible. There is a sharp transition from dynein-directed to bidirectional to kinesin-directed motion when increasing the number of kinesin from $N_+ = 0$ to 1 to 2 for fixed dynein numbers in the range of 13. This could correspond to the experimental transition described above. However, the number of plus and minus motors that can bind to the MT varies in the experimental motility assay. We therefore performed several simulations, each with a fixed number of N_- ciliary dyneins and N_+ kinesins. We varied the number of dyneins in the range $N_- = 13 \pm 4$, which corresponds to the numbers of a Poisson distribution with parameter 13 within its standard deviation $\sqrt{13}$. As the number of involved kinesins is small, we allow it to vary only by ± 1, which corresponds to a Poisson distribution with a small parameter. The number N_+ of kinesins was increased in order to mimic the change in kinesin surface density. As the authors of [162] estimated that the number of active kinesins changes from 1 to 2 in the density range $25 - 50$ molecules/$\mu\mathrm{m}^2$, we scale the

[5] The high dynein unbinding and binding rates lead to a time-scale separation, i.e. the dynein binding/unbinding dynamics equilibrates fast when the number of involved kinesins changes. As long as the dynein (un-)binding rates are much larger then the kinesin rates and the dynein desorption constant is $K_- \sim 3$, we obtain the same results. For example, dividing both ϵ_- and π_- by a factor of 10 does not change the motility diagram Fig. 5.7(a) and also fits the velocity data in Fig. 5.8.

number of kinesins so that a surface density of 50 molecules/μm^2 corresponds to $N_+ = 2$. The average velocities in kinesin and dynein direction are shown in Fig. 5.8. They agree with the experimental results. The dynein directed velocities in Fig. 5.8(b) drop to zero fast when the number of involved kinesins reaches 2. The kinesin directed velocity increases quickly as soon as 1 kinesin is at work, but it takes more than 5 kinesins to reach the single kinesin velocity v_{F+}. The weak ciliary dyneins thus act as 'friction' for the winning kinesins because of the fast (un-)binding dynamics of a large number of dyneins.

Kinesin 1 and cytoplasmic dynein. The authors of [162] also examined a motility assay of kinesin 1 and cytoplasmic dynein, but unfortunately only discuss it qualitatively. They found that bidirectional motion occurred when the numbers of involved kinesins and dyneins are similar, and for motor numbers $N_+ \sim N_- \gtrsim 1$. This is in agreement with cytoplasmic dynein being a motor of approximately same strength than kinesin 1, and with our results from Sec. 4.3.4. For about 10 times higher numbers of both motor types, bidirectional motion became suppressed, i.e. during 1 minute most MTs moved unidirectionally. This is in agreement with the large switch times for large motor numbers predicted by our model, see Sec. 4.5.1.

Summary. We have explained the results of the kinesin-dynein motility assay by [162] within our tug-of-war model without a fitting procedure, simply by choosing reasonable parameters for the involved motors. While the qualitative comparison is robust, the quantitative comparison has to be taken cautiously because of the different geometries, i.e. bead assay and motility assay, the small amount of data and the limited time and space resolution of this rather old experiment.

5.4 Summary

In this chapter we have discussed experiments concerning bidirectional cargo transport. All available experimental observations are consistent with our model. It reproduces the correct time and length scales of switching, which are of the order of seconds and micrometers, respectively, and the observed fast velocities of the order of micrometers per second. Furthermore, it can explain various observations which have so far been thought to be inconsistent with a tug-of-war, see Sec. 4.1.2. First, our tug-of-war exhibits fast bidirectional motion due to a dynamic instability which results in having only one motor type active most of the time. Second, stall forces in plus and minus direction can be balanced although there is net transport into the plus or the minus direction, because the cargo motion is determined by many motor properties, not only by the motor forces. Third, cargo transport can be affected in various ways by perturbations such as cellular regulation or mutations: (i) one direction is enhanced and the other impaired, (ii) both directions are impaired, or (iii) one direction is affected and the other direction unaltered. Forth, regulation can be incorporated into our model by assuming that the identified regulatory mechanisms target the motor properties directly. Furthermore, our model reproduces experimental transport characteristics such as double exponential run length distributions and a correlation of run length and velocity.

Besides this qualitative agreement of our tug-of-war model with the experimental observations, we have quantitatively reproduced the data of one *in vivo* and one *in vitro* system, namely the bidirectional transport of lipid-droplets in *Drosophila* embryos, and the bidirectional transport of MTs in a kinesin-dynein motility assay. We hope that more quantitative data will be accumulated so that our model can be tested in more detail. In particular, an *in vitro* bead assay would be ideal, where the motor parameters could be changed by varying the ATP or salt concentration, by using the dynein accessory protein dynactin etc.

Chapter 6

Summary, discussion and outlook

Summary

In the preceding chapters, we have studied the large-scale bidirectional traffic of molecular motors. This traffic is vital for cells in order to maintain their highly organized structure, as is especially evident for long cellular processes such as neuronal axons or fungal hyphae. In these thin tubular compartments with lengths ranging from tens to thousands of microns, the MTs form an isopolar array along the tube axis along which plus motors walk to the tip and minus motors walk to the cell body. It is obvious that the cell needs traffic in both directions. Otherwise the plus motors would accumulate near the tip, and the minus motors near the cell body. We have quantified the jamming effect of such unidirectional plus or minus end traffic in a tubular geometry in Chap. 3. The cell can avoid such traffic problems by employing both plus and minus motors on single cargos, which can then move bidirectionally. We have studied bidirectional transport by two teams of opposing motors in Chap. 4 and Chap. 5.

Single motors (Chap. 2). Our analysis is based on a simple coarse grained description of a single molecular motor on time and length scales of a few seconds and microns. On these scales, the motor can bind to the filament, walk along it, and unbind from it, and does so in a stochastic way. Our choice of the rates which describe these processes is based on the load-dependent transport parameters of the motors as measured in single molecule experiments.

Motor traffic jams in tubular geometries (Chap. 3). We have investigated the traffic of many such motors in a half-open tube geometry which mimics axons or hyphae. The motors act independently according to the single motor properties described in Chap. 2, and feel each other only via steric hindrance. This mutual exclusion in combination with the confined geometry leads to motor traffic jams at either end of the tube, depending on the direction of the motors. For minus motors, the jam length also represents the penetration length of the motors. Surprisingly, jamming is enhanced by slow active and fast diffusional transport, see Eq. (3.17) and Fig. 3.6. It is also enhanced by a high density of motors supplied at the open tube end. Although the current can be optimized with respect to this boundary motor density, in the stationary state the tubes are either essentially full or essentially empty. In axons or hyphae, which are mimicked by this tube geometry, additional processes are therefore necessary to maintain efficient transport.

Bidirectional transport as a motor tug-of-war (Chap. 4). One possibility is that motors of opposite directionality are simultaneously on single cargos, which can then move bidirectionally. Such bidirectional transport is indeed observed for many cellular cargos including mitochondria, endosomes, lipid-droplets, melanosomes, and even viruses. It is a matter of debate how cargo transport by opposing motors is organized. Do the plus and minus motors perform a tug-of-war on the cargo? Or is there an additional coordination complex which prevents opposing motor from being active at the same time? While it is clear from experiments that bidirectional cargo transport shows cooperative and complex features, there is no direct evidence for a coordination machinery. We have therefore proposed a tug-of-war model in which the motors on the cargo act independently with the single-motor properties described in Chap. 2,

and feel each other only via the mechanical interaction with their common cargo. Contrary to what is often expected from a naive view of a tug-of-war, our model reproduces the cooperative and complex bidirectional transport found in experiments, as explicitly shown in Chap. 5.

In order to study the tug-of-war of two motor species in a systematic and quantitative way, we introduced a model in Sec. 4.2 in which the cargo is pulled by a fluctuating number of active plus and minus motors, see Fig. 4.3. When both plus and minus motors are active, they block each other and the cargo is almost immobile; we label this cargo state as (0). When only plus or only minus motors are active, the cargo exhibits fast plus motion (+) or fast minus motion (−), respectively. The observable cargo motion is dominated by states that have a high probability to be occupied. Depending on the number and properties of the involved motors, the cargo switches stochastically between either 1, 2 or 3 of these high-probability states. This leads to the seven motility states (+), (−), (0), (−+), (0+), (−0) and (−0+). They are characterized by distinct cargo trajectories, velocity distributions and run time distributions. For example, in the motility state (−+), which is most typical for bidirectional motion, the cargo switches stochastically between fast plus and fast minus motion. The somewhat surprising persistence of fast plus and minus motion in our tug-of-war model is caused by a dynamic instability arising from the strongly nonlinear force-dependence of the single-motor unbinding rate.

In Sec. 4.3, we obtained a complete classification of the possible motility states for the symmetric tug-of-war, see Figs. 4.6 and 4.7, and for the asymmetric tug-of-war, see Figs. 4.9–4.11. The latter comprises the most important *in vivo* transport by kinesin 1 and cytoplasmic dynein. Besides performing numerical calculations, we used three different analytical approximations. For motors with large forces such as kinesin 1 and 'strong' dynein, we obtained an analytic theory in Sec. 4.4.1.2, see Fig. 4.14. The mean field theory of Sec. 4.4.2 captures qualitatively the motility behaviour of our model, see Fig. 4.18. The sharp maximum approximation of Sec. 4.4.3 captures this motility behaviour even quantitatively with the four simple inequalities (4.70), which can be used to rapidly estimate the motility state of an experimental system.

A prominent feature of bidirectional transport is directional switching, which we investigated in Sec. 4.5.1 and 4.5.2. The switch times increase exponentially with the motor number, see Fig. 4.25(a), in agreement with analytic results from the large force approximation. It indicates a non-equilibrium phase transition for large motor numbers. The switch times exhibit a strong dependence on the motor parameters, whereas the velocities are less affected, see Figs. 4.26 and 4.27. These dependencies can be directly tested in *in vitro* experiments.

Our model can be easily extended to include frictional and external forces. Friction strongly affects the velocity distribution, see Fig. 4.34. For large friction as in the cytoplasm, it exhibits peaks which could be used to estimate the number of involved motors or the motor stall forces *in vivo*. External forces, such as exerted by an optical trap, lead to hysteresis effects, see Fig. 4.36.

Bidirectional transport in experiments (Chap. 5). Our tug-of-war model for bidirectional cargo transport exhibits surprisingly complex and cooperative features which reproduce the following experimental observations on bidirectional motor transport:

- **Fast and processive motion**. A naive picture of a motor tug-of-war leads to the expectation that cargo motion should be slow because the opposing motors block each other. We have shown, however, that for strong motors such as kinesin 1 and 'strong' dynein, a dynamic instability leads to fast plus and minus motion. Furthermore, although the motors pull at each other, the cargo processivity increases roughly exponentially with the motor number, so that cargos pulled by two small teams of motors can travel over long distances without unbinding from the filament.

- **Transport characteristics**. Our model makes direct predictions for experimentally accessible quantities such as run times or lengths, and velocities. We have found that the distributions of run times and length are double exponential. For biological parmeter ranges, their averages are of the order of seconds and microns, respectively. Velocities are of the order of single-motor velocities, and thus not substantially reduced by the tug-of-war.

- **Regulation**. Various molecules involved in cellular regulation of motor transport have been identified, such as the dynein accessory protein dynactin, kinases or G-proteins. We propose that cellular regulation directly targets the motors and mimic it in our model by changing the motor parameters. We found that cargo motility is very sensitive to such changes: By small parameter changes, cargo motion can change from fast plus end motion to bidirectional motion to fast minus end motion, for example. The cell could use this sensitivity for efficient cellular regulation.
- **Interdependence of directions**. Variation in the single motor parameters does not only mimic cellular regulation but also mutation. Either perturbation can lead to various effects on transport in plus and minus direction: (i) one direction is enhanced and the other impaired, (ii) both directions are impaired, or (iii) one direction is affected and the other direction unaltered. Enhancement and impairment usually affect switch times or distances, while the instantaneous velocities are often changed only to a small amount.

Besides this qualitative agreement of model and experiment, we were able to quantitatively reproduce the data of bidirectional transport of lipid-droplets in *Drosophila* embryos in Sec. 5.2, and of the only published *in vitro* experiment, a kinesin-dynein motility assay, in Sec. 5.3.

In summary, our tug-of-war model is a straightforward and simple scenario for *in vivo* and *in vitro* bidirectional transport by two teams of opposing motors. It exhibits complex cooperative motility patterns. It avoids motor back-transport and jamming problems and allows for efficient cellular regulation. It is consistent with all available experimental observations, and its prediction are accessible to further experiments.

Discussion

In our model, cargos are transported by two motor teams which oppose each other. This might seem counterintuitive: Why shouldn't the cell prevent opposing motors from obstructing each other? Why shouldn't it use only unidirectional teams? Or single motors instead of teams?

First, using only unidirectional motors on a single cargo is not sufficient to maintain cellular transport in an efficient way. As the cellular MT cytoskeleton is typically isopolar, plus end cargos would accumulate at the MT plus ends, and minus end cargos at the MT minus ends. Even if motors are interchanged at the MT ends, which would solve the cargo jamming problem, it would still leave the problem how the plus (minus) motors reach the MT minus (plus) ends in order to start their journeys. Having motors of opposite directionality on one cargo is an elegant solution to this problem.

One would think that the cell should then carefully coordinate the activities of opposite directional motors in order to avoid wasting time and energy of motors working against each other. With our model we have shown that such a coordination happens 'automatically', i.e. in a self-organized manner, without an extra coordination machinery. A dynamic instability arising from the nonlinear load-dependence of the motor unbinding rate causes an unbinding cascade, which leads to only plus or only minus motore being active most of the time. The motor's obstructive pulling at each other is thus not a nuisance, but actually causes the desired behaviour! A prerequisite for this unbinding cascade is that the involved motors should have a higher stall than detachment force, exhibit a small backward velocity, and be processive. This is typically the case for biological motors employed in long range traffic such as kinesin or dynein.

The requirements of bidirectional transport impose constraints on the motor parameters. This may be one reason for the counterintuitive property of kinesin 1 to be able to produce high forces (high stall force) without being able to sustain them for a long time (lower detachment than stall force). It may also be the reason for the intermediate single motor processivity of only about a second before unbinding: longer unbinding times would slow down the unbinding cascade and lead to lower velocities and longer pauses.

The rather small single-motor processivity is compensated by using motor teams instead of

single motors. When one motor unbinds, the other motors tether the cargo to the filament, thereby preventing the cargo from diffusing away and giving the unbound motor a chance to rebind. We have shown that already rather small motor teams lead to a cargo processivity which is large enough to travel through the whole cell without unbinding. Furthermore, motor teams can endure larger forces, which might be important for large cargos in the viscous cytoplasm.

One of the most important reasons for cellular bidirectional transport might be simple and efficient regulation. A tug-of-war is simple and efficient because it does not involve any further coordination machinery. And, due to its sensitivity to the number and properties of the involved motors, it can be easily regulated. The cell can change the transport behaviour, like the times traveled in one direction, the net transport direction of the cargo, simply by finetuning the motor properties. Such a regulation is particularly fast and efficient if the opposite teams are of similar 'strength'. This might be the reason why the cell does not always use one strong and one weak team, which would lead to unidirectional motion. The observed bidirectional cargo motion may thus be a signature of this regulatory mechanism. Furthermore, bidirectional transport could also help the cargo in search for the correct target, in error correction in case of a misplaced cargo, or in avoiding obstacles on the filament.

Outlook

Our model is consistent with all existing experimental observations. However, the amount of quantitative data is rather small, and no systematic quantitative *in vitro* experiments have been performed. An *in vitro* bead assay with opposing motors would be the best experimental setup to test our model predictions. Observables such as switch times and lengths or velocities are easily accessible. Even the effect of parameter changes could be investigated by changing the ATP concentration, using genetically modified motors, employing accessory proteins such as dynactin, changing the buffer salt concentration etc. One problem of such a bead assay may be to determine the number of involved motors, as mostly the motors bind to the beads stochastically and unspecifically. This could be overcome by using functionalized motor-cargo-links, e.g. biotin-streptavidin or complementary DNA sequences. The symmetric tug-of-war could also be realized by using only one type of motors on the bead, but a bidirectional array of MTs.

In vivo experiments could address totally different types of questions which are related to biological function rather than to the mechanical interaction of the motors. How does cellular regulation work? Which molecules are involved, and how do they act on the motors? While our model cannot answer these questions directly, it could help in identifying which motor properties are changed by specific regulatory molecules.

Our model could be extended in various ways. First, it could be refined. One possibility would be geometrical effects like steric hindrance of the motors. Other motor-motor interactions could also be included, which should however be based on experimental observations. Furthermore, the cargo shape, or rotation of the cargo could be taken into account. The latter effect would lead to a fluctuating number of motors which are available for transport. Another refinement would be to include more details into our description of a single motor. Also, transport by three teams of motors could be investigated. This is relevant for example for melanosomes which are transported by teams of kinesin 2, cytoplasmic dynein, and myosin 5.

Second, large scale bidirectional cargo transport could be further investigated. Particular appealing systems are the long tubular neurons or hyphae with unidirectional axial MT arrays. What is the stationary state of traffic of bidirectional cargos in these tubular compartments? What is the effect of regulation on these stationary states? In axons there is evidence that dynein is transported to the MT plus ends by kinesin, but that kinesin is degraded at the axon terminal. In fungal hyphae, more than two motor players seem to be involved: In the fungus *Ustilago maydis*, endosomes are transported bidirectionally by kinesin 3 and dynein, but the dyneins are transported to the MT plus ends by kinesin 1. The complexity and diversity of biological transport systems provides many challenging questions for future research.

Appendix

A.1 Calculation of the desorption constant

In this appendix, we estimate the filament desorption constant for our model from the experimental desorption constant, which we need in order to derive our model parameters from experimental measurements.

The experimental desorption constant K_{exp} is the ratio of the forward rate k_1 to the backward rate k_{-1} of the reaction

$$M + F \rightleftharpoons MF \tag{A.1}$$

which describes (reversible) binding of a motor M to a filament site F, i.e.

$$K_{\text{exp}} = k_1/k_{-1}. \tag{A.2}$$

The analogous theoretical desorption constant is the ratio of the unbinding rate of a single motor from the filament to the binding rate of a single motor to the filament when the motor is 'close' to the filament. However, the meaning of 'close' can be different in different model situations.

For a single motor on a bead which is tethered to the filament by other motors, as considered in Chap. 4, 'close' means the distance of the bead from the filament which is of the order of 100 nm. The corresponding bead model desorption constant is denoted as

$$K = \epsilon_0/\pi_0 \tag{A.3}$$

with the unbinding and binding rates ϵ_0 and π_0 of a single motor on a bead under no force when the bead is as close to the filament as when tethered to it by at least one motor, see Sec. 2.2.

For the lattice model of Sec. 3.1, 'close' means that the motor is on a lattice site adjacent to the filament, i.e. for MT motors in a distance of $l = 8\,\text{nm}$ from the filament. The corresponding lattice model desorption constant is denoted as

$$K_{\text{L}} = \epsilon/\pi_{\text{ad}} = \tilde{\epsilon}/\tilde{\pi}_{\text{ad}} \tag{A.4}$$

with the lattice model unbinding and binding rates ϵ and π_{ad} of the original latice model resp. $\tilde{\epsilon}$ and $\tilde{\pi}_{\text{ad}}$ of the two-state approximation of Sec. 3.1.

A.1.1 Experimental desorption constant

The experimental desorption constant K_{exp} defined in Eq. (A.2) is equal to

$$K_{\text{exp}} = [M][F]/[MF], \tag{A.5}$$

where $[M]$, $[F]$ and $[MF]$ are the (molar) concentrations of free motors, free filament sites and bound motors, respectively. Let there be N_{si} filament sites available for binding of the N motors in the system. If N_{b} and N_{ub} denote the number of bound and unbound motors, so that $N = N_{\text{b}} + N_{\text{ub}}$, one has

$$[M] = \frac{N_{\text{ub}}}{N_{\text{A}} V_{\text{S}}} \qquad \text{and} \qquad [MF] = \frac{N_{\text{b}}}{N_{\text{A}} V_{\text{S}}} \tag{A.6}$$

where N_{A} is the Avogadro constant and V_{S} is the system volume. If there are very many filament binding sites N_{si} available, i.e. $N_{\text{si}} \gg N$, then the number of free filament sites (with no motors bound) is approximately equal to the total number of filament sites, and one has

$$[F] \approx \frac{N_{\text{si}}}{N_{\text{A}} V_{\text{S}}}. \tag{A.7}$$

This leads to the desorption constant

$$K_{\text{exp}} \approx \frac{N_{\text{si}} N_{\text{ub}}}{N_{\text{b}}} \frac{1}{N_{\text{A}} V_{\text{S}}}. \tag{A.8}$$

A.1.2 Lattice model desorption constant

In the lattice model of Sec. 3.1, the binding and unbinding currents, i.e. the number of motors per time unit τ, are approximately (neglecting any effects due to non-constant motor densities on the filament or in solution)

$$J_{\text{bind}} \approx N_{\text{ub}} \frac{\pi_{\text{ad}}}{6\tau} P_{\text{si}} \qquad \text{and} \qquad J_{\text{unbind}} \approx N_{\text{b}} \frac{n_{\text{ad}}\epsilon}{6\tau}, \tag{A.9}$$

where $n_{\text{ad}} = 4$ is the number of lattice sites next to the filament. P_{si} is the probability to find a lattice site adjacent to the filament, from where binding can occur:

$$P_{\text{si}} = n_{\text{ad}} N_{\text{si}}\, l^3 / V_{\text{S}} \tag{A.10}$$

In the stationary state, one has

$$J_{\text{bind}} = J_{\text{unbind}} \qquad \Rightarrow \qquad \frac{N_{\text{ub}}\, N_{\text{si}}}{N_{\text{b}} V_{\text{S}}} = \frac{1}{l^3} \frac{\epsilon}{\pi_{\text{ad}}}. \tag{A.11}$$

Inserting this into Eq. (A.8) leads to

$$K_{\text{L}} = \epsilon/\pi_{\text{ad}} \approx K_{\text{exp}}\, N_{\text{A}} l^3 \approx 3 \cdot 10^{-4}\, K_{\text{exp}}/\mu\text{M} \tag{A.12}$$

where the Avogadro constant $N_{\text{A}} = 6.02 \cdot 10^{23}/\text{M/l}$ and the lattice constant $l = 8\,\text{nm}$ appropriate for MT filaments has been inserted. With a typical experimental desorption constant of kinesin 1, $K_{\text{exp}} \sim 0.5\,\mu\text{M}$, one obtains as an order of magnitude for the lattice model desorption constant

$$K_{\text{L}} = \epsilon/\pi_{\text{ad}} \sim 10^{-4}. \tag{A.13}$$

A.1.3 Bead model desorption constant

In the lattice model considered above, the binding rate π_{ad} is the binding rate for a motor on a lattice site adjacent to the filament, i.e. in a distance of the order of 10 nm. For the bead model considered in Chap. 2 however, the binding rate π_0 for an unbound motor attached to a bead in a distance of the order of 100 nm is relevant. This binding rate is smaller because the motor head diffusively searches a region V_{search} and binds only with the binding rate π_{ad} when it reaches a volume V_{bind} close enough to the filament. Thus, the binding rate is reduced

$$\pi_0 = P_{\text{close}}\, \pi_{\text{ad}} \tag{A.14}$$

by the probability P_{close} for the motor to be sufficiently close to bind to the filament,

$$P_{\text{close}} = V_{\text{bind}}/V_{\text{search}}. \tag{A.15}$$

In order to make a simple estimation of the order of magnitude, the regions for searching and binding can be approximated as cubes:

$$V_{\text{search}} = x_{\text{search}} \cdot y_{\text{search}} \cdot z_{\text{search}} \qquad \text{and} \qquad V_{\text{bind}} = x_{\text{bind}} \cdot y_{\text{bind}} \cdot z_{\text{bind}} \tag{A.16}$$

The motor head searches for the filament in a region with lengths $x_{\text{search}} \approx y_{\text{search}} \approx z_{\text{search}} \approx 200\,\text{nm}$ corresponding to twice the motor length. The binding region close to the filament is related to the motor length $x_{\text{bind}} \approx 100\,\text{nm}$, the filament diameter $y_{\text{bind}} \approx 25\,\text{nm}$ and the size of the motor head $y_{\text{bind}} \approx 10\text{nm}$ (both for MT motors). Neglecting geometric effects which lead to a non-homogeneous probability density for the motor head inside of V_{search} and V_{bind} and to a non-homogeneous binding probability inside of V_{bind}, one thus obtains

$$P_{\text{close}} \sim 10^{-3}. \tag{A.17}$$

This leads to

$$\pi_0 = 10^{-3}\,\pi_{\mathrm{ad}} \tag{A.18}$$

and finally

$$K = \epsilon_0/\pi_0 = K_{\mathrm{L}}/P_{\mathrm{close}} \approx 0.3\,K_{\mathrm{exp}}/\mu\mathrm{M}. \tag{A.19}$$

Using kinesin 1 values as above, one obtains an estimation of the bead model desorption constant

$$K = \epsilon_0/\pi_0 \sim 10^{-1}. \tag{A.20}$$

A.2 More about motor traffic jams

This appendix is related to motor traffic jams in tubular compartments discussed in Chap. 3. First, we discuss the parameter adaption for the model for large-scale motor traffic of this chapter in Sec. A.2.1. Then we describe the calculations of the jamming behaviour for the closed tube in Sec. A.2.2 and and for the half-open ASEP in Sec. A.2.3.

A.2.1 Parameter adaption: from small to large length scales

In Chap. 3 we describe a generic model for large-scale molecular motor traffic in a continuous and in a lattice version. These models do not make assumptions about the detailed motor mechanism. They can also be applied to various types of 'motor particles' which consist of cargo particles with one or several molecular motors attached. They can be adapted to the various situations and to special motors or cargos by appropriately choosing the model parameters.

Single motors. If the particles are single motors or cargos carried by single motors, then the rates of these large-scale models are directly related to the single-motor rates under no external force discussed in Chap. 2:

$$\begin{array}{rcrcll} \text{large-scale traffic rates} & & & & \text{single motor on bead} & \\ \tilde{\epsilon} & = & 4\epsilon/(6\tau) & = & \epsilon(F=0) & = \epsilon_0 \\ \tilde{\pi}_{\mathrm{ad}} & = & 4\pi_{\mathrm{ad}}/(6\tau) & = & \pi(F=0)/P_{\mathrm{close}} & = \pi_0/P_{\mathrm{close}} \\ v_{\mathrm{b}} & = & \alpha l/\tau & = & v(F=0) & = v_F \end{array} \tag{A.21}$$

Special care has to be taken for the binding rate, because in the large-scale model the binding rate $\tilde{\pi}_{\mathrm{ad}}$ describes binding of a motor very close to the filament (about one filament repeat distance of 8 nm away from the filament), while in the bead model the binding rate π_0 describes binding of a motor on a bead in about 100 nm distance from the filament. Therefore, the binding rate of the motor on the bead is smaller by a factor P_{close} describing the probability for the motor to come sufficiently close to the filament to bind, see App. A.1. For MT motors, $P_{\mathrm{close}} \approx 10^{-3}$. Of course the unbound diffusion coefficient D_{ub} cannot be inferred from the smaller length scale model because it is a new feature of the larger length scale. It is related to the motor or cargo size and the effective viscosity of the surrounding solution as described in Sec. 1.1.

Motor-cargo complexes. If the particle is a motor-cargo complex transported by more than one motor as discussed in Chap. 4, the parameter adaption is more complex, because the large length scale model describes the motion of the particle by only three rates $\tilde{\epsilon}$, $\tilde{\pi}_{\mathrm{ad}}$ and v_{b}, while in a more detailed consideration on smaller length scales these rates depend in a complicated way on the dynamics of the many motors. For example, unbinding from the filament on large length scales is described by the single parameter $\tilde{\epsilon}$. A cargo transported by $N > 1$ motors, however, can be bound to the filament by a variable number $n < N$ of motors and can unbind from the filament only if all motors are unbound at the same time. Unbinding of the motor-cargo complex is therefore determined by the first passage time to the state with

no motors bound where unbinding can occur. This passage time is in general not exponentially distributed and can therefore not be described by a single rate. A reasonable course graining approximation in going from the smaller length scale (II) to the larger length scale (III) is to take the unbinding rate as the inverse mean first passage time T_0 to the state with no motors bound. Analogously, the velocity on the larger length scale can be approximated as the mean velocity of the cargo when it is bound to the filament, which can be calculated as the quotient of the mean walking distance X_0 and the mean walking time T_0 before unbinding. The binding rate on the large length scale (III) is the rate for binding of any of the N motors on the cargo. If the N motors are independent, this rate is simply N times the binding rate π_0 of a single motor. Again, this rate has to be divided by a factor of P_{close} because of the different motor-filament distance in the two models. In total:

$$\begin{array}{rcll} \text{large-scale traffic rates} & & \text{cargo transported by } N \text{ motors} & \\ \tilde{\epsilon} & = & 1/T_0 & \\ \tilde{\pi}_{\text{ad}} & = & N \cdot \pi_0 / P_{\text{close}} & \text{(A.22)} \\ v_{\text{b}} & = & X_0/T_0 & \end{array}$$

Note that these identifications reproduce the correct walking time Δt_{b} and distance Δx_{b} for the large length scale model, which are the first passage time and length to unbinding:

$$\Delta t_{\text{b}} = 1/\tilde{\epsilon} = T_0 \qquad \text{and} \qquad \Delta x_{\text{b}} = v_{\text{b}}/\tilde{\epsilon} = X_0 \tag{A.23}$$

The model parameters can be adapted to specific motors or motor-cargo-complexes by using the measured parameters of this motor or motor-cargo-complex, see Sec. 2.3, and by adjusting the unbound diffusion constant D_{ub} to the size of the motor-cargo complex, see Sec. 1.1.

A.2.2 The closed tube

In Chap. 3, we have considered the large scale traffic of many motors in a half open tube. This geometry is inspired by the geometry of neuronal axons or fungal hyphae, which are closed at one end, the tip, and coupled to the cell body, which provides a motor reservoir, at the other end. A related system is one with closed boundaries at both ends which has been studied in [73, 92]. This geometry mimics the outer part of an axon in a ligation experiment, in which axonal transport has been blocked by a cut, a crush, a cold block, or a ligature [147]. In this appendix, we analyze it with the adsorption equilibrium approximation introduced in Sec. 3.2 for the half-open tube.

In the closed tube, motors cannot enter or leave the system, and the total number of motors within the tube is conserved:

$$N = \int_0^L \left[\rho_{\text{b}}(x) + \phi \rho_{\text{ub}}(x)\right] \, dx \tag{A.24}$$

For this closed system, the same arguments as for the half-open system can be applied, however the integral constraint Eq. (A.24) makes the analysis more complicated.

Typical profiles for the closed system and motors moving to the right ($v_{\text{b}} > 0$) are displayed in figure Fig. A.1(a). The profiles show the same two characteristic length scales as in the case of the half-open system: the bulk length ξ and the jam length L_*. The bulk length ξ, which is independent of the boundary densities, is again given by equation Eq. (3.8)).

Density profiles. Depending on their direction of motion, the motors jam up at one of the closed ends. In this region, the motors move slowly, and the adsorption equilibrium approximation Eq. (3.11) can be applied, which leads again to an implicit equation for the bound density:

$$\frac{x}{L} = \frac{1}{V}\left[g(\rho_{\text{b}}(x), K) - g(\rho_{\text{b}}(0), K)\right] \tag{A.25}$$

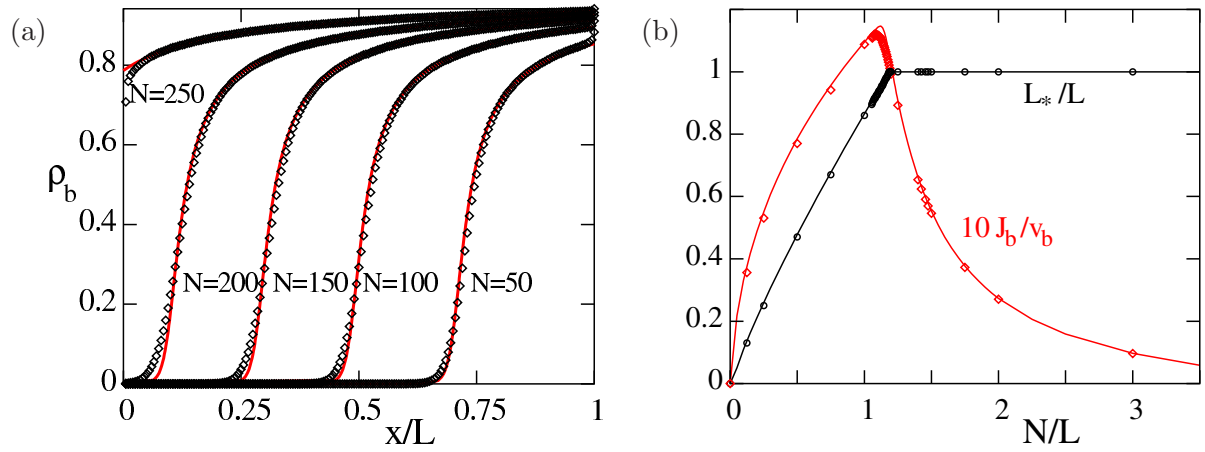

Fig. A.1: (a) Density profiles ρ_b for the closed tube for various particle numbers N as obtained from Monte Carlo simulations ($\diamond$) and from the analytical jam region approximation Eq. (A.25) (solid red lines). Parameters are $\alpha = 0.03$, $\epsilon = 0.01$, $\pi_{ad} = 1$ and $\phi = 4$. (b) Jam length L_* (black $\circ$) and average bound current J_b (red $\diamond$) for the closed tube as functions of the number N of motors within the tube. The data points are from simulations, the lines display the corresponding results from the adsorption equilibrium approximation as given by Eqs. (A.25) and (A.33). The other parameters are as in (a).

with the function g as defined in equation Eq. (3.16). This equation corresponds to Eq. (3.15), however, the left boundary density $\rho_b(0)$ is now unknown. It can be determined from the particle conservation constraint Eq. (A.24), which can be integrated when using the adsorption equilibrium approximation. This leads to:

$$V \frac{N}{L(1+\phi)} = F(\rho_b(L), K, \phi) - F(\rho_b(0), K, \phi) \tag{A.26}$$

with the function

$$F(\rho, K, \phi) = \frac{1}{K} \ln \left[\frac{\left| \frac{1}{1-K} - \rho \right|}{1-\rho} \right] - \frac{1}{1-(1-K)\rho} \left[1 + \frac{K}{2} \frac{\phi}{1+\phi} \frac{1}{1-(1-K)\rho} \right]. \tag{A.27}$$

Together with

$$V = g\left(\rho_b(L), K\right) - g\left(\rho_b(0), K\right) \tag{A.28}$$

(obtained from equation Eq. (A.25) by setting $x = L$) one has two nonlinear equations for the boundary densities $\rho_b(0)$ and $\rho_b(L)$, which are needed in equation Eq. (A.25). The resulting density profiles agree well with the Monte Carlo profiles in the jam region, see Fig. A.1(a).

The jam length. Because of the particle number constraint Eq. (A.24), it is difficult to obtain an explicit equation for the jam length L_*. However, two approximations described below give a rough but robust estimate of the jam length:

$$\frac{L_*}{L} = \frac{N}{L(1+\phi)} + \frac{1}{V} f_c(K, \phi) \tag{A.29}$$

where the function f_c depends on the specific approximation. The first term $N/L/(1+\phi)$ describes a 'compact jam': it is the value of the jam length if all motors fill up every lattice site at the right end of the tube irrespective of whether it is a filament or a non-filament site. The second term is a correction term which describes an increase of the jam length due to the diffusive backward current of the motors. Eq. (A.29) predicts that for fixed K, the scaled jam lengths $V\, L_*/L$ as a function of the scaled motor density $V\, N/(1+\phi)/L$ should fall on a Master curve. This is indeed the case, see Fig. A.2(a).

In order to obtain corrections to the compact jam term, we first approximate the left boundary density $\rho_b(0) \approx 0$ and the right boundary density $\rho_b(1) \approx 1$. By using this in

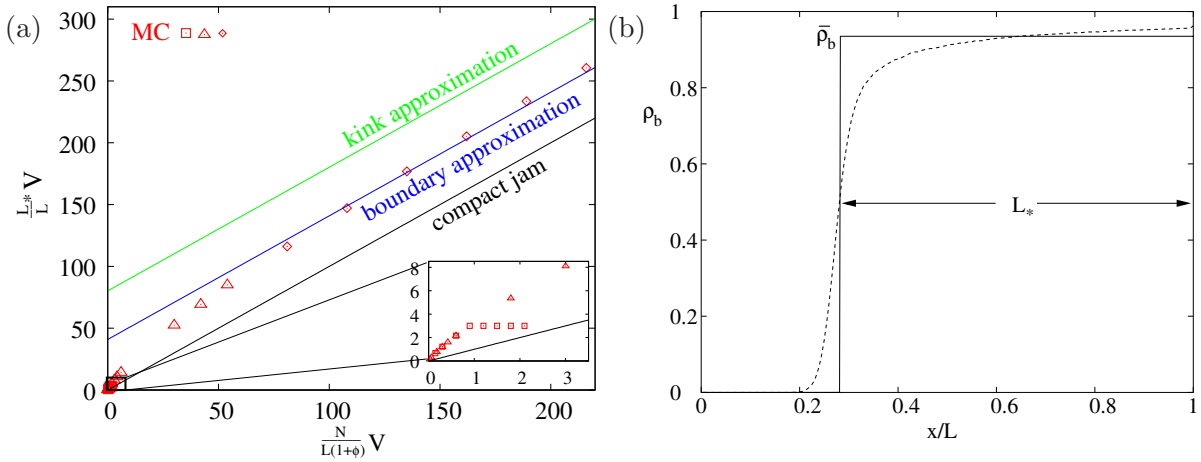

Fig. A.2: (a) The scaled jam lengths $V\,L_*/L$ as a function of the scaled motor density $V\,N/(1+\phi)/L$ from various MC simulations ($\epsilon = 0.01$, $\pi_{\rm ad} = 1$, $\phi = 5$, and ◇ $\alpha = 0.9$, $N = 300 \ldots 900$; △ $\alpha = 0.0005 \ldots 0.9$, $N = 200$; □ $\alpha = 0.01$, $N = 50 \ldots 700$) fall on a Master curve. For large scaled motor densities, the scaled jam length increases linearly, as predicted by the compact jam, the kink approximation Eq. (A.32), or the boundary approximation Eq. (A.30). The jam length for $\alpha = 0.01$, $N = 50 \ldots 700$ □, which can be seen in the inset, saturate for $L_* = L$. (b) Approximation of the bound density profile $\rho_{\rm b}$ (dashed line) by a kink (solid line).

Eqs. (A.25), (A.26) and (A.28) and carefully treating the divergences of the functions $F(\rho, K, \phi)$ and $g(\rho, K)$ for $\rho = 0$ and $\rho = 1$, we obtain the jam length as in Eq. (A.29) with

$$f_{\rm c}(K,\phi) = \frac{1}{2}\frac{(1-K^2)}{K}\frac{\phi}{(1+\phi)} - \frac{1-K^2}{K}\ln(1-K) + K\ln K - g(\frac{1}{2}, K) \tag{A.30}$$

Next we approximate the bound density profile by a kink of constant density $\overline{\rho}_{\rm b}$ located at the shock position L_* as shown in Fig. A.2(b). The shock position L_* and the bound and unbound kink densities $\overline{\rho}_{\rm b}$ and $\overline{\rho}_{\rm ub}$ can be obtained from the following conditions:

$$\begin{aligned}
&\text{Adsorption equilibrium:} && \overline{\rho}_{\rm ub}(1-\overline{\rho}_{\rm b}) = K\overline{\rho}_{\rm b}(1-\overline{\rho}_{\rm ub}) \\
&\text{Particle conservation:} && L_*(\overline{\rho}_{\rm b} + \phi\overline{\rho}_{\rm ub}) = N \\
&\text{Current balance:} && J_{\rm b} = \textstyle\int_0^L v_{\rm b}\rho_{\rm b}(1-\rho_{\rm b}) = v_{\rm b}L_*\overline{\rho}_{\rm b}(1-\overline{\rho}_{\rm b}) \\
& && = J_{\rm ub} = -\phi D_{\rm ub}\textstyle\int_0^L \rho'_{\rm ub}(x)dx = -\phi D_{\rm ub}\overline{\rho}_{\rm ub}
\end{aligned} \tag{A.31}$$

These three conditions lead to a polynomial equation of third order for the jam length L_*, which in the limit of large rescaled motor densities $V\,N/(1+\phi)/L$ is solved by Eq. (A.29) with

$$f_{\rm c}(K,\phi) = \frac{K+\phi}{K(1+\phi)}. \tag{A.32}$$

While the compact jam approximation (first term in Eq. (A.32)) underestimates the jam length, both the boundary approximation Eq. (A.30) and the kink approximation Eq. (A.32) overestimate the jam length, see Fig. A.2(a). However, for large scaled motor density $V\,N/(1+\phi)/L$, the boundary approximation becomes very good.

Comparing the closed tube jam length Eq. (A.32) with the half-open tube jam length Eq. (3.17), they show similar behaviour: they are proportional to the inverse Péclet number V and to a function depending on the desorption constant K and the tube cross section ϕ. However, the term $N/L/(1+\phi)$, which describes a compact jam, only appears for the closed tube. It is caused by the constaint Eq. (A.24) of fixed particle number which is absent in the case of the half-open tube.

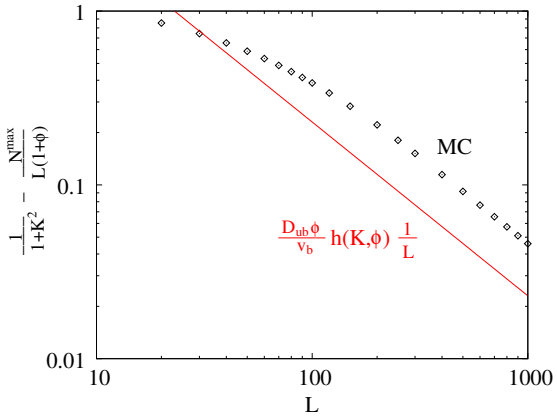

Fig. A.3: For tubes with large lengths L, the extremizing motor density $\frac{N^{\max}}{L(1+\phi)}$ approaches the limit $\frac{1}{1+K^2}$: The difference of the two values in the Monte Carlo simulation (black $\diamond$) tends to zero as $1/L$, as predicted by Eq. (A.36) (red solid line). Simulation parameters are $\alpha = 0.1$, $\epsilon = 0.01$, $\pi_{\text{ad}} = 1$ and $\phi = 4$.

The average bound current. The average bound current and its maximum can be calculated in the same way as for the half-open tube, leading to:

$$\frac{J_{\text{b}}}{v_{\text{b}}} = \frac{1}{V}\frac{K}{(1-K)^2}\left[\frac{1}{\frac{1}{1-K} - \rho_{\text{b}}(L)} - \frac{1}{\frac{1}{1-K} - \rho_{\text{b}}(0)}\right] \tag{A.33}$$

with an extremum as function of the particle number N at

$$j_{\text{b}}\left(\rho_{\text{b}}(0)\right) = j_{\text{b}}\left(\rho_{\text{b}}(L)\right) \quad \text{or} \quad \rho_{\text{b}}(0) = 1 - \rho_{\text{b}}(L). \tag{A.34}$$

Thus, from equation Eq. (A.26), the maximum occurs for the particle number

$$\frac{N^{\max}}{L(1+\phi)} = \frac{1}{V}\left[F(1-\rho_{\text{b}}(L)) - F(\rho_{\text{b}}(L))\right]. \tag{A.35}$$

The results for the average current agree quite well with the simulation results, see Fig. A.1(b). Only near the current extremum the Monte Carlo curve is slightly sharper than the curve from the adsorption equilibrium approximation. This leads to a different value for the current extremizing particle number $N^{\max}$, see Fig. A.3.

For a very long tube, the current extremum occurs at particle number

$$\frac{N^{\max}}{L(1+\phi)} \approx \frac{1}{1+K^2}\left(1 + \frac{1}{L}\frac{D_{\text{ub}}\phi}{v_{\text{b}}}h(K,\phi)\right) \tag{A.36}$$

with $h(K,\phi) = \frac{(1-K)^2}{K} - \frac{1}{K}\ln K - \frac{(1-K)(1+K^2)}{2K}\frac{2+(3+K)\phi}{1+\phi}$. It thus approaches $\frac{1}{1+K^2}$ for large L with a correction that scales as $1/L$. This is confirmed in simulations, see Fig. A.3.

A.2.3 Solution of the mean field half-open ASEP

In Sec. 3.6.1 we consider the half-open ASEP. Its dynamics is described by the equation

$$\partial_t \rho(x,t) = D\partial_x^2 \rho(x,t) - v\partial_x \rho(x,t)\left(1-\rho(x,t)\right), \tag{A.37}$$

where the first term describes diffusion with diffusion constant D, while the second term describes directed motion with velocity v. The factor $1-\rho$ implements hard-core exclusion. Half-open boundary conditions mean that the left boundary density is fixed to $\rho(0,t) = \rho_{\text{in}}$. In Sec. 3.6.1 we determined the stationary state of this system, Eq. (3.33), which is characterized by a jam with length L_* given by Eq. (3.34). In this appendix, we calculate the full time-dependent solution of Eq. (A.37), subject to the initial condition

$$\rho(x,0) = \rho_{\text{in}}\Theta(-x) \tag{A.38}$$

which describes an initially empty system. This allows to study the building up of the jam with time-dependent length $L_*(t)$.

A.2.3.1 Burgers equation

Eq. (A.37) can be mapped onto the noiseless Burgers equation

$$\partial_t u(x,t) = D\partial_x^2 u(x,t) + vu(x,t)\partial_x u(x,t) \tag{A.39}$$

via $u(x,t) = 2\rho(x,t) - 1$. The initial and boundary conditions transform to:

$$u(x,t) = (2\rho_{\rm in} - 1)\Theta(-x) - \Theta(x) \qquad \text{and} \qquad u(0,t) = 2\rho_{\rm in} - 1 =: u_{\rm in} \tag{A.40}$$

A.2.3.2 Exact solution via Cole-Hopf transformation

The Burgers equation in turn can be mapped onto a diffusion equation

$$\partial_t w(x,t) = D\partial_x^2 w(x,t) \tag{A.41}$$

via the Cole-Hopf transform

$$w(x,t) = \exp\left(\frac{v}{2D}\int^x u(x',t)dx'\right) \tag{A.42}$$

$$u(x,t) = \frac{2D}{v}\,\partial_x \log w(x,t) = \frac{2D}{v}\frac{\partial_x w(x,t)}{w(x,t)}, \tag{A.43}$$

if a time-dependent factor in the function w is chosen appropriately. The boundary and initial conditions translate into

$$\partial_x w(0,t) = \frac{v}{2D}u_{\rm in}w(0,t) \qquad \text{and} \qquad w(x,0) = \mathrm{e}^{-\frac{v}{2D}x}. \tag{A.44}$$

A solution to the diffusion equation with this boundary and initial condition can be found by means of Green functions [15]:

$$\begin{aligned} w(x,t) &= \frac{1}{2}\,\mathrm{e}^{-\frac{v}{2D}(x-\frac{1}{2}vt)}\left[2 - \mathrm{erfc}\left(\frac{x}{\sqrt{4Dt}} - \frac{v}{2}\sqrt{\frac{t}{D}}\right)\right] \\ &+ \frac{1}{2}\frac{\rho_{\rm in}}{1-\rho_{\rm in}}\mathrm{e}^{\frac{v}{2D}(x+\frac{1}{2}vt)}\,\mathrm{erfc}\left(\frac{x}{\sqrt{4Dt}} + \frac{v}{2}\sqrt{\frac{t}{D}}\right) \\ &- \frac{1}{2}\frac{(2\rho_{\rm in}-1)^2}{1-\rho_{\rm in}}\mathrm{e}^{\frac{v}{2D}u_{\rm in}(x+\frac{1}{2}vu_{\rm in}t)}\,\mathrm{erfc}\left(\frac{x}{\sqrt{4Dt}} + \frac{v}{2}u_{\rm in}\sqrt{\frac{t}{D}}\right) \end{aligned} \tag{A.45}$$

From this, the time-dependent density profile can be calculated by

$$\rho(x,t) = \frac{D}{v}\frac{\partial_x w(x,t)}{w(x,t)} + \frac{1}{2} \tag{A.46}$$

From this, the jam length $L_*(t)$, which is defined via $\rho(L_*,t) = 1/2$, can be determined numerically from

$$\partial_x w(L_*,t) = 0 \tag{A.47}$$

For small times, one obtains a diffusive behaviour

$$L_*(t) \approx \frac{2\rho_{\rm in}-1}{\rho_{\rm in}}\sqrt{\pi D}\sqrt{t}, \tag{A.48}$$

and for large times an exponential approach of the stationary value:

$$L_*(t) \approx \frac{D}{v}\log\left(\frac{\rho_{\rm in}}{1-\rho_{\rm in}}\right) + \frac{D}{v}\frac{(2\rho_{\rm in}-1)^2}{1-\rho_{\rm in}}\left(\frac{1-\rho_{\rm in}}{\rho_{\rm in}}\right)^{\rho_{\rm in}}\mathrm{e}^{-t/t_{rel}} \tag{A.49}$$

with the large time relaxation time

$$t_{\rm rel} = \left[\frac{v^2}{D}\rho_{\rm in}(1-\rho_{\rm in})\right]^{-1}. \tag{A.50}$$

The same relaxation time is obtained for the total density and for the relaxation of a small perturbation of the stationary density ρ.

A.2.3.3 Biased diffusion without hard core

If hard-core exclusion is neglected, the dynamic equation Eq. (A.37) becomes

$$\partial_t \rho = D\partial_x^2 \rho - v\partial_x \rho. \tag{A.51}$$

The solution with boundary condition $\rho(0,t) = \rho_{\text{in}}$ and initial condition $\rho(x,0) = 0$ is

$$\rho(x,t) = \frac{1}{2}\rho_{\text{in}} \mathrm{e}^{\frac{v}{D}x} \mathrm{erfc}\left[\frac{x}{\sqrt{4Dt}} - \sqrt{\frac{v^2}{4D}t}\right] + \frac{1}{2}\rho_{\text{in}} \mathrm{erfc}\left[\frac{x}{\sqrt{4Dt}} + \sqrt{\frac{v^2}{4D}t}\right]. \tag{A.52}$$

For large times, the jam length L_* approaches its stationary value $L_*^{\text{stat}} = -\frac{D}{v}\ln(2\rho_{\text{in}})$ roughly exponentially

$$L_*(t) - L_*^{\text{stat}} \sim \frac{1}{t^{3/2}} \exp\left[t/t_{\text{rel}}^{\text{noHC}}\right] \tag{A.53}$$

with the relaxation time $t_{\text{rel}}^{\text{noHC}} = 4D/v^2$. This is always smaller than the relaxation time Eq. (A.50) for diffusion with hard core:

$$t_{\text{rel}}^{\text{noHC}} = \frac{4D}{v^2} \quad < \quad \frac{D}{v^2}\frac{1}{\rho_{\text{in}}(1-\rho_{\text{in}})} = t_{\text{rel}} \tag{A.54}$$

As expected, hard core exclusion slows down the dynamics. This slowing down is inversely proportional to the undimensionalized in-current $j_{\text{in}} = \rho_{\text{in}}(1-\rho_{\text{in}}) < \frac{1}{4}$. For maximal in-current $\rho_{\text{in}} = \frac{1}{2}$, the dynamics is as fast as for biased diffusion without hard core.

A.3 Calculations related to Master equations

In this appendix we describe calculations related to Master equations which we need in Chap. 4. In Sec. A.3.1 we present a diagram method for calculating the stationary solution of the Master equation, which we use in Sec. A.3.2 to show that cargo unbinding from the filament does not affect the stationary probability conditioned on being bound to the filament. In Sec. A.3.3 we derive formulas for the average sojourn and return times of a Markov process, which we use in order to calculate run times in the tug-of-war model. In Sec. A.3.4 we deal with a Markov process with substates, which is a generalization of the situation considered in Sec. 4.2.1.

The general form of the Master equation for the time evolution of the probability p_i to be in the state i, $i = 1, \ldots, N$, is

$$\partial_t p_i = \sum_{j \neq i} \omega_{ji} p_j - \omega_i \, p_i. \tag{A.55}$$

Here, ω_{ji} denotes the transition rate from state j to state i, and $\omega_i = \sum_{j \neq i} \omega_{ij}$ is the total out-rate from state i.

A.3.1 The diagram method for the stationary state

In this appendix we describe the diagram method for calculating the stationary state solution of the Master equation (A.55), i.e. the solution of

$$\sum_{j \neq i} \omega_{ji} p_j - \omega_i \, p_i = 0. \tag{A.56}$$

This equation is a linear equation for the probability vector $\{p_i\}$ and can therefore be solved in principle by matrix methods. The diagram method is a more intuitive way to accomplish this task 'by hand'. It is useful for general arguments, which is why we use it in Sec. A.3.2.

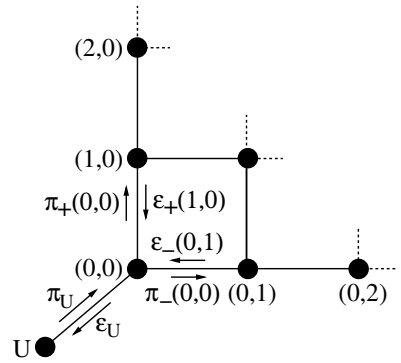

Fig. A.4: Lower left corner of the tug-of-war states network with the addition of state U representing an unbound freely diffusing cargo.

However, it is inconvenient for numerical calculations and tractable only for a small number of states. The diagram method is based on the Kirchhoff rules for electrical networks and has been rediscovered several times. A recent pedagogic introduction can be found in [51].

The states i in the Master equation form the vertices of a network, with a total of N vertices. Two vertices i and j are connected by two directed links weighted with the transition rates ω_{ij} and ω_{ji}. In order to get the stationary state p_n (stationary state probability to be in vertex n), the diagram method works as follows:

1. Construct the complete set of *partial diagrams*. A partial diagram is a diagram with the maximum number of lines that can be included without forming a closed cycle.

2. Construct the *directional diagrams* for state n: add arrows to the partial diagrams flowing towards state n (i.e. all paths must end in n). Flows in the directional diagram may converge but never diverge (this would require a cycle in the partial diagram). Each directional diagram represents the product of the rates ω_{ij} of the arrows of the directional diagram, i.e. a product of N rates ω_{ij}.

Then the stationary probability to be in vertex n is given by

$$p_n = \frac{\text{sum of directional diagrams of state } n}{\text{sum of } \textit{all} \text{ directional diagrams}} \tag{A.57}$$

A.3.2 Independence from cargo (un)binding

In this appendix we show that in the tug-of-war model of Sec. 4.2 the stationary probabilities of the cargo conditioned on being bound to the filament are independent of the rates connecting it to its unbound diffusive state.

The cargo state is characterized by the number n_+ of plus and n_- of minus motors that link it to the filament. Cargo unbinding can only occur when no motors link the cargo to the filament, i.e. in the state $n_+ = n_- = 0$. This state can be split into two states, see Fig. A.4: an unbound diffusing state U where the cargo is far away from the filament, and a state $(0,0)$ where the cargo is close to the filament as if bound by motors (but no motor *is* bound). The cargo is in the $(0,0)$ state, if for example the last motor linking it to the filament has just unbound a short time ago. From state $(0,0)$, the cargo can 'rebind' to the filament due to binding of a plus or a minus motor. Alternatively, the cargo can 'unbind' from the filament by diffusing away into the unbound state U. This is described by the unbinding rate ϵ_U. The binding rate π_U from state U to state 0 describes the probability that the freely diffusing cargo comes close enough to the filament for a motor to bind.

The rates leading from the $(0,0)$ state to the states with one bound plus resp. minus motor are the rates for the binding of the respective motor when the cargo is close to the filament, i.e. the rates $\pi_+(0,0)$ resp. $\pi_-(0,0)$ described in Sec. 4.2.[1] Analogously, the rates leading into the

[1] All the rates $\pi_\pm(n_+, n_-)$ use the single motor rates $\pi_{0\pm}$ of Chap. 2 which are the rates for the binding of a plus resp. minus motor to the filament when the cargo is close to the filament.

state $(0,0)$ via unbinding of a single plus resp. minus motors are just the rates $\epsilon_+(1,0)$ resp. $\epsilon_-(0,1)$ described in Sec. 4.2.

The rates π_U and ϵ_U relate to diffusion of the cargo in the surrounding solution and therefore depend on the geometry of the system, e.g. the location of the filaments or the volume and viscosity of the surrounding medium. The rate π_U is the rate for the cargo coming close to the filament when it is freely diffusing in the surrounding solution, while ϵ_U is the rate of diffusing away when close but not bound to the filament.

Let $P(n_+, n_-)$ denote the (stationary) probability of having n_+ plus and n_- minus motors linking the cargo to the filament, and $P(U)$ the (stationary) probability of being in the diffusive unbound state U. As experiments only monitor bound cargos, they consider the conditional probabilities, i.e. conditioned on the cargo being bound:

$$p(n_+, n_-) = P(n_+, n_-)/\left[1 - p(U)\right] \tag{A.58}$$

for $0 \leq n_+ \leq N_+$ and $0 \leq n_- \leq N_-$. The state $(0,0)$ is included here, since in this state the cargo has not diffused away yet.

In the stationary state, these conditional probabilities do not depend on the rates π_U and ϵ_U for binding and unbinding of the cargo. To show this we consider the calculation of the stationary state via the diagram method explained in App. A.3.1. Let Π_i^n denote the product of rates associated with the ith directional diagram of state n, where n can be one of the state (n_+, n_-) with $0 \leq n_+ \leq N_+$ and $0 \leq n_- \leq N_-$, or U. Then the stationary state probability of state n is given by

$$P(n) = \textstyle\sum_i^n \Pi_i^n / S. \tag{A.59}$$

Here, $S = \sum_n \sum_i^n \Pi_i^n$ is the sum of all directional diagrams. $\sum_i^n$ denotes the sum over all directional diagrams i of state n, and $\sum_n$ the sum over all states. Because of the equality

$$1 - P(U) = \left(S - \sum_i \Pi_i^U \right) / S, \tag{A.60}$$

the conditional probability to be in state n under the condition not to be in state U is:

$$p(n) = \frac{P(n)}{1 - P(U)} = \frac{\sum_i \Pi_i^n}{S - \sum_i \Pi_i^U} \tag{A.61}$$

Now consider the directional diagrams Π_i^n in more detail. They all contain the line $U - (0,0)$, as this line is never part of a cycle. Any directional diagram Π_i^U for state U contains the rate ϵ_U, but not the rate π_U, as all paths in these directional diagrams must end in state U. On the other hand, all directional diagrams Π_i^n with $n \neq U$ contain the rate π_U but not ϵ_U (otherwise there would be a path ending in U, but all paths must end in n). Thus in Eq. (A.61), ϵ_U does not appear (the terms in the total sum S in the denominator containing ϵ_U are substracted) and the rates π_U appear exactly once in every term in the numerator and denominator and thus cancel out. Thus $p(n)$ does not depend on the rates π_U and ϵ_U.

A.3.3 Sojourn and return times in a stationary Markov process

In this appendix we calculate some average times associated with a continuous-time discrete-space random walk that is described by the Master equation Eq. (A.55). We are interested in the stationary state solution with $\partial_t p_i = 0$ for all states i. Furthermore, we are often interested in a subset A of states. Such a subset has the stationary state probability

$$p(A) = \sum_{i \in A} p_i, \tag{A.62}$$

which is simply the sum of all probabilities of the states belonging to A. When talking about average times, one should average over trajectories in the stationary state. In the case of starting in a subset A of states, this means that the starting probabilities are the stationary probabilities confined to the subset A:

$$p_i(t=0) \;=\; p_i/p(A) \;\text{ for }\; i \in A, \quad \text{ and } \; 0 \;\text{ else}$$

This differs from the typically considered case of starting in a single state i_0.

A.3.3.1 Average sojourn times

For a Markov process described by the Mater equation Eq. (A.55), the waiting or sojourn time in a single state i is exponentially distributed with parameter ω_i, i.e. the average sojourn time for a single state is simply

$$\tau_i = 1/\omega_i. \tag{A.63}$$

For a subset A, the current (number of transits per unit time) out of A is

$$j_A = \sum_{i\in A, j\notin A} p_i\,\omega_{ij}. \tag{A.64}$$

In the stationary state, this is equal to the current into A, i.e. out of the complement A^C:

$$j_{A^C} = \sum_{i\in A^C, j\in A} p_i\,\omega_{ij} = j_A. \tag{A.65}$$

The number of visits to A in total time T is equal to the number of transitions into or out of A:

$$n_A = T\,j_{A^C} = T\,j_A. \tag{A.66}$$

The total time spent in A in time T is $t_A = T\,p(A)$. Thus, the average time spent in A during one visit is:

$$\tau_A = \frac{t_A}{n_A} = \frac{p(A)}{j_A} = \frac{p(A)}{\sum_{i\in A, j\notin A} p_i\,\omega_{ij}} \tag{A.67}$$

This sojourn time is not equal to the weighted average of the single sojourn times, $\tau_A \neq \sum_{i\in A} \tau_i\, p_i/p(A)$.

A.3.3.2 Average return times

The average return time to a single state i is [3]

$$T_i = \frac{1}{p_i\,\omega_i} \tag{A.68}$$

This is a special case of the average return time to a subset A which we derive now in a heuristic way. In the stationary state the walk is a sequence of visits to the subset A and to its complement A^C. The return time to A is then measured in the following way: when the walk reaches A, the clock is started. It then spends some time in A (the sojourn time τ_A on average), then leaves A and spends some time in A^C (the sojourn time τ_{A^C} on average) until it returns to A, at which time the clock is stopped, one return time is noted, and the clock is started again for the measurement of the next return time. The average return time is then determined by averaging over all times measured in this way with the result

$$T_A = \tau_A + \tau_{A^C} = \frac{p(A)}{j_A} + \frac{p(A^C)}{j_{A^C}} = \frac{p(A)}{j_A} + \frac{1-p(A)}{j_A} = \frac{1}{j_A} = \frac{1}{\sum_{i\in A, j\notin A} p_i\,\omega_{ij}}. \tag{A.69}$$

A.3.4 Master equations with substates

In this appendix we consider a system that can occupy states which are sorted into groups labeled by $i = 1, \ldots, N$. Each group i consists of n_i substates, but we are not interested in which substate the system actually is, only in what group i it is. An example for this is a cargo with N_+ plus and N_- minus motors, of which n_+ plus and n_- minus motors are bound to a microtubule filament. We are not interested *which* of the N_+ plus motors are bound to the microtubule but only *how many* of them are bound in total, i.e. in the number n_+ (and analogous for the minus motors). Thus the states of interest are the states (n_+, n_-), and each of these states has $\binom{N_+}{n_+}\binom{N_-}{n_-}$ substates which correspond to a different choice of motors binding the cargo to the microtubule.

We label the states of the system by (i, k), where $i = 1, \ldots, N$ are the states of interest and k denumber n_i substates of state i. Let $p_{i,k}$ be the probability to be in state (i, k) and p_i the probability to be in state i (no matter what k) and $p(k|i)$ the conditional probability to be in k when knowing to be in the ensemble of states i. These quantities are connected via

$$p_i = \sum_k p_{i,k} \qquad \text{and} \qquad p(k|i) = \frac{p_{i,k}}{p_i}, \tag{A.70}$$

and obey the normalizations

$$\sum_k p(k|i) = 1 \qquad \text{and} \qquad \sum_i p_i = 1. \tag{A.71}$$

The full Master equation (for all states, including the substates) reads

$$\partial_t p_{i,k} = -\sum_{i'k'} \left[p_{i,k}\alpha_{ik\to i'k'} - p_{i',k'}\alpha_{i'k'\to ik} \right] = -\sum_{i'k'} J_{ik\to i'k'} \tag{A.72}$$

with the transition rates $\alpha_{ik\to i'k'}$ from states (i, k) to (i', k') and the current $J_{ik\to i'k'} = p_{i,k}\alpha_{ik\to i'k'} - p_{i',k'}\alpha_{i'k'\to ik}$ from (i, k) to (i', k'). The Master equation can also be expressed as

$$\begin{aligned} \partial_t p_{i,k} &= -\sum_{i'\neq i} \left[p_i \sum_{k'} p(k|i)\alpha_{ik\to i'k'} - p_{i'} \sum_{k'} p(k'|i')\alpha_{i'k'\to ik} \right] \\ &\quad -p_i \sum_{k'} \left[p(k|i)\alpha_{ik\to ik'} - p(k'|i)\alpha_{ik'\to ik} \right] \quad = \quad -\sum_{i'\neq i} J_{ik\to i'k'} - p_i \sum_{k'} J^i_{kk'} \end{aligned}$$

with $J^i_{kk'} = p(k|i)\alpha_{ik\to ik'} - p(k'|i)\alpha_{ik'\to ik}$. The first term describes the flow between different states i, i', the last term describes flow inside of the state ensemble i. Summing over k leads to

$$\begin{aligned} \partial_t p_i &= -\sum_{i'\neq i} \left[p_i \underbrace{\sum_{kk'} p(k|i)\alpha_{ik\to i'k'}}_{=:\omega_{ii'}} - p_{i'} \underbrace{\sum_{kk'} p(k'|i')\alpha_{i'k'\to ik}}_{=:\omega_{i'i}} \right] \\ &\quad - p_i \sum_{kk'} \underbrace{\left[p(k|i)\alpha_{ik\to ik'} - p(k'|i)\alpha_{ik'\to ik} \right]}_{=J^i_{kk'}} \quad = \quad -\sum_{i'\neq i} \left[p_i\omega_{ii'} - p_{i'}\omega_{i'i} \right] - p_i \sum_{kk'} J^i_{kk'} \end{aligned}$$

The last term describes flow inside of state i; the total sum is zero:

$$\sum_{kk'} J^i_{kk'} = \sum_{kk'} \left[p(k|i)\alpha_{ik\to ik'} - p(k'|i)\alpha_{ik'\to ik} \right] = \sum_{kk'} p(k|i)\alpha_{ik\to ik'} - \sum_{kk'} p(k|i)\alpha_{ik\to ik'} = 0$$

This shows that the dynamics of p_i does not depend on the dynamics inside of state i. Thus, for the states i of interest, one obtains the Master equation

$$\partial_t p_i = -\sum_{i' \neq i} [p_i \omega_{ii'} - p_{i'} \omega_{i'i}] \tag{A.73}$$

with the effective rates

$$\omega_{ii'} = \sum_{kk'} p(k|i) \alpha_{ik \to i'k'}. \tag{A.74}$$

However, this is yet not of much use as the rates contain the probabilities $p(k|i)$ which are unknown (unless, of course, the full Master equation has already been solved).

If the rates for the transition between the states of interest $\alpha_{ik \to i'k'}$ do not depend on the substates k, k', i.e. if $\alpha_{ik \to i'k'} = \alpha_{ii'}$, then the effective rate from state i to state i' is the number of substates of the final state i' times the substate transition rate:

$$\omega_{ii'} = \sum_{kk'} p(k|i) \alpha_{i \to i'} = n_{i'} \alpha_{ii'} \tag{A.75}$$

In this case one can use a Master equation for the effective states p_i only, because the substate dynamics drops out. This happens for the initially mentioned example of a cargo transported by N_+ plus and N_- minus motors. A transition between two of the (n_+, n_-)-states occurs via binding or unbinding of a plus or a minus motor. For this transition, it is not important *which* of the motors binds or unbinds.

A.4 More about tug-of-war motility diagrams

This appendix gives more details about the motility diagrams of the tug-of-war model of Chap. 4. In Sec. A.4.1, we investigate an alternative classification of motility states for the symmetric tug-of-war considered in Sec. 4.3.3. In Sec. A.4.1 we show that the motility diagrams are not affected substantially by the detailed form of the single motor force-velocity-relation. Sec. A.4.3 adds some details about the mean field approximation of Sec. 4.4.2, and Sec. A.4.4 presents a refined version of the sharp maximum approximation of Sec. 4.4.3.

A.4.1 Alternative motility characterization in the symmetric tug-of-war

In Sec. 4.3.3, we have characterized the motility states of the symmetric tug-of-war by the maxima of the motor number probability distribution $p(n_+, n_-)$ to have n_+ active plus and n_- active minus motors. In this section, we investigate an alternative characterization by the maxima of the probability distribution for the difference of active plus and minus motors.

In the symmetric tug-of-war the cargo velocity depends only on the difference $\Delta = n_+ - n_-$ of the number of active plus and minus motors, see Eq. (4.7). We therefore consider the corresponding probability distribution:

$$p(\Delta) = \sum_{n=\min(0,\Delta)}^{\min(N,N-\Delta)} p(n_+ + \Delta, n_-) \tag{A.76}$$

which is one-dimensional and therefore more intuitive in a graph than the two-dimensional probability $p(n_+, n_-)$, see Fig. A.5. Similar to the motor number probability $p(n_+, n_-)$, the probability $p(\Delta)$ displays either 1, 2 or 3 maxima, and thereby defines analogous motility states (0), $(-+)$ and $(-0+)$, see Fig. A.5 and Fig. A.6. For small motor force ratio f, the probability $p(\Delta)$ has a single maximum at $\Delta = 0$, and the cargo is in the (0) motility state. For large f, the probability $p(\Delta)$ has two maxima at $\Delta \neq 0$, and the cargo is in the $(-+)$ motility state. For

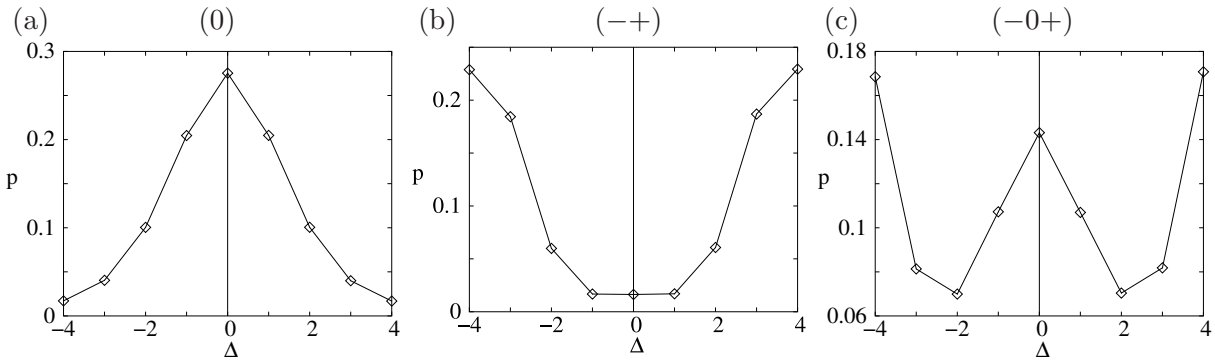

Fig. A.5: Probability distributions $p(\Delta)$ of the difference $\Delta = n_+ - n_-$ of active plus and minus motors for the symmetric tug-of-war of $N_+ = N_- = 4$ plus and minus motors. In the no-motion motility state (0), $p(\Delta)$ has a single peak at $\Delta = 0$ (a), while it has two peaks at $\Delta \neq 0$ in the $(-+)$ motility state of fast plus and minus motion (b). In the $(-0+)$ motility state all three types of maxima exist (c). Parameters are as in Fig. 4.6.

intermediate f, all three types of maxima coexist, leading to the $(-0+)$ motility state.

The motility diagrams defined via the maxima of $p(n_+, n_-)$ and $p(\Delta)$ are qualitatively similar, compare Fig. 4.7 and Fig. A.6. However, the transition lines are significantly shifted. The main reason is that the probability $p(\Delta)$ is defined via a sum, see Eq. (A.76). One consequence of this is that cargo unbinding cannot be detected anymore, as a maximum at $\Delta = 0$ can be at (n, n) with $n > 0$ (bound) or at $n = 0$ (unbound). Therefore, the $p(\Delta)$-motility diagrams of Fig. A.6 do not feature an unbound cargo state. Furthermore, for desorption constants close to the unbinding line, $K \lesssim N$, the maximum of the probability distribution fails to recognize the two fast-motion maxima at $(1, 0)$ and $(0, 1)$ because the sum of the probabilities of the neighbouring states $(0, 0)$ and $(1, 1)$ is larger than the maxima in this region.

We therefore use the classification by maxima of $p(n_+, n_-)$ in our main work. They are directly related to the cargo states (n_+, n_-), while the sum defining the probability $p(\Delta)$ in Eq. (A.76) also sums over states $p(n_+, n_-)$ with low probability. In addition, $p(\Delta)$ is no longer a good quantity to consider in the case of an asymmetric tug-of-war of different species of plus and minus motors, because then the motors are not equally strong.

A.4.2 Alternative force-velocity relation

In the tug-of-war model of Chap. 4 we use the linear force-velocity-curve Eq. (2.6) for a single motor which captures the essential features of experimental force-velocity curves. It has the advantage that we can derive explicit formulas for the forces and velocities of the motors as in Eqs. (4.6) and (4.7). In this section we examine how the detailed form of the single motor force-velocity relation influences our results. We therefore use an alternative form of the single motor force-velocity relation. A model for the motor stepping kinetics lead to the following force-velocity-curve [127]:

$$v(F) = v_F \frac{e^{-F/F_v} - e^{-F_s/F_v}}{1 - e^{-F_s/F_v}} \tag{A.77}$$

where $F_v = \mathrm{k_B}T/l$ is the characteristic force associated with the step size l. For MT motors one has $l = 8\,\mathrm{nm}$ and $F_v = 0.5\,\mathrm{pN}$. The force-velocity curve Eq. (A.77) is shown in Fig. A.7(a). For kinesin parameters, it looks quite different from our piecewise linear force-velocity-curve Eq. (2.6) and also from the experimental data shown in Fig. 2.2(a), but has similar qualitative features: it decreases monotonously with the force and exhibits slow backward motion. Unfortunately, with the force-velocity relation Eq. (A.77) the velocity balance equation Eq. (4.5) is transcendent and cannot be solved analytically. We therefore only use it in the computer simulation, where we solve it numerically by using Ridder's method [126].

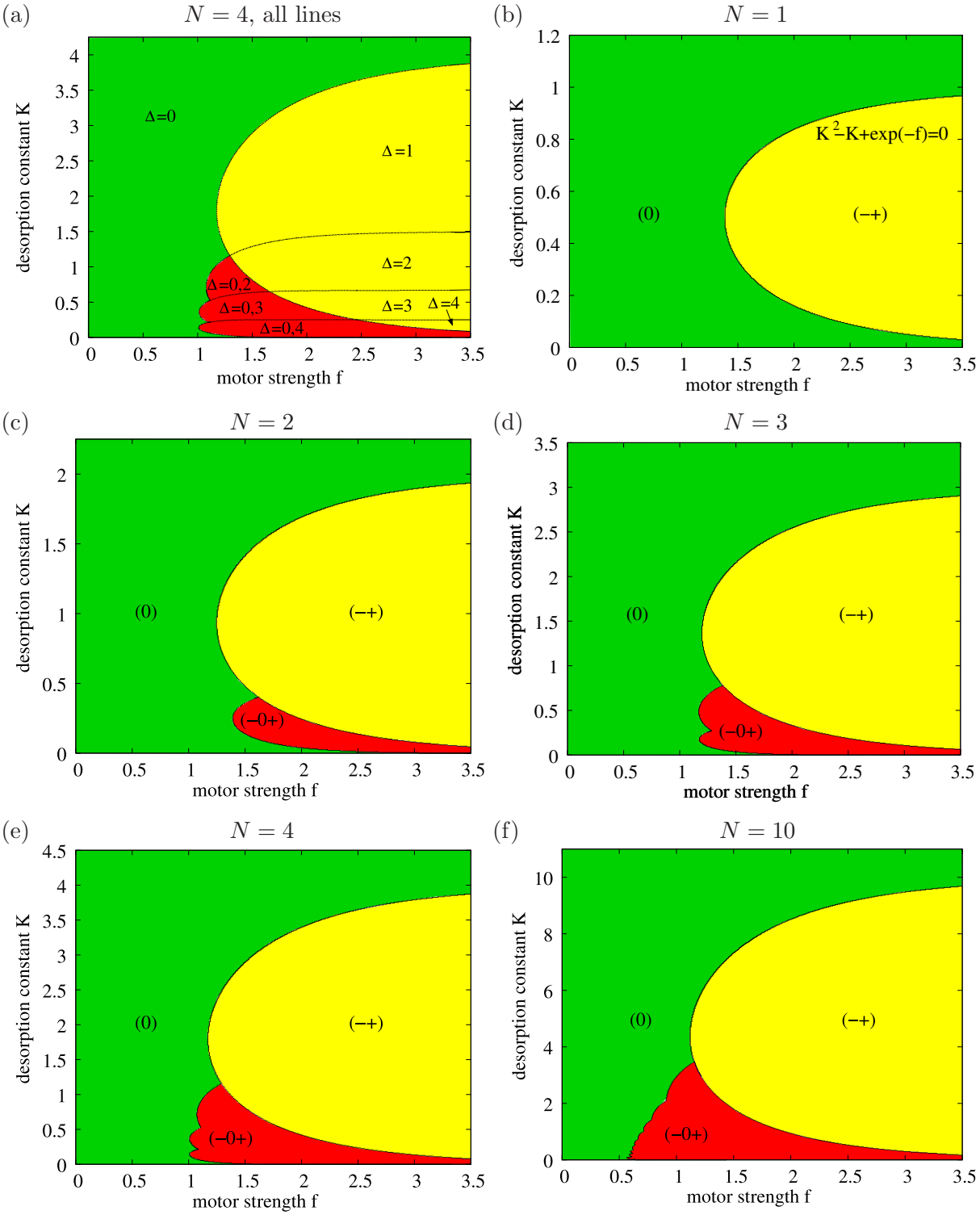

Fig. A.6: Motility diagram for the symmetric tug-of-war of $N = N_+ = N_-$ plus and minus motors as in Fig. 4.7. However, in contrast to Fig. 4.7 where the motility states (0), $(-+)$ and $(-0+)$ are defined via the maxima of the probability distribution $p(n_+, n_-)$ of the numbers n_+ and n_- of active plus and minus motors, here they are defined via maxima of the probability distribution of the difference $\Delta = n_+ - n_-$ of the number of active plus and minus motors. Although this is an intuitive theoretical classification, the experimentally relevant motility diagrams are the ones in Fig. 4.7 which are determined by the observable cargo states (n_+, n_-). Motor parameters are kinesin-like except the stall force F_s and the unbinding rate ϵ_0 which are varied. For $N = 1$, the transition line between the (0) and $(-+)$ motility states can be analytically calculated from the stationary state solution of the Master equation 4.1. It is given by the equation $K^2 - K + \exp(-f) = 0$.

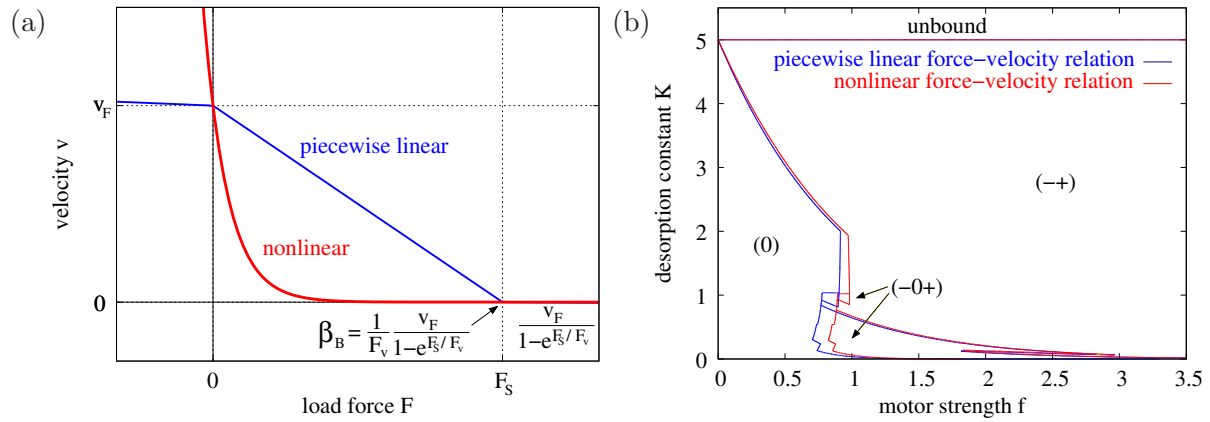

Fig. A.7: (a) Alternative force-velocity-relations $v(F)$ as given by Eq. (A.77) (red), and piecewise-linear Eq. (2.6) (blue). Parameters are for kinesin: $F_s = 6\,\mathrm{pN}$, $F_v = 0.5\,\mathrm{pN}$, $v_F = 1\,\mu\mathrm{m/s}$, $v_B = 0.006\,\mu\mathrm{m/s}$. (b) Motility diagram for the symmetric tug-of-war of $N_+ = N_- = 5$ motors with the nonlinear force-velocity relation of Eq. (A.77) (red), compared to the motility diagram with the piecewise linear force-velocity relation Eq. (2.6) (blue).

The motility diagrams of the symmetric tug-of-war of $N_+ = N_- = 5$ plus and minus motors with the same single motor parameters are compared in Fig. A.7(b). They look very similar except that the transition lines for the diagram with the nonlinear force-velocity relation are shifted to higher motor forces f. The reason is that this force-velocity relation decreases very fast to low velocities, see Fig. A.7(a), which has the same effect as a lower stall force F_s resp. a lower motor strength f.

In the case of a tug-of-war of $N_+ = 5$ kinesins against $N_- = 5$ dyneins (except the varied minus motor parameters F_{s-} and ϵ_{0-}), the same seven motility states in approximately the same parameter regions appear for both velocity relations, compare Fig. A.8 and Fig. 4.10. However, the exact location of the transition lines shift: The effectively lower stall force of the nonlinear force velocity relation leads to less cooperative effects because of less motor-motor interaction. This reduces the regions with 'cooperative' motility states like $(-+)$ and $(-0+)$, and increases regions of 'uncooperative' ones like (0) or $(+)$.

In summary the two different single motor force-velocity relations Eq. (2.6) and Eq. (A.77) lead to qualitatively similar results, especially to the same motility states for similar single motor parameter regions. Our model results therefore do not depend strongly on the exact form of the force-velocity relation, as long as it decreases monotonically with external force and exhibits slow backward motion.

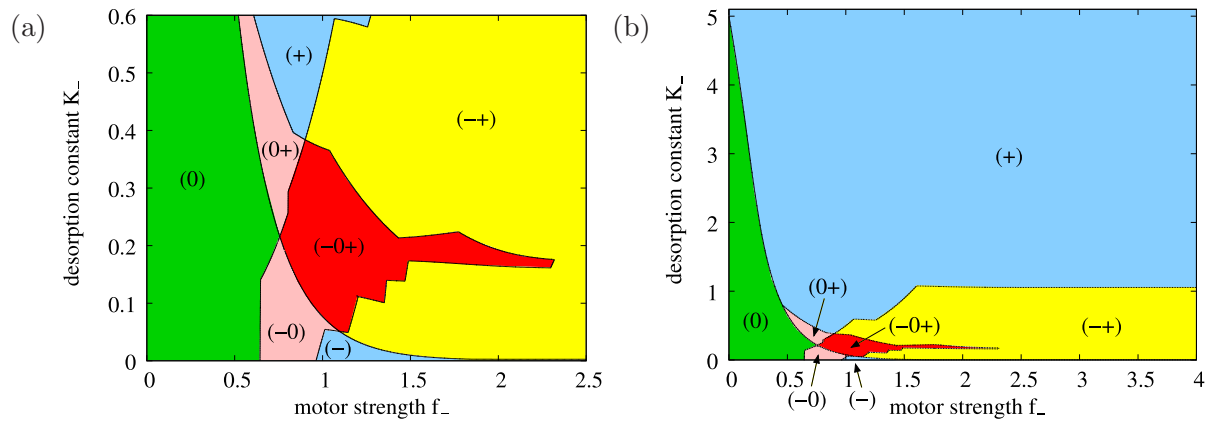

Fig. A.8: Motility diagram for the tug-of-war of $N_+ = 5$ kinesins against $N_- = 5$ dynein motors with the nonlinear force-velocity relation Eq. (A.77).

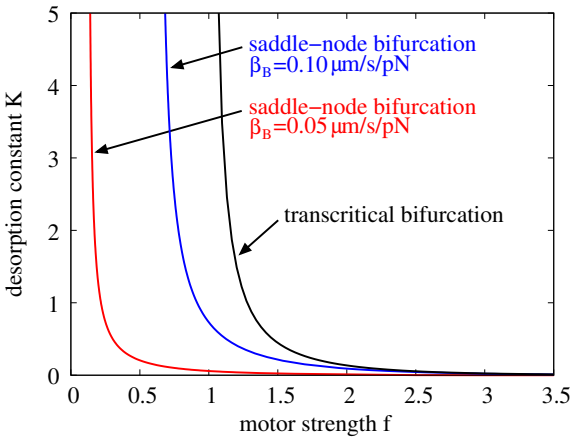

Fig. A.9: Mean field motility diagrams, as in Fig. 4.18, with varying β_B: The saddle-node bifurcation line, which separates the (0) and (−0+) motility states, wanders to the $f = 0$-axis for decreasing superstall velocity slopes $\beta_B = 0.1$ and $0.05\,\mu$m/s/pN. The transcritical bifurcation line, which separates the (−0+) and (−+) motility states, is unaffected.

A.4.3 More about the mean field approximation

In this appendix, we present more details of the mean field approximation in Sec. 4.4.2. We consider the dependence of the motility behaviour on the backward velocity in the symmetric tug-of-war, and we describe the calculation of the motility diagrams in the asymmetric case.

A.4.3.1 Small and zero backward velocity

In Sec. 4.4.2.2 we consider the symmetric tug-of-war in mean field approximation. Its parameters are the force ratio f, the desorption constant K and the ratio $\nu = v_B/v_F = \beta_B/\beta_F$ of forward-backward velocity slopes[2]. The motility diagrams shown in Fig. 4.18 detail the dependency on f and K; here we consider the dependency on ν by varying β_B.

Biological motors usually have a small backward velocity resp. a small superstall slope β_B. If β_B is decreased, the transcritical bifurcation line is not changed as it is independent of the backward velocity, see Eq. (4.66), and the phase portrait near the symmetric FP is still adequately described by Eq. (4.62). The saddle-node bifurcation line, however, wanders towards the $f = 0$ axis for smaller β_B, see Fig. A.9, and disappears for $\beta_B = 0$, see Fig. A.10(b). In the bifurcation diagram like in Fig. 4.17(a), this means that the saddle-node bifurcation of the unstable FP with $x_+ > x_-$ occurs at smaller and smaller f until it finally it disappears: the

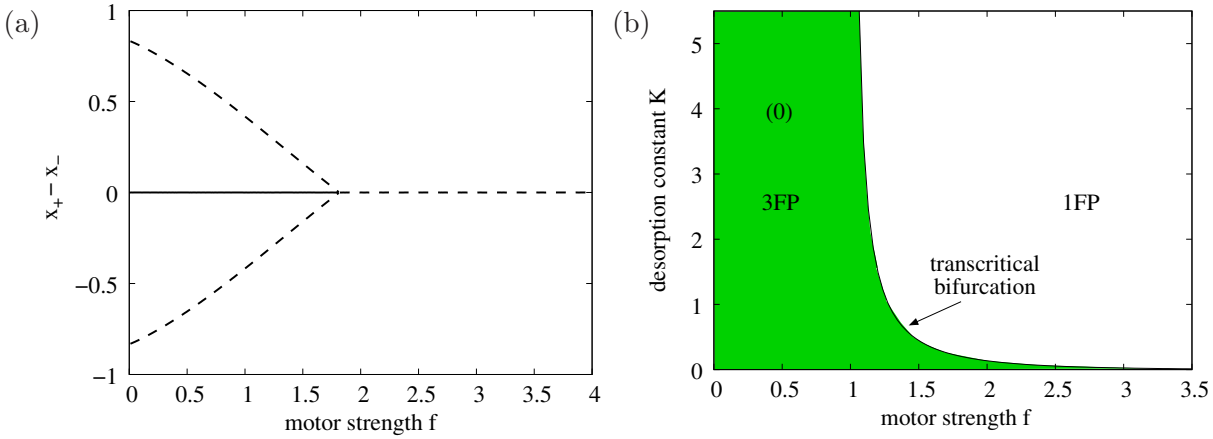

Fig. A.10: Mean field theory for zero superstall slope $\beta_B = 0$: The saddle-node bifurcation and the corresponding stable plus and minus motion FPs disappear as seen in (a) the bifurcation diagram and (b) the motility diagram.

[2] Note that although the backward velocity v_B is a more intuitive quantity than the superstall velocity slope $\beta_B = v_B/F_s$, the latter is in fact a more reasonable quantity to consider. For example in the motility diagrams like in Fig. 4.7 or Fig. 4.18, the motor stall force F_s is varied and the superstall slope β_B, *not* the backward velocity $v_B = \beta_B F_s$, is kept constant.

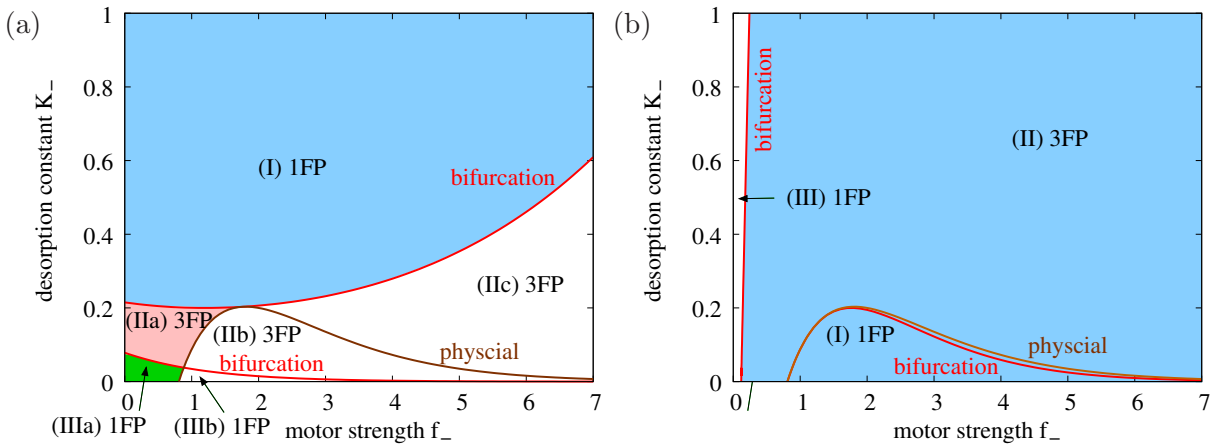

Fig. A.11: Mean field motility diagrams for the tug-of-war of kinesin-like plus against dynein-like minus motors except the minus motor stall force F_{s-} and unbinding rate ϵ_{0-} which are varied, and superstall slope $\beta_B = 0.05\,\mu$m/s/pN for (a) $G = \nu$ or (b) $G = 1/\nu$. Red lines mark saddle-node bifurcation lines, brown lines are lines with $x_+ f_+ = x_- f_-$. The colours mark the motility states characterized via the stable and physical FPs: (+) in (a) resp. (−) in (b) (light blue) and (0+) (pink). The regions marked (I-III), which are characterized via the FPs (FP), are explained in the text.

unstable FP tends to $(x_+, x_-) = (1/(1+K), 0)$ for $f \to 0$, but never reaches it; it disappears at $f = 0$, see Fig. A.10(a). This leads to a motility diagram with a single stable zero motion FP for small f and no stable FP for large f, see Fig. A.10(b).

The reason for this 'strange' behaviour is that the minus motor unbinding rate, which for $\nu = 0$ is equal to $x_+\epsilon_{0+}\,\exp(f x_+/x_-)$, diverges for $x_- \to 0$. This divergence is 'unphysical' in the sense that it does not appear for the stochastic system with finite motor numbers, where the unbinding rate is finite for $n_- = 1$ and equal to ϵ_{0+} for $n_- = 0$ and no intermediate values are possible. The divergence in the mean field theory for $\nu = 0$ can be 'rescued' by introducing a cutoff in the unbinding rate, which prevents the divergence for $x_- \to 0$ and which leads to the re-appearance of the saddle-node bifurcation.

A.4.3.2 Calculation of the asymmetric motility diagram

In Sec. 4.4.2.3 we considered the asymmetric kinesin-dynein tug-of-war in mean field approximations. Here we describe briefly how the motility diagrams of Fig. 4.19 are calculated.

We set all single motor parameters as in Tab. 2.1 and vary the minus motor stall force F_{s-} and unbinding rate ϵ_{0-}. The FP, which are solutions of Eq. (4.51), are solutions of the equivalent nullcline equations

$$x_- = \frac{x_\pm G \ln\left[(1-x_\pm)/(K_\pm x_\pm)\right]}{(f_+ + G f_-) - \ln\left[(1-x_\pm)/(K_\pm x_\pm)\right]} = h_\pm(x_\pm), \tag{A.78}$$

with the slope ratio $G = \beta_{0+}/\beta_{0-}$, which is equal to $G = \beta_{B+}/\beta_{F-} = \nu < 1$ for $x_+ f_+ > x_- f_-$ (winning plus motors) and to $G = 1/\nu > 1$ for $x_+ f_+ < x_- f_-$ (winning minus motors). As for the symmetric mean field approximation in Sec. 4.4.2.2, we solve the mean field equations separately for $G = \nu$ and $G = 1/\nu$, and then sort out the physical solutions as shown in Fig. A.11. Fig. A.11(a) and (b) show the bifurcation lines (marked in red) for $G = \nu$ and $G = 1/\nu$, respectively, which identify three regions:

(I) 1 FP: 1 stable FP with $x_+ \gg x_-$ for $G = \nu$ and with $x_+ \ll x_-$ for $G = 1/\nu$

(II) 3 FP: 1 stable FP with $x_+ \gg x_-$ for $G = \nu$ and with $x_+ \ll x_-$ for $G = 1/\nu$, and 1 stable and 1 unstable FP with $x_+ f_+ \sim x_- f_-$

(III) 1 FP: 1 stable FP with $x_+ f_+ \sim x_- f_-$

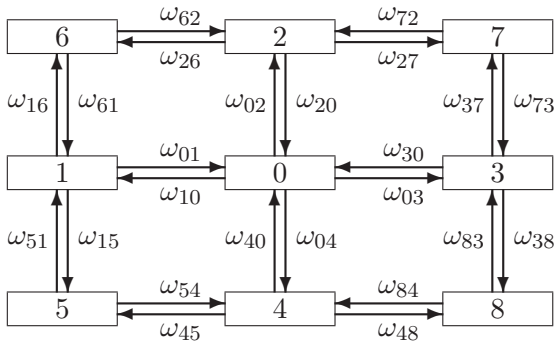

Fig. A.12: The maximum point at 0, its direct neighbours 1, 2, 3, 4, and its diagonal neighbours 5, 6, 7, 8, and the rates connecting them.

Only FPs with $x_+f_+ > x_-f_-$ for $G = \nu$ and with $x_+f_+ < x_-f_-$ for $G = 1/\nu$ are physical. The physical separation line with $x_+f_+ = x_-f_-$, given by

$$K_- = \left[\frac{f_-}{f_+}\left(1 + K_+\,\mathrm{e}_+^f\right) - 1\right]\,\mathrm{e}^{-f_-} \tag{A.79}$$

(marked in brown in Fig. A.11), separates the zero motion FPs with $x_+f_+ \sim x_-f_-$ into physical and unphysical solutions (the plus resp. minus motion FP with $x_+ \gg x_-$ resp. $x_+ \ll x_-$ are always physical). For $G = \nu$ (winning plus motors) one has, see Fig. A.11(a):

(a) all zero motion FP are physical, i.e. have $x_+f_+ > x_-f_-$

(b) 1 zero motion FP is unphysical. If a second zero motion FP exists, it is physical.

(c) all zero motion FP are unphysical, i.e. have $x_+f_+ < x_-f_-$

For $G = 1/\nu$ (winning minus motors), the physical separation line Eq. (A.79) is always in the 3FP-region, see Fig. A.11(b), and it is always the unstable zero motion FP. This means that for this case there is never a physical stable zero motion FP.

The regions with physical and stable FPs are marked with the appropriate colours in Fig. A.11. Putting these regions of Fig. A.11(a) and (b) together leads to the motility diagram shown in Fig. 4.19. In Fig. 4.19(b), also cargo unbinding has been taken into account, i.e. the line where both FP values x_+, x_- become smaller than $1/N$ for $N = 5$.

A.4.4 Refined sharp maximum approximation

In Sec. 4.4.3 we calculated an approximate motility diagram for the tug-of-war by assuming that the probability $p(n_+, n_-)$ to have n_+ plus and n_- minus motors bound is concentrated around its maxima, i.e. is non-zero only on the maximum point and its direct nearest neighbours. This lead to the conditions Eq. (4.70) for the existence of a maximum at (n_+, n_-). In a more detailed consideration, we compare the maximum not only to its *next* neighbours, labeled 1, 2, 3, 4 in Fig. 4.20 and Fig. A.12, but also to its diagonal neighbours, labeled 5, 6, 7, 8 in Fig. A.12. However, solving the Master equation involving all the points $0, \ldots, 8$ leads to nonanalytical expressions. Therefore we use the condition that the 'effective rate', e.g. $\omega_{50,\mathrm{eff}}$ from 5 to 0 should be larger than the reverse effective rate $\omega_{05,\mathrm{eff}}$ from 0 to 5. These 'effective rates' are taken to be proportional to the product of the rates on the path from 5 to 0 resp. from 0 to 5. There are two ways to reach 0 from 5, namely via 1 or 4, leading to the two conditions

$$\frac{\omega_{50,\mathrm{eff,via1}}}{\omega_{0,5,\mathrm{eff,via1}}} = \frac{\omega_{51}\omega_{10}}{\omega_{01}\omega_{15}} > 1 \qquad \text{and} \qquad \frac{\omega_{50,\mathrm{eff,via4}}}{\omega_{0,5,\mathrm{eff,via4}}} = \frac{\omega_{54}\omega_{40}}{\omega_{04}\omega_{45}} > 1. \tag{A.80}$$

If

$$\frac{\omega_{50,\mathrm{eff,via1}}}{\omega_{0,5,\mathrm{eff,via1}}} > \frac{\omega_{50,\mathrm{eff,via4}}}{\omega_{0,8,\mathrm{eff,via4}}} \tag{A.81}$$

the connection from 5 to 0 is predominantly via 1, and the first equation of Eq. (A.80) is the relevant one; in the opposite case it is the second equation. The other diagonal neighbours 6,

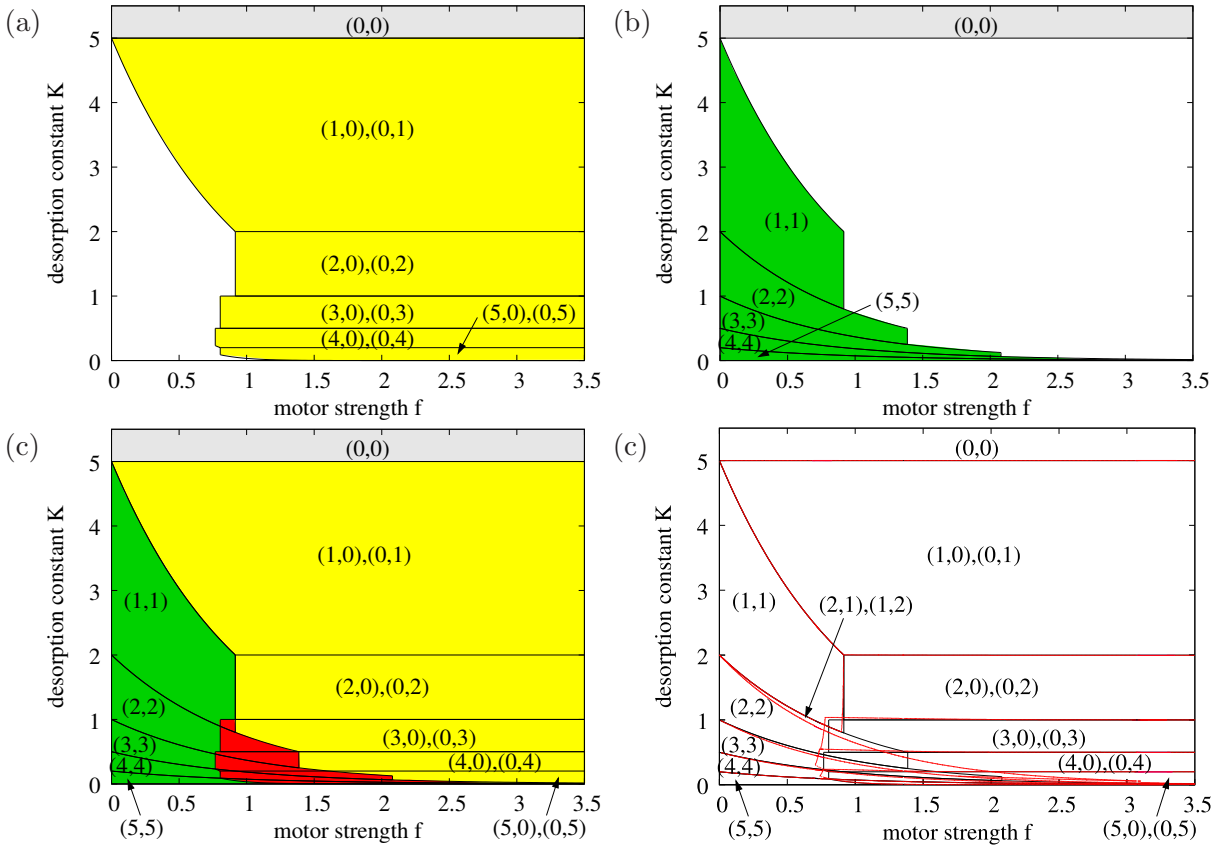

Fig. A.13: Motility diagrams for the symmetric tug-of-war of $N_+ = N_- = 5$ plus against minus motors. (a)-(c) Construction of the motility diagram in the refinedsharp maximum approximation. (a) Transition lines for the maxima $(n, 0)$ and $(0, n)$ according to Eq. (4.72) and Eq. (A.82). (b) Transition lines for the maxima (n, n) according to Eq. (4.73) and Eq. (A.83). (c) Overlay of (a) and (b) gives the full motility diagram. The colours mark the regions of the motility states (0) (green), $(-+)$ (yellow) and $(-0+)$ (red). In the red region, there are three maxima, one no motion maximum and two fast motion maxima coming from the corresponding green and yellow regions. (d) The agreement of the diagrams from the refined sharp maximum approximation (black lines) and the full numerical diagram (red lines) is very good.

7 and 8 are treated analogously. Because this leads to a total of eight conditions in addition to the four conditions Eq. (4.70), we only treat the symmetric case of $N = N_+ = N_-$ motors with identical parameters (except their preferred direction). In this case, the maxima of the probability distribution $p(n_+, n_-)$ either have only one motor type bound, $(n, 0)$ and $(0, n)$, or an equal number of both motor types bound, (n, n), with $n = 1, \ldots, N$.

- **Fast motion maxima with only one motor species bound**: A maximum $(n, 0)$ with only plus motors bound has the neighbours 2, 3, 4, 7 and 8. Comparison with the direct neighbours 2, 3, 4 leads to the conditions Eq. (4.72). Comparison with the diagonal neighbour 7 leads to the extra condition:

$$f > \frac{1}{n-1} \ln \frac{nN}{N-n+1} \qquad \text{for } n = 2, \ldots, N, \tag{A.82}$$

  while comparison with the neighbour 8 gives a less restrictive condition. The maximum at $(1, 0)$ has to be treated separately. Its transition lines are also described by Eq. (4.72), but the refined version does not give an extra condition. The conditions for a maximum at $(0, n)$ are the same because of symmetry. The transition lines for the maxima at $(n, 0)$ and $(0, n)$ are shown in Fig. A.13(a).

- **No motion maximum with an equal number of bound plus motors**: For a maximum at (n, n) the symmetry allows to compare only to the neighbours 1 and 2, 5, 6

and 7 because the other conditions are identical. Comparison with its direct neighbours 1 and 2 leads to the conditions Eq. (4.73), and comparison with neighbour 7 (the other comparisons lead to less restrictive conditions) leads to:

$$f < n \ln \frac{(N-n+1)(n+1)}{n(N-n)} \qquad \text{for } n = 1, \ldots, N-1 \tag{A.83}$$

The maximum at (N, N) has to be treated separately. Its transition lines are also described by Eq. (4.73), but the refined version does not give an extra condition. The transition lines for the maxima at (n, n) are shown in Fig. A.13(b).

Putting together the transition lines for both types of maxima leads to Fig. A.13(c). The maxima $(n, 0)$ and $(0, n)$ with only one motor type bound define the $(-+)$ phase (yellow), while the maxima (n, n) with both types of motors bound define the (0) phase (green). The overlap region is the $(-0+)$ phase (red). This motility diagram approximates the full numeric motility diagram very well, see Fig. A.13(d). The analytic equations of the sharp maximum approximation can therefore be used to estimate the transition lines. However, the equations describing the transition lines become rather 'messy', especially in the non-symmetric case (not shown). It is therefore more useful to use the non-refined sharp maximum approximation of Sec. 4.4.3 which is less accurate but more manageable.

A.5 Fitting experimental data

This appendix deals with some aspects of handling experimental data of bidirectional cargo transport, as discussed in Chap. 4 and 5. In Sec. A.5.1 we investigate the effects of experimental cutoffs. In Sec. A.5.2 we describe the details of the fitting procedure for the lipid-droplet data of Sec. 5.2. In this procedure, we use the Spearman rank correlation defined in Sec. A.5.3.

A.5.1 Time and velocity cutoffs

In this appendix we investigate quantitatively the influence of the time and velocity cutoffs on experimentally relevant quantities such as run times and velocities.

Experimental cutoffs. Measurements of run and switch times are always subject to finite temporal and spatial resolutions, which depend on the imaging method and image acquiring equipment used. The spatial resolution can be reduced to nanometre precision when tracking only the centre of the moving particle, for example by fitting a Gaussian to a fluorescence signal of the fluorescently labeled cargo, which is sometimes called fluorescence imaging at one nanometre accuracy (FIONA) as reviewed e.g. in [80]. Therefore the time resolution limit is more critical. A typical time resolution is the standard video frame rate of 30 frames per second, i.e. $\Delta t = 0.03\,\mathrm{s}$ [42, 45], but it can vary as much as from $\Delta t = 2.2\,\mathrm{s}$ [124] to $\Delta t = 0.002\,\mathrm{s}$ [82]. Due to the finite time resolution and to fluctuations of the cargo inside of the cell, it is often hard to decide whether the cargo is moving slowly or pausing. A pause is therefore operationally defined to be a period of time where the cargo moves with a velocity smaller than some 'small' cutoff velocity v_{cut}. Choices for v_{cut} are in the range of $0.05\,\mu\mathrm{m/s}$ [42, 45] and $0.1\,\mu\mathrm{m/s}$ [124].

Time resolution. The main effect of a finite time resolution is that short runs or pauses of duration smaller than the measurement time interval Δt cannot be detected. This leads to longer run and switch times for higher Δt, see Fig. A.14(a), as e.g. a short pause ending a run, or a short minus run interrupting a plus run remain unnoticed. As a consequence, the velocity decreases with the time interval. For large measurement time intervals $\Delta t \gtrsim 0.1\,\mathrm{s}$, pauses remain completely undetected[3], and the run and switch times resp. velocities become identical, see Fig. A.14(a).

[3] For the chosen set of parameters, the average pause time at infinite time resolution $\Delta t = 0$ is only 0.02 s.

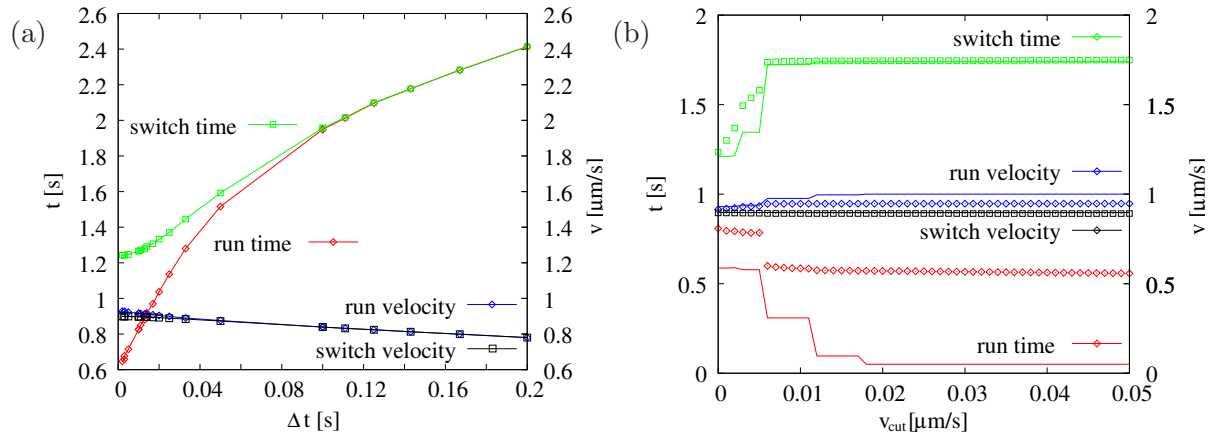

Fig. A.14: Influence of measurement time interval Δt and velocity cutoff v_{cut} on the run and switch times as well as run and switch velocities for the symmetric tug-of-war of 4 against 4 kinesin-like motors: (a) The run and switch times (red diamonds and green squares) increase with the time interval Δt, while the run and switch velocities (blue diamonds and black squares) decrease. For large time intervals, runs ans switches become identical. Data are with zero velocity cutoff. (b) The run times (red diamonds and line) decrease with the velocity cutoff v_{cut}, while the switch times (green squares and line) increase. The run and switch velocities (blue diamonds and line, and black squares and line) are almost unaffected. The comparison of infinite time resolution (solid lines) with finite time resolution (data points, for $\Delta t = 0.01s$) shows that the switch times (green) and velocities (black) are similar in both cases, while the run times (red) differ substantially.

Velocity cutoff. The main effect of the velocity cutoff v_{cut} is to change the definition of a 'pause'. With $v_{\text{cut}} = 0\,\mu$m/s, only cargos with exactly zero velocity are counted as pausing, which is an unreasonable definition for experiments. When the velocity cutoff v_{cut} is increased, more and more cargo states count as pauses. In our model this means that all states (n_+, n_-) with cargo velocities $v_C(n_+, n_-) < v_{\text{cut}}$ become pausing states. For the symmetric tug-of-war of 4 against 4 kinesin-like motors, the possible (absolute) values of the velocities of the cargo are 0, 0.002, 0.003, 0.006, 0.012, 0.018 and 1 μm/s, where zero velocity corresponds to cargo states (n, n) and maximal velocity $1\,\mu$m/s to states $(n, 0)$ and $(0, n)$. When the velocity cutoff is increased beyond one of these values, the run times show a sharp decrease as the number of states counting as 'run states' decreases, see Fig. A.14(b). Correspondingly, the run velocity increases because the left-over run states have higher velocity. This furthermore leads to an increase of the run velocity because less and less slow motion states with $n_+ > 0$ and $n_- > 0$ are counted as run states until finally only the states with one motor species bound count as run states. Then the velocity reaches the maximal possible value, the single motor velocity $1\,\mu$m/s. The switch times increase with the velocity cutoff: a period of plus motion (including pauses), for example, ends if the cargo reaches a minus run state, whose number becomes smaller and smaller for increasing v_{cut}. When the velocity cutoff passes the maximal slow-motion value $0.018\,\mu$m/s, all quantities remain constant if v_{cut} is further increased: For v_{cut} larger than the largest slow motion velocity ($0.018\,\mu$m/s in the particular case considered), the velocity cutoff has no influence any more.

When the velocity cutoff and time measurement interval are both nonzero, the run and switch times are larger because, as discussed above, short pauses and motion reversals remain undetected, compare lines and data points in Fig. A.14(b). For a finite velocity cutoff, this effect is stronger for the run than for the switch times because the run times are affected more when pauses are not detected. For finite time resolution, the steps in the curves of the run and switch times and velocities are smeared out.

Conclusion. In conclusion, the quantitative values of the run and switch times and velocities depend strongly on the experimental time resolution and on the definition of a pause via a velocity cutoff. One therefore has to be careful when comparing experimental and theoretical

data. A typical experimental time measurement interval is $\Delta t = 0.03\,\mathrm{s}$, and a typical and velocity cutoff is $v_{\mathrm{cut}} = 0.05\,\mu\mathrm{m/s}$. This means that usually the slow motion states with $n_+ > 0$ and $n_- > 0$ cannot be distinguished from pause states, see Fig. A.14(b), but that run and switch times can still be distinguished, see Fig. A.14(a).

A.5.2 Fitting of the *Drosophila* lipid-droplet data

In Sec. 5.2 we apply our tug-of-war model to the bidirectional transport of lipid-droplets in *Drosophila* embryos as studied by [44, 45, 176]. In this appendix, we describe in detail our fitting procedure, and we tabulate the numerical results.

For the bidirectional transport of lipid-droplets in early *Drosophila* embryos, various transport characteristics were measured in two different embryonic phases, labeled wild type phase II and III, Wt II and Wt III, and three different heterozygous dynein mutation backgrounds, labeled $Dhc^{6-10}/+$, $Dhc^{8-1}/+$ and Dhc^{8-1}/Dhc^{6-10} during phase II.

Motor numbers and stall forces in Wt II. We first considered the Wt II data. From cargo stall force measurements, the experimenters concluded that the droplets are pulled in the plus and minus direction by five plus and five minus motors, respectively [176]. Since the number of active motor fluctuates stochastically, these numbers represent the average number of pulling motors. We therefore chose the total number of plus and minus motors to be $N_+ = N_- = 6$.[4] The droplets are transported by dynein [44] and an unknown plus motor which we call kin?. The single motor parameters of dynein are only partly known, and for the stall force different labs have reported different results, see Tab. 2.3. In the droplet experiments, cargo stall force measurements indicate a single motor stall force of 1.1 pN for both plus and minus motors[5] [176]. We used this value for the stall forces of both motors and varied the remaining 10 single motor parameters $F_{d\pm}$, $\epsilon_{0\pm}$, $\pi_{0\pm}$, $v_{F\pm}$ and $v_{B\pm}$ in order to fit the experimental data.

Trajectory analysis. We generated cargo trajectories with the Gillespie algorithm and analyzed them in close analogy with the analysis of the experimental trajectories of [44, 45]. In particular, we used the experimental time resolutions and definitions of runs and pauses, which is crucial for the numerical values of results such as run times or velocities, see App. A.5.1. For example, short runs or pauses, which are easily accessible in simulations, may be unobservable in experiments because they are below time resolution or buried in noise. The cargo displacement[6] is recorded at video frequency of $30\,\mathrm{s}^{-1}$. The obtained trajectories, such as the one shown in Fig. 5.4(c), are segmented into runs and pauses by using the definitions from [44, 45]: A cargo is considered to be moving into the plus (minus) direction if its velocity v_C is larger than 50 nm/s (smaller than $-50\,\mathrm{nm/s}$) and pausing else. A run has to be at least 30 nm and 0.16 s long, and a pause must be longer than 0.23 s and cover a distance smaller than 30 nm. The run velocity is defined as the ratio of run length and run time. The experiments distinguished pauses after plus and after minus runs. We adopted this distinction although both in the experiments and in our simulations both types of pauses are very similar, see Tab. A.1. Furthermore, the experimenters defined 'short runs' of length 30-100 nm and 'long runs' of length 500-1000 nm, and calculated average velocities of both types of runs. We followed this procedure. For the experimental determination of plus and minus droplet stall forces, the droplets had to be moving in a given direction 'for a few seconds' in order to decide their direction before the measurements were performed [44, 176]. We therefore averaged escape and stall force values only over 'very long' runs that last more than 3 s. The stall forces were calculated according to Eq. (4.83), and a droplet was counted as escaping at a force F_{ext} if its stall force was higher than F_{ext}.

Fitting procedure. For fitting, we compared 10 transport characteristics, namely plus and minus run lengths, plus and minus stall forces, pause times after plus and minus travel, and plus

[4] We ignore that the total number of motors could vary for different cargos. The numbers N_+ and N_- are therefore average numbers of motors per cargo. [5] For dynein, this value is in agreement with the stall force reported by [100]. The low stall force for the unknown plus motor implies that this motor should be different from kinesin 1 because the kinesin 1 stall force is 6 pN. [6] The spatial resolution in the experiments is of the order of nanometers and therefore unproblematic.

Motor direction	average stall force [pN] +	−	average run length [μm] +	−	average pause time [s] after +	−	average velocity [μm/s] short runs +	−	long runs +	−	net effect on motion +/−
Wt II (sim.)	5.4	5.3	0.84	0.66	0.61	0.61	0.21	0.21	0.42	0.47	- / -
Wt II (exp.)	5.5	5.5	0.84	0.62	0.55	0.62	0.21	0.22	0.43	0.47	
Dhc^{6-10}/+ (sim.)	5.2	5.0	0.58	0.53	0.54	0.54	0.21	0.23	0.41	0.50	↓ / ↓
Dhc^{6-10}/+ (exp.)	5.5	5.5	0.56	0.49	0.60	0.62	0.21	0.22	0.46	0.55	
Dhc^{8-1}/+ (sim.)	5.3	5.1	0.41	0.32	0.66	0.66	0.20	0.21	0.39	0.37	↓ / ↓
Dhc^{8-1}/+ (exp.)	5.1	5.5	0.38	0.29	0.71	0.70	0.21	0.23	0.37	0.40	
Dhc^{8-1}/Dhc^{6-10} (sim.)	5.0	3.9	0.29	0.15	0.71	0.75	0.14	0.21	0.29	0.33	↓ / ↓
Dhc^{8-1}/Dhc^{6-10} (exp.)	4.7	3.7	0.31	0.17	0.71	0.76	0.17	0.20	0.29	0.33	
Wt III (sim.)	4.3	4.4	0.42	0.60	0.59	0.59	0.20	0.20	0.40	0.45	↓ / -
Wt III (exp.)	4.4	4.4	0.42	0.60	-	0.60	-	0.20	-	0.44	
$F_{s-}/\mathrm{pN} = 1.1 \rightarrow 0.8$	5.3	3.9	0.83	0.25	0.75	0.83	0.16	0.24	0.39	0.47	- / ↓
$F_{d-}/\mathrm{pN} = 0.75 \rightarrow 1.0$	4.9	5.3	0.24	0.80	0.74	0.73	0.14	0.20	0.35	0.47	↓ / ↑
$\epsilon_{0-}/\mathrm{s}^{-1} = 0.27 \rightarrow 0.5$	5.5	4.9	2.0	0.35	0.44	0.45	0.27	0.23	0.45	0.48	↑ / ↓
$\pi_{0-}/\mathrm{s}^{-1} = 1.6 \rightarrow 2.5$	5.4	5.5	0.35	0.97	0.67	0.65	0.22	0.20	0.40	0.48	↓ / ↑
$v_{F-}/\frac{\mu\mathrm{m}}{\mathrm{s}} = 0.65 \rightarrow 1.0$	5.3	5.4	0.85	1.4	0.59	0.60	0.21	0.24	0.42	0.70	- / ↑
$v_{B-}/\frac{\mathrm{nm}}{\mathrm{s}} = 72 \rightarrow 6.0$	5.8	5.3	2.1	0.65	0.63	0.66	0.43	0.21	0.52	0.47	↑ / -
$N_- = 6 \rightarrow 5$	5.3	4.4	1.3	0.37	0.55	0.58	0.21	0.22	0.42	0.46	↑ / ↓

Tab. A.1: Mutation and regulation in lipid-droplet transport: results of the fits to the *Drosophila* lipid-droplet data. The first 10 lines show a comparison of the average plus and minus stall forces, the average plus and minus run lengths, the average times of pauses after plus and after minus runs, and the average velocities of short and long runs in plus and in minus direction as obtained in simulation (sim.) and experiment* (exp.) for wild type phase II (Wt II) and III (Wt III), and for three different dynein mutations (Dhc^{6-10}/+, Dhc^{8-1}/+, and Dhc^{8-1}/Dhc^{6-10}). The last column describes the net effect on motion (run lengths and velocities) as compared to the Wt II values: motion can be enhanced (↑), impaired (↓) or unaltered (-).
The last seven lines show the effect of a change of one single motor parameter from the Wt II value, given in front of the arrow, to the value given after the arrow in the first column.

*The experimental values are taken from [44, 45, 176] as follows: The average stall forces for Wt II and Wt III are directly given in [176]; the other stall forces are read off from the diagrams in Fig. 3 in [44] and Fig. 2, 3 in [45] by applying the procedure described in the experimental procedures of [176]. The average run lengths are from Tab. II in [44] and Tab. I in [45], the average pause times from Tab. I in [44] and Tab. II in [45]. The average velocities for short and long runs have been read off from histograms in Fig. 7 in [44] and Fig. 4 in [45]. Missing values indicated by '-' were not available.

	Wt II		Dhc^{6-10} /+	Dhc^{8-1} /+	Dhc^{8-1} /Dhc^{6-10}	Wt III	
Motor direction	plus	minus	minus	minus	minus	plus	minus
stall force F_s [pN]	1.1	1.1	1.1	1.1	0.85	1.1	1.1
detachment force F_d [pN]	0.82	0.75	0.88	0.84	1.1	0.82	0.81
unbinding rate ϵ_0 [s^{-1}]	0.26	0.27	0.45	0.37	0.54	0.26	0.27
binding rate π_0 [s^{-1}]	1.6	1.6	1.8	2.0	1.8	1.4	1.6
forward velocity v_F [μm/s]	0.55	0.65	0.69	0.49	0.44	0.56	0.63
back velocity v_B [nm/s]	67	72	77	76	53	68	73

Tab. A.2: Single motor parameters for the fits to *Drosophila* lipid-droplet transport in wild type phase II (Wt II) and III (Wt III), and for three different dynein mutations (Dhc^{6-10}/+, Dhc^{8-1}/+, and Dhc^{8-1}/Dhc^{6-10}). The motor numbers are $N_+ = N_- = 6$ except for Wt III with $N_+ = N_- = 5$. The plus motor parameters for the dynein mutations are as for the plus motors in Wt II.

and minus velocities of short and long runs[7] as shown in Tab. A.1. For this purpose, we defined a 'distance function' between model and experiment results as the sum of squared differences between the experimentally measured and simulated quantities. As the different quantities are of different order of magnitude, they were rescaled in such a way that the experimental values are of order unity. We then minimized this distance function with respect to the unknown model parameters.

For the wild type phase II (Wt II) fit, these are the 10 unknown single motor parameters $F_{d\pm}$, $\epsilon_{0\pm}$, $\pi_{0\pm}$, $v_{F\pm}$ and $v_{B\pm}$. We first chose 'reasonable' set of parameters. Here 'reasonable' means that the motor parameters must be of the order of magnitude of experimental single-motor parameters and that the simulation results must be of the order of magnitude of the experimental results. We then used the Nelder-Mead downhill simplex algorithm [113, 126] to minimize the distance function starting from this initial choice. As this is only a local minimum, we repeated this procedure for several starting parameter sets until we found a minimum that reproduces the experimental data within about 10 %.

In wild type phase III (Wt III), reduced stall forces led to the conclusion that the average number of motors pulling the cargo in both directions is only four motors. We therefore took the total number of motors on the cargo to be $N_+ = N_- = 5$. For the Wt III fit, the single-motor parameters were set to the Wt II values. Then the simplex algorithm was started from this parameter set to minimize the 'distance function' with the Wt III experimental values.

For the dynein mutation fits, only the six minus motor parameters F_{s-}, F_{d-}, ϵ_{0-}, π_{0-}, v_{F-}, v_{B-} were used as fitting parameters because the mutation only affects the dyneins, and does so in an unknown way.[8] The plus motor parameters were kept fixed at the values from the Wt II fit since droplet motion in the dynein mutation background were investigated in embryonic phase II.

Fit results. A comparison of the experimental data and the corresponding fit result simulation data is shown in Tab. A.1. As required in the fitting procedure, they all agree within 10%. The single motor parameters resulting from all these fits are shown in Tab. A.2. They are within the expected range of motor parameters. The unbinding and binding rates are of the order of $1\,s^{-1}$ as measured for motors like kinesin 1 [84, 139, 161] and kinesin 3 [157]. The

[7] We did not use quantities that are extremely sensitive to the detectability of pauses, such as the percentage of direction reversals associated with pauses, or the average time between pauses, because pauses in simulation are more readily detected than in experiment. We also did not use 'secondary' quantities that were obtained by further processing of the data, such as fits to run length or pause time distributions or quantities calculated from these fits. [8] We ignore mixed dynein populations in the heterozygous mutation backgrounds. Our motor numbers and motor parameters are effective average parameters.

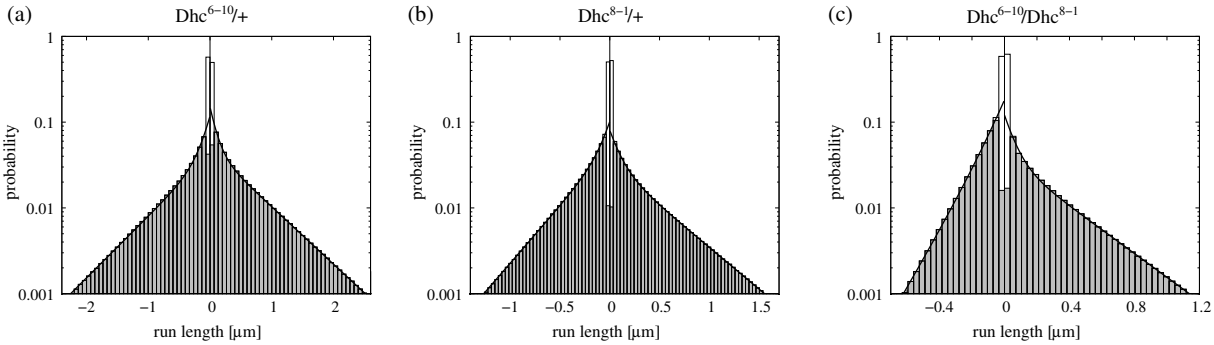

Fig. A.15: Run length distributions for three different dynein mutations labeled (a) $Dhc^{6-10}/+$, (b) $Dhc^{8-1}/+$, and (c) Dhc^{8-1}/Dhc^{6-10}. Minus (plus) run lengths are negative (positive). The gray bars are obtained when using the experimental cutoffs of a minimum length of 0.16 s and 30 nm, while the white bars are obtained without the cutoffs. In all cases, the run length distribution can be fitted by a double exponential function corresponding to the solid line. The two decay lengths of the double-exponential fits are listed in Tab. A.3.

values of the dynein parameters are discussed in Sec. 5.2.

Although not used in the fitting procedure, the distributions of run length show the same qualitative and similar quantitative behavior in simulation and experiment. Fig. A.15 shows the run length distributions of the dynein mutation backgrounds. Just as the wild type run length distribution shown in Fig. 5.5(a), they can be well fitted with by a double exponential function, as found in the experiments. The short and long decay lengths of these fits are listed in Tab. A.3. The short decay lengths are about 0.1 μm, while the long decay lengths are of the order of 1 μm and vary in the different genetic backgrounds. Although not used for fitting, simulation and experimental values are of the same order of magnitude and agree within 50%.

A.5.3 Spearman rank correlation

This appendix defines the Spearman correlation coefficient, which has been used in Sec. 5.2 in order to test for correlation without making assumptions about the linearity of the correlation and the distribution of the data.

The linear correlation coefficient The standard measure for correlation of two data sets x_i and y_i with $i = 1, \ldots, N$ is the linear correlation coefficient

$$r = \frac{\sum_i (x_i - \langle x \rangle)(y_i - \langle y \rangle)}{\sqrt{\sum_i (x_i - \langle x \rangle)^2}\sqrt{\sum_i (y_i - \langle y \rangle)^2}} \tag{A.84}$$

Decay length		Wt II		$Dhc^{6-10}/+$		$Dhc^{8-1}/+$		Dhc^{8-1}/Dhc^{6-10}		Wt III	
[μm]		sim.	exp.	sim.	exp.	sim.	exp.	sim.	exp.	sim.	exp.
short	plus	0.099	0.067	0.010	0.088	0.094	0.074	0.059	0.052	0.13	0.096
	minus	0.13	0.098	0.13	0.10	0.083	0.091	0.079	0.044	0.14	0.083
long	plus	0.95	1.1	0.65	0.78	0.45	0.40	0.31	0.44	0.48	0.78
	minus	0.80	1.1	0.61	0.90	0.33	0.65	0.14	0.21	0.67	1.1

Tab. A.3: Mutation and regulation in lipid-droplet transport: results of the fit to the *Drosophila* lipid-droplet data that have not been used in the fitting procedure. In all phases and genetic backgrounds, the run length distributions can be fitted by a double exponential function, see Fig. 5.5 and Fig. A.15, with the short and long decay lengths given here. Although not used for fitting, the simulation and experimental values are of the same order of magnitude; the maximal error is 50%. The experimental decay length values are from Tab. I in [45], and Tab. II in [44].

where $\langle x \rangle$ and $\langle y \rangle$ are the arithmetic means of $\{x_i\}$ resp. $\{y_i\}$. This coefficient r measures the linear correlation of the x_i and y_i. It varies between -1 (complete negative correlation, i.e. $y_i = a \cdot x_i + b$ with a negative a) and 1 (complete positive correlation i.e. $y_i = a \cdot x_i + b$ with a positive a). A value $r = 0$ indicates no linear correlation.

Statistical significance. In order to judge whether a detected correlation is statistically significant, one can use hypothesis testing. To do this, one establishes the 'null hypothesis' that the data are not correlated. Assuming that the x's and y's are normally distributed, one can then calculate the probability p of observing the data $\{x_i, y_i\}$ under the assumption that the null hypothesis is true, see e.g. [126]. This p-value is called the significance level of the test. It is the maximum probability, assuming the null hypothesis, that the given data set $\{x_i, y_i\}$ is observed. Thus if p is smaller than some significance level α, it is unlikely that the null hypothesis is true, i.e. it is unlikely that the data are uncorrelated. In this case one concludes, that the data are correlated with a significance $p < \alpha$. Standard values for α are 0.1, 0.05, or 0.01 [134].

Problems of linear correlation. The linear correlation coefficient faces two major problems: It only measures linear correlation and thus may fail if the data are correlated in a nonlinear way, and in order to estimate its statistical significance one needs the assumption of normally distributed data. Both problems are overcome by using the Spearman rank correlation.

Spearman rank correlation. The Spearman rank correlation assesses how well an arbitrary monotonic function can describe the relationship between two variables, without making any assumptions about linearity of the correlation or the distribution of the data. First, the data are sorted according to their rank. This means that the data $\{x_i\}$ are sorted in ascending order according to their numerical value. The position of the data point x_i is its rank R_i. In the same way each data point y_i gets its rank S_i. The Spearman rank correlation coefficient is then simply the linear correlation coefficient of the ranks [134]:

$$r_s = \frac{\sum_i (R_i - \langle R \rangle)(S_i - \langle S \rangle)}{\sqrt{\sum_i (R_i - \langle R \rangle)^2} \sqrt{\sum_i (S_i - \langle S \rangle)^2}} \tag{A.85}$$

As the rank ordering does not care about the precise numerical value but only about whether one value is larger than the other, r_s is a measure of any monotonic correlation of the original data, not only of linear correlation. The ranks are a list of integers with a known distribution: Each integer between 1 and N occurs precisely once. Because of this, no assumptions about the distributions of the original data are needed to calculate the significance probability p of the Spearman rank correlation.

List of Symbols

D_{b}	diffusion constant of bound motor motion, see Eq. (3.1) on p. 17
D_{ub}	diffusion constant of unbound motor motion, see Eq. (3.2) on p. 17
F	force
F_{C}	cargo force, see Eq. (4.2) on p. 35
F_d	motor detachment force, see Eq. (2.1) on p. 8
$F_{d+(-)}$	plus (minus) motor detachment force
F_{ext}	external force, e.g. applied by an optical trap, see Sec. 4.2.5
F_s	motor stall force, see Eq. (2.3) on p. 10
$F_{s+(-)}$	plus (minus) motor stall force
$F_{s,\mathrm{C}}$	cargo stall force, see Eq. (4.83) on p. 80
F_+	load force felt by a single plus motor, see Eq. (4.2) on p. 35
F_-	force generated by a single minus motor, see Eq. (4.2) on p. 35
F_v	characteristic force of the nonlinear force-velocity relation of Eq. (A.77) on p. 116
f	motor force ratio $f = F_s/F_d$ of stall and detachment force, see Eq. (4.23) on p. 41
$f_{+(-)}$	plus (minus) motor force ratio of stall and detachment force
g_n	'birth rate' of the relabeled one-dimensional Markov process of Sec. 4.4.1.2
G	ratio of the single minus and plus motor force-velocity curve slopes, $G = \beta_{0-}/\beta_{0+}$, see Sec. 4.4.2.2
$h_{+(-)}$	nullcline functions of the mean field approximation, see Eq. (4.54) on p. 61
j_{b}	bound motor current, $j_{\mathrm{b}} = v_{\mathrm{b}}\rho_{\mathrm{b}}(1-\rho_{\mathrm{b}})$, see below Eq. (3.20) on p. 23
J_{b}	total bound motor current in the tube, see Eq. (3.20) on p. 23
L	tube length, see Fig. (3.1) on p. 16
L_*	jam length for motor traffic in the tube, see Eq. (3.17) on p. 23
l	motor step size, lattice constant, see Sec. 3.1
K	filament desorption constant $K = \epsilon_0/\pi_0$, see Eq. (4.23) on p. 41
K_{LK}	desorption constant for the ASEP+LK, $K_{\mathrm{LK}} = \omega_{\mathrm{D}}/\omega_{\mathrm{A}}$, see Sec. 3.6.2
$K_{+(-)}$	filament desorption constant of a plus (minus) motor
K_{exp}	experimental filament desorption constant, see Eq. (A.2) on p. 102
$\mathrm{k_B}$	Boltzmann constant
N	number of plus or minus motors on the cargo if $N_+ = N_-$, see Eq. (4.23) on p. 41, or total number of motors in the tube, see Eq. (A.24) on p. 105
N_{A}	Avogadro constant

$N_{+(-)}$	total number of plus (minus) motors on the cargo, see Sec. 4.2.1
$n_{+(-)}$	number of active plus (minus) motors, see Sec. 4.2.1
P_{close}	probability for the motor head to be so close to the filament that it can bind, see Eq. (A.15) on p. 103
$p(\cdot)$	probability of the quantity given in the brackets
$p_{+(-)}$	probability of a plus (minus) motor to be bound to the filament, see Eq. (4.25) on p. 55
R	tube radius, see Fig. (3.1) on p. 16
r	(hydrodynamic Stokes) cargo radius, see Eq. (1.3) on p. 2
r_n	'death rate' of the relabeled one-dimensional Markov process of Sec. 4.4.1.2
$s_{+(-)}$	point where the random walk leaves the plus (minus) boundary, see Eq. (4.32) on p. 56
T	absolute temperature, see Eq. (1.2) on p. 2, or total time of a random walk, see Eq. (A.66) on p. 113
T_{P}	average pause time (until a plus or minus run begins), see Sec. 4.3.2
T_0	average first passage time to state with no motors bound, see Eq. (A.22) on p. 105 and Eq. (A.68) on p. 113
T_+	average time of a plus run (until a pause or a minus run begins), see Sec. 4.3.2
T_-	average time of a minus run (until a pause or a plus run begins), see Sec. 4.3.2
T_{+-}	average plus switch time, including pauses. Equal to the average time of a plus run until switch to minus direction, see Sec. 4.3.2
T_{-+}	average minus switch time, including pauses. Equal to the average time of a minus run until switch to plus direction, see Sec. 4.3.2
T_i	average return time to state i, see Eq. (A.68) on p. 113
t	time
t_{rel}	relaxation time to the stationary state, see Eq. (3.39) on p. 27
V	Péclet number, relative importance of deterministic to Brownian motion, see Eq. (1.1) on p. 2
v	velocity
v_A	single motor assisting velocity (under assisting load), see Eq. (2.6) on p. 10
v_B	single motor backward velocity, see Eq. (2.6) on p. 10
$v_{\text{B}+(-)}$	single plus (minus) motor backward velocity
v_{b}	bound motor velocity, see Sec. 3.1
v_C	cargo velocity, see Eq. (4.5) on p. 35
v_{cut}	velocity cutoff that defines the maximal velocity of a pause, see App. A.5.1
v_F	single motor forward velocity, see Eq. (2.6) on p. 10
$v_{\text{F}+(-)}$	single plus (minus) motor forward velocity
$v(F)$	force-velocity relation of a single motor, see Eq. (2.6) on p. 10
v_0	single motor velocity parameter. Equal to v_B, v_F, v_A under superstall, substall and assisting load, respectively, see Eq. (2.6) on p. 10
$v_{0+(-)}$	single plus (minus) motor velocity parameter
$w_{+(-)}$	probability that a cargo binds to the filament with a plus (minus) motor, see Sec. 4.5.3

X	thermodynamic force of a cycle, see Eq. (4.12) on p. 37
X_+	average distance of a plus run (until a pause or a minus run begins), see Sec. 4.3.2
X_-	average distance of a minus run (until a pause or a plus run begins), see Sec. 4.3.2
X_{+-}	average plus switch distance, including pauses. Equal to the average distance of a plus run until switch to minus direction, see Sec. 4.3.2
X_{-+}	average minus switch distance, including pauses. Equal to the average distance of a minus run until switch to plus direction, see Sec. 4.3.2
X_0	average first passage distance to state with no motors bound, see Eq. (A.22) on p. 105 and Eq. (A.68) on p. 113
x	coordinate along filament, see Sec. 3.1
x_{S}	symmetric fixed point in mean field theory, see Eq. (4.58) on p. 62
$x_{+(-)}$	rescaled number of average active plus (minus) motors, $x_\pm = \langle n_\pm \rangle / N_\pm$, for the mean field calculation, see Eq. (4.48) on p. 59
(y, z)	coordinates transverse to the filament, see Sec. 3.1
α	forward stepping probability of a motor in unit time τ, see Sec. 3.1
β_A	slope of the motor force-velocity curve in the assisting force regime, $\beta_A = v_A/F_s$, see Eq. (2.5) on p. 10
β_B	slope of the motor force-velocity curve in the superstall load regime, $\beta_B = v_B/F_s$, see Eq. (2.4) on p. 10
γ_{S}	Stokes friction coefficient, see Eq. (1.2) on p. 2
Δ	difference of bound plus and minus motors, $\Delta = n_+ - n_-$
Δt	time resolution of measurement, see App. A.5.1
Δt_{b}	average unbinding time, i.e. average time of walking on the filament before unbinding, see Eq. (A.23) on p. 105 and Eq. (4.80) on p. 75
Δx_{b}	average walking distance before unbinding, see Eq. (3.9) on p. 20
Δx_{ub}	average diffusion distance before rebinding, see Eq. (3.9) on p. 20
$\delta(\cdot)$	delta-function of the quantity in the brackets
ϵ	detachment parameter. The motor unbinding probability per unit time τ is $\epsilon/6$, see Sec. 3.1
$\tilde{\epsilon}$	motor unbinding rate, $\tilde{\epsilon} = 4\epsilon/(6\tau)$, see Sec. 3.1
$\epsilon(F)$	load-dependent unbinding rate of single motor, see Eq. (2.1) on p. 8
$\epsilon_{+(-)}(n_+, n_-)$	unbinding rate of a single plus (minus) motor on a cargo with n_+ active plus and n_- active minus motors, see Eq. (4.3) on p. 35
ϵ_U	unbinding rate of the cargo from the filament, see App. A.3.2
ϵ_0	single motor unbinding rate with zero force, see Eq. (2.1) on p. 8
$\epsilon_{0+(-)}$	single plus (minus) motor unbinding rate with zero force
η	viscosity of the surrounding solution, see Eq. (1.3) on p. 2
λ	superposition parameter, see Eq. (4.6) on p. 35
ν	velocity ratio $\nu = \beta_B/\beta_F = v_B/v_F$ of backward to forward velocity, see Eq. (4.23) on p. 41
ν_{FA}	single motor velocity ratio, is equal to v_F/v_A under assisting load and to 1 else, see Eq. (4.17) on p. 38
ξ	characteristic length scale of approach of the bulk value, see Eq. (3.7) on p. 20

ω_{A}	attachment rate for the ASEP+LK, see Eq. (3.40) on p. 28
ω_{D}	detachment rate for the ASEP+LK, see Eq. (3.40) on p. 28
ω_i	Master equation total out-rate from state i, see Eq. (A.55) on p. 110
ω_{ij}	Master equation transition rate from state i to state j, see Eq. (A.55) on p. 110
π_{ad}	motor binding probability to filament in discrete time, see Sec. 3.1
$\tilde{\pi}_{\mathrm{ad}}$	motor binding rate to filament, $\tilde{\pi}_{\mathrm{ad}} = 4\pi_{\mathrm{ad}}/(6\tau)$, see Sec. 3.1
$\pi(F)$	load-dependent binding rate of single motor, see Eq. (2.2) on p. 9
$\pi_{+(-)}(n_+, n_-)$	binding rate for a single plus (minus) motor on a cargo with n_+ active plus and n_- active minus motors, see Eq. (4.3) on p. 35
π_U	binding rate of the cargo to the filament, see App. A.3.2
π_0	single motor binding rate with zero force, see Eq. (2.2) on p. 9
$\pi_{0+(-)}$	single plus (minus) motor binding rate with zero force
ρ_{b}	bound motor density, see Sec. 3.1
$\rho_{\mathrm{b,in}}$	bound motor density at open tube end, see Sec. 3.1
ρ_{in}	left boundary density for the ASEP, see Sec. 3.6.1
ρ_{LK}	bulk solution of the ASEP+LK, see Eq. (3.42) on p. 28
ρ_{ub}	unbound motor density, see Sec. 3.1
$\rho_{\mathrm{ub,in}}$	unbound motor density at open tube end, see Sec. 3.1
τ	unit time, for unbound diffusion $\tau = l^2/(6D_{\mathrm{ub}})$, see Sec. 3.1
τ_i	average return time to state i, see Eq. (A.63) on p. 113
ϕ	tube cross section, see Eq. (3.2) on p. 17
$\langle\cdot\rangle$	average value of the quantity inside the brackets

Overview of the model parameters

	motion on filament	attachment to filament	detachment from filament	diffusion in solution
Rate of a single motor on bead under force F	$v(F)$	$\pi(F)$	$\epsilon(F)$	–
Hopping probability in the lattice model	α	$\pi_{\mathrm{ad}}/6$	$\epsilon/6$	$1/6$
Rate in continuous version of the lattice model	v_{b} $= \alpha l/\tau$	$\tilde{\pi}_{\mathrm{ad}}$ $= 4\pi_{\mathrm{ad}}/(6\tau)$	$\tilde{\epsilon}$ $= 4\epsilon/(6\tau)$	D_{ub} $= l^2/(6\tau)$
Cargo rate with n_+ plus and n_- minus motors	$v(n_+, n_-)$	$\pi(n_+, n_-)$	$\epsilon(n_+, n_-)$	–

The table above compares the parameters of the various model situations considered in this work. A single motor which experiences the load force F, as described in Chap. 2, moves on the filament with velocity $v(F)$, attaches to the filament with rate $\pi(F)$ and unbinds from it with rate $\epsilon(F)$. A motor or a motor-cargo complex of the discrete-time lattice model of Chap. 3 hops forward with probability α, binds to the filament with probability $\pi_{\mathrm{ad}}/6$ and unbinds from it with probability $\epsilon/6$. All probabilities are per unit time τ, which is chosen so that unbound diffusion on the lattice occurs with probability $1/6$. In the

continuous version of the lattice model used in Chap. 3, the probabilities become rates and the motor moves forward with velocity v_b, binds to the filament with rate $\tilde{\pi}_\mathrm{ad}$, unbinds from it with rate $\tilde{\epsilon}$, and diffuses when unbound with diffusion constant D_ub. A cargo pulled by n_+ plus and n_- minus motors as considered in Chap. 4 moves forward with velocity $v(n_+, n_-)$. The rate for binding of a single motor is given by $\pi(n_+, n_-)$, and the rate for unbinding of a single motor by $\epsilon(n_+, n_-)$.

List of abbreviations

ADP	adenosine diphosphate
AIC	Akaike information criterion
ASEP	asymmetric simple exclusion process
ATP	adenosine triphosphate
BIC	Bayes information criterion
cAMP	cyclic adenosine monophosphate
$Dhc^{6-10}/+$, $Dhc^{8-1}/+$, Dhc^{8-1}/Dhc^{6-10}	dynein heavy chain mutations in *Drosophila* embryos
FP	fixed point
GFP	green fluorescent protein
GTP	guanosine triphosphate
G-protein	guanine nucleotide binding protein
LK	Langmuir kinetics
(M)FPT	(mean) first passage time
MAP	microtubule associated protein
MT	microtubule
mRNA	messenger ribonucleic acid
PKA	protein kinase A
Wt II, Wt III	wild type phase II, III in *Drosophila* embryos

Bibliography

[1] F.J. Ahmad, J. Hughey, T. Wittmann, A. Hyman, M. Greaser, and P.W. Baas. Motor proteins regulate force interactions between microtubules and microfilaments in the axon. *Nature Cell Biol.*, 2:276–280, 2000.

[2] B. Alberts, D. Bray, A. Johnson, J. Lewis, M. Raff, K. Roberts, and P. Walter. *Essential cell biology. An introduction to the molecular biology of the cell.* Garland, New York, 1998.

[3] D. J. Aldous and J. A. Fill. *Reversible Markov chains and random walks on graphs.* Monograph in preparation, available at Aldous' homepage `http://www.stat.berkeley.edu/~aldous/RWG/book.html`, 1999-2001.

[4] A. Ashkin, K. Schütze, J.M. Dziedzic, U. Euteneuer, and M. Schliwa. Force generation of organelle transport measured *in vivo* by an infrared laser trap. *Nature*, 348:346–348, 1990.

[5] M. Badoual, F. Jülicher, and J. Prost. Bidirectional cooperative motion of molecular motors. *Proc. Natl. Acad. Sci. USA*, 99:6696–6701, 2000.

[6] E. Bananis, J.W. Murray, R.J. Stockert, P. Satir, and A.W. Wolkoff. Regulation of early endocytoc vesicle motility and fission in a reconstitued system. *J. Cell Sci.*, 116:2749–2761, 2003.

[7] J. Beeg, S. Klumpp, R. Dimova, R. Serral Gracià, E. Unger, and R. Lipowsky. Transport of beads by several kinesin motors. *Biophys. J.*, in press, 2008.

[8] G.I. Bell. Models for the specific adhesion of cells to cells. *Science*, 200:618–627, 1978.

[9] S.M. Block, C.L. Asbury, J.W. Shaevitz, and M.J. Lang. Probing the kinesin reaction cycle with a 2d optical force clamp. *Proc. Natl. Acad. Sci. USA*, 100:2351–2356, 2003.

[10] A. Blocker, F.F. Severin, J.K. Burkhardt, J.B. Bingham, H. Yu, J.C. Olivo, T.A. Schroer, A.A. Hyman, and G. Griffiths. Molecular requirements for bi-directional movement of phagosomes along microtubules. *J. Cell Biol.*, 137:113–129, 1997.

[11] K.J. Böhm. Homepage of molecular motors lab. `http://www.imb-jena.de/www_elmi/`, 2006.

[12] S.T. Brady. A novel brain ATPase with properties expected for the fast axonal transport motor. *Nature*, 317:73–75, 1985.

[13] J.K. Burkhardt, C.J. Echeverri, T. Nilsson, and R.B. Vallee. Overexpression of the dynamitin (p50) subunit of the dynactin complex disrupts dynein-dependent maintenance of membrane organelle distribution. *J. Cell Biol.*, 139:469–484, 1997.

[14] O. Campas, Y. Kafri, K.B. Zeldovich, J. Casademunt, and J.-F. Joanny. Collective dynamics of interacting molecular motors. *Phys. Rev. Lett.*, 97:038101, 2006.

[15] H.S. Carslaw and J.C. Jaeger. *Conduction of heat in solids.* Oxford University Press, Oxford, 1959.

[16] J.H. Carson, Y. Cui, and E. Barbarese. The balance of power in RNA trafficking. *Curr. Opin. Neurobiol.*, 11:558–563, 2001.

[17] N.J. Carter and R.A. Cross. Mechanics of the kinesin step. *Nature*, 435:308–312, 2005.

[18] S.R. Chada and P.J. Hollenbeck. Mitochondrial movement and positioning in axons: the role of growth factor signaling. *J. Exp. Biol.*, 206:1985–1992, 2003.

[19] D. Chowdhury, L. Santen, and A. Schadschneider. Statistical physics of vehicular traffic and some related systems. *Phys. Rep.*, 329:199–329, 2000.

[20] C.M. Coppin, D.W. Pierce, L. Hsu, and R.D. Vale. The load dependence of kinesin's mechanical cycle. *Proc. Natl. Acad. Sci. USA*, 94:8539–8544, 1997.

[21] T.L. Culver-Hanlon, S.A. Lex, A.D. Stephens, N.J. Quintyne, and S.J. King. A microtubule-binding domain in dynactin increases dynein processivity by skating along microtubules. *Nat. Cell Biol.*, 8:264–270, 2006.

[22] A.B. Dahlström, K.K. Pfister, and S.T. Brady. The axonal transport motor 'kinesin' is bound to anterogradely transported organelles: quantitative cytofluorimetric studies of fast axonal transport in the rat. *Acta Physiol. Scand.*, 141:469–476, 1991.

[23] K.J. De Vos, J. Sable, K.E. Miller, and M.P. Sheetz. Expression of phosphatidylinositol (4,5) bisphosphate-specific pleckstrin homology domains alters direction but not the level of axonal transport of mitochondria. *Mol. Biol. Cell*, 14:3636–3649, 2003.

[24] S.W. Deacon, A.S. Serpinskaya, P.S. Vaughan, M.L. Fanarraga, I. Vernos, K.T. Vaughan, and V.I. Gelfand. Dynactin is required for bidirectional organelle transport. *J. Cell Biol.*, 160:297–301, 2003.

[25] T. Duke. Molecular model of muscle contraction. *Proc. Natl. Acad. Sci. USA*, 96:2770–2775, 1999.

[26] T. Duke. Cooperativity of myosin molecules through strain-dependent chemistry. *Phil. Trans. R. Soc. Lond. B*, 355:529–538, 2000.

[27] S.A. Endow and H. Higuchi. A mutant of the motor protein kinesin that moves in both directions on microtubules. *Nature*, 406:913–916, 2000.

[28] T. Erdmann and U.S. Schwarz. Stability of adhesion clusters under constant force. *Phys. Rev. Lett.*, 92:108102, 2004.

[29] M.R. Evans, R. Juhász, and L. Santen. Shock formation in an exclusion process with creation and annihilation. *Phys. Rev. E*, 68:026117, 2003.

[30] G. Fink. Max Planck Institute for Terrestrial Microbiology. *Personal communication*, 2007.

[31] V.E. Foe and B.M. Alberts. Studies of nuclear and cytoplasmic behaviour during the five mitotic cycles that precede gastrulation in drosophila embryogenesis. *J. Cell Sci.*, 61:31–70, 1983.

[32] J.J. Freed and M.M. Lebowitz. Association of a class of saltatory movements with microtubules in cultured cells. *J. Cell Biol.*, 45:334–354, 1970.

[33] P.E. Gallant. The axonal transport motor 'kinesin' is bound to anterogradely transported organelles: quantitative cytofluorimetric studies of fast axonal transport in the rat. *J. Neurocytol.*, 29:779–782, 2000.

[34] A. Gennerich and D. Schild. Finite-particle tracking reveals submicroscopic-size changes of mitochondria during transport in mitral cell dendrites. *Phys. Biol.*, 3:45–53, 2006.

[35] S.P. Gilbert, M.L. Moyer, and K.A. Johnson. Alternating site mechanism of the kinesin ATPase. *Biochemistry*, 37:792–799, 1998.

[36] D.T. Gillespie. A general method for numerically simulating the stochastic time evolution of coupled chemical reactions. *J. Comp. Phys.*, 22:403–434, 1976.

[37] F. Gittes, E. Meyhöfer, S. Baek, and J. Howard. Directional loading of the kinesin motor molecule as it buckles a microtubule. *Biophys. J.*, 70:418–429, 1996.

[38] L.S.B. Goldstein and Z. Yang. Microtubule-based transport systems in neurons: the roles of kinesins and dyneins. *Annu. Rev. Neurosci.*, 23:39–71, 2000.

[39] S. Grill, K. Kruse, and F. Jülicher. Theory of mitotic spindle oscillations. *Phys. Rev. Lett.*, 94:108104, 2005.

[40] S.P. Gross. Hither and yon: a review of bi-directional microtubule-based transport. *Phys. Biol.*, 1:R1–R11, 2004.

[41] S.P. Gross, Y. Guo, J.E. Martinez, and M.A. Welte. A determinant for directionality of organelle transport in Drosophila embryos. *Curr. Biol.*, 13:1660–1668, 2003.

[42] S.P. Gross, M.C. Tuma, S.W. Deacon, A.S. Serpinskaya, A.R. Reilein, and V.I. Gelfand. Interactions and regulation of molecular motors in Xenopus melanophores. *J. Cell Biol.*, 156:855–865, 2002.

[43] S.P. Gross, M. Vershinin, and G.T. Shubeita. Cargo transport: two motors are sometimes better than one. *Curr. Biol.*, 17:R478–R486, 2007.

[44] S.P. Gross, M.A. Welte, S.M. Block, and E.F. Wieschaus. Dynein-mediated cargo transport in vivo: a switch controls travel distance. *J. Cell Biol.*, 148:945–955, 2000.

[45] S.P. Gross, M.A. Welte, S.M. Block, and E.F. Wieschaus. Coordination of opposite-polarity microtubule motors. *J. Cell Biol.*, 156:715–724, 2002.

[46] Y. Guo, S. Jangi, and M.A. Welte. Organelle-specific control of intracellular transport: Distinctly targeted isoforms of the regulator klar. *Mol. Biol. Cell*, 16:1406–141, 2005.

[47] F.K. Gyoeva. Interaction of molecular motors. *Mol. Biol.*, 4:614–622, 2005.

[48] A. Habermann, T.A. Schroer, G. Griffiths, and J.K. Burkhardt. Immunolocalization of cytoplasmic dynein and dynactin subunits in cultured macrophages: enrichment on early endocytic organelles. *J. Cell. Sci.*, 114:229–240, 2001.

[49] DD Hackney. The rate-limiting step in microtubule-stimulated ATP hydrolysis by dimeric kinesin head domains occurs while bound to the microtubule. *J. Biol. Chem.*, 269(23):16508–16511, 1994.

[50] T. Hamasaki, M.E. Holwill, K. Barkalow, and P. Satir. Mechanochemical aspects of axonemal dynein activity studied by in vitro microtubule translocation. *Biophys. J.*, 69:2569–2579, 1995.

[51] T.L. Hill. *Free energy transduction and biochemical cycle kinetics.* Springer, New York, 1989.

[52] N. Hirokawa, R. Sato-Yoshitake, N. Kobayashi, K.K. Pfister, G.S. Bloom, and S.T. Brady. Kinesin associates with anterogradely transported membranous organelles in vivo. *J. Cell Biol.*, 114:295–302, 1991.

[53] N. Hirokawa, Y. Yoshida, R. Sato-Yoshitake, and T. Kawashima. Brain dynein (MAP1C) localizes on both anterogradely and retrogradely transported membranous organelles *in vivo*. *J. Cell. Biol.*, 111:1027–1037, 1990.

[54] J. Howard. *Mechanics of Motor Proteins and the Cytoskeleton.* Sinauer Associates, Sunderland (Mass.), 2001.

[55] A.J. Hunt, F. Gittes, and J. Howard. The force exerted by a single kinesin molecule against a viscous load. *Biophys. J.*, 67:766–781, 1994.

[56] Y. Imafuku, Y.Y. Toyoshima, and K. Tawada. Length dependence of displacement fluctuations and velocity in microtubule sliding movement driven by sea urchin sperm outer arm β dynein in vitro. *Biophys. Chem.*, 67:117–125, 1997.

[57] R. Juhaśz and L. Santen. Dynamics of an exclusion process with creation and annihilation. *J. Phys. A: Math. Gen.*, 37:3933–3944, 2004.

[58] F. Jülicher. Max Planck Institute for the Physics of Complex Systems. *Personal communication*, 2006.

[59] F. Jülicher and J. Prost. Cooperative molecular motors. *Phys. Rev. Lett.*, 75:2618–2621, 1995.

[60] F. Jülicher and J. Prost. Spontaneous oscillations of collective molecular motors. *Phys. Rev. Lett.*, 78:4510–4513, 1997.

[61] C. Kaether, P. Skehel, and C.G. Dotti. Axonal membrane proteins are transported in distinct carriers: a two-color video microscopy study in cultured hippocampal neurons. *Mol. Biol. Cell*, 11:1213–1224, 2000.

[62] S. Kamimura and K. Takahashi. Direct measurement of the force of microtubule sliding in flagella. *Nature*, 293:566 – 568, 1981.

[63] T.L. Karr and B.M. Alberts. Organization of the cytoskeleton in early Drosophila embryos. *J. Cell Biol.*, 102:1494–1509, 1986.

[64] S. Katz, J.L. Lebowitz, and H. Spohn. Nonequilibrium steady-states of stochastic lattice gas models of fast ionic conductors. *J. Stat. Phys.*, 34:497–537, 1984.

[65] S. Katz, J.L. Lebowitz, and H. Spohn. Phase transitions in stationary nonequilibrium states of model lattice systems. *Phys. Rev. B*, 28:1655 – 1658, 1984.

[66] S.J. King and T.A. Schroer. Dynactin increases the processivity of the cytoplasmic dynein motor. *Nature Cell Biol.*, 2:20–24, 2000.

[67] G.A. Klein, K. Kruse, G. Cuniberti, and F. Jülicher. Filament depolymerization by molecular motors. *Phys. Rev. Lett.*, 49:108102, 2005.

[68] S. Klumpp. *Movements of molecular motors: Diffusion and directed walks.* PhD thesis, University of Potsdam, 2003.

[69] S. Klumpp and R. Lipowsky. Traffic of molecular motors through tube-like compartments. *J. Stat. Phys.*, 113:233–268, 2003.

[70] S. Klumpp and R. Lipowsky. Phase transitions in systems with two species of molecular motors. *Europhys. Lett.*, 66:90–96, 2004.

[71] S. Klumpp and R. Lipowsky. Cooperative cargo transport by several molecular motors. *Proc. Natl. Acad. Sci. USA*, 102:17284–17289, 2005.

[72] S. Klumpp, M.J.I. Müller, and R. Lipowsky. Cooperative transport by small teams of molecular motors. *Biophys. Rev. Lett.*, 1:353–361, 2006.

[73] S. Klumpp, Th. M. Nieuwenhuizen, and R. Lipowsky. Self-organized density patterns of molecular motors in arrays of cytoskeletal filaments. *Biophys. J.*, 88:3118–3132, 2005.

[74] H. Kojima, M. Kikumoto, H. Sakakibara, and K. Oiwa. Mechanical properties of a single-headed processive motor, inner-arm dynein subspecies-c of Chlamydomonas studied at the single molecule level. *J. Biol. Phys.*, 28:335–345, 2002.

[75] H. Kojima, E. Muto, H. Higuchi, and T. Yanagida. Mechanics of single kinesin molecules measured by optical trapping nanometry. *Biophys. J.*, 73:2012–2022, 1997.

[76] S. Kondo, R. Satoyoshitake, Y. Noda, H. Aizawa, T. Nakata, Y. Matsuura, and N. Hirokawa. KIF3A is a new microtubule-based anterograde motor in the nerve axon. *J. Cell Biol.*, 125:1095–1107, 1994.

[77] S. Konzack, P.E. Rischitor, C. Enke, and R. Fischer. The role of the kinesin motor KipA in microtubule organization and polarized growth of *Aspergillus nidulans*. *Mol. Biol. Cell*, 16:497–506, 2005.

[78] H.A. Kramers. Brownian motion in a field of force and the diffusion model of chemical reactions. *Physica*, 7:284–304, 1940.

[79] K. Kruse and F. Jülicher. Oscillations in cell biology. *Curr. Opin. Cell Biol.*, 17:20–26, 2005.

[80] C. Kural, H.Balci, and P.R. Selvin. Molecular motors one at a time: FIONA to the rescue. *J. Phys.: Condens. Matter*, 17:S3979–S3995, 2005.

[81] C. Kural, H. Kim, S. Syed, G. Goshima, V. Gelfand, and P.R. Selvin. Kinesin and dynein move a peroxisome in vivo: a tug-of-war or coordinated movement? *Science*, 308:1469–1472, 2005.

[82] C. Kural, A.S. Serpinskaya, Y.-H. Chou, R.D. Goldman, V.I. Gerlfand, and P.R. Selvin. Tracking melanosomes inside a cell to study molecular motors and their interaction. *Proc. Natl. Acad. Sci. USA*, 104:5378–5382, 2007.

[83] J. Lane and V. Allan. Microtubule-based membrane movement. *Biochim. Biophys. Acta*, 1376:27–55, 1998.

[84] C. Leduc, O. Campas, K.B. Zeldovich, A. Roux, P. Jolimaitre, L. Bourel-Bonnet, B. Goud, J.-F. Joanny, P. Bassereau, and J. Prost. Cooperative extraction of membrane nanotubes by molecular motors. *Proc. Natl. Acad. Sci. USA*, 101:17096–17101, 2004.

[85] J.H. Lenz, I. Schuchardt, A. Straube, and G. Steinberg. A dynein loading zone for retrograde endosome motility at microtubule plus ends. *EMBO J.*, 25:2275–2286, 2006.

[86] V. Levi, A.S. Serpinskaya, E. Gratton, and V.I. Gelfand. Organelle transport along microtubules in Xenopus melanophores: evidence for cooperation between multiple motors. *J. Cell Biol.*, 90:318–327, 2006.

[87] J.Y. Li, K.K. Pfister, S. Brady, and A. Dahlström. Axonal transport and distribution of immunologically distinct kinesin heavy chains in rat neurons. *J. Neurosci. Res.*, 58:226–241, 1999.

[88] S. Liepelt. Max Planck Institute for Colloids and Interfaces. *Personal communication*, 2007.

[89] L.A. Ligon, M. Tokito, J.M. Finklestein, F.E. Grossmann, and E.L.F. Holzbaur. A direct interaction between cytoplasmic dynein and kinesin I may coordinate motor activity. *J. Biol. Chem.*, 279:19201–19208, 2004.

[90] R. Lipowsky, Y. Chai, S. Klumpp, S. Liepelt, and M.J.I. Müller. Molecular motor traffic: From biological nanomachines to macroscopic transport. *Physica A*, 372:34–51, 2006.

[91] R. Lipowsky and S. Klumpp. 'Life is motion' – multiscale motility of molecular motors. *Physica A*, 352:53–112, 2005.

[92] R. Lipowsky, S. Klumpp, and Th. M. Nieuwenhuizen. Random walks of cytoskeletal motors in open and closed compartments. *Phys. Rev. Lett.*, 87:108101, 2001.

[93] A. Lockhart, I.M.-T.C. Crevel, and R.A. Cross. Kinesin and Ncd bind through a single head to microtubules and compete for a shared MT binding site. *J. Mol. Biol.*, 294:763–771, 1995.

[94] K. Luby-Phelps. Cytoarchitecture and physical properties of cytoplasm: volume, viscosity, diffusion, intracellular surface area. *Int. Rev. Cytol. - Survey Cell Biol.*, 192:189–221, 2000.

[95] G.W. Luxton, S. Haverlock, K.E. Coller, S.E. Antinone, A. Pincetic, and G.A. Smith. Targeting of herpesvirus capsid transport in axons is coupled to association with specific sets of tegument proteins. *Proc. Natl. Acad. Sci. USA*, 102:5832–5837, 2005.

[96] C.T. MacDonald, J.H. Gibbs, and A.C. Pipkin. Kinetics of biopolymerization on nucleic acid templates. *Biopolymers*, 6:1–25, 1968.

[97] R. Mallik, B.C. Carter, S.A. Lex, S.J. King, and S.P. Gross. Cytoplasmic dynein functions as a gear in response to load. *Nature*, 427:649–652, 2004.

[98] R. Mallik and S.P. Gross. Molecular motors: strategies to get along. *Curr. Biol.*, 14:R971–R982, 2004.

[99] R. Mallik and S.P. Gross. Molecular motors as cargo transporters in the cell - The good, the bad and the ugly. *Physica A*, 372:65–69, 2006.

[100] R. Mallik, D. Petrov, S.A. Lex, S.J. King, and S.P. Gross. Building complexity: an in vitro study of cytoplasmic dynein with in vivo implications. *Nature*, 427:649–652, 2005.

[101] I.V. Maly. A stochastic model for patterning og the cytoplasm by the saltatory movement. *J. thero. Biol.*, 216:59–71, 2002.

[102] E.-M. Mandelkow, E. Thies, B. Trinczek, J. Biernat, and E. Mandelkow. MARK/PAR1 kinase is a regulator of microtubule-dependent transport in axons. *J. Cell Biol.*, 67:99–110, 2004.

[103] J. Marro and R. Dickman. *Nonequilibrium phase transitions in lattice models*. Cambridge University Press, Cambridge, 1999.

[104] E. Meyhöfer and J. Howard. The force generated by a single kinesin molecule against an elastic load. *Biophys.*, 92:574–578, 1995.

[105] N. Mizuno, S. Toba, M. Edamatsu, J. Watai-Nishii, N. Hirokawa, Y.Y. Toyoshima, and M. Kikkawa. Dynein and kinesin share an overlapping microtubule-binding site. *EMBO J.*, 23:2459–2467, 2004.

[106] N.R. Morris and P.J. Hollenbeck. The regulation of bidirectional mitochondrial transport is coordinated with axonal outgrowth. *J. Cell Sci.*, 104:917–927, 1993.

[107] M.J.I. Müller, S. Klumpp, and R. Lipowsky. Molecular motor traffic in a half-open tube. *J. Phys.: Condens. Matter*, 17:S3839–S3850, 2005.

[108] M.J.I. Müller, S. Klumpp, and R. Lipowsky. Tug-of-war as a cooperative mechanism for bidirectional cargo transport by molecular motor. *Accepted for publication in PNAS*, 2008.

[109] V. Muresan, C.P. Godek, T.S Reese, and B.J. Schnapp. Plus-end motors override minus-end motors during transport of squid axon vesicles on microtubules. *J. Cell. Biol.*, 135:383–397, 1996.

[110] J.W. Murray, E. Bananis, and A.W. Wolkoff. Reconstitution of ATP-dependent movement of endocytic vesicles along microtubules in vitro: an oscillatory bidirectional process. *Mol. Biol. Cell*, 11:419–433, 2000.

[111] Numerical Algorithms Group (NAG). *NAG C++ library*. `www.nag.co.uk`, Oxford UK, 2007.

[112] A.A. Nascimento, J.T. Roland, and V.I. Gelfand. Pigment cells: a model for the study of organelle transport. *Annu. Rev. Cell Dev. Biol.*, 19:469–491, 2003.

[113] J.A. Nelder and R. Mead. A simplex-method for function minimization. *Comp. J.*, 7:308–313, 1965.

[114] Th. M. Nieuwenhuizen, S. Klumpp, and R. Lipowsky. Walks of molecular motors in two and three dimensions. *Europhys. Lett.*, 58:468–474, 2002.

[115] Th. M. Nieuwenhuizen, S. Klumpp, and R. Lipowsky. Walks of molecular motors interacting with immobilized filaments. *Physica A*, 350:122–130, 2005.

[116] H. Nilsson and M. Wallin. Evidence for several roles of dynein in pigment transport in melanophores. *Cell Motility Cytoskel.*, 38:397–409, 1997.

[117] K. Nishinari, Y. Okada, A. Schadschneider, and D. Chowdhury. Intra-cellular transport of single-headed molecular motors KIF1A. *Phys. Rev. Lett.*, 95:118101, 2005.

[118] M. Nishiura, T. Kon, K. Shiroguchi, R. Ohkura, T. Shima, Y.Y. Toyoshima, and K. Sutoh. A single-headed recombinant fragment of dictyostelium cytoplasmic dynein can drive the

robust sliding of microtubules. *J. Biol. Chem.*, 22:22799–22802, 2004.

[119] M. Nishiyama, H. Higuchi, and T. Yanagida. Chemomechanical coupling of the forward and backward steps of single kinesin molecules. *Nat. Cell Biol.*, 4:790–797, 2002.

[120] C. Pangarkar, A.T. Dinh, and S. Mitragotri. Dynamics and spatial organization of endosomes in mammalian cells. *Phys. Rev. Lett.*, 15:158101, 2005.

[121] A. Parmeggiani, T. Franosch, and E. Frey. Phase coexistence in driven one dimensional transport. *Phys. Rev. Lett.*, 90:086601, 2003.

[122] A. Parmeggiani, T. Franosch, and E. Frey. Totally asymmetric simple exclusion process with langmuir kinetics. *Phys. Rev. E*, 70:046101, 2004.

[123] J. Pecreaux, J.C. Röper, K. Kruse K, F. Jülicher, A.A. Hyman, S.W. Grill, and J. Howard. Spindle oscillations during asymmetric cell division require a threshold number of active cortical force generators. *Curr. Biol.*, 16:2111–2122, 2006.

[124] A.D. Pilling, D. Horiuchi, C.M. Lively, and W.M. Saxton. Kinesin-1 and dynein are the primary motors for fast transport of mitochondria in Drosophila motor axons. *Mol. Biol. Cell*, 17:2057–1068, 2006.

[125] V. Popkov, A. Rákos, R.D. Willmann, A.B. Kolomeisky, and G.M. Schütz. Localization of shocks in driven diffusive systems without particles number conservation. *Phys. Rev. E*, 67:066117, 2006.

[126] W.H. Press, S.A. Teukolsky, W.T. Vetterling, and B.P. Flannery. *Numerical recipes in C++ : the art of scientific computing*. Cambridge University Press, New York, 2002.

[127] H. Qian. A simple theory of motor protein kinestics and energetics. *Biophys. Chem.*, 83:3543, 2000.

[128] L. Rebhun. Structural aspects of saltatory particle movement. *J. Gen. Physiol.*, 50:223–239, 1967.

[129] S.L. Reck-Peterson, A. Yildiz, A.P. Carter, A. Gennerich, N. Zhang, and R.D. Vale. Single-molecule analysis of dynein processivity and stepping behavior. *Cell*, 126:335–348, 2006.

[130] A.R. Reilein, S.L. Rogers, M.C. Tuma, and V.I. Gelfand. Regulation of molecular motor proteins. *Int. Rev. Cytol.*, 204:179–238, 2001.

[131] A.R. Reilein, I.S. Tint, N.I. Peunova, G.N. Enikolopov, and V.I. Gelfand. Regulation of organelle movement in melanophores by protein kinase A (PKA), protein kinase C (PKC), and protein phosphatase 2A (PP2A). *J. Cell Biol*, 142:803–813, 1998.

[132] V. Rodionov, A.J. Hope, T.M. Svitkina, and G.G. Borisy. Functional coordination of microtubule-based and actin-based motility in melanophores. *Curr. Biol.*, 8:165–168, 1998.

[133] S.L. Rogers, I.S. Tint, P.C. Fanapour, and V.I. Gelfand. Regulated bidirectional motility of melanophore pigment granules along microtubules in vitro. *Proc. Natl. Acad. Sci. USA*, 94:3720–3725, 1997.

[134] L. Sachs. *Angewandte Statistik: Anwendung statistischer Methoden*. Springer, Berlin, 1992.

[135] H. Sakakibara, H. Kojima, Y. Sakai, E. Katayama, and K. Oiwa. Inner-arm dynein c of Chlamydomonas flagella is a single-headed processive motor. *Nature*, 400:586–590, 1999.

[136] L. Santen and C. Appert. The asymmetric exclusion process revisited: fluctuations and dynamics in the domain wall picture. *J. Stat. Phys.*, 106:187–199, 2002.

[137] M. Schliwa and G. Woehlke. Molecular motors. *Nature*, 422:759–765, 2003.

[138] B. Schmittmann and R.K.P. Zia. *Statistical mechanics of driven diffusive systems. In C. Domb and J.L. Lebowitz, editors, Phase transitions and critical phenomena Vol. 17.* Academic Press, London, 1995.

[139] M.J. Schnitzer, K. Visscher, and S.M. Block. Force production by single kinesin motors. *Nature Cell Biol.*, 2:718–723, 2000.

[140] I. Schuchardt, D. Aßmann, E. Thines, C. Schuberth, and G. Steinberg. Myosin-5, kinesin-1, and kinesin-3 cooperate in hyphal growth of the fungus ustilago maydis. *Mol. Biol. Cell*, 16:5191–5201, 2005.

[141] G.M. Schütz. *Exactly solvable models for many-body systems far from equilibrium. In C. Domb and J.L. Lebowitz, editors, Phase transitions and critical phenomena Vol. 19.* Academic Press, San Diego, 2001.

[142] R.N. Seetharam and P. Satir. High speed sliding of axonemal microtubules produced by outer arm dynein. *Cell Motil. Cytoskeleton*, 60:96–103, 2005.

[143] U. Seifert. Rupture of multiple parallel molecular bonds under dynamic loading. *Phys. Rev. Lett.*, 84:2750–275, 2000.

[144] A. Seitz and T. Surrey. Processive movememnt of single kinesins on crowded microtubules visualized using quantum dots. *EMBO J.*, 25:267–277, 2006.

[145] H.S. Sheptner, B.M. Paschal, and R.B. Vallee. Characterization of the microtubule-activated ATPase of brain cytoplasmic dynein (MAP-1C). *J. Cell Biol.*, 107:1001–1009, 1988.

[146] C. Shingyoji, H. Higuchi, M. Yoshimura, E. Katayama, and T. Yanagida. Dynein arms are oscillating force generators. *Nature*, 393:711–714, 1998.

[147] G.J. Siegel, B.W. Agranoff, K. Fisher, R.W. Alberts, and M.D. Uhler. *Basic Neurochemistry: Molecular, Cellular and Medical Aspects.* American Society for Neurochemistry, Philadelphia, 1999.

[148] D.A. Smith and R.M. Simmons. Models of motor-assisted transport of intracellular particles. *Biophys. J.*, 80:45–68, 2001.

[149] G.A. Smith, B.J. Murphy, S.P. Gross, and L.W. Enquist. Local modulation of plus-end transport targets herpesvirus enry and egress in sensory axons. *Proc. Natl. Acad. Sci. USA*, 101:16034–16039, 2004.

[150] J. Snider, F. Lin, N. Zahedi, V. Rodionov, C.C. Yu, and S.P. Gross. Intracellular actin-based transport: How far you go depends on how often you switch. *Proc. Natl. Acad. Sci. USA*, 101:13204–13209, 2004.

[151] G. Steinberg. Organelle transport and molecular motors in fungi. *Fungal Gen. and Biol.*, 24:161–177, 1998.

[152] S.H. Strogatz. *Nonlinear dynamics and chaos.* Perseus Books, Cambridge, Massachusetts, 1994.

[153] M. Suomalainen, M.Y. Nakano, K. Boucke, S. Keller, and U.F. Greber. Adenovirus-activated PKA and p38/MAPK pathways boost microtubule-mediated nuclear targeting of virus. *EMBO J.*, 20:1310–1319, 2001.

[154] M. Suomalainen, M.Y. Nakano, S. Keller, K. Boucke, R.P. Stidwill, and U.F. Greber. Microtubule-dependent plus- and minus end-directed motilities are competing processes for nuclear targeting of adenovirus. *J. Cell Biol.*, 144:657–672, 1999.

[155] K. Svoboda and S.M. Block. Force and velocity measured for single kinesin molecules. *Cell*, 77:773–784, 1994.

[156] S. Toba, T.M. Watanabe, L. Yamaguchi-Okimoto, Y.Y. Toyoshima, and H. Higuchi. Overlapping hand-over-hand mechanism of single molecular motility of cytoplasmic dynein. *Proc. Natl. Acad. Sci. USA*, 103:5741–5745, 2006.

[157] M. Tomishige and R.D. Vale. Conversion of Unc104/KIF1A kinesin into a processive motor after dimerization. *Science*, 297:2263–2267, 2002.

[158] M.C. Tuma and V.I. Gelfand. Molecular mechanisms of pigment transport in melanophores. *Pigment Cell Res.*, 12:283–294, 1999.

[159] M.C. Tuma, A. Zill, N. Le Bot, I. Vernos, and V. Gelfand. Heterotrimeric kinesin II is the microtubule motor protein responsible for pigment dispersion in Xenopus melanophores. *J. Cell Biol*, 143:1547–58, 1998.

[160] R.D. Vale. The molecular motor toolbox for intracellular transport. *Cell*, 112:467–480, 2003.

[161] R.D. Vale, T.S. Funatsu, D.W. Pierce, L. Romberg, Y. Harada, and T. Yanagida. Direct observation of single kinesin molecules moving along microtubules. *Nature*, 380:451 – 453, 1996.

[162] R.D. Vale, F. Malik, and D. Brown. Directional instability of microtubule transport in the presence of kinesin and dynein, two opposite polarity motor proteins. *J. Cell Biol.*, 119:1589–1596, 1992.

[163] R.D. Vale, T.S. Reese, and M.P. Sheetz. Identification of a novel force-generating protein, kinesin, involved in microtubule-based motility. *Cell*, 42:39–50, 1985.

[164] C. Valetti, D.M. Wetzel, M. Schrader, M.J. Hasbani, S.R. Gill, T.E. Kreis, and T.A. Schroer. Role of dynactin in endocytic traffic: effects of dynamitin overexpression and colocalization with CLIP-170. *Mol. Biol. Cell*, 10:4107–4120, 1999.

[165] R.B. Vallee and M. P. Sheetz. Targeting of motor proteins. *Science*, 271:1539–1544, 1996.

[166] N.G. van Kampen. *Stochastic processes in physics and chemistry.* Elsevier, Amsterdam, 1992.

[167] A. Vilfan and E. Frey. Oscillations in molecular motor assemblies. *J. Phys.: Condens. Matter*, 17:S3901–S3911, 2005.

[168] A. Vilfan, E. Frey, and F. Schwabl. Force-velocity relations of a two-state crossbridge model for molecular motors. *Europhys. Lett.*, 45:283–28, 1999.

[169] K. Visscher, M.J. Schnitzer, and S.M. Block. Single kinesin molecules studied with a molecular force clamp. *Nature*, 400:184–189, 1999.

[170] Z. Wang, S. Khan, and M.P. Sheetz. Single cytoplasmic dynein molecule movements: characterization and comparison with kinesin. *Biophys. J.*, 69:2011–2023, 1995.

[171] Z. Wang and M.P. Sheetz. One-dimensional diffusion on microtubules of particles coated with cytoplasmic dynein and immunoglobins. *Cell Struct. Func.*, 24:373–383, 1999.

[172] F.D. Warner and J.H. McIlvain. Kinetic properties of microtubule-activated 13 S and 21 S dynein ATPases. Evidence for allosteric behaviour associated with the inner row and outer row dynein arms. *J. Cell Sci.*, 83:251–267, 1986.

[173] R. Wedlich-Söldner, A. Straube, M.W.Friedrich, and G. Steinberg. A balance of KIF1A-like kinesin and dynein organizes early endosomes in the fungus *Ustilago maydis*. *EMBO J.*, 21:2946–2957, 2002.

[174] M.A. Welte. Bidirectional transport along microtubules. *Curr. Biol.*, 14:R525–R537, 2004.

[175] M.A. Welte, S. Cermelli, J. Griner, A. Viera, Y. Guo, D.H. Kim, J.G. Gindhart, and S.P. Gross. Regulation of lipid-droplet transport by the perilipin homolog LSD2. *Curr. Biol.*, 15:1266–1275, 2005.

[176] M.A. Welte, S.P. Gross, M. Postner, S.M. Block, and E.F. Wieschaus. Developmental regulation of vesicle transport in Drosophila embryos: forces and kinetics. *Cell*, 92:547–557, 1998.

[177] Inc. Wolfram Research. *Mathamatica*^{R} *5.2 and 6.* Champaign, USA, 1988-2007.

[178] R. Wubbolts, M. Fernandes-Borja, I. Jordens, E. Reits, S. Dusseljee, C. Echeverri, R.B.

Vallee, and J. Neefjes. Opposing motor activities of dynein and kinesin determine retention and transport of MHC class II-containing compartments. *J. Cell Sci.*, 112:785–795, 1999.

[179] Z. Yang and L.S.B. Goldstein. Characterization of the KIF3C neural kinesin-like motor from mouse. *Mol. Biol. Cell*, 9:249–261, 1998.

Fig. A.16: Molecular motor researchers playing molecular motors playing tug-of-war. From right to left: Stefan Klumpp, Yan Chai, Janina Beeg, Steffen Liepelt, Christian Korn, and Melanie Müller.

Acknowledgments

At the end I want to thank the people who supported me during my work on this thesis.

First of all I thank my supervisor Prof. Dr. Reinhard Lipowsky for introducing me to the topic of molecular motor traffic, and for his ideas and support during my work. I am also very grateful to my 'semi-supervisor' Dr. Stefan Klumpp for all our discussions and his generous help even after his moving to the United States.

Furthermore, I thank the people of the MPI-KG theory department for the pleasant working atmosphere, and my office mates for a comfortable office ambiance. I especially thank the department's 'motor guys' for enjoyable discussions and other activities on molecular motors, see Fig. A.16. Also thanks to Gunnar Linke and Jörg Menche for their incredible knowledge of Unix and Gnuplot. I am very grateful to Stefan Klumpp, Krzysztof Baczynski, Janina Beeg, Yan Chai and Lothar Reich for proofreading parts of the manuscript.

I thank Gero Fink and Cécile Leduc for discussions on motor experiments and modelling, and Katrin Messerschmidt and Lothar and Marlis Reich for helping a physicist find a way through the biochemical jungle of molecular motors.

Finally, I want to thank my parents and my friends for their support.